Universitatea Politehnica din Bucureşti
Universitat Politècnica de Catalunya

PhD Thesis

Contributions to aerostructures morphing with piezoelectric actuators

Şcoala doctorală de inginerie aerospaţială
Escola Tècnica Superior d'Enginyeries Industrial i Aeronàutica de Terrassa

Supervisors: Prof. Ion Fuiorea
Prof. Lluís Gil Espert
Author: Albert Arnau Cubillo
Date: July 2019

Contents

List of notation

Symbol	*Meaning*
c	Specific heat
D	Electric displacement
$\tilde{D}$	Electric displacement temperature coefficient
d	Piezoelectric charge matrix
e	Piezoelectric stress matrix
E	Electrical field intensity
E_c	Coercive electrical field
E_t	Transition electrical field
$\tilde{E}$	Pyroelectric voltage coefficient
$E_{x/y/z}$	Elastic modulus in the x/y/z direction
g	Piezoelectric voltage matrix
G	Shear modulus
k	Electromechanical coupling factor
p	Pyroelectric coefficient
P	Polarization vector
P_s	Spontaneous polarization magnitude
$\tilde{P}$	Pyroelectric polarization coefficient
Q	Electrostrictive constant with respect to polarization
S	Strain vector
s	Elastic compliance matrix
s^D	Elastic compliance matrix at constant electric displacement
s^E	Elastic compliance matrix at constant electric field
t	Thickness
T	Stress vector
U	Internal energy
V	Voltage
α^D	Thermal expansion coefficient at constant electric displacement
α^E	Thermal expansion coefficient at constant electric field
β^T	Thermal expansion coefficient at constant stress
Γ	Gibbs potential
ε_0	Dielectric permittivity of the vacuum
ε^T	Dielectric permittivity matrix at constant stress
ν	Poisson coefficient
θ	Temperature
θ_c	Curie temperature
ρ	Density
Ψ	Entropy

Abstract

Since the first models developed in the late 19th century the applications of piezoelectric materials have been progressively growing in number. The capacity of this materials to couple electric and mechanic fields makes them perfect candidates in the study of geometrical morphing.

Their application in aeronautical products has been traditionally seen from two different perspectives: their use as sensors and as actuators. Both functions present potential benefits and improvements with promising applications. While the investigations in the past years focused mainly in the analysis and integration of piezoelectric materials in structures as means of implementing what is known as structural health monitoring systems, the application of this type of materials as actuators in the geometrical control of structures also awakes interest in the scientific community.

In its present state of development, the technology for morphing control of structures using piezoelectric actuators is not yet advanced enough as to integrate such systems in commercial products. However, the field is in continuous development and the evolution of the materials and the integration solutions bring the technology closer to industrial application.

This thesis aims at studying the feasibility of application of piezoelectric-actuated morphing aeronautical structures in current aircraft concepts. The analysis is performed at a theoretical level analyzing the static and dynamic performance of currently available actuators and motion amplification technologies.

The research presented in this thesis is directed in two different applications of utilization of the actuators: as static actuators producing deformation of the aerodynamic surface and as dynamic actuators controlling a classic aerodynamic control surface. In each of the applications a different type of piezoelectric actuator architecture has been used: a piezoelectric patch has been selected for static morphing applications and a piezoelectric-stack-based actuation system for the dynamic control of the conventional control surface.

The static experiments performed aimed at demonstrating the suitability of piezoelectric actuators as morphing devices. This analysis was performed analyzing the deflections produced in the trailing edge of an aerodynamic profile. On the dynamic experiments a wing was conceived to experience flutter at very low speeds and the piezoelectric actuator was used as actuating element in an anti-flutter system.

The analysis of the obtained experimental results for both types of systems shows promising results as the actuating configurations managed to perform as designed. The static experiments showed substantial deformation of the trailing edge of the wing profile making this configuration mature enough for further experimentation such as wind tunnel testing. The deflections produced were, however, not significant enough for the direct application into larger scale configurations. Scalability of the technological solutions remains one of the major challenges of the technology in the morphing applications.

The dynamic results showed good performance of the actuators in the anti-flutter demonstrator during wind tunnel testing. The experiments showed the stability of the system well passed the flutter velocity and allow for further experimentation in structures presenting higher flutter speeds.

With the development of the next generation of advanced piezoelectric ceramics, with piezoelectric coefficients twice as large in comparison to PZT-based ceramics, the application of the deforming structure concept is very promising for application in larger demonstrators in both static and dynamic applications. The next generation of piezoelectric materials presents itself as a first step into a solution to the scalability of the technology for application into full-scale demonstrators.

Acknowledgments

Firstly I would like to express my gratitude to both my tutors in the present thesis, Dr. Ion Fuiorea and Dr. Lluís Gil Espert without whose support and encouragement the research and the thesis would not have been completed. My thanks also to all the professors and auxiliary personnel that made possible to develop this thesis as a cotutelate degree between the UPB and the UPC.

Besides, I would like to thank Dr. Lucian Pislaru-Dinescu and the team at ICPE-CA. Their inestimable help made possible to perform the interferometric experiments for the characterization of the dynamic behavior of the piezoelectric patch. Their support in the research both as guidance and equipment resulted in the research results presented in the thesis.

I would like to thank also, Dr. Ioan Ursu. As the coordinator of the AFDPA project took me into the researchers team and provided the necessary information and infrastructure to research the dynamic behavior of a piezoelectric-actuated control system.

I would like to thank my colleagues Ionel Popescu and Dr. Lica Flore for their support in the experiments performed at Straero facilities in the mechanical characterization of the AFDPA system.

Lastly I would like to show my appreciation to all the people that helped and supported me in the development of the research presented in this thesis and that helped me finish it successfully.

Introduction

Morphing structures have been present in aviation since its origins. The first aircraft concepts used twisting wingtips to achieve lateral control following the example of birds. This technology, though very efficient aerodynamically, proved too complex as the aircraft evolved and was readily abandoned in favor of articulated control surfaces distributed at discrete locations throughout the aerodynamic surfaces. Articulated of control surfaces presented advantages in terms of simplicity of actuation and structural integration and allowed for a reasonably good aerodynamic efficiency. This evolution implied, though, a significant compromise as fixing the geometry of the aerodynamic surfaces means optimizing the aircraft for a particular flight condition. At that flight condition, adopted as design condition, the control surfaces are neutral thus maximizing the aerodynamic efficiency of the vehicle. This implies in most of the cases that the aircraft aerodynamics are optimized at a particular cruise regime, considering a narrow weight, speed and altitude domain; in any other flight condition the aerodynamic efficiency decreases. This decrease is particularly relevant when the control surfaces of the aircraft are in a position different than neutral.

This approach has proven a very useful compromise in the development of aircraft so far. Currently, though, aviation is reaching the limits of efficiency under this assumption as it is not possible anymore to obtain significant aerodynamic improvements with the restriction of having a single optimal flight condition. The latest aircraft use the control surfaces as means of optimizing the aerodynamic performance throughout the flight. In this regard, the latest Boeing models use the flaps and ailerons to optimize the span-wise lift distribution thus increasing efficiency. Airbus implemented in its latest aircraft the functionality of ailerons as load alleviation controls offering the aircraft control over the lift distribution close to the wingtips, the part of the wing that plays the most important role in the reduction of drag. These innovations have been possible mainly due to the electrification of aircraft and the use of fly-by-wire and fly-by-light control systems, which allow for an unprecedented flexibility of the control surface actuation systems design in comparison with mechanical systems.

In the effort of increasing aerodynamic efficiency throughout the flight envelop, one of the possible technologies that emerge as candidates is the morphing of aerostructures. This technology implies modifying the aerodynamic shape of the aircraft or a part of it. The geometrical change of the aerodynamic shape of the aircraft completely changes the paradigm as a different geometry can be adopted according to the flight condition in order for the aircraft to fly at optimum efficiency throughout the flight. Moreover, morphing the aircraft's aerodynamic shape allows for continuous shapes which, in turn, leads to cleaner aerodynamics reducing drag and noise.

The morphing of aerostructures can be performed through a diversity of actuators with radically different technological approaches: hydraulic actuators, piezoelectric actuators, shape memory alloys and electrostrictive actuators among others. Each type of actuation technology presents different characteristics which makes them suitable for particular applications. Hydraulic systems represent the technology currently in application in most primary and secondary commercial aircraft controls. These systems, although very robust and powerful, present major disadvantages such as the weight and the necessity of a source of hydraulic power to operate. Electrically-driven actuators present the advantage that the energy source is to some extent already existing on the aircraft through the aircraft's electric system. Due to this, in the past years, the research in aircraft controls has been focusing on "more electric aircraft" with the aim of reducing the complexity of the systems installed thus reducing the weight of the aircraft systems.

Piezoelectric actuators are a type of electrically-driven devices that allow for a very fast response of the output while developing a high specific force when compared to the conventional hydraulic control systems. These materials, discovered in the late 19^{th} century, are currently extensively used in sensing applications and in actuation applications at early experimental level. Piezoelectrics are crystalline materials that produce a deformation when subject to an electrical field. As this effect depends on the type and orientation of the crystals within the material, the actuator can be shaped in any geometry required with very few restrictions. This flexibility in the geometry of the actuator allows for its complete integration in the structure to be controlled. Due to the high forces they produce, the materials have the potential of morphing the structure and in the proper distribution and actuation sequence, the capacity of controlling complex geometries of the desired structure. Moreover, piezoelectric materials present an excellent dynamic response which makes them very good candidates for dynamic actuation applications.

These characteristics make piezoelectric materials an obvious candidate as actuators when considering advanced structural morphing in aircraft applications. The piezoelectric actuators present, though, some challenges such as the high actuation voltages required for actuation or the small deformations they are able to produce.

Piezoelectric materials are studied in this thesis in two main applications that explode the main advantages that the materials present in comparison to conventional actuators: as a replacement of conventional actuators in hinged control surfaces in rapid response dynamic applications and as actuators for morphing applications in quasi-static regime. These applications are introduced from the theoretical point of view, numerically and experimentally to provide a complete analysis on their benefits.

1. State of the art

This chapter presents a brief introduction into the state of the art leading to the investigations performed during the thesis. The analysis performed on the state of the art starts broad and generic in order to present a clear picture of the field of application of the research and progressively narrows as it deepens into the particularities of the thesis.

According to this philosophy, is is pertinent to start with a brief historical review of the integration of control surfaces in aviation as one of the main goals of the thesis is to determine whether conventional actuators can be substituted by piezoelectric actuators in aviation. The review continues to analyze the basic architecture and of conventional control surfaces in which part of the research of this thesis focuses in Sec. 6. The analysis proceeds with a more in-depth presentation of the morphing of aerostructures in the laboratory and also airborne applications, without entering in detail on the type of actuation used in achieving such morphing.

The piezoelectric materials are introduces in terms of phenomenology, types and major applications through history until the present status. The modeling of the piezoelectric materials, from the mathematical, physical and chemical point of view is detailed in Sec. 3.

This part of the research concludes with the other significant application analyzed in this thesis: the application of piezoelectric actuators in the control of morphing aeronautical structures. This review presents important configurations that helped define the starting point for the experiments performed during the preparation of the thesis.

1.1 Aircraft control surfaces

The need for aerodynamic control exists since the beginning of aviation. This control is required to modify the flight trajectory of the vehicle at will, independently of its nature. The role of the control surfaces is to temporally modify the aerodynamic forces actuating on the vehicle in a controlled manner to produce a change in its flying attitude which will translate into a modification of the trajectory.

There are multiple ways of affecting the forces that act on a flying vehicle, out of which the most extensively used are the control surfaces. Control surfaces can be either conventional or morphing. A control surface is a component of an aerodynamic surface of the vehicle which can modify its position relative to the rest of the aerodynamic surface thus modifying the external shape of the vehicle and the forces acting on it. Aircraft presenting a conventional configuration (see Fig. 1.1) have this control surfaces divided into two categories: primary and secondary control surfaces.

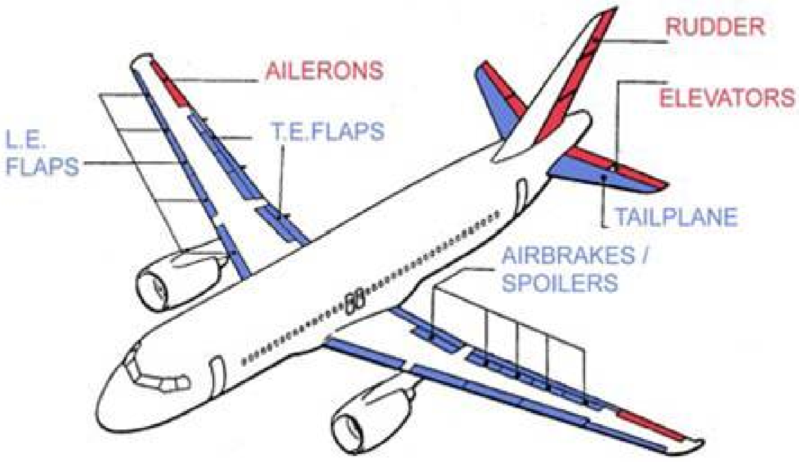

Figure 1.1: Primary (red) and secondary control surfaces (blue) in a conventional aircraft configuration.

The primary control surfaces are the elements which have as the main objective the modification and control of the vehicle trajectory (ailerons, elevator, rudder, etc.) while the secondary control surfaces allow for an optimization of the aircraft performance in specific flight phases (flaps, slats, aerodynamic brakes, trims, etc.). Secondary control surfaces also have an effect on the vehicle trajectory although it is not their main objective to produce such effect. E.g. flaps increase the lift produced by the wings thus pushing the flight path of the vehicle upwards if no correction is applied through the other control surfaces.

Another very extended method for attitude control is the modification of the center of gravity. This method is used as a primary control system on smaller flying vehicles. In these vehicles the modification of the center of gravity is used as means to produce a change in the relative position of aerodynamic elements of the vehicle thus resulting in a change of the trajectory. Large passenger aircraft use center of gravity adjustment as a secondary control system without modification of the aerodynamic shape of the vehicle. The aim of this application is to optimize the performance of the vehicle aerodynamic surfaces.

Other control methods used in aviation include the orientation of the engine exhaust gases to direct the thrust in the desired direction (thrust vectoring) or active flow control (AFC). The applications related to these technologies are either experimental or restricted to non-conventional aircraft. As an example, commercial airliners use thrust reversing (which could be considered as a simple form of thrust vectoring) during the landing maneuver to slow the aircraft while on ground. This technology presents, though, almost no applicability during flight.

This thesis will focus mainly in the application of piezoelectric actuated-morphing in the first type of systems of the three presented. The other two types of systems are considered of no interest to the present thesis because of the applications in which they are implemented.

1.2 Conventional control surfaces

The most extensively used method for the alteration of the aerodynamic forces actuating on flying vehicles (specially aircraft, as per the object of this thesis) is the modification of the external geometry through what are called control surfaces.

The function of the control surfaces is commonly distinguished between primary and secondary control surfaces depending on the influence on the aerodynamics and performance of the vehicle.

- **Primary control surfaces:** include all the elements that have as a main function the modification of the aircraft attitude to affect its trajectory. This group includes: ailerons, elevator, rudder and mixed control surfaces such as elevons.
- **Secondary control surfaces:** include all the aerodynamic elements that modify the geometry of the aircraft but their goal is not to modify the attitude of the aircraft even if their actuation produces such effect. Examples of this are: lift augmentation devices (flaps, slats, variable geometry leading edges, etc.) trim tabs and surfaces, spoilers, etc.

Despite the difference in the utilization of the presented control surfaces they all have in common the fact that they consist in rigid elements that are actuated as rigid solids through a kinematic mechanism.

The differences in the integration of the control surfaces into a particular aircraft come from the design of the actuation mechanism on itself, and not from the design of the control surface. In this aspect, a very light aircraft and a large passenger aircraft share exactly the same principles and design philosophy when it comes to control surfaces while the actuation systems present no similarity at all. In this aspect, the evolution of the control systems since their first implementation in 1903 is the history of the systems designed to actuate these control surfaces.

Different technologies exist in the actuation of the control surfaces:

- **Cables and bars:** the use of a direct link between the pilot control system in the cockpit and the desired control surfaces distributed throughout the aircraft was the first system ever to be implemented in aircraft and is still the most widely used system in recreational aviation and small passenger aircraft. The movement of the pilot control stick or yoke is transmitted through cables and pulleys or push-rods to the control surface directly linking the motion of the stick with the motion of the control surface.
- **Servo-hydraulic systems:** as the aircraft produced started growing in size the control surfaces became heavier and presented larger inertia and the forces actuating on them became to strong for the pilot to directly actuate the controls. At that moment servo-actuated control surfaces were introduced in aviation. In this systems, the pilot does no longer actuate on the control surface directly but instead he operates a hydraulic distribution valve. The distribution valve uses hydraulic fluid to move the control surfaces through hydraulic actuators. In these systems the pilot has still a proportionality between the motion of the control column and the motion of the control surface.
- **Fly-by-wire:** the introduction of electronics on aviation (avionics) and specially computers triggered a revolution in the architecture of control systems. Fly-by-wire refers to the pilot actuating the control surfaces through electrical signals, which are previously processed by a computer. In this systems the pilot's inputs are sent to a computer that translates them into a control surface position change. The computer signal is then translated to a hydraulic distribution valve that uses the same principle as in servo-hydraulic systems to actuate the control surfaces. In this case, though, the direct mechanical link between the pilot and the control surface does not exist. The main consequence of this is that the pilot does not feel the reaction forces of the control surfaces in the commands.

The global tendency of the control technologies used in aviation can be seen from the evolution of the systems used, in this aspect, the industry tends towards what is often referred to as a more electric aircraft (MEA). Several projects exist with this goal in mind. The integration of electric actuators in aircraft, though, is not advanced enough for this technology to be applied in a full-scale demonstrator as of now.

This thesis, through the usage of piezoelectric actuators, presents a possible way for the electrification of the control surfaces towards the goal of more electric aircraft. The application of piezoelectric actuators is considered, as mentioned in the introduction of the thesis in two main applications of the piezoelectric actuators. One of the studied approaches is the actuation of conventional control surfaces.

The applicability of this technology is consistent with the development of more advanced fly-by-wire systems that provide not only control of the aircraft attitude but also optimization of the flight performance and load alleviation during flight. These secondary technologies are continuously being developed by the lead aircraft manufacturers and the latest aircraft models already implement versions of this technology. The application of piezoelectric actuators in these architectures is analyzed in later chapters of the thesis with a comprehensive analysis of advantages and disadvantages of such implementation.

1.3 Morphing of aeronautical structures

An alternative approach to the modification of the aircraft external geometry is the controlled deformation of some surfaces. This geometrical modification is known as structural morphing. Morphing is used in aviation to define structures in which the external shape of the vehicle changes through the deformation of the vehicle skin. This definition allows for the distinction of two main cases of morphing: the cases in which only the structure shell deforms and having underneath a mechanically compliant structure, and the structures in which the internal structural elements of the vehicle also suffer a deformation.

The concept of morphing to modify the aerodynamic characteristics of a vehicle is not new in aviation. Morphing of the wingtips was already implemented in the early models of the Wright aircraft in 1903 to provide roll control of the aircraft. Since then, the application of the technology stagnated due to the simplicity of conventional control structures. In the recent past, reaching the limits of the optimization of the aerodynamics of the aircraft implementing conventional control surfaces and having powerful numerical analysis tools in hand, the concept of morphing reappeared at research level as a possible step towards greater efficiency.

Different types of morphing can be identified when classified according to the type of deformation they produce on the wing. Wingspan morphing, for example, is used to refer to a modification of the span of the aircraft.[1] Depending on the type of deformation, the wing can be planarly deformed, present an out-of-plane transformation or imply a modification of the aerodynamic surface profile.[2] The main historical disadvantage of morphing is the fact that, whenever using conventional actuators, the actuation systems required are heavy enough to compensate for the aerodynamic advantages they present. This is the main reason why research in morphing has not found application so far in the aeronautical industry.

The evolution or materials, particularly the discovery of advanced ferroelectric materials (with piezoelectric properties far greater than the piezoelectric materials naturally existing in nature) and the discovery of shape memory alloys (SMAs), and the spreading of numerical calculation techniques in the design of aircraft (which allows for aerodynamic configurations very close to the theoretical limits of performance for particular flight conditions) allowed to revise the application of morphing geometries as means to increase the domain in which the aircraft performs at the optimum efficiency.

This section presents the concepts developed in terms of geometrical morphing applied to aircraft without detailing the actuation methods involved in the research as those are presented further on in Sec. 1.4.5. The concepts are separated in two categories depending on their level of maturity: laboratory implementation and airborne implementation.

1.3.1 Laboratory implementation

The implementation of morphing geometries has had a wide development at laboratory level. The main focus of the research has been the control of the morphing of aerodynamic surfaces actuating on a single type of morphing. The experiments combining different forms of morphing (e.g. chord and twist) are rare as the complexity of such demonstrators is significantly higher.

Two main groups of experiments can be differentiated when comparing the type of structures used: a first approach is to design an inner mechanism that is the main load carrying element of the structure which actuates in a manner in which an attached morphing skin is deformed at will (see example on Fig. 1.2). The second main approach is to consider a load-carrying structure that deforms while the skin deforms to the desired shape (see Fig. 1.4).

Compliant structure morphing concepts consider a non-structural (or load-carrying) skin which deforms due to the movement of a mechanism embedded in the profile. In this type of mechanisms the only element subject to (desired) deformation is the skin. This concept has been thoroughly studied in DLR as part of two European projects which considered the design and manufacturing of a full-scale demonstrator for a morphing drooped nose leading edge device of a wing (see Fig. 1.2).

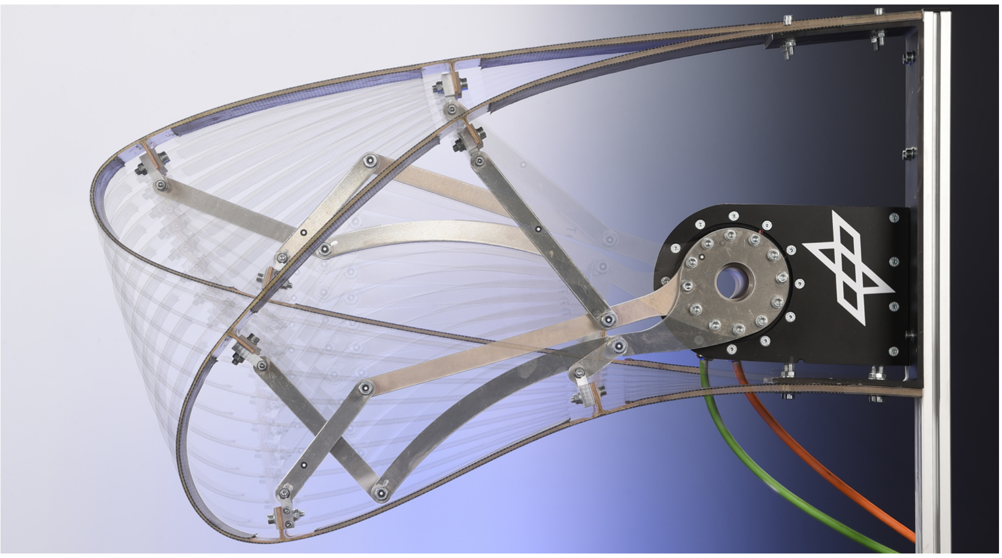

Figure 1.2: Demonstrator performed in DLR for a morphing leading edge device with a compliant actuating mechanism.

One of the most recent and interesting approaches to the span-wise torsion morphing of wing surfaces using compliant structures is the one presented in the NASA experiments on the MADCAT project (Mission

Adaptive Digital Composite Aerostructure Technologies). [3] One of the wind tunnel morphing models developed is shown in Fig. 1.3. This concept proposes a flap-less design in which a reticulated structure throughout the wing actuates as both mechanism for torsional control and load-carrying structure.

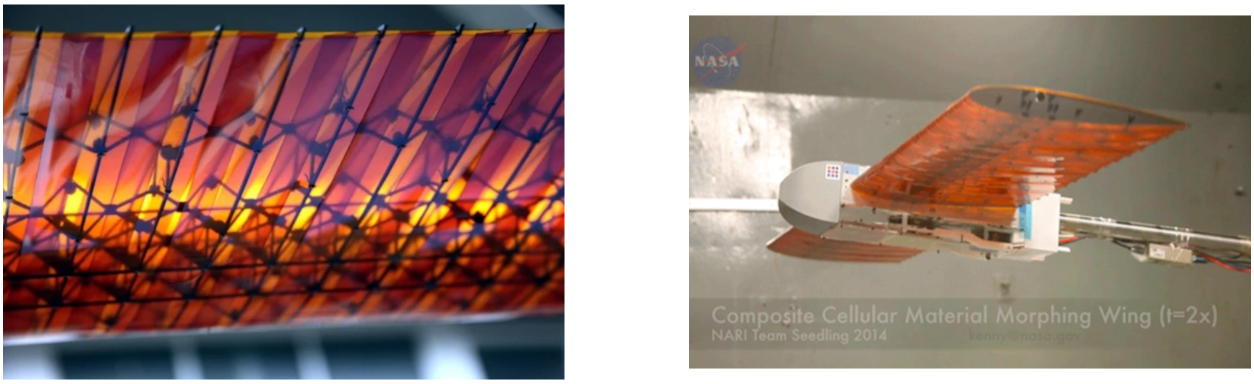

Figure 1.3: MADCAT project wind tunnel demonstrator developed by NASA, detail of the structure (left) and overview of the model (right).

The project performed wind tunnel experiments on the design concluding that the efficiency obtained is equivalent to conventional structures while reducing the weight by approximately 90%. Further experiments included the MIT with the scope of automatizing the manufacturing process. This part of the project however presents no relation to morphing.[4]

In the second category is the experiments performed on elastic load-carrying structures. This category includes all the load-carrying structures that undergo a deformation which drives the morphing of the actuated structure. This type of mechanisms have been experimented on all kinds of aerodynamic surfaces, including wings, tail surfaces and lift augmentation devices.

Although the type of experiments performed in lift augmenting devices in [5] or [6] present interesting approaches to the morphing problem, the application of morphing systems in wings is the main focus of the thesis. Hence, other morphing applications are considered outside of the scope of the present thesis.

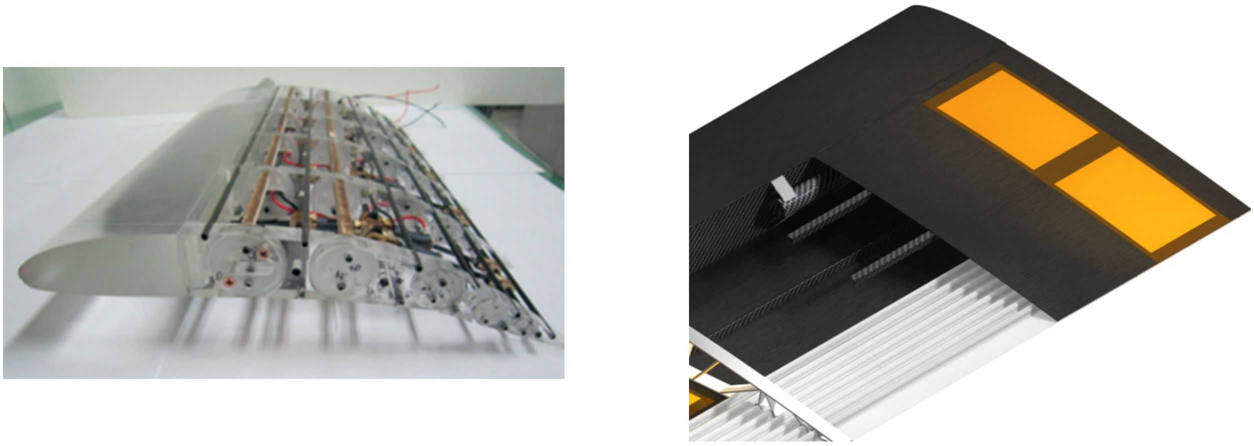

Figure 1.4: Examples of non-load-carrying skin structure morphing (left) and structural skin morphing system (right).

Two main lines of research are identified analyzing the experiments performed in the recent years in morphing of load-carrying structures: experiments with the aim of controlling span-wise torsion distribution in the wing and experiments aimed at controlling profile camber for individual sections of the wing. In the first category, different approaches exist such as internal structures with non-load-carrying skins ([7] or [8]) or structures in which the skin is a main structural element ([9] or [10]). An example of each of these approaches is shown in Fig. 1.4.

A conclusion from the analysis of the state of the art in terms of aerodynamic surfaces morphing is that an approach of a load-carrying skin is beneficial when combined with surface actuators. This combination is one of the approaches analyzed further on in this thesis.

1.3.2 Airborne morphing concepts

The list of projects implementing morphing technology with airborne demonstrators is less extensive than the laboratory experiments presented in the previous section. This section does not consider projects with discontinuous aerodynamic skin such as variable sweep technology (widely used in military aircraft through history) as it is of no interest to the present research.

Two main research projects have been selected to represent the state of the art in application of morphing structures in aviation (both commercial and military) while different projects exist as small scale flying demonstrators (UAVs). The two full-scale projects are the Aviation Partners - FlexSys Flexfoil technology, applied to a NASA research aircraft (see Fig. 1.6) and the DARPA morphing aircraft technologies program AFTI/F-111 demonstrator (see Fig. 1.7). These projects are detailed below.

The Aviation Partners - FlexSys project Flexfoil is the first morphing project that achieved the level of light test maturity in a full-scale commercial flight demonstrator. The project, developed by Aviation Partners and FlexSys and integrated in an existing testing aircraft by NASA, aimed at substituting the trailing edge flaps of a business jet with a morphing system with increased performance. The ground demonstrator of the system can be seen in Fig. 1.5.

The system uses a composite skin and a compliant one-piece jointless mechanism to achieve the desired motion. The system is currently being flight-tested in the NASA facilities (a picture during the testing campaign can be seen in Fig. 1.6).

The DARPA morphing project is prior to Flexfoil and represents one of the first modern projects that implemented compliant structural design in the morphing of a real aircraft wing. The project involved substituting the leading and trailing edge control surfaces in an F-111 aircraft by a deformable wing structure that could accomplish the same requirements with increased aerodynamic performance and dynamic response. The developed wing is shown implemented in the airborne demonstrator in Fig. 1.7. [11]

1.4 Piezoelectric actuation

Piezoelectricity is the property of some materials to present a coupling between the mechanical and the electric fields. This means that piezoelectric materials produce an electrical charge in two opposing sides of the material when subject to a mechanical stress and vice-verse. In this thesis the piezoelectric materials are studied only as actuators (transformation from electrical field to mechanical field) which means studying the converse piezoelectric effect.

Figure 1.5: Flexfoil ground demonstrator showing the deformation capability for both leading and trailing edge devices.

Figure 1.6: Flexfoil system integrated in a NASA Gulfstream 3 for flight testing during 2018.

Figure 1.7: AFTI F-111 prototype developed by DARPA and flown by NASA as part of the DARPA morphing program.

Piezoelectric actuation presents notable advantages in comparison to other actuation systems, one of the main advantages it poses is the adaptability of the system to the structure to be actuated. This versatility resides on the fact that piezoelectric actuators produce a deformation of their crystalline strustures which macroscopically translates as a displacement. The fact that the motion in the piezoelectric actuator is intrinsic to the material itself has the advantage that the actuator can be designed in virtually any form (as long as it is capable, in such geometry, to produce the desired deformation).

This characteristic of the piezoelectric materials has been extensively used in the past applications of the material.

1.4.1 Historical background

The history of the discovery of the piezoelectric materials is a recent one. Their discovery and analysis goes back to the 18^{th} century when scientists theorized their existence although they were not formally discovered until the 19^{th} century. Since their discovery piezoelectric materials draw few attention in terms of their applicability and not until well in the 20^{th} century they found extensive application. The second half of the 20^{th} century saw its in-depth study as more an their utilization grew until the present days. In spite of this history, not until very recent years, piezoelectric materials started arousing interest in terms of structural morphing particularly in the aerospace industry, due to the significant drawbacks that this type of materials present in such applications.

This section presents an in-depth historical development of the piezoelectric materials and their study from the historical point of view (an analysis of the modeling of this type of materials is presented in Sec. 3).

The discovery of piezoelectricity has its roots in a related phenomenon called pyroelectricity in which some materials present polarization when subject to a temperature change. This phenomenon is known since the times of the ancient Greece when in the 4^{th} century BC the philosopher Theophrastus wrote the first description of the phenomenon in the tourmaline crystal. [12]

During the eighteenth century, Carolus Linnaeus was the first to relate the pyroelecric properties of Tourmaline to electricity and called the material *lapis electricus*. [13] The first scientific article on the field was written in 1756 by Franz U.T. Aepinus and presented in the Royal Academy of Sciences in Berlin. [14] The article related the pyroelectric properties to electricity rather than to friction (as it was thought until that time) [15] by noticing the opposite polarities found in opposing ends of the crystal.

Basing their research on the discoveries by Linnaeus and Aepinus, René Just Haüy and Antoine César Becquerel theorized a similar relation between electrical and mechanical fields in 1801 [16] and in 1823 [17] respectively although their experiments proved rather inconclusive as their results were too influenced by the effects of friction (triboelectricity) due to the insulators used. [18]

Piezoelectricity was formally discovered by Pierre and Jacques Curie in 1880. The two brothers were the first to unequivocally demonstrate the effect and perform the first characterization of the phenomenon. [19] Their discovery was published in April 8th, 1880 in the French Mineralogy Society and at the Academy of Sciences on August 24th. The related articles were published in 1880 and 1881. [20] [21] The Curie brothers experimented on the tourmaline crystal through what is currently known as piezoelectric direct effect (a stress field on the crystal results on an electrical charge displacement between two opposite faces of the crystal).

Hankel called this phenomenon the piezoelectric effect, deriving the word from the greek “$\pi\iota\acute{\varepsilon}\zeta\varepsilon\nu$" (to press). [22] In 1881, Lippmann theorized the existence of a converse piezoelectric effect, where electrical energy could be transformed into mechanical energy, based on the thermodinamics of the phenomenon. [23] The Curie brothers confirmed Lippmann's theory experimentally demonstrating that the crystals underwent a mechanical stress proportional to the applied electrical field.

Voigt published the first extensive piezoelectric model based on thermodynamic potentials analysis in 1890 [24] and the equations describing the linear behavior of the piezoelectric materials developed in tensor form in 1894. [25] He later extended the model in a further study in 1910. In his analysis, Voigt considered both piezoelectric and pyroelectric properties as his analysis was thermodynamic (macroscopic) and did not enter details at the atomic level. Moreover, his work included a classification of the 20 crystalline structures capable of piezoelectricity, categorized and presenting their respective piezoelectric constants in the tensorial notation he developed. [26]

The first major application of piezoelectricity appeared in World War I (1918) when Langevin used a quartz transducer to detect underwater objects through echolocation, giving birth to the precursor of the SONAR (SOund, NAvigation and Ranging), the ASDIC (Allied Submarine Detection Investigation Committee). [27] [28] In the period between wars, single crystal Rochelle salt became the standard transducer in SONAR devices developed. [29]

In 1921, Valasek published an article highlighting the piezoelectric properties of Rochelle Salt ($KNaC_4H_4O_6 \cdot 4H_2O$). Valasek presented an analygy in the piezoelectric and magnetic behavior of materials in terms of theoretical modeling. The electric displacement, the electric field and the polarization are analogue to the magnetic B, H and current intensity. Moreover, polarization presented an hysteresis behavior analogue to the magnetic behavior of iron. [30]

This discovery revolutionized the field of piezoelectricity as ferroelectric materials were discovered with piezoelectric constants more than 100 times higher than the materials used until that moment. [31] Despite his work, Valasek never used the term ferroelectricity to describe this behavior, which had been proposed by Schroedinger in 1912 in the connection with the idea that polar liquids might become spontaneously electrified when solidified. [32].

Rochelle salt presents the problem, though, that it loses the ferroelectric properties with slight chemical composition changes making it hard to mass-produce so it never allowed for more than laboratory experimentation and very restricted military application.

The following years saw a rapid advance on the development of the piezoelectric theories developed by the hand of Cady (considered the father of modern piezoelectricity). Cady developed the quartz crystal-controlled oscillator and the narrow-band quartz crystal filter in 1921. [33]

At the end of World War II barium titanate ($BaTiO_3$) was first produced. [34] Barium titanate was a cheap to produce ferroelectric piezoelectric material with perovskite crystalline structure (see Sec. 1.4.3) that could be polled artificially[1] to obtain piezoelectric constants several times higher than naturally occurring piezoelectric materials.

Devonshire developed the theory of ferroelectric phase transition in his works in 1949 [35] and 1951 [36] based on the Landau-Ginzburg phase transition thermodynamic theory for barium titanate. The theory explained the conditions in which a symmetric paraelectric crystal (or phase) changed its structure to a ferroelectric crystal upon cooling and vice-versa.

Barium titanate would become obsolete a few years later when in 1954 lead zirconate titanate ($PbZrO_3$-$PbTiO_3$) or PZT, was studied by Jaffe. [37] This material is a solid metallic solution that presents maximum properties close to the 50%-50% composition between the two ceramics that form it. [38] PZT ceramics present piezoelectric properties that far exceed the barium titanate.

Currently efforts are being made to find ceramics with better piezoelectric properties than PZT in an effort to increase the performance of the piezoelectric applications and to eliminate the use of lead in this field of application. These materials are presented in detail in Sec. 1.4.3.

1.4.2 Standards on piezoelectricity

Several standards exist worldwide that intend to set a common frame for the development of piezoelectric materials. These regulations and standards frequently present the linear theory as the base of any study for the simplicity it presents. The first, and most important, standard available is the ANSI/IEEE Std 176-1987. This standard was preceded by a version by the same publisher in 1949, 1958 and 1978. Military standards exist in the United States and also European ones have been published and adopted by several countries around the world. This section looks into these standards with more detail.

---

[1] The manufacturing of piezoelectric materials is detailed in Sec. 1.4.4

1.4.2.1 ANSI/IEEE Standards

The Institute of Electrical and Electronics Engineers (IEEE) has published several standards regarding piezoelectricity, ferroelectricity and magnetostrictive materials. The most important standards for this report are the following:

- **176-1987 Standard on Piezoelectricity:** this standard was first published in 1949 and revised in 1958 and 1978. It presents an overview of the theoretical formulation for piezoelectric materials with an insight in crystallography. It also presents solutions for the static homogeneous case and considerations for the measurement of elastic, piezoelectric and dielectric properties. The theoretical considerations are referred further on in this thesis in Sec. 3.2.1. [39] [40]
- **178-1958 (R1972) Standards on Piezoelectric Crystals:** this standard considers the determination of the elastic, piezoelectric and dielectric constants of piezoelectric crystals and also their electromechanical coupling factor.
- **179-1961 (R1971) Standards on Piezoelectric Crystals:** the standard contains information on standard practices for measurements of piezoelectric crystals.

1.4.2.2 MIL-STD 1376B

The standard was published by the Defence Department of the United States of America and adopted by the Navy. This standard presents the classification of piezoelectric materials according to the so called "Navy type" presented later on in Sec. 1.4.3. The standard was cancelled in 1999 but it is still used as a reference by piezoelectric ceramics manufacturers in the classification of materials. [41] [42]

1.4.2.3 CENELEC Standards

The European Comitee for Electrotechnical Standardisation (CENELEC) is the recognised entity to publish standards in the field of piezoelectricity. The standard that concerns piezoelectric ceramics is the EN 50324 (Piezoelectric properties of ceramic materials and components) in its three parts presented below: [43]

- **50324-1:** Definitions and classifications
- **50324-2:** Methods of measurement and properties - low power
- **50324-3:** Methods of measurement - high power

This standard is adopted by several countries that have published their versions on the standard like England (BS EN 50324), Germany (DIN EN 50324) or Romania (SR EN 50324) among others. [44]

1.4.2.4 Other standards

Other piezoelectric standards include the published by the International Electrotechnical Commission (IEC) such as the IEC 60483 (1976-01) which is a guide to dynamic measurements of piezoelectric ceramics with high electromechanical coupling. [45] Also remarkable are the standards published by the Japanese Industrial Standards Committee (JISC) such as the EMAS-6100 about electronic test methods for the characterisation of piezoelectric ceramic oscillators. [46]

1.4.3 Materials used

Piezoelectric materials can be either natural or synthetic. This section presents a short enumeration of the most common piezoelectric materials focusing on the materials that are relevant in their application in actuators.

1.4.3.1 Natural piezoelectric materials

Natural piezoelectric materials can be separated in two categories, crystalline materials or non-crystalline materials. Some crystals such as tourmaline, quartz or Rochelle salt exist in nature and present piezoelectric properties. These type of materials, as detailed in Sec. 1.4.1 were the ones that propitiated the discovery of piezoelectricity. Other materials exist, however, which present piezoelectric properties and are not crystals such as silk, some types of wood, rubber or bone among others. All these materials have in common a structure in which an applied stress results in a net polarization. This type of materials present modest piezoelectric properties in comparison to synthetic materials and have seldom been used ever since the discovery of ferroelectrics.

1.4.3.2 Synthetic piezoelectric materials

Synthetic piezoelectric materials are not found in nature and have been discovered and developed in an effort to obtain mechanical and piezoelectric properties that natural piezoelectric materials do not possess. Synthetic piezoelectric materials are for the major part ferroelectric ceramics. Only these materials are analyzed in the thesis because of the characteristics that they present. The analysis on crystallography presented in Sec. 3.1.2 details that out of the 32 crystallographic classes, 20 have the potential for piezoelectricity. Out of this, 10 show spontaneous polarization without any mechanical stress, the remaining 10 present polarization in the presence of a mechanical field. The perovskite crystalline structure (present in $BaTiO_3$) is, since its discovery, the most frequent structure in the piezoelectric materials used nowadays. A very frequently used solution involves the solid solution of two ceramics with perovskite structure to form the piezoelectric material (as is the case with PZT).

Piezoelectric materials with a different structure than perovskite also exist but are a minority and represent a small fraction of the manufactured piezoelectric materials. [47] Because of the small importance of this materials in the fabrication of piezoelectric actuators this materials are not considered in the present analysis.

Some of the most relevant or mostly used synthetic piezoelectric materials (ferroelectric ceramics) are presented below:

- **Barium titanate:** ($BaTiO_3$) it has been the most extensively studied material since the discovery of ferroelectricity in 1945. It presents perovskite structure at high temperatures. As the temperature lowers, different structures can be observed: cubic (over $393K$), tetragonal (between $278K$ and $393K$), orthorhombic (between $183K$ and $278K$), and rhombohedral (below $183K$). [48]

- **Lead titanate:** ($PbTiO_3$) it was originally used in paints because of its optical characteristics until the discovery of its ferroelectric properties. [49] Lead titanate is isomorph with barium titanate and has a Curie temperature of $763K$. Its tetragonal structure has a distortion of 1.06, which is a relatively large value in comparison with the ideal perovskite cubic structure. It has no other phase transformations. [50]
- **Lead zirconate titanate (PZT):** ($Pb[Zr_xTi_{1-x}]O_3$) it is a ferroelectric solution of lead zirconate ($PbZrO_3$) and lead titanate ($PbTiO_3$). Despite the lead zirconate being antiferroelectric, the addition of more than 10% of lead titanate turns the solution ferroelectric. Solutions richer in titanate are tetragonal while the ones richer in zirconate are rhombohedral. The addition of titanate reduces the Curie temperature. At a composition close to 50% for each compound, the dielectric constant and the radial coupling show a pronounced maximum. [50]
- **Potassium niobate:** ($KNbO_3$) it is a perovskite ferroelectric crystal with orthorhombic structure. Its structure transitions from cubic (above $691K$), to tetragonal (between $476K$ and $691K$), orthorhombic (between $223K$ and $476K$) and rhombohedral (below $223K$). Because of its optical characteristics, its mainly used in lasers. [51]
- **Lithium niobate:** ($LiNbO_3$) is a versatile ferroelectric material thoroughly characterised because large crystals can be produced using crystal growing techniques. It presents a Curie temperature of $1418K$. It is used in laser applications due to its optical performance. [52]
- **Lithium tantalate:** ($LiTaO_3$) this material was discovered to be ferroelectric in 1949 by Matthias and Remeika. Its Curie temperature is around $890K$. Despite its polarization being not as large as in the lithium niobate, it is used in the optical field due to its large electro-optical coefficient. [51]

1.4.3.3 Classifications

According to the different standards available on piezoelectricity and presented in Sec. 1.4.2 different classifications arise for piezoelectric materials depending on their general characteristics, specially piezoelectric and dielectric but also in terms of operating temperature range (Curie and depolarization temperatures) and mechanical properties.

The classification of piezoelectric materials according to their coercive fields (the coercive field is the electrical field required to develop the maximum polarization of the material, see Sec. 3.1.1) can be done as presented: [53]

- **Hard ceramics:** a piezoelectric ceramic is considered hard when its coercive field is large ($> 1kV/mm$). These piezoelectric materials show an extensive linear region but small strain magnitudes. Usually, this type of materials present high Curie temperatures ($T_c > 250\,°C$).
- **Soft ceramics:** when the coercive field of the ceramic is between $0.1kV/mm$ and $1kV/mm$ it is called a soft piezoelectric ceramic. These ceramics present large field-induced strains and also a relatively large hysteresis. The Curie temperatures for these materials is usually between $150\,°C$ and $250\,°C$.

- **Electrostrictors:** when the ceramic has a coercive field lower than $0.1kV/mm$, the material presents approximately a quadratic dependence of strain with the electrical field. These materials are usually referred to as electrostrictive materials.

Despite being currently obsolete, the MIL-STD 1376B standards proposed a classification of the materials that is presently used. The classification proposed six groups of materials as follows: [41]

- **Type I:** is a modified PZT (Lead Zirconate Titanate) for medium-to-high power applications, like acoustic ones. They have good resistance to depoling at high electric drive and stress.
- **Type II:** is a modified PZT with a higher charge sensitivity. It has better time stability and is suitable for passive devices. These type of materials cannot be used in high electric drive applications due to dielectric heating.
- **Type III:** they are similar to type I piezoelectrics but greatly improved for high electric drive applications by significantly reducing the losses produced. The dielectric and mechanical losses present a reduced dependency with electrical field.
- **Type IV:** modified BT (barium titanate) for moderate electric drive applications. They present a lower piezoelectric activity than types I, II and III and also a lower Curie temperature.
- **Type V:** they present a composition between types II and IV and also intermediate piezoelectric properties.
- **Type VI:** similar to type II, these materials provide higher charge sensitivity and dielectric constants. The result of this is a lower Curie temperature.

The properties for each of the types of piezoelectric materials according to this standard is presented in Table 1.1.

Table 1.1: Classification of piezoelectric materials according to the standard DOD STD-1376B. [41]

Designation	Commercial name	Material	Notes
Type I	PZT-4	PZT	High power (Hard)
Type II	PZT-5A/PC5	PZT	High sensitivity (Soft)
Type III	PZT-8	PZT	High power (Hard)
Type IV	PC-3	BT	High power (Hard)
Type V	PZT-5J	PZT	High sensitivity (Soft)
Type VI	PZT-5H	PZT	High sensitivity (Soft)

1.4.3.4 Lead-Free piezoelectric materials

Different factors contribute to the search for piezoelectric materials (specifically ferroelectric ceramics) that do not present lead in their structure. The main reason is environmental; PZT contains around 60% of lead in its structure. [54] Due to the harmful effects associated to lead, substitutes are being investigated that are lead-free. Another reason for lead-free piezoelectric materials is the impossibility to be co-fired with nickel; this forces the electrodes to be silver or palladium significantly increasing the cost of the actuator. [55]

The development of lead-free piezoelectrics has been focused on the perovskite-structure crystals such as the barium titanate ($BaTiO_3$), potassium niobate ($KNbO_3$) bismuth-sodium titanate ($(Bi_{1/2}Na_{1/2})TiO_3$) and bismuth-potassium titanate ($(Bi_{1/2}K_{1/2})TiO_3$). The solid solutions from these materials are also good candidates. Perovskite-structured ceramics present high piezoelectric constants and high Curie and depolarization temperatures which makes them suitable for actuators. [56]

1.4.4 Manufacturing of piezoelectric materials

As mentioned in Sec. 1.4.3 different types of piezoelectric materials exist, from naturally occurring ones to synthetic materials. For the purpose of the present thesis only the synthetic piezoelectric materials are of interest, and out of these, ferroelectric ceramics present relevance in the field of structural morphing and actuation. Ferroelectric ceramics are generally poly-crystalline structures of materials presenting a perovskite crystalline structure and showing a clear polarization direction. This polarization direction is not present in the fabrication of synthetic ferroelectric ceramics from the beginning, it only appears in later stages of fabrication of the material, as it is explained in this section.

The manufacturing of piezoelectric materials depends on the structure of the material. A single-crystal material of an electroactive material naturally presents a polarization direction and, hence, requires no conditioning further than the creation of the crystalline structure itself. On the other hand, ferroelectric materials are often synthesized at high temperatures and their structure results in a poly-crystal. Each of the crystalline domains presents a polarization in a random direction which, overall, translates into a material in which the different crystal polarization directions cancel each other. This type of materials require further processing after manufacturing of the material that allows for macroscopic piezoelectric properties.

Both manufacturing methods are presented here, with focus, though, on the manufacturing of ferroelectric ceramics due to the interest they present in terms of modern applications. It is out of the scope of the thesis to analyze in depth non-conventional manufacturing methods for special ferroelectric ceramics as their application in actuation is non-existent currently. The conventional fabrication of ferroelectric ceramics follows de procedure presented: [57]

- **Synthesis of the ferroelectric powders:** a stoichiometric mixture of the constituents of the ceramic is calcined in an oven at a temperature of around $800-1000\,℃$ for a period of $1-2h$. This causes a solid-state reaction that results in the aggregates of the ceramic. The aggregates are then crushed and milled into a fine powder.
- **Sintering and compaction of the powders into ferroelectric ceramics:** the powder is mixed with a binder and laid into green preforms. The preforms are then subject to sintering at high temperature. The sintering temperature is lower than the melting point. Hot isostatic pressure (HIP) can be applied during this process to increment the density of the resulting ceramic thus increasing the material mechanical performance.
- **Electric poling of the ferroelectric ceramic:** during cooling the material undergoes a transformation from the paraelectric phase to the ferroelectric phase (see Sec. 3.1.1). This transformation occurs due to the change of the crystalline temperature across the Curie point. In each of the crystals of the material, the polarization is randomly oriented resulting in a null net polarization of the material. The application of a high electric field at elevated temperatures results in the alignment of the crystalline

domains. This alignment is locked when the piezoelectric is cooled with the electric field still applied; thus, permanent polarization is obtained. During poling, the orientation of the piezoelectric domains produces a mechanical deformation that is locked in place upon cooling (permanent strain).

These steps represent the basic method for ceramic manufacturing through sintering with an additional poling step in which the material develops its macroscopic piezoelectric properties. Apart from this base method, different procedures and variations allow for the improvement of the properties of the material, either mechanical or piezoelectric. Some of these methods are presented below:

- **Single-crystal growth:** diverse methods exist to create single-crystal piezoelectric materials. The most common are the hydrothermal synthesis [58] and the Czochralski method [59]. As presented in Sec. 3.1.1, single crystal piezoelectric materials present piezoelectric constants several orders of magnitude higher than conventional poly-crystalline structures. Because of this, before the discovery of ferroelectrics, single crystal piezoelectric materials found applicability in the development of transducers (see Sec. 1.4.1).
- **Doping:** improves the solid reaction process. Doped materials present significantly enhanced properties in comparison to the original materials. The current research focuses on the inestigation of doped piezoelectric materials in order to substitute lead-based piezoelectrics such as PZT. An example of a doped material is the $Bi_{3.25}Nd_{0.75}Ti_3O_{12}$ beeing the original piezoelectric the $Bi_4Ti_3O_{12}$. [60]
- **Coprecipitation:** is a wet chemical method aimed to improve the quality of the powder precursors for the sintering process. A liquid solution with the desired metallic salts is forced to precipitation. A posterior thermal dissolution of the precipitate results in very good quality perovskite powders. There is not a unique method of obtaining a precipitate of the desired salts; in order to obtain the PZT precursors, a route is the hydroxide coprecipitation. [61] [62]
- **Alkoxide hydrolysis (Sol-Gel):** the procedure uses metal alkoxides mixed in alcohol in the desired proportions. When water is added a hydrolysis reaction occurs resulting in alcohol and metal oxides and metal hydrates. A solution of the required cations in water is used in the hydrolysis reaction in order to produce the desired metal oxides and hydrates. The obtained solution is kept at a moderate temperature (around 70ºC) for a period of time in order to obtain the gel. The gel is then dried at high temperature (200ºC) to obtain a very fine powder. The powder can be then treated at different temperatures to obtain the desired single-phase powder. [63]
- **Thin-film fabrication:** this method is applied to obtain very thin films of ferroelectric perovskites. Two main procedures exist for the fabrication of films:
  - *Liquid-phase methods:* a suspension of the piezoelectric powder with additives (as sintering aids) in a volatile liquid (for example ethanol) is prepared. The suspension must have a certain viscosity and rheology for the screen-printing process. This process consists on spraying at high pressure the suspension onto a substrate in the desired form and through several passes to achieve the required width. [64]
  - *Gas-phase methods:* different methods exist to create thin films starting with a piezoelectric powder suspension in a gas. The suspension is then directed to a target surface through different methods such as the following: ion beam deposition [65], metal organic chemical vapour deposition [66], RF-planar magnetron sputtering [67] or pulse-laser deposition [68].

1.4.5 Types of actuators

Different types of approaches exist in the construction of piezoelectric actuators depending on the application they need to fulfill. Given the fact that piezoelectric materials present very significant differences from on to another, given the great differences between the behavior of the different chemical compositions (even if the crystalline structure is the same), the materials to be used in an actuator largely depend on the application intended.

Moreover, when considering a specific material for an actuator, the direction in which the crystal is cut (relative to the macroscopic shape of the actuator) and the direction in which the crystal is poled during fabrication (see Sec. 1.4.4) drastically modifies the behavior of the actuator. E.g. two PZT ceramics may present two piezoelectric matrices with different configuration of the non-zero coefficients depending on the poling direction and the cutting plane. This particularity of piezoelectrics is explained in more detail in Sec. 3.1.2.

1.4.5.1 Basic actuator geometries

Throughout the utilization of piezoelectric materials in actuators different geometries are most commonly used due to their advantages in particular applications. The most common configurations for piezoelectric actuators are presented below:

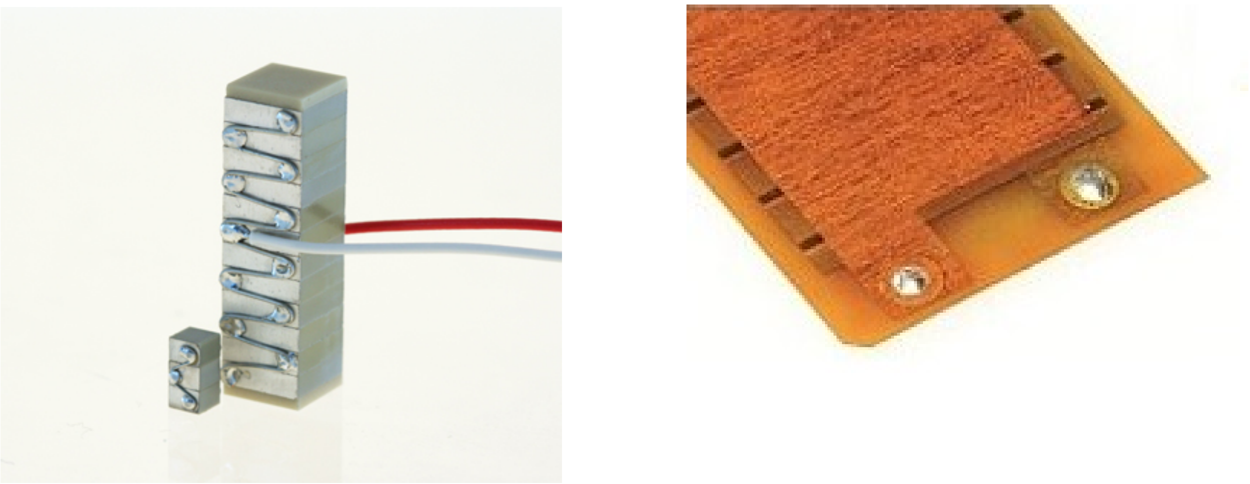

Figure 1.8: Examples of piezoelectric actuators in stack (left) and patch (right) configuration.

- **Stacks:** taking advantage of the change in dimension in the direction of polarization it is possible to create linear actuators with multiple piezoelectric material layers oriented in the same direction and having electrodes between them. This arrangement allows for a high actuating electric field in the piezoelectric material at a significantly lower voltage than a single piezoelectric block. These actuators provide high actuating forces throughout a large frequency spectrum and linear deformations of small amplitude which generally require a mechanical amplifier. An example is shown in Fig. 1.8.
- **Uni-morphs:** this type of actuators are layers of piezoelectric material mounted on flat metallic foils (that act as electrode) on one side only. Contrary to the stacks, that deform longitudinally, the uni-morphs are designed to produce planar deformations that result in a bending of the substrate.

- **Bi-morphs:** this type of actuators are formed by two separate piezoelectric layers attached to a substrate in between; these layers can be actuated independently. The alternative actuation of the layers produces lateral deflection of the substrate while synchronized actuation generates an elongation or contraction of the actuator.
- **Patches:** piezoelectric patches are single layers of poly-crystalline material polarized in the thickness direction. When they are actuated the material contracts or expands in the polarization direction but actuates also in-plane producing a deformation in the directions perpendicular to the polarization direction (in the same manner than uni-morphs). Usually patches are embedded in a resin that prestresses the material conferring the actuator the capacity to expand without producing cracks in the ceramic to a significantly higher degree when compared to uni-morphs. This type of actuators are usually used in bending applications of a substrate to which they are bonded. An example is shown in Fig. 1.8.
- **THUNDER:** is a derivation of the uni-morph actuator developed by NASA in which a layer of piezoelectric material (PZT) is attached on a metal layer at an elevated temperature; upon cooling, the difference in coefficients of expansion leads to a curvature. When the piezoelectric material is actuated, the curvature of the part changes and can be controlled. [69]
- **Rainbow:** this actuator is also a type of unimorph actuator. This actuators are produced by chemically reducing a piezoelectric ceramic at high temperature. This creates a layer of highly metallic non-piezoelectric material in the monolithic structure. In the cooling process, deformation appears as a consequence of the difference in thermal expansion. The resulting shape in the RAINBOW actuators is dome-shaped and are able to produce large axial displacements. [70]

1.4.5.2 Integration of the actuators

In most applications, the piezoelectric material needs to be fixed to a substrate; this is the case of piezoelectric patches and THUNDER and RAINBOW actuators. Different methods exist to perform the bonding between the actuator and the substrate. The most common methods are the following:

- **Clamping:** is a technique seldom used in piezoelectric actuators because of the operating conditions of the piezoelectric material. The most common applications for piezoelectric components are static deformations or controlled vibrations. In this environment, as clamping can only be performed at discrete points throughout the material, it cannot ensure proper behavior in the areas where there is no clamping (buckling, local resonance, etc).
- **Gluing:** is a very widespread method for piezoelectric material integration to the respective substrate due to the strong and flexible interface created. The main drawback this technique presents is that the glue (which is usually epoxy or acrylate) is usually hot setting and non-conducting. In composite structures, this implies that the manufacturing process of the structure will need to take into account the integration of the piezoelectric actuator during the curing of the material. The manufactured assembly will have, moreover, a low maximum operating temperature as glues usually present this characteristic.

  Regarding electrical conductivity, as the glues are rarely conductive materials, in the applications where electrical conductivity is required between the piezoelectric material and the substrate, action is taken to ensure this characteristic of the bonding. The required conductivity can be achieved through different methods: a first method is to use conductive glue. This has the problem that short-circuits may appear due to the 3D conductivity of the glue. A second option is to roughen the surface and glue the piezoelectric under pressure to ensure contact points with the substrate. The main drawback is the low reproducibility of the method. A third option is to mix nickel powder in the glue and cure applying pressure. Since the nickel particles are almost ideal spheres, they tend to form a monolayer between the surfaces. Around 2% of nickel is enough to provide the necessary electrical connectivity with almost no influence on the glue strength. [71]

- **Soldering:** this method presents the advantage of ensuring electrical conductivity between the piezoelectric material and the substrate. The main drawback is that the resulting bonding is not flexible and the piezoelectric deformation causes fatigue in the bond, this may result in problems in dynamic actuation applications.

The need for a substrate is directly linked to the type of actuator intended for each application. For an actuator of type stack, the sole fitting of the actuator between the components to be moved may be enough installation; this case is the proposed configuration for the AFDPA project [72]. When the installation of the piezoelectric actuator does not require bonding with a substrate, the electrical connections need to be performed in a different way. The most common solution is to solder the necessary cables to the actuator in some silver or nickel electrodes.

1.4.5.3 Displacement amplification

Due to the very small deformations obtained with piezoelectric actuators, in most of the applications, some form of displacement amplification is required. Mechanical amplification systems are good suited to this type of actuators as the forces developed by piezoelectric materials are usually high.

In the design of amplifiers, it is necessary to consider the maximum force that the piezoelectric actuator is able to develop (known as blocking force). Upon facing a force with this magnitude, the actuator will not be able to produce any strain. In this condition, the mechanical work that the piezoelectric actuator develops (force times displacement) is zero as the displacement of the actuator is also zero.

On the other hand, when the actuator faces no opposing force on the direction of the displacement generated, the work develop is also zero. The work of the actuator reaches a maximum value between these two extremes; the maximum is found at the point where the stiffness of the amplifying mechanism equals the stiffness of the actuator.

The applicability of this analysis to the practical calculation of the amplifying mechanisms is more complex than simply calculating the optimal stiffness as in some design applications (as in Sec. 7.2.4). The obtained displacement of the actuator was considered significantly more important than the actuator-amplifier blocking force.

In this thesis, two displacement amplification methodologies have been used in tandem with two different types of piezoelectric actuators. These amplification systems are detailed in Sec. 6.2 and in Sec. 7.1. The first of the systems takes advantage of the deformation of the piezoelectric actuator in the direction of polarization and uses a compliant kinematic amplification system while the second system studied uses

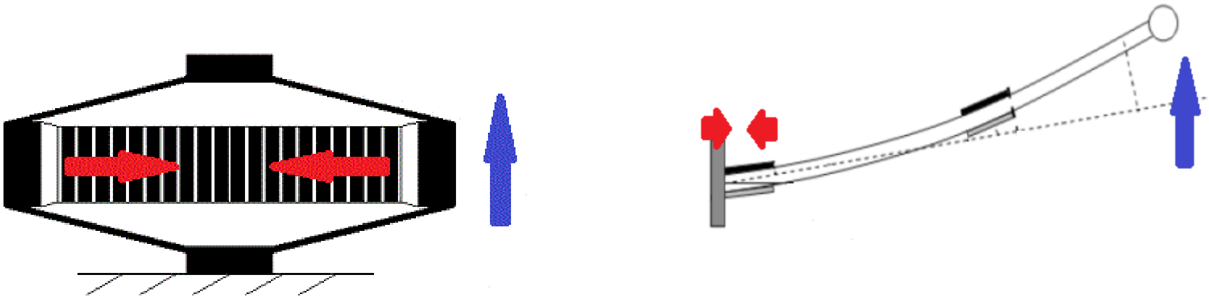

Figure 1.9: Examples of amplification mechanisms used in piezoelectric actuator applications showing the piezoelectric displacement direction (red) and the resulting amplified motion (blue).

the in-plane deformation (perpendicular to the polarization plane) to bend a cantilever thin aluminum plate. [73]

1.5 Piezoelectric actuators in aerostructures morphing

The application of piezoelectric actuators in the morphing of aerospace structures is not a wide area. The utilization of this type of actuators in static applications is not widespread because of the difficulties that arise. This thesis presents in the experimental and numerical parts some of these difficulties.

Because of this low level of development of the technology, the application of piezoelectric actuators in aerostructures morphing is restricted to the laboratory implementation including wind tunnel testing of small-scale demonstrators. This section presents a brief overall on the status of these experiments.

The majority of the experiments that analyzed a full wing profile geometry considered a rigid leading edge and a deformable trailing edge with a working skin. [74] This configuration allows for a modification of the curvature of the aerodynamic profile with the simplicity of a structural element of the wing in the rigid part of the airfoil section. In this configuration, the actuators used are bonded in the upper and lower skin of the airfoil and work in tandem: one contracts while the opposite expands to produce a bending in the airfoil trailing edge. [75] This mechanism is shown in Fig. 1.10 and is the option later on used in the morphing profile experiments of this thesis.

Figure 1.10: Example of a piezoelectric driven wing profile morphing application with rigid leading edge and flexible trailing edge. [76]

Another approach used is the consideration of a non-loaded aerodynamic skin and a morphing internal structure throughout the chord of the profile. In this case, a deformation of the internal structure produces a bending on the median line of the profile which causes the elastic skin to deform. This configuration is presented in Fig. 1.11. [77]

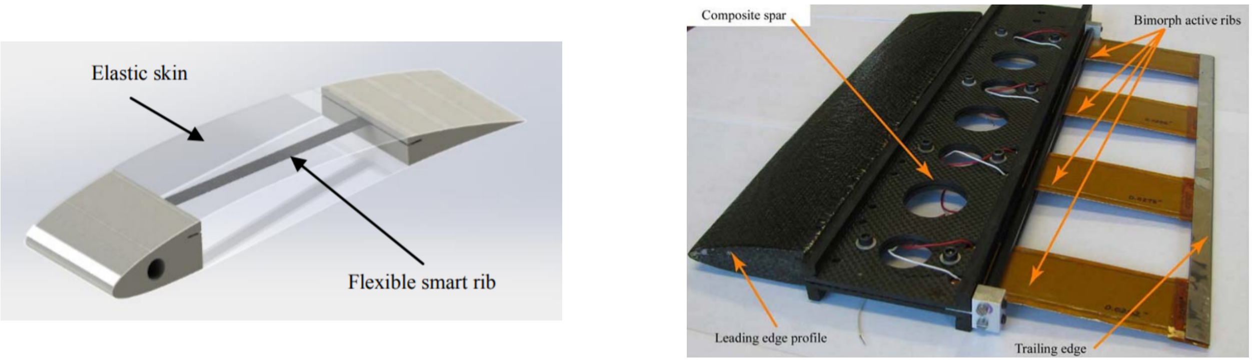

Figure 1.11: Examples of airfoil with a morphing internal structure and an elastic skin that deforms when the internal structure is bent. (sources: [77] left and [78] right)

It is also possible to design morphing airfoils in which the leading edge is also elastic. In this approach, the integration of the structure into the mechanism is more complex as the strength structure needs either to be elastic or a compliant mechanism. At this stage, no concepts have yet been developed which successfully managed to integrate a morphing elastic span-wise structure into a wing with a morphing-airfoil. Experiments have been performed in which a compliant strength structure is integrated in a morphing wing airfoil. This configuration is presented in Fig. 1.12. [78] In this configuration the results obtained are similar in terms of amplitude of the trailing edge displacement and the complexity of implementing a compliant structure does not present clear advantages over other concepts.

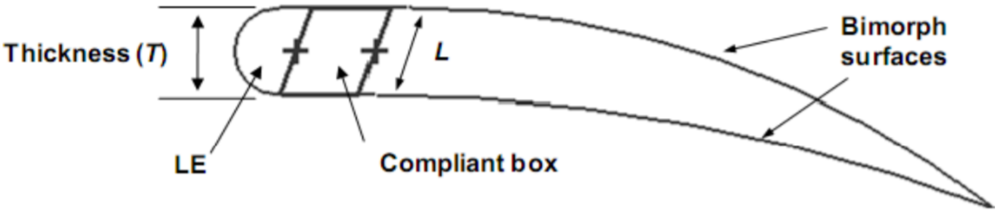

Figure 1.12: Compliant structure implemented as load-carrying structure of a morphing airfoil. [78]

A trade-off of these two actuation concepts is difficult as the two concepts present advantages and disadvantages in the design. On the one side, the complexity of the tandem skin actuators involves the utilization of a structural skin which the bending bi-morph configuration does not present. Oppositely, the manufacturing of the aerodynamic structure for the non-load-carrying airfoil skin is significantly more complex in this later configuration. Overall, there is no clear superior concept between the presented solutions.

The main practical case-study applications for piezoelectric actuators are in micro air vehicles (or small UAVs). This happens due to the difficulties that the scaling of the technology presents. Flight experiments have been performed in small-scale demonstrators so far. [79] The main challenge in the implementation of piezoelectric-actuated morphing devices in this type of vehicles is the miniaturization of the electric drivers for the system (which requires high voltage in the actuation). This happens because the commonly used batteries in this type of vehicles do not provide sufficient voltage.

2. Objectives

This thesis presents a study on the applicability of piezoelectric actuators in the morphing of aerospace structures with the aim of determining whether the technology is mature enough for such application and whether the application is feasible in the near future.

Given the maturity of the piezoelectric actuator technologies (presented in Sec. 1) two different concepts of actuation have been chosen for further analysis in this thesis. A first concept considers a conventional control surface in which the actuator is replaced by a piezoelectric actuator. In the second approach, the control surfaces are blended into the aircraft structure and embedded piezoelectric actuators are used to produce elastic deformations on the outer shape of the structure which result in the desired geometry change.

The analysis of these two selected technological approaches is performed in different stages throughout this thesis: a review of the present piezoelectric technology status in the actuators field and a state of the art in the morphing of aeronautical structures (already presented), a review on the relevant theoretical formulations applied to the piezoelectric materials, a characterization of a particular piezoelectric actuator chosen as the representative actuator to evaluate the feasibility of structural morphing, a parallel approach in the application of piezoelectric materials into the control through rapid-response conventional control surfaces, a study on the morphing of a representative structure and the related numerical analysis followed, lastly, by the analysis on the feasibility of applying the presented technologies into current aircraft design philosophies.

This thesis proposes, ultimately, a study of what can be the next step in the optimization of aircraft aerodynamics: the integration of the control surfaces in the aircraft structure so there is no distinction between fixed and mobile parts anymore. This implies integrating the control surfaces into the aircraft structure so a part of the aircraft structure itself is responsible for the control of the aircraft. This concept allows for an unprecedented level of adaptability of the external shape of the aircraft which allows for the optimization of the aerodynamic configuration regardless of the local flight conditions. The impact of the integration of morphing piezoelectric-actuated control surfaces has been evaluated in comparison to present technology. The scope of this analysis has been to determine whether the technology is mature enough for industrial implementation. This analysis is considered in a simplified manner as a detailed study is out of the scope of the present thesis.

3. Theoretical aspects

After the state of the art of the piezoelectric applications to the morphing of aeronautical structures, this chapter presents the physical principles of piezoelectricity from the phenomenological and from the mathematical modeling point of view.

As briefly presented in the previous chapter, piezoelectric materials are a type of materials that present coupling between the mechanical and electrical fields. This coupling occurs due to electrical asymmetries of the crystalline structure of the material. To present an in-depth explanation of this phenomenon, a brief introduction to crystallography helps in understanding the nature of the phenomenon at a microscopic level. At a macroscopic level, the behavior of piezoelectric materials is also detailed.

Piezoelectric materials are, due to the nature of the phenomenon, non-linear materials. This occurs because the polarization causing the piezoelectric phenomenon appears only in a specific electric field, temperature and mechanical field range. When approaching the limits of the piezoelectric region in a material the behavior starts deviating from linearity. In this thesis, though, all the experiments and implementation cases of piezoelectric materials consider the behavior of the materials as linear; hence, only the linear behavior is studied from the mathematical formulation point of view.

In terms of mathematical modeling of the materials, the linear theory of piezoelectricity is introduced; this theory is implemented later on in the numerical models simulated in the last chapter of this thesis. The linear modeling of the phenomenon is done in the constitutive equations of the material through a piezoelectric term that relates the electric field to stress through a piezoelectric matrix. Different forms exist for expressing this constitutive relation depending on the variables involved (electric field, voltage, strain, stress, etc).

Non-linearity in this type of materials is qualitatively presented in this thesis. Even though the mathematical model implemented throughout the thesis does not account for them, different phenomena contribute to the non-linearity of the piezoelectric behavior throughout the domain, not only on the extremes. An example of this behavior is hysteresis.

3.1 Piezoelectric materials

The behavior of piezoelectric materials can be studied through different approaches depending on the scale at which the phenomenon is analyzed but also depending on the scientific discipline used as a reference. For instance, the same material properties can be analyzed from the crystallographic point of view at microscopic level or from the chemical composition at macroscopic level. The phenomenology can be studied without entering on the material properties from the physical perspective through the analysis of the relation between the mechanical and electric fields.

The following sections detail the piezoelectric phenomenology occurring in piezoelectric materials presented as the general physical behaviors associated to piezoelectricity but also detailing the crystallographic approach to understand the micro-structures involved in the phenomenon and the chemical point of view, which helps understand the existence of limits in the phenomenology of piezoelectricity.

The combination of the different explanations of the phenomenon provides a complete understanding necessary to model the behavior physically and, later in the thesis, numerically.

3.1.1 Piezoelectric phenomenology

This section presents the different phenomena that involve electric and mechanical field coupling in their different forms. This helps situating the piezoelectric phenomenon within the multiple other possible couplings that may exist concerning electrical, magnetic, thermal or mechanical fields. This couplings appear mostly due to asymmetries in the crystalline structure of the material which allows for a polarization of the material. [57]

Polarization is a dielectric phenomenon in which positive and negative charges separate at different ends of the material creating an electric dipole or dipoles in the material. This phenomenon is described by Eq. 3.1. Basically, the electric displacement in a material is a function of the applied electrical field and the intrinsic polarization already present.

$$D = \varepsilon_0 E + P \tag{3.1}$$

Polarization can be spontaneous (when it occurs without the application of any external electrical field) or forced (when an external electric material causes it) and if it is retained in the absence of any external electrical field it is called permanent. The qualities of spontaneous and permanent polarization are not incompatible. The materials that present permanent polarization are called polar materials. These materials are not uncommon in nature, one of the most common polar substances is water (the polar nature of water is presented in Fig. 3.1).

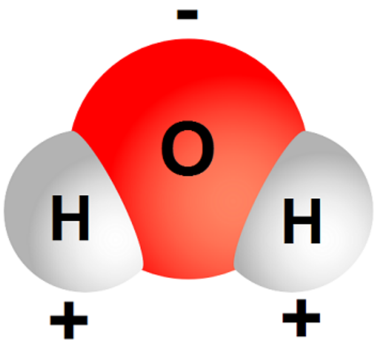

Figure 3.1: Molecule of water depicting the dipole it presents due to its asymmetry.

Paraelectric materials, on the other hand, are materials that do not present permanent polarization. In these materials the polarization is roughly proportional to the applied electrical field and when the electrical field disappears they return to the initial electric state.

Piezoelectric materials, as presented in Sec. 1.4, are materials that present an electric charge displacement throughout the material (and thus a net dipole) under the application of external mechanical stress and vice-verse. These materials present an asymmetric molecular structure which causes a permanent polarization in the material. When the structure is deformed, the microscopical structure of the material is altered and the polarization is changed, this change in polarization produces an electric displacement according to Eq. 3.1. This effect is called direct piezoelectric effect. In the converse effect, the opposite is also true, when an electric field actuates on the polar structure, the material microstructure deforms due to the electric interaction with the material dipole. This microscopical deformation has its macroscopic effect on the material strain field.

Among piezoelectric materials, it is possible to identify a particular group called ferroelectric materials. A ferroelectric material is a material that presents at least two microstructures (or solid phases) depending on the temperature. Above a certain temperature, the material presents a symmetric paraelectric microstructure while at low temperatures the material presents a non-symmetric polar phase. This polar phase can be induced through the application of an electric field of enough intensity and reversed through the application of an equivalent electric field of the opposite sign. The temperature at which a ferroelectric material (or ferroelectric ceramic) changes phase is called Curie temperature while the electric field that causes the material to switch polarization is called coercive field. Examples of these materials are mostly crystals such as the Rochelle salt (222 crystalline structure), the potassium dihydrogen phosphate ($\bar{4}2m$ crystalline structure) of the barium titanate ($m3m$). Details on the crystalline notation are found in Sec. 3.1.2. [80] [81] [82]

The polarization characteristics of ferroelectric materials can be seen in Fig. 3.2. When surpassing a given coercive field (E_c) the polarization suddenly increases to a spontaneous polarization (P_s) which remains then almost constant. The coercive field and the value of the polarization attained depend on the material. The material behaves like a spontaneous polarization piezoelectric until the electric field is lowered to a point $-E_c$, where the polarization flips to $-P_s$. This behavior is explained by internal dipoles in the material that flip their orientation if the electrical field is sufficiently intense. In poly-crystalline materials, each of the grains of the material presents a dipole which, given an electric field intense enough (E_c), reorient generating a net polarization in the material.

This type of materials presents a maximum electric field at which the material loses its dielectric properties and at which the electric behavior of the material changes drastically. From that point onward the material does no longer behave like a piezoelectric material. The analysis of this transition is not within the scope of this thesis due to the lack of application of this phenomenon to the actuation of mechanical structures. Nevertheless, the point at which such electric field is attained is important as it defines the maximum actuation field with which a piezoelectric material can be actuated without losing its properties.

Another behavior that can be observed is the anti-ferroelectric phenomenon. Anti-ferroelectric materials present paraelectric behavior under low electrical fields and ferroelectric behavior under high ones. The main difference with ferroelectric materials is that no permanent polarization is observed (when the electric field is 0). This phenomenon can be explained by a microstructure consisting (electrically) of sets of anti-parallel-oriented dipoles. When the applied electrical field is low, the anti-parallel condition is maintained and no polarization is observed, behaving like a paraelectric material. When the electrical field increases past a transition electrical field (E_t), the dipoles reorient in the direction of the external field and the ma-

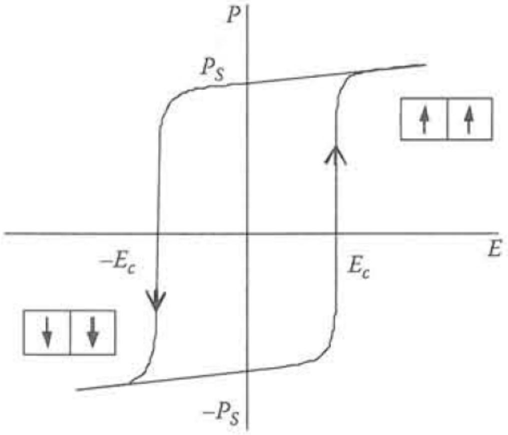

Figure 3.2: Ferroelectric behaviour [83]

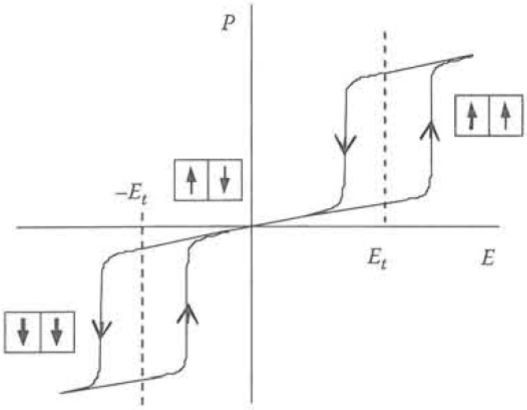

Figure 3.3: Antiferroelectric behaviour [84]

terial shows a permanent polarization-like behavior. The electrical field - polarization graphic for this type of materials is presented in Fig. 3.3. Anti-ferroelectric materials are not used as actuators due to their paraelectric behavior at low electric fields.

It is interesting to study a type of ferroelectric materials called ferroelectric perovskites because of the singular behavior that they present. Perovskites are a family of crystalline oxides which present a cubic face-centered structure (FCC) at elevated temperatures and a non-symmetrical crystalline structure at low temperatures. At high temperatures, the material behaves as a paraelectric and as the temperature is decreased, the latices of the structure shrink up to a point where the structure is no longer stable. At this point, the central cation snaps off-center to other minimum-energy locations in the structure. This change of position results in an electric dipole and a mechanical strain, which distorts the structure elongating it in one direction. This transition is presented in Fig. 3.4 for the barium titanate structure. The different possibilities of resulting crystalline structures for this distorted geometry are presented in Sec. 3.1.2.

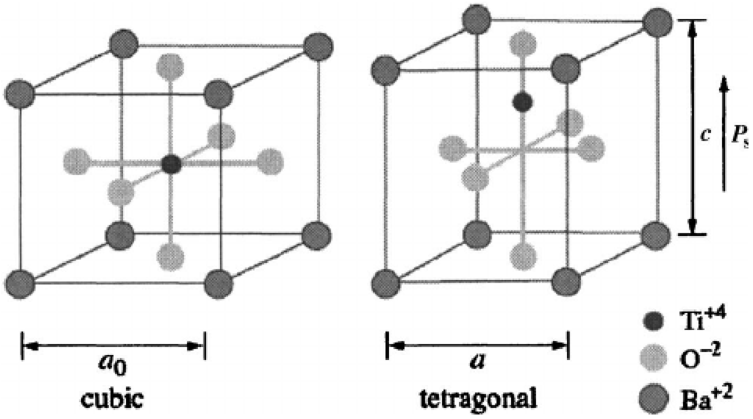

Figure 3.4: Barium titanate microstructure unit cells at high temperature (left) and at a temperature lower than the Curie temperature (right). [85]

When the perovskite crystal is in the ferroelectric phase, strain and polarization can be induced by an electrical field. The induced strain and polarization are the additional magnitudes produced by the applied electrical field. The maximum displacement to which the crystal can be subjected is the polarization saturation. When the electrical field is low in intensity, the perovskites can be analyzed with the model presented if Eq. 3.2 where Q is the electrostrictive constant with respect to polarization.

$$\begin{aligned} P &= P_s + \varepsilon E \\ S &= QP^2 \end{aligned} \tag{3.2}$$

Within the perovskite crystals it is possible to define a sub-group in which the piezoelectric response is dominant. Such materials are the piezoelectric ceramics. They can be found commercially as simple perovskites like the barium titanate ($BaTiO_3$) or as solid-state solutions like the lead zirconate-titanate (or PZT) with formulation $Pb(Zr,Ti)O_3$.

A classification emerges when the coercive fields of the piezoelectric ceramics are compared. This classification is already introduced in Sec. 1.4.3.3.

Couplings like the relation between mechanical and electric fields are not uncommon in nature, other types of couplings are pyroelectricity, in which materials present dependence between polarization and temperature, or magnetostriction, where the mechanical field presents coupling with the magnetic field. These types of materials are, though, out of the scope of this thesis.

3.1.2 Crystallographic structures

The piezoelectric materials are crystalline solids. Because of this, the properties of the material can be traced down to the properties of each of the crystals conforming the macroscopic structure. This section aims to clarify and present some introductory aspects of crystals.

The geometry and properties of the crystalline arrangement of the structure of a piezoelectric are directly linked to the mathematical modeling of the macroscopic piezoelectric phenomenon. A crystal belonging to a certain class will have a piezoelectric matrix with certain constants being 0 because it belongs to such class, independently of any geometry of the macroscopic structure.

This brief introduction into crystallography starts with a presentation of the different crystal systems and its classes and continues with the analysis of the piezoelectric activity in each of the crystal classes.

3.1.2.1 Crystal systems

A crystal can be defined as a solid in which the atoms are arranged in a certain geometrical pattern that repeats throuhout the body. [39] Each of the repeating patterns in the body is called unit cell and can be considered as a parallelepiped. The sides of the unit cell stand in each of the directions in one of the vertices (considered the origin of coordinates) are noted a, b and c and are called crystallographic axes (see Fig. 3.5). The angles α, β and γ are defined between the axes b and c, a and c, and a and b respectively. [86] [87]

7 crystal systems can be defined depending on the symmetry that the unit cells present. [88] [89]

- **Triclinic system:** is characterized for not having neither symmetry axes nor symmetry planes. Usually, the length of the crystallographic axes is different and so are α, β and γ. The usual convention for the axes is taking the Z axis parallel to c and in the direction so d_{33} is positive. The x axis is taken in

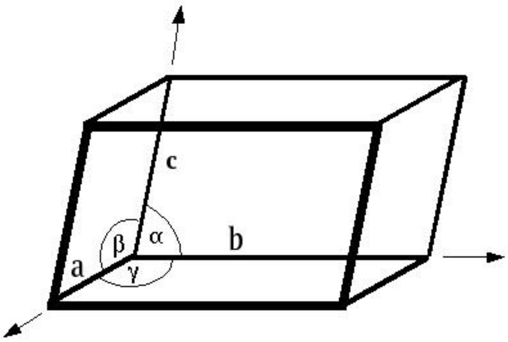

Figure 3.5: Exemplification of the crystallographic coordinate system in a triclinic generic crystal [86]

the plane ac and so d_{11} is positive. y completes the right-hand triad parallel to the plane ac. A generic shape for a triclinic system is shown in Fig. 3.5.

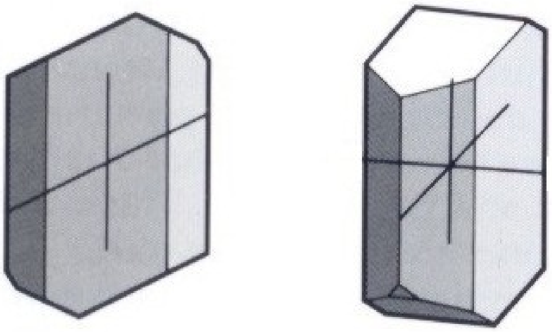

Figure 3.6: Example of a monoclinic generic crystal. Two of the axes are at $90°$ and the third at a different angle. The y axis is the one that presents the 2-fold symmetry. [90]

- **Monoclinic system:** the crystals in this system present either a 2-fold symmetry, or a single plane of reflection symmetry, or both. The axes b and y are taken in the 2-fold axis or the symmetry axis (if both exist they are the same) and in the direction so d_{22} is positive. The shortest axis is named c and is parallel to z. An example of a generic monoclinic crystal is presented in Fig. 3.6.

- **Orthorhombic system:** this system has three mutually perpendicular 2-fold axes, or two mutually perpendicular planes of reflection symmetry, or both. In most of the crystals z is the polar axe, x and y are chosen so x is parallel to the shortest remaining axe. This configuration is shown in Fig. 3.7.

- **Tetragonal system:** this system presents a single 4-fold axis or a 4-fold inversion axis. A possible configuration of this system is depicted in Fig. 3.8. c and z axes are taken along the 4-fold axis. As a and b are equivalent are usually noted as a_1 and a_2 and taken to minimise the cell volume generally.

- **Trigonal and hexagonal systems:** these two systems are usually presented together. They present a 3-fold or 6-fold axis respectively which is always called the c (z) axis. There are three equivalent secondary axes perpendicular to c and at an angle of $120°$ between them and are named a_1, a_2 and a_3. The crystal is considered trigonal if its cross section presents three sides while in an hexagonal crystal there are six sides. Both systems are shown in Fig. 3.9.

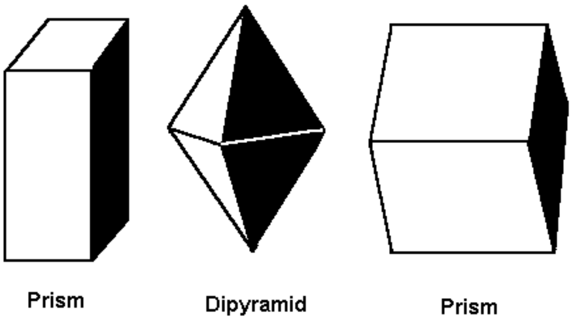

Figure 3.7: Examples of the three shapes of an orthorhombic crystal. All the axes are perpendicular to each other but of different lenths. [91]

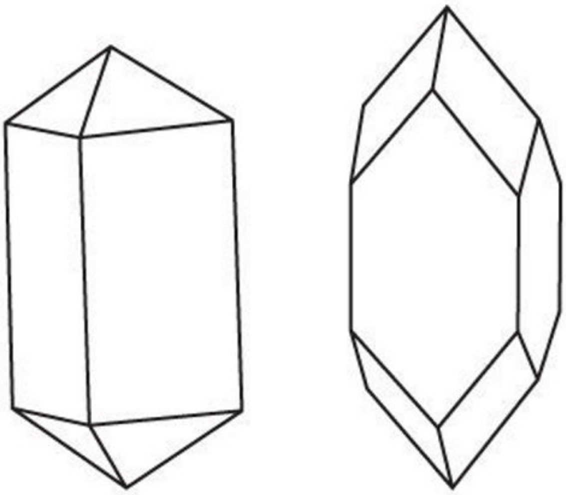

Figure 3.8: Example of two tetragonal crystal lattices. In both lattices all the axes are perpendicular to each other being two of them of the same length. [92]

- **Cubic system:** three equivalent axes noted as a_1, a_2 and a_3 are taken parallel to the axes of 4-fold symmetry or to the 2-fold axes (if there is no true 4-fold symmetry). One of the axes is arbitrarily chosen as z and the rest are taken to obtain a positie $d_{14} = d_{36}$. This configuration is shown in Fig. 3.10.

Each of these systems is divided into point groups (or classes) according to their symmetry about a point. 32 classes can be defined following to this criteria. Out of these classes, only 20 present the characteristics to be piezoelectric.

3.1.2.2 International crystallographic system (Hermann-Mauguin notation)

The crystal classes are noted with the Hermann-Mauguin notation. This notation is considered the international crystallographic system since it was introduced in the International tables for crystallography [95].

The notation indicates a rotation axis by a number where its reciprocal denotes the part of a full rotation about the axis in order to bring the crystal into an equivalent position. The number 1 indicated that the

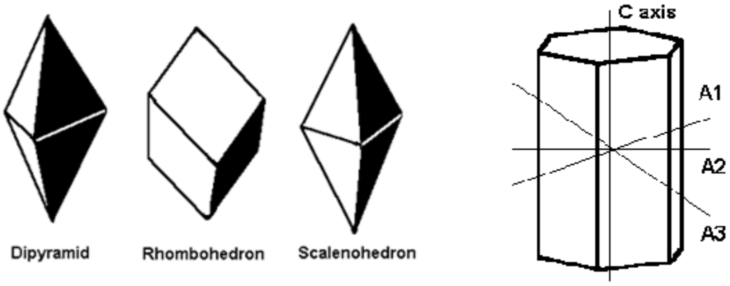

Figure 3.9: Examples of crystals belonging to the trigonal (left three) and hexagonal systems (right). [93]

Figure 3.10: Pyrite mineral showing different cubic crystalline regions. [94]

crystal has no symmetry because a full turn is required to bring the crystal into an equivalent position. E.g. 2 indicates a twofold symmetry about the related axis.

A reflection plane is noted as "m". If an axis has a reflection plane perpendicular to it, it is noted by the number associated to the axis and "$/m$". [96]

The designation for the different classes consists of 1, 2 or 3 numbers each of which indicates a symmetry about a different direction in the crystal. Crystallographically identical directions are grouped together under a single symbol. [97]

3.1.2.3 Occurrence of piezoelectricity

As mentioned in the previous sections, certain conditions need to be met for the crystal to present piezoelectric properties.

Depending on the symmetry of each of the crystals, the piezoelectric phenomenon appears described by different coefficients of the piezoelectric matrix. Each symmetry condition reduces the number of independent constants. From the initial 18 independent constants that the triclinic system presents, some cubic crystals present only 1 independent piezoelectric constant. Several methods exist to determine which constants in the piezoelectric matrix are 0 depending on the crystalline configuration. [82] It is not in the scope of this thesis, though, to detail them. The conclusions of these methods are presented in Table 3.1 as the form of the piezoelectric matrices according to the different 20 classes that present piezoelectric phenomena.

3.1.3 Chemical characteristics

The crystalline analysis presented in the previous section provides insight into the micro-mechanics of the piezoelectric materials. This analysis is not complete without presenting the materials from the phase transition point of view. In this section, the analysis in terms of chemical composition and phase for the ferroelectric materials is presented. Only the lead zirconate-titanate (PZT) is presented as only this type of material is used later on in the experimental part of the thesis.

Lead zirconate titanate is a perovskite ferroelectric ceramic with chemical composition $PbZr_xTi_(1-x)O_3$. It is a solid state solution of lead zirconate and lead titanate. The particular composition of the material depends on the manufacturer as the mechanical, piezoelectric and dielectric properties of the material vary depending on the proportion between zirconate and titanate groups in the material composition.

As mentioned in this chapter, ferroelectric ceramics do not behave as such throughout any temperature conditions but rather they present a Curie temperature at which the material transitions from piezoelectric to paraelectric. In the particular case of PZT, this temperature of transition is not constant with the chemical composition of the material because lead zirconate and lead titanate present different phase transition temperatures. The variation of the crystalline structure of the material as a function of the chemical composition and temperature is represented in a phase diagram, presented for PZT in Fig. 3.11.

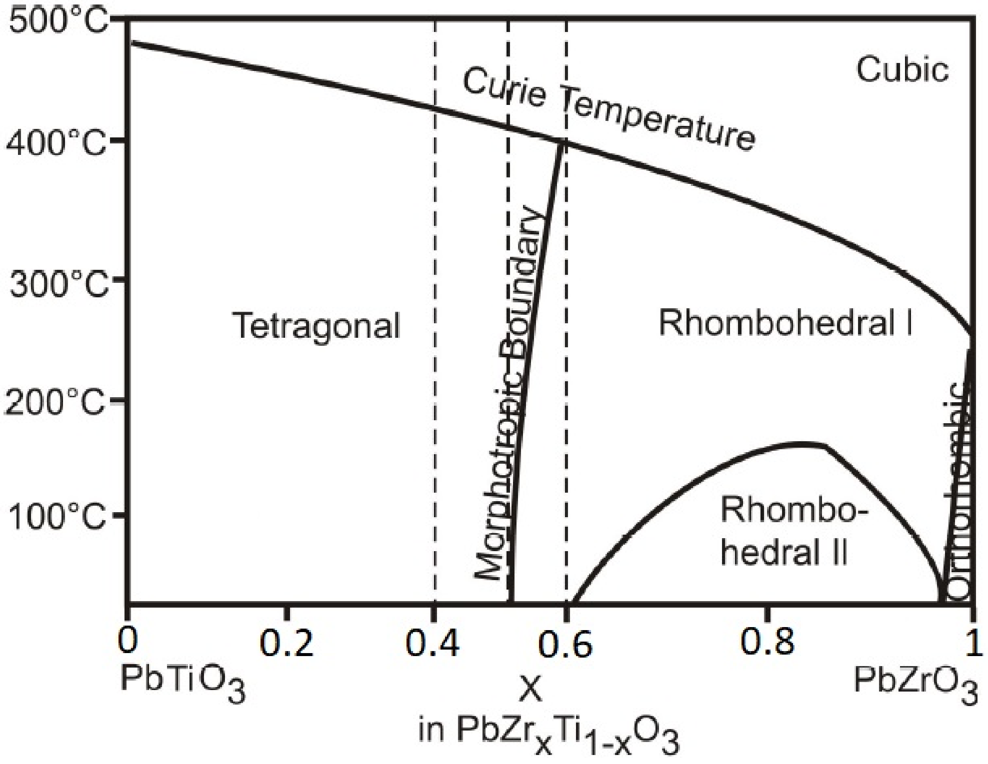

Figure 3.11: Phase diagram for PZT representing the different possible crystalline structures and the transition boundaries.

	Triclinic		
$\begin{pmatrix} \bullet & \bullet & \bullet & \bullet & \bullet & \bullet \\ \bullet & \bullet & \bullet & \bullet & \bullet & \bullet \\ \bullet & \bullet & \bullet & \bullet & \bullet & \bullet \end{pmatrix}$	Class 1		
	Monoclinic		
$\begin{pmatrix} \cdot & \cdot & \cdot & \bullet & \cdot & \bullet \\ \bullet & \bullet & \bullet & \cdot & \bullet & \cdot \\ \cdot & \cdot & \cdot & \bullet & \cdot & \bullet \end{pmatrix}$	Class 2 $(2 \parallel x_2)$	$\begin{pmatrix} \cdot & \cdot & \cdot & \bullet & \bullet & \cdot \\ \cdot & \cdot & \cdot & \bullet & \bullet & \cdot \\ \bullet & \bullet & \bullet & \cdot & \cdot & \bullet \end{pmatrix}$	Class 2 $(2 \parallel x_3)$
$\begin{pmatrix} \bullet & \bullet & \bullet & \cdot & \bullet & \cdot \\ \cdot & \cdot & \cdot & \bullet & \cdot & \bullet \\ \bullet & \bullet & \bullet & \cdot & \bullet & \cdot \end{pmatrix}$	Class m $(m \perp x_2)$	$\begin{pmatrix} \bullet & \bullet & \bullet & \cdot & \cdot & \bullet \\ \bullet & \bullet & \bullet & \cdot & \cdot & \bullet \\ \cdot & \cdot & \cdot & \bullet & \bullet & \cdot \end{pmatrix}$	Class m $(m \perp x_3)$
	Orthorhombic		
$\begin{pmatrix} \cdot & \cdot & \cdot & \bullet & \cdot & \cdot \\ \cdot & \cdot & \cdot & \cdot & \bullet & \cdot \\ \cdot & \cdot & \cdot & \cdot & \cdot & \bullet \end{pmatrix}$	Class 222	$\begin{pmatrix} \cdot & \cdot & \cdot & \cdot & \bullet & \cdot \\ \cdot & \cdot & \cdot & \bullet & \cdot & \cdot \\ \bullet & \bullet & \bullet & \cdot & \cdot & \cdot \end{pmatrix}$	Class $mm2$
	Tetragonal		
$\begin{pmatrix} \cdot & \cdot & \cdot & B & C & \cdot \\ \cdot & \cdot & \cdot & C & -B & \cdot \\ A & A & \bullet & \cdot & \cdot & \cdot \end{pmatrix}$	Class 4	$\begin{pmatrix} \cdot & \cdot & \cdot & B & C & \cdot \\ \cdot & \cdot & \cdot & -C & B & \cdot \\ A & -A & \cdot & \cdot & \cdot & \bullet \end{pmatrix}$	Class $\bar{4}$
$\begin{pmatrix} \cdot & \cdot & \cdot & A & \cdot & \cdot \\ \cdot & \cdot & \cdot & \cdot & -A & \cdot \\ \cdot & \cdot & \cdot & \cdot & \cdot & \cdot \end{pmatrix}$	Class 422	$\begin{pmatrix} \cdot & \cdot & \cdot & \cdot & B & \cdot \\ \cdot & \cdot & \cdot & B & \cdot & \cdot \\ A & A & \bullet & \cdot & \cdot & \cdot \end{pmatrix}$	Class $4mm$
$\begin{pmatrix} \cdot & \cdot & \cdot & A & \cdot & \cdot \\ \cdot & \cdot & \cdot & \cdot & A & \cdot \\ \cdot & \cdot & \cdot & \cdot & \cdot & \bullet \end{pmatrix}$	Class $\bar{4}2m$		
	Trigonal		
$\begin{pmatrix} A & -A & \cdot & D & E & -2B \\ -B & B & \cdot & E & -D & -2A \\ C & C & \bullet & \cdot & \cdot & \cdot \end{pmatrix}$	Class 3	$\begin{pmatrix} A & -A & \cdot & B & \cdot & \cdot \\ \cdot & \cdot & \cdot & \cdot & -B & -2A \\ \cdot & \cdot & \cdot & \cdot & \cdot & \cdot \end{pmatrix}$	Class 32
$\begin{pmatrix} \cdot & \cdot & \cdot & \cdot & C & -2A \\ -A & A & \cdot & C & \cdot & \cdot \\ B & B & \bullet & \cdot & \cdot & \cdot \end{pmatrix}$	Class $3m$ $(m \perp x_1)$	$\begin{pmatrix} A & -A & \cdot & \cdot & C & \cdot \\ \cdot & \cdot & \cdot & C & \cdot & -2A \\ B & B & \bullet & \cdot & \cdot & \cdot \end{pmatrix}$	Class $3m$ $(m \perp x_2)$
	Hexagonal		
$\begin{pmatrix} \cdot & \cdot & \cdot & B & C & \cdot \\ \cdot & \cdot & \cdot & C & -B & \cdot \\ A & A & \bullet & \cdot & \cdot & \cdot \end{pmatrix}$	Class 6	$\begin{pmatrix} \cdot & \cdot & \cdot & \cdot & B & \cdot \\ \cdot & \cdot & \cdot & B & \cdot & \cdot \\ A & A & \bullet & \cdot & \cdot & \cdot \end{pmatrix}$	Class $6mm$
$\begin{pmatrix} \cdot & \cdot & \cdot & A & \cdot & \cdot \\ \cdot & \cdot & \cdot & \cdot & -A & \cdot \\ \cdot & \cdot & \cdot & \cdot & \cdot & \cdot \end{pmatrix}$	Class 622	$\begin{pmatrix} A & -A & \cdot & \cdot & \cdot & -2B \\ -B & B & \cdot & \cdot & \cdot & -2A \\ \cdot & \cdot & \cdot & \cdot & \cdot & \cdot \end{pmatrix}$	Class $\bar{6}$
$\begin{pmatrix} \cdot & \cdot & \cdot & \cdot & \cdot & -2A \\ -A & A & \cdot & \cdot & \cdot & \cdot \\ \cdot & \cdot & \cdot & \cdot & \cdot & \cdot \end{pmatrix}$	Class $\bar{6}m2$ $(m \perp x_1)$	$\begin{pmatrix} A & -A & \cdot & \cdot & \cdot & \cdot \\ \cdot & \cdot & \cdot & \cdot & \cdot & -2A \\ \cdot & \cdot & \cdot & \cdot & \cdot & \cdot \end{pmatrix}$	Class $\bar{6}m2$ $(m \perp x_2)$
	Cubic		
$\begin{pmatrix} \cdot & \cdot & \cdot & \cdot & \cdot & \cdot \\ \cdot & \cdot & \cdot & \cdot & \cdot & \cdot \\ \cdot & \cdot & \cdot & \cdot & \cdot & \cdot \end{pmatrix}$	Class 432	$\begin{pmatrix} \cdot & \cdot & \cdot & A & \cdot & \cdot \\ \cdot & \cdot & \cdot & \cdot & A & \cdot \\ \cdot & \cdot & \cdot & \cdot & \cdot & A \end{pmatrix}$	Class 23 or $\bar{4}3m$

Table 3.1: Piezoelectric matrices for different crystal classes arranged in systems. "·" means the coefficient is 0, "•" means independent non-zero coefficient, and letters represent relations between coefficients.

It is possible to see that the transition from the lead zirconate tetragonal structure to the lead titanate structure rhomboedral structure (morphotropic boundary) happens at room temperature close to the 50% molar proportion. As the temperature increases the morphotropic boundary is not constant in terms of molar proportion which makes this type of materials difficult to characterize in high temperature applications. In the present thesis, though, the piezoelectric materials used have only been operated at room temperature so any analysis of phase transition is out of the scope of the thesis.

Two parameters in the phase diagram are very relevant in the manufacturing process for any piezoelectric material: the composition point at which the solid-state solution presents the maximum piezoelectric properties and the Curie temperature for that composition. Depending on the molar composition of the solid state solution the resulting PZT presents significant differences in the piezoelectric properties. As presented in Fig. 3.12 the electromechanical coupling of the material presents a clear maximum at a point close to 52% molar percentage of lead zirconate. The d_{33} constant also shows a similar behavior as seen in Fig. 3.13. Because of this behavior the majority of PZTs present chemical compositions close to this point.

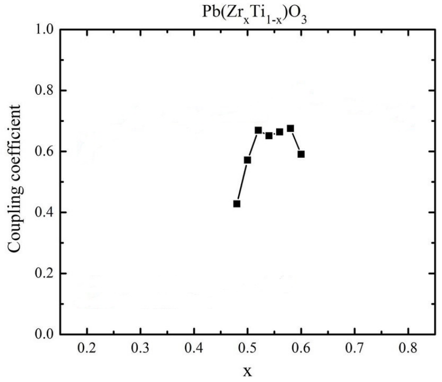

Figure 3.12: Representation of the value for the electromechanical coupling factor (k_p) for the chemical composition of the solid state solution in PZTs. [98]

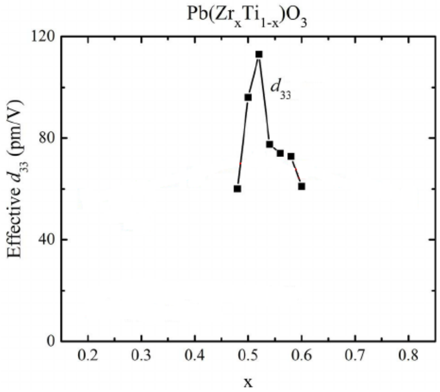

Figure 3.13: Representation of the value for the piezoelectric constant d_{33} for the chemical composition of the solid state solution in PZTs. [99]

The Curie temperature is important as it defines both the minimum temperature to be reached during the poling process (see Sec. 1.4.4) and the maximum operating temperature of the material. In this thesis, the Curie temperature with the implication of poling temperature is not relevant as the material is provided by the manufacturer already poled. The notion of maximum operating temperature is, though, very significant as it must not be exceeded during the soldering of the electrodes. If that was to happen, the material would depolarize and the microstructure of the material would transition to a cubic structure thus losing its piezoelectric properties. When cooling back to the piezoelectric phase the random orientation of the crystals would result in a zero net polarization of the material.

The piezoelectric properties of PZT can be improved through the addition of small quantities of dopants such as niobate (Nb), itrium (Y) or lithium (Li) (commonly up to 2.5% of the molar fraction). [100] [101] The dopants modify the microstructure of the material and may be of two types: donor or acceptor dopands. Donor dopands have a valence higher than the element they substitute in the microstructure while acceptor dopands have a lower valence than the element they substitute. [102] An in-depth analysis of the doping of PZT materials is out of the scope of this thesis because it enters the field of materials engineering.

3.1.4 Mechanical behavior

It is not possible to generalize and speak on the mechanical properties of piezoelectric materials because piezoelectricity refers to a behavior which completely different types of materials present (from organic fibers to synthetic ceramics). This section presents, as for the chemical analysis, the mechanical properties of the piezoelectric materials used in this thesis: PZT ceramics.

The mechanical properties of PZT, while different in terms of structural modeling, present common qualitative behavior with any other non-piezoelectric ceramic. These materials are characterized for their high density (in the range of steel), high compressive strength, a very low tensile strength and brittle. The physical modeling of the material is presented in Sec. 3.2. This section presents qualitative considerations on the behavior of PZT relevant to the experiments performed throughout the thesis.

The asymmetry in the tensile and compression behavior of the ceramic piezoelectric materials makes them very fragile during operation. The application of electric fields that induce tensile stress fields in the material causes fractures at values significantly lower than the depolarization which translates into a pronounced asymmetry in the piezoelectric behavior of the material.

Because of this, the actuation limits of piezoelectric materials are usually defined by the depolarization electric field in compression mode and by the failure tensile stress in the extension mode. Note that piezoelectric ceramics do not present an elastic limit as they are brittle materials.

To mitigate this effect some piezoelectric actuators are pre-stressed mechanically by an embedding material. The value of the pre-stressing mechanical field for this type of actuators is generally the maximum permissible extension of the material. Pre-stressing the material has no influence on the physical constants of the material or the maximum permissible electric fields, it only shifts the position of the zero-electric-field stress while maintaining the limits. This confers the actuator the capacity of limited actuation in extension by reducing the capacity of compression by the same amount.

3.2 Modeling of piezoelectric materials

The behavior of piezoelectric materials can only be properly quantified and evaluated with a physical model that predicts their behavior. The behavior of piezoelectric materials is intrinsically non-linear as their response is characterized by an hysteresis behavior. Despite this, when the electric field, the stress field and the temperature are kept under certain levels, the material presents a behavior that can be accurately approximated with a linear model.

This section presents the linear model, which has been used in the numerical part of this thesis. The intrinsic and external effects that result in non-linearity of the piezoelectric actuator are also presented in this chapter as the phenomenology helps understand the behavior of the actuators. However, these effects remain of qualitative interest for the research performed as the functioning intended for the actuator can be considered well within the limits of the linear behavior.

As the actuators are pushed in terms of temperature, electric field or mechanical field, different phenomena occur such as depolarization, which completely transform the behavior of the material. In these situations of degraded piezoelectric properties the material cannot be considered a piezoelectric material anymore and is of no interest to the present research.

3.2.1 Linear behavior

Despite being non-linear by nature, whenever the actuating electrical and mechanic fields are low enough, piezoelectric materials can be assumed to behave like linear materials. This hypothesis is assumed later on in this thesis during the analysis of the piezoelectric materials. This section presents the linear theory of piezoelectricity.

The linear theory of piezoelectricity couples the electric and mechanical fields into the constitutive equations of the material. The equations and their development from the fundamental thermodynamic principles are presented. The presented theory accounts for the static behavior of the materials as only this aspect of the phenomenon is relevant for the present thesis (dynamic applications of the piezoelectric actuators are considered in the thesis but the hypothesis of quasi-static behavior can be assumed in most situations given the low frequency of the actuation in relation to the high bandwidth that the studied piezoelectric actuators present).

The static understanding of the piezoelectric phenomenology presented in Sec. 3.1.1 is critical for the analysis of the tested actuators throughout the thesis.

3.2.1.1 Constitutive equations

The linear behavior of any piezoelectric material can be described through a term in the constitutive equations of the material. The piezoelectric term in this case is included to the mechanical (or thermo-mechanical) constitutive equations as presented in Eq. 3.3 in tensor notation. [103] In this equation the term δ_{ij} represents the Kronecker delta ($\delta i j = 1$ if $i = j$ and $\delta_{ij} = 0$ otherwise). [104]

$$\begin{aligned} S_{ij} &= s^E_{ijkl} T_{kl} + d_{kij} E_k + \delta_{ij} \alpha^E_i \Delta\theta \\ D_i &= d_{ikl} T_{kl} + \varepsilon^T_{ik} E_k + \tilde{D}_i \theta \end{aligned} \tag{3.3}$$

In the particular cases analyzed in this thesis the thermal component in the general thermo-piezoelectric constitutive equations is not relevant as the temperature has been considered constant throughout all the experiments and numerical analysis performed. The constitutive equation can be expressed for the particular case analyzed and for the particular case of PZT material as presented in matrix form in Eq. 3.4. Note that in this equation the material is considered transversely isotropic and the piezoelectric matrix is particularized for a PZT presenting 3 different piezoelectric constants d_{13}, d_{33} and d_{42}.

$$
\begin{aligned}
S_i &= \begin{bmatrix} s_{11} & s_{12} & s_{13} & 0 & 0 & 0 \\ s_{12} & s_{11} & s_{13} & 0 & 0 & 0 \\ s_{13} & s_{13} & s_{33} & 0 & 0 & 0 \\ 0 & 0 & 0 & s_{44} & 0 & 0 \\ 0 & 0 & 0 & 0 & s_{44} & 0 \\ 0 & 0 & 0 & 0 & 0 & s_{66} \end{bmatrix} T_j + \begin{bmatrix} 0 & 0 & d_{13} \\ 0 & 0 & d_{13} \\ 0 & 0 & d_{33} \\ 0 & d_{42} & 0 \\ d_{42} & 0 & 0 \\ 0 & 0 & 0 \end{bmatrix} E_k \\
D_i &= \begin{bmatrix} 0 & 0 & 0 & 0 & d_{42} & 0 \\ 0 & 0 & 0 & d_{42} & 0 & 0 \\ d_{13} & d_{13} & d_{33} & 0 & 0 & 0 \end{bmatrix} T_j + \begin{bmatrix} \varepsilon_{11} & 0 & 0 \\ 0 & \varepsilon_{11} & 0 \\ 0 & 0 & \varepsilon_{33} \end{bmatrix}
\end{aligned}
\tag{3.4}
$$

The linear model described by these equations defines a model with 6 mechanical, 3 piezoelectric and 2 dielectric independent constants. The definition of these 11 independent constants characteristic of the material are enough to represent how the material behaves according to the liner theory.

Mechanically the compliance matrix s can be expressed for a transversely isotropic material as a function of the constants of the material as presented in Eq. 3.5. [105] This formulation is used later on in Sec. 5 during the numerical modeling of the material to characterize the material from the data provided by the manufacturer of the material.

$$
s = \begin{bmatrix} 1/E_x & -\nu_{xy}/E_y & -\nu_{xz}/E_z & 0 & 0 & 0 \\ & 1/E_y & -\nu_{yz}/E_z & 0 & 0 & 0 \\ & & 1/E_z & 0 & 0 & 0 \\ & & & 1/G_{xy} & 0 & 0 \\ & & & & 1/G_{yz} & 0 \\ & & & & & 1/G_{xz} \end{bmatrix}
\tag{3.5}
$$

This formulation is valid for any orthotropic behavior, the consideration of the material as transversely isotropic allows for the definition of the following relations which reduce the number of mechanical independent variables to 5:

$$
\begin{aligned}
E_x &= E_y \\
\nu_{xz} &= \nu_{yz} \\
G_{xz} &= G_{yz} \\
G_{xy} &= \frac{E_x}{1+\nu_{xy}}
\end{aligned}
$$

The constitutive equations for piezoelectricity are usually presented in the form shown in Eq. 3.6. In such formulation they are useful in the representation of piezoelectric sensing devices.

$$
\begin{aligned}
S_{ij} &= s^D_{ijkl} T_{kl} + g_{kij} D_k + \delta_{ij} \alpha^D_i \Delta\theta \\
E_i &= g_{ikl} T_{kl} + \beta^T_{ik} D_k + \tilde{E}_i \theta
\end{aligned}
\tag{3.6}
$$

It is also possible to express the constitutive equations for piezoelectric actuators as a function of the polatization induced in the material as presented in Eq. 3.7.

$$\begin{aligned} S_{ij} &= s^E_{ijkl} T_{kl} + d_{kij} E_k + \delta_{ij} \alpha^E_i \Delta\theta \\ P_i &= d_{ikl} T_{kl} + \kappa^T_{ik} E_k + \tilde{P}_i \theta \end{aligned} \tag{3.7}$$

Piezoelectric materials, as elements that ultimately transform mechanical energy into electrical energy and vice-verse, can be analyzed from the energetic point of view. This approach allows for the definition of the electromechanical coupling coefficients. These coefficients express the energetic relation between the input energy and the stored energy in its transformed form. This definition is not to be confused with the definition of the efficiency of the actuator, which relates the output transformed energy in relation to the input energy.

Depending on the application of the piezoelectric material as a sensor or as an actuator, the electromechanical coupling can be defined differently. The generic formulations are presented in Eq. 3.8 for the converse and direct piezoelectric effect respectively. [106]

$$\begin{aligned} k^2 &= \frac{stored\, mechanical\, energy}{input\, electrical\, energy} \\ k^2 &= \frac{stored\, electrical\, energy}{input\, mechanical\, energy} \end{aligned} \tag{3.8}$$

The general formulation presented can be particularized according to the mode in which the piezoelectric material actuates or senses. An example of commonly used electromechanical coupling notations is shown in Eq. 3.9 for a piezoelectric material working in the polarization direction and the transverse mode.

$$\begin{aligned} k^2_{33} &= \frac{d^2_{33}}{s^2_{33} \varepsilon^2_{33}} \\ k^2_{31} &= \frac{d^2_{31}}{s_{11} \varepsilon^2_{33}} \end{aligned} \tag{3.9}$$

The efficiency of a piezoelectric actuator or sensor can be defined as the output mechanic/electrical energy in relation to the input electrical/mechanic energy in an actuator or sensor respectively as presented in Eq. 3.10. This definition is not very relevant for the actuator application in this thesis as the majority of the electrical energy input is not transformed to mechanical energy but rather stored in the material as electrostatic energy (much like a capacitor). Whenever the source is not actuating anymore the material discharges the electrical energy stored back to the circuit. According to the efficiency definition, accounting for this non-converted electrical energy, piezoelectric materials reach levels of energetic efficiency of $97-99\%$. This measure though, is not an expression for the mechanical energy that the actuator supplies but rather a measure of the energetic dissipation, which, for this type of materials is very low. [107]

$$\begin{aligned} \eta &= \frac{output\, energy}{input\, electrical\, energy} \\ \eta &= \frac{output\, energy}{input\, mechanical\, energy} \end{aligned} \tag{3.10}$$

3.2.1.2 Derivation of the piezoelectric formulation

The constitutive piezoelectric equations can be derived from the thermodynamic principles starting from the Gibbs potential expression as presented in Eq. 3.11. If an adiabatic reversible system is considered then the differential of internal energy can be expressed as presented in Eq. 3.12. [108]

$$\Gamma = U - T_{ij}S_{ij} - E_k D_k - \theta \Psi \tag{3.11}$$

$$dU = T_{ij}dS_{ij} + E_k dD_k + \theta d\Psi \tag{3.12}$$

Considering Eq. 3.11 and Eq. 3.12 the differential Gibbs potential can be expressed as shown in Eq. 3.13.

$$d\Gamma = -S_{ij}dT_{ij} - D_k dE_k - \Psi d\theta \tag{3.13}$$

The linearization of the Taylor development for Eq. 3.13 leads to the equation presented in Eq. 3.14

$$d\Gamma = \left(\frac{\partial \Gamma}{\partial T_{ij}}\right)_{E,\theta} dT_{ij} + \left(\frac{\partial \Gamma}{\partial E_k}\right)_{T,\theta} dE_k + \left(\frac{\partial \Gamma}{\partial \theta}\right)_{T,E} d\theta \tag{3.14}$$

The comparison of Eq. 3.13 and Eq. 3.14 leads to the expressions for the strain, electrical displacement and entropy presented in Eq. 3.15 and thus to the derivative expression of these same variables presented in Eq. 3.16.

$$\begin{aligned} S_{ij} &= -\left(\frac{\partial \Gamma}{\partial T_{ij}}\right)_{E,\theta} \\ D_k &= -\left(\frac{\partial \Gamma}{\partial E_k}\right)_{T,\theta} \\ \Psi &= -\left(\frac{\partial \Gamma}{\partial \theta}\right)_{T_E} \end{aligned} \tag{3.15}$$

$$\begin{aligned} dS_{ij} &= \left(\frac{\partial S_{ij}}{\partial T_{lm}}\right)_{E,\theta} dT_{lm} + \left(\frac{\partial S_{ij}}{\partial E_n}\right)_{T,\theta} dE_n + \left(\frac{\partial S_{ij}}{\partial \theta}\right)_{T,E} d\theta \\ dD_k &= \left(\frac{\partial D_k}{\partial T_{lm}}\right)_{E,\theta} dT_{lm} + \left(\frac{\partial D_k}{\partial E_n}\right)_{T,\theta} dE_n + \left(\frac{\partial D_k}{\partial \theta}\right)_{T,E} d\theta \\ d\Psi &= \left(\frac{\partial \Psi}{\partial T_{lm}}\right)_{E,\theta} dT_{lm} + \left(\frac{\partial \Psi}{\partial E_n}\right)_{T,\theta} dE_n + \left(\frac{\partial \Psi}{\partial \theta}\right)_{T,E} d\theta \end{aligned} \tag{3.16}$$

In the equations presented in Eq. 3.16 it is possible to identify the elastic compliance coefficients, piezoelectric strain constants, coefficients of thermal expansion, dielectric permittivities and pyroelectric coefficients as follows:

$$s^{E,\theta}_{ijlm} = \left(\frac{\partial S_{ij}}{\partial T_{lm}}\right)_{E,\theta}$$

$$d^{\theta}_{ijn} = \left(\frac{\partial S_{ij}}{\partial E_n}\right)_{T,\theta} = \left(\frac{\partial D_n}{\partial T_{ij}}\right)_{E,\theta}$$

$$\alpha^{E}_{ij} = \left(\frac{\partial S_{ij}}{\partial \theta}\right)_{T,E} = \left(\frac{\partial \Psi}{\partial T_{ij}}\right)_{E,\theta}$$

$$\varepsilon^{T,\theta}_{kn} = \left(\frac{\partial D_k}{\partial T_{ij}}\right)_{T,\theta}$$

$$p^{T}_{k} = \left(\frac{\partial D_k}{\partial \theta}\right)_{T,E} = \left(\frac{\partial \Psi}{\partial E_k}\right)_{T,\theta}$$

$$\frac{\rho c^{T,E}}{\theta_0} = \left(\frac{\partial \Psi}{\partial \theta}\right)_{T,E}$$

Integrating Eq. 3.16 and substituting the aforementioned coefficients leads to the constitutive equations presented in Sec. 3.2.1.1 and shown in Eq. 3.17.

$$\begin{aligned} S_{ij} &= s^{E,\theta}_{ijlm} T_{lm} + d^{\theta}_{ijn} E_n + \alpha^{E}_{ij} \Delta\theta \\ D_k &= d^{\theta}_{klm} T_{lm} + \varepsilon^{T,\theta}_{kn} E_n + p^{T}_{k} \Delta\theta \\ \Delta\Psi &= \alpha^{E}_{lm} T_{lm} + p^{T}_{n} E_n + (c^{T,E}/T_0)\Delta\theta \end{aligned} \tag{3.17}$$

If the temperature is considered to be constant the temperature-related terms can be neglected and the equations shown in Eq. 3.3 are obtained. Note that the equation for the entropy is not included as it is of no relevance to the experiments and calculations performed throughout the thesis.

3.2.2 Non-linear phenomena

Piezoelectric materials are, by nature, non-linear materials which behave close to linearity in a particular range. In the present thesis, the piezoelectric materials are used in a range of electric and mechanical fields in which the linearity assumption does not present large deviations from reality.

The most relevant causes for non-linear behavior in piezoelectric materials are hysteresis and dielectric losses. The analysis of these causes is presented in this section in a qualitative manner to provide an insight into the phenomenology of piezoelectric materials. A mathematical analysis of this phenomenon and its implementation in the subsequent calculations has been considered out of the scope of the thesis because the work regime of the actuators in the experiments performed has been either static or at low frequency and the deviations due to transitory phenomenon are of no significance in comparison with the causes presented.

3.2.2.1 Hysteresis

Piezoelectric actuators present hysteresis between electric field and polarization as the main cause of the non-linear behavior. [109] Although the origin of this hysteresis behavior in piezoelectric materials is not completely understood, the accepted explanation is the displacement or sliding of polarization of the domain walls within the material. [110] As in the case of PZT, most of the piezoelectric ceramics are poly-crystalline. The boundaries (or domain walls) between the different crystalline domains of a macroscopic material present discontinuities of the piezoelectric properties throughout the material at a microscopic level. The boundaries between regions with different microstructures or orientations present electric interaction between them that causes changes in the polar orientation of the domains when submitted to an external electrical field.

A consequence of this effect is that the hysteresis behavior in poly-crystalline materials is more pronounced than such of single crystals. It is also important to note that any solid-state solution (such as PZT) cannot, by definition, be a single-crystal material. This implies that, to some extent, the material presents hysteresis throughout its operational range. The characteristic hysteresis curve for a PZT piezoelectric material (PIC255 as tested experimentally further on in the thesis) is presented in Fig. 3.14 as obtained during the experimental characterization of the material.

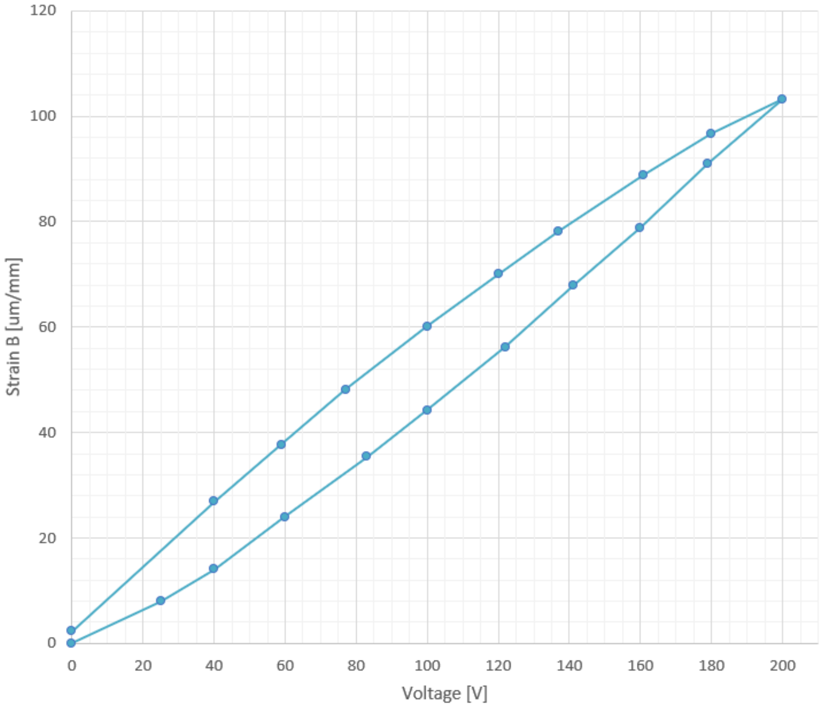

Figure 3.14: Representative hysteresis loop as obtained during the experimental part of the thesis.

Because of hysteresis, the response of a given piezoelectric material to a defined input signal presents a high degree of unpredictability. [111] It is possible to improve the hysteresis behavior of a piezoelectric material if the driving is performed through the electric charge rather than voltage. [112] Hysteresis is associated with energy dissipation as there is a direct relation between the amplitude of the hysteresis loop and the dissipated energy by the material. [113]

From a macroscopic point of view, the explanation for the phenomenon is that the number of dipoles in the material aligned with the applied electric field changes over time. [114] These changes in the orientation of the material dipoles do not occur instantly causing a drift over time of the material response. This effect is seen in the experiments performed on the piezoelectric actuator in Sec. 7.

3.2.2.2 Electromechanical losses

The notion of electromechanical transformation of energy introduced in Sec. 3.1.1 and the equations that define and quantify this transformation account for the linear part of the piezoelectric phenomenon. The linear theory does not account, though, for second order effects that appear the moment that the conditions in the material are not intrinsically constant.

The assumptions presented in the linear constitutive equations of piezoelectricity account for no change in the temperature at which the material operates. This hypothesis, valid for cases in which the environment temperature is kept constant, does not account for the change in temperature originated in the material due to energy loss in the electromechanical energy transformation.

Despite having a very high energetic efficiency, piezoelectric materials present dielectric losses like any conventional material. The electric charge dissipates in the form of heat and increase the local temperature of the material. [115] As piezoelectric materials are ceramics, they present a very low thermal conductivity and a high thermal inertia which causes the material to unevenly modify its local temperature distribution when an internal heat is produced. This uneven and transient temperature variation modifies the piezoelectric response of the material outside of the response predicted by the linear theory (in the initial assumption the linear piezoelectric theory used disregards the influence of temperature variation). A possible solution to model such phenomenon in the material constitutive equations would be to include a temperature-dependent term. Such term would inevitably include a time-dependency which would result in a model to complex for its practical implementation.

The dielectric losses have not been considered in the material models used throughout this thesis as the main applications of interest concern static applications and such losses become significant in the dynamic regime. In order to avoid transient piezoelectric response variations due to temperature, after each actuation voltage variation the experiments considered a time for the temperature to stabilize in the new condition before experimental data was obtained.

4. Characterization of a piezoelectric actuator

The first step in the analysis of any piezoelectric material is the characterization of its mechanical, electric and piezoelectric properties. The properties to be determined are the ones already introduced in Sec. 3 during the presentation of the linear piezoelectric theory.

To determine the piezoelectric properties and behavior of the material a specific patch actuator has been selected, this actuator presents high piezoelectric coefficients in the directions perpendicular to the polarization direction which makes it an interesting choice for the morphing part of the experiments.

The first part of the research focused on methods for determining the extension of the piezoelectric patch without interfering with the mechanics of the motion of the actuator. The different experiments are presented in this section together with the obtained results.

The following two sections present the experiments that provided successful results: through interferometry and through tensometry. This chapter primarily focuses on these two methodologies. The experiments are complementary as interferometry determined the behavior of the patch in the polarization direction (thickness) while the tensometric experiments determined the in-plane behavior.

The results obtained following these tests are also used in different manners. On the one hand, the static results are used later on in the calibration process of the numerical simulations while the dynamic tests allow for the definition of the maximum operation conditions for this type of actuators.

4.1 First experiments

The initial experiments performed aimed at the determination of the in-plane piezoelectric constants for the piezoelectric patch available for the experiments. The tests envisioned allow for the determination of the constants in the patch with the minimal interaction with the material as not to distort the behavior of the material.

The experiments have not reached maturity for testing in the piezoelectric patch itself and a dummy material has been used to demonstrate the capability of the experiment to obtain the desired results in terms of order of magnitude of the parameters measured and in terms also of accuracy of the readings.

The method designed consists in marking the piezoelectric patch at two very near points oriented in the desired direction of measurement. The marking is performed on the pre-stressing resin and not on the active element of the actuator itself so any indents on the piezo-active ceramic are avoided. The piezoelectric patch is then introduced in a microscope and the distance between the two original points measured when the piezoelectric actuator is not powered. The piezoelectric material is then powered and the distance measured again.

The difference of distances (elongation of the piezoelectric material) can be transformed into deformation through the definition of strain presented in Eq. 4.1 and this deformation can be used to determine the piezoelectric constant of the material for the direction measured.

$$\varepsilon = \frac{\Delta d}{d} \tag{4.1}$$

This method would also work in multiple directions provided that at least two points of measurement exist in the desired direction.

The method for measurement of the deformations has been tried with a piezoelectric dummy made of paper to validate the method without the risk of affecting the piezoelectric patch. Different markings have been performed using different tools reaching the results shown in Fig. 4.1.

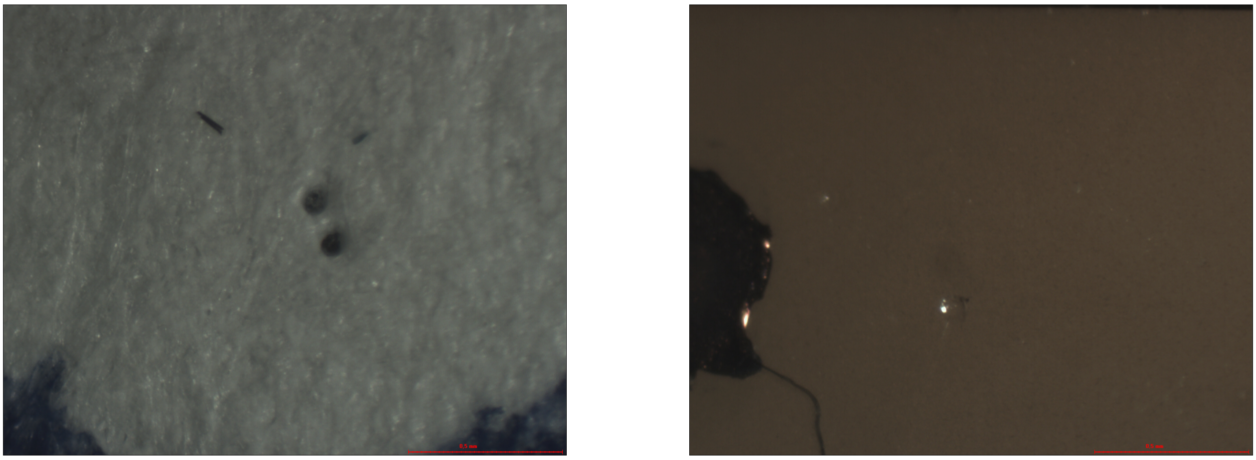

Figure 4.1: Dummy piezoelectric patch (left) and strain gauge (right) with markings as seen through the microscope.

This method presents, though, different problems that make it unpractical for the study of the morphing of structures:

- At the moment of the experiments, there is no method available to mark the specimens with finer print and closer distance that the shown above in the pictures. The distance between points achieved is too large in comparison to the deformation of the piezoelectric patch so the measurements would present no accuracy.
- The measurement of the deformations in the piezoelectric material can only be performed in a microscope that allows for the measurement of the distances in the sample. This means that the microscope has to have a camera calibrated to the augmentation, which is a type of equipment that the university could not offer throughout the test campaign, only for punctual experiments.

- The dependency of the microscope equipment also implied that no measurements could be performed in any other test bench that was not the microscope itself. This fact restricts the geometry of the specimens to a point in which no morphing experiments can be performed without incurring in technologies out of reach for the level of research proposed in this thesis.
- The powering of the actuator at the voltages required inside the microscope is a working condition for which the microscope is not prepared and it could affect or distort the behavior of the electronic systems without control on such distortion.

Because of the uncertainties that this method presents and the limitations it imposes in terms of more complex tests, this approach has been abandoned. Other methodologies have been used as means of continuing the performed research. These methodologies are presented as means for characterization of the piezoelectric patch and the analysis of morphing of structures with embedded actuators in Sec. 4.2, Sec. 4.3 and Sec. 7.

4.2 Interferometric experiments

The second part of the experiments performed in order to analyze the behavior of the piezoelectric patch has been performed through interferometry with the scope of analyzing the thickness (polarization direction) deformation of the patch. The deformation of the material in this direction is relevant as the piezoelectric coefficients of this type of materials are highest in such direction.

The interferometry tests performed at the *Micro-nano Technologies Laboratory* of the institute *INCDIE ICPE-CA* with the help of Dr. Ing. Pislaru-Danescu Lucian are presented in this section of the report. The tests have been performed to analyze the thickness behavior of the piezoelectric patch in both the static and the dynamic regimes for different types and frequencies of excitation signals to determine the limits of actuation of the actuator.

The main advantage in this type of experiments is that the method is not influenced, like in the strain gauge measurements, by adhesives and the behavior of the used sensors. As interferometry uses light to measure distance, any measurement does not modify the behavior of the element.

The experiments have been conducted over the time of three days in the laboratory at *INCDIE ICPE-CA* in the following order:

- Configuration verification and general identification of the behavior
- Static tests and square signal tests
- Dynamic behavior tests with different excitation signal shapes

4.2.1 Objectives

The interferometric testing is devised as a way of understanding the behavior of the piezoelectric patch in the polarization direction in which the strains produced are the largest. The results are used to study the phenomenology that the chosen piezoelectric material presents in the actuator in terms of static and dynamic actuation. However, due to the anisotropy of the material, a calibration of the piezoelectric constants in the numerical model cannot be directly performed with this type of tests as the morphing implementation of the actuator uses the strain produced in the direction perpendicular to the polarization direction.

The objectives for these experiments have been the following:

- Determine the transverse piezoelectric deformation as a function of the frequency of excitation.
- Determine the transverse piezoelectric deformation as a function of the waveform to which the piezoelectric patch is subject: namely square, sine, triangle or ramp.

4.2.2 Equipment used and experimental setting

During the experiments the equipment used has been provided by *INCDIE ICPE-CA* within the used laboratory. The tested piezoelectric patch has been the P-876.A12 available from the previous experiments. The list of the used equipment is presented below. The model of each of the components used is presented with a brief description of their respective capabilities.

- **Agilent 5529A/55292A Laser Interferometre:** it is a displacement measuring system with nanometric precision. It is used to determine displacements of a deformed component or system in the sine of electric or magnetic fields without interacting with these fields. It is normally used with piezoelectric patches, magnetostrictive materials, electrostrictive materials, sensors, actuators, micro-motors of electromechanic components, etc. The interferometer system consists of the following components necessary for a correct linear measurement:
  - Agilent 5519A/B Laser head
  - Agilent 10766A linear interferometer
  - Agilent 10767A retro-reflector
  - Height regulating system
  - Data acquisition PC with specific software
  - Agilent 10888A remote control
  - Agilent 10757D air sensor
  - Agilent 10757D material temperature sensor
  - Agilent 10753B tripod
- **Tektronix DPO 4032 Oscilloscope:** digital phosphor oscilloscope with a bandwidth of $350MHz$.
- **Rigol DG2021A Function/Arbitrary Waveform Generator:** signal generator with a bandwidth of $25MHz$ and a data transfer speed of $100MSa/s$.
- **Tabor Electronics WW2074 Arbitrary Waveform Generator:** arbitrary signal generator with dual channel and a data transfer speed of $200MS/s$. Bandwidth of $80MHz$ for sinus signal, $16bit$ resolution and $10V_{p-p}$, 50Ω output.

- **Tegam model 2350 High Voltage Amplifier:** output voltage of $400V_{p-p}$ $(\pm 200V)$ and output current of $40mA$ with a slew rate greater than $250V/\mu s$ with dual channel capacity.

The setting of the experiments has been the same for all the performed tests. The piezoelectric patch has been placed in a granite block to provide a stable, vibration-free environment without any influential electrical characteristics. The piezoelectric patch has been wired to the output of the Tegan amplifier. The signal that actuates the piezoelectric patch is read with the Tektronix oscilloscope to monitor real-time the actuating electric signal and have a reliable reference for the results post-processing. A block diagram of the experimental setting is represented in Fig. 4.2.

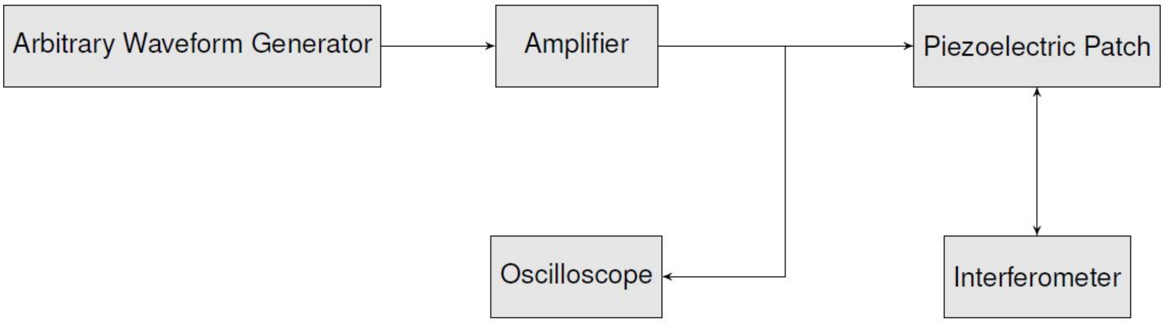

Figure 4.2: Block diagram of the experimental setting used during the interferometric testing.

The input signal to the amplifier is generated by the arbitrary waveform generator. Two arbitrary waveform generators have been used during the experiments: the Rigol waveform generator was used in the first part of the experiments due to its simplicity in the set-up of square waveform while the Tabor Electronics waveform generator was used in the variable duty cycle tests and the tests with waveforms different than square due to its higher versatility. The output quality of the signal from both arbitrary waveform generators was very good as has been seen in the oscilloscope captures. A figure of the laboratory setting is shown in Fig. 4.3 showing the interferometry equipment, the granite table with the piezoelectric patch, the signal amplifier, generator and oscilloscope.

4.2.3 Boundary conditions and environmental conditions

The boundary conditions in the interferometric experiments have been imposed by the experimental set-up required in order to measure the thickness deformation of the piezoelectric patch. Two types of boundary conditions have been considered in this experiment: mechanical and electric.

The mechanical boundary conditions refer to the support of the test specimen during the experiments. In this case the piezoelectric patch was laying on a granite block without any attachment other than the friction between both materials. Over the piezoelectric, one of the prisms used in the interferometer held the piezoelectric patch without other forces than its own weight. This configuration is illustrated in Fig. 4.4. The high mass of the granite block ensures that no interference occurs between the excitation frequencies of the piezoelectric patch and the natural frequencies of the support table. The natural frequencies of the support table are very low in comparison to any of the natural frequencies relevant in the performed experiments.

The electrical boundary conditions have been the different excitation signals acting across the electrodes of the piezoelectric patch. The waveforms used in the excitation of the piezoelectric have been: square,

Figure 4.3: Laboratory setting used in the interferometric testing performed in the *Micro-nano Technologies Laboratory* of the institute *INCDIE ICPE-CA*. From left to right, the oscilloscope, the arbitrary waveform generators, the amplifier, the interferometer, the piezoelectric patch and the support table with the granite block can be seen.

square with variable duty cycle, sinus, triangular and ramp. Each of the waveforms allows for the study of different aspects of the response of the piezoelectric actuator. These aspects are detailed in Sec. 4.2.5 together with the analysis of the results.

In the square and ramp waveforms, different duty cycles have been used in order to analyze the influence of the stabilization time between the changes of voltage and the influence of the voltage slope in the piezoelectric response. The duty cycle for both waveforms has been defined as follows according to the forms presented in Fig. 4.5 and Fig. 4.6 for the square and ramp waveforms respectively.

The definition of duty cycle is:

$$k[\%] = \frac{t_1}{T} \times 100 = \frac{t_1}{t_1 + t_2} \times 100$$

this definition is also valid for the ramp de-axing factor according to the notation presented in Fig. 4.6.

In terms of environmental testing conditions, the tests have been done in the *INCDIE ICPE-CA* facilities. The humidity and temperature have not been controlled but room temperature conditions of $20\,^{\circ}C$ can be safely assumed. These conditions are similar to other testing performed on the piezoelectric thus allowing for a direct comparison of previously obtained results on the patch without temperature correction of the results being necessary.

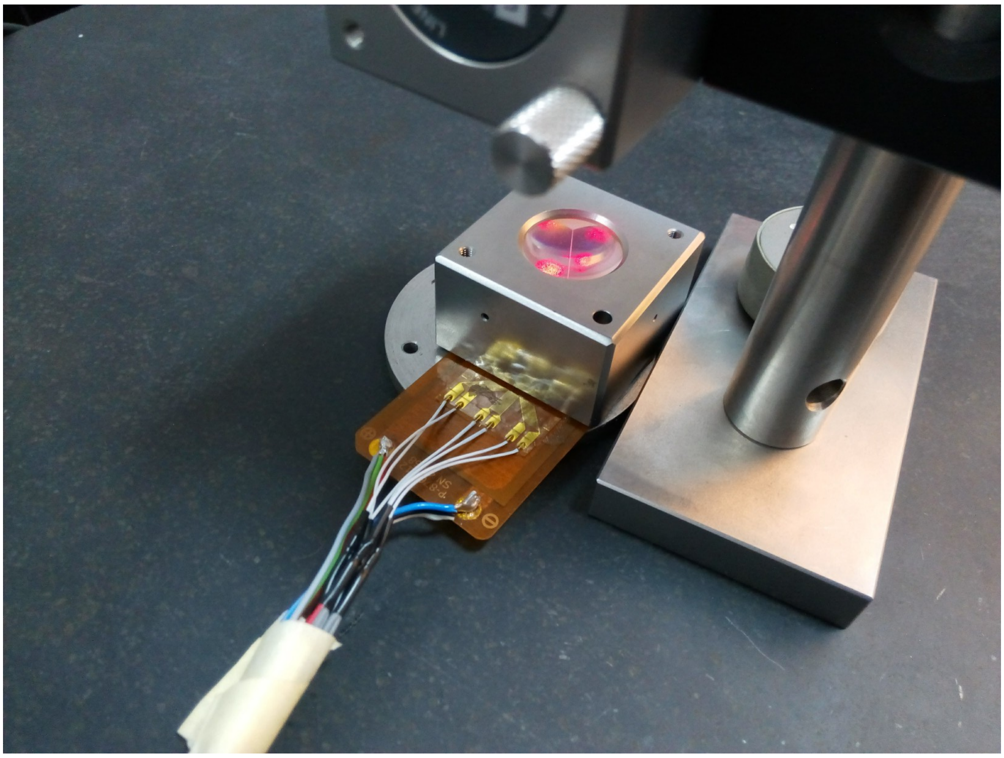

Figure 4.4: Detail of the piezoelectric patch placement under the interferometer prism.

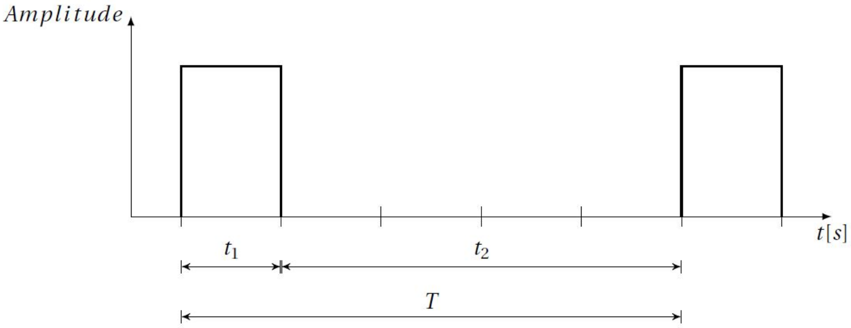

Figure 4.5: Square waveform representation with the definition of duty cycle used during the tests.

4.2.4 Test results

The testing results of the interferometric experiments are presented in this section. The testing is divided into static and dynamic experiments. The static experiments aim to determine how does the piezoelectric deform when inertial forces are negligible while dynamic tests account for the dynamic forces of the piezoelectric patch in different environments marked by different boundary conditions in terms of shape of the actuating signal.

The presented results are organized by type of input signal used to excite the piezoelectric. The differentiation between static and dynamic results is performed during the analysis of the results as without previous knowledge it is not possible to know the time-span of inertial effects in the piezoelectric depending on the type of excitation waveform.

Table 4.1 presents the list with the input signals used to analyze the response of the piezoelectric patch.

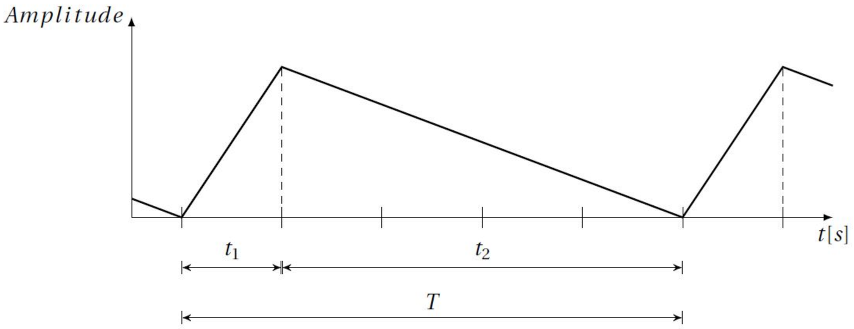

Figure 4.6: Ramp waveform representation with the definition of the de-axing factor used during the tests.

The order in which the tests are presented on the table is the same as they are presented in the figures below.

Table 4.1: List of input waveforms used in the interferometric experiments.

Waveform	**Duty cycle**	**Freq. [Hz]**	**Waveform**	**Duty cycle**	**Freq. [Hz]**
Square	$k = 50\%$	0.2	Square	$k = 70\%$	0.5
Square	$k = 50\%$	0.5	Square	$k = 70\%$	10
Square	$k = 50\%$	1	Sine		10
Square	$k = 50\%$	2	Sine		50
Square	$k = 50\%$	20	Sine		100
Square	$k = 50\%$	50	Sine		1000
Square	$k = 50\%$	80	Triangle		0.5
Square	$k = 50\%$	100	Triangle		1
Square	$k = 50\%$	120	Triangle		5
Square	$k = 20\%$	0.5	Triangle		10
Square	$k = 20\%$	10	Triangle		100
Square	$k = 40\%$	0.5	Ramp	$k = 10\%$	0.5
Square	$k = 40\%$	10	Ramp	$k = 10\%$	1

The results presented for the performed tests include the capture from the interferometer software with the acquisition signal representing the deformation of the piezoelectric patch in the direction of polarization (its thickness direction), and (when available) the capture of the excitation signal from the oscilloscope. The comparison between both images allows to determine how does the piezoelectric patch behave.

4.2.4.1 Square waveform for 50% duty cycle

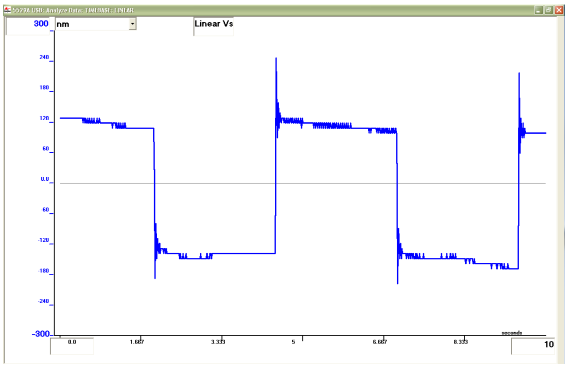

Figure 4.7: Piezoelectric thickness response with square excitation at $200V$, with duty cycle 50% at $0.2Hz$

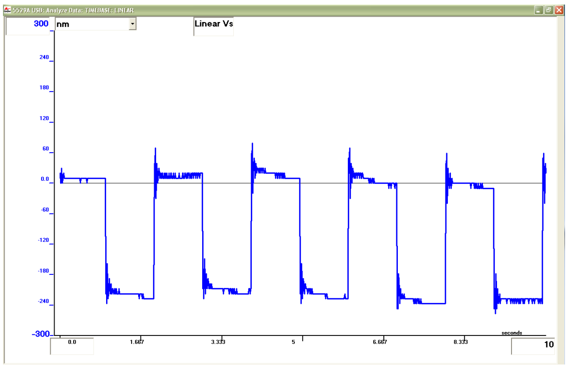

Figure 4.8: Piezoelectric thickness response with square excitation at $200V$, with duty cycle 50% at $0.5Hz$

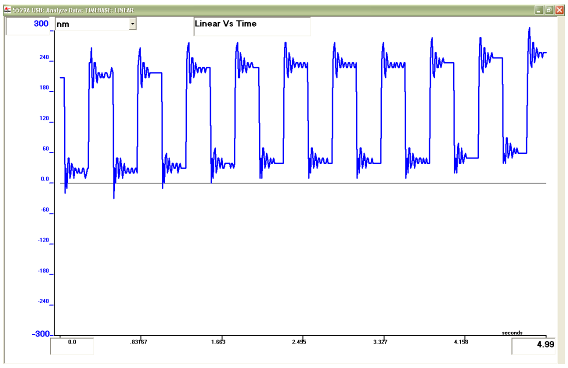

Figure 4.9: Piezoelectric thickness response with square excitation at $200V$, with duty cycle 50% at $2Hz$

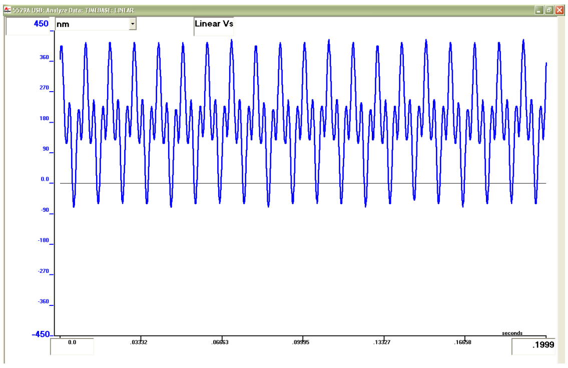

Figure 4.10: Piezoelectric thickness response with square excitation at $200V$, with duty cycle 50% at $100Hz$

4.2.4.2 Sinus waveform

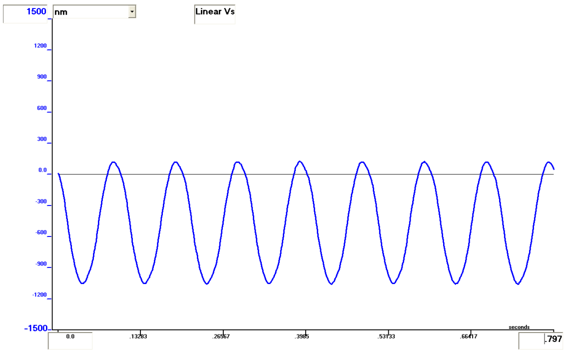

Figure 4.11: Piezoelectric thickness response with sine excitation at $200V$ at $10Hz$

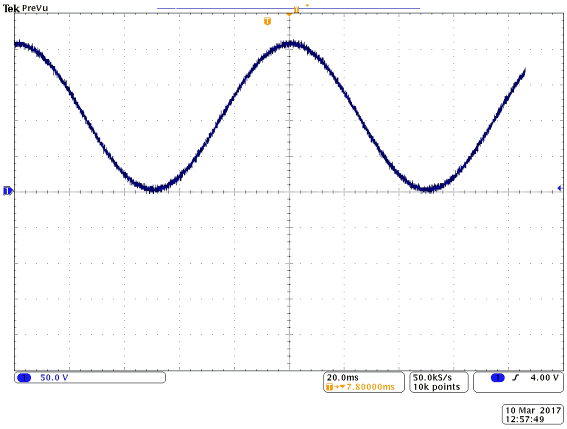

Figure 4.12: Excitation signal from the power amplifier at $200V$ at $10Hz$

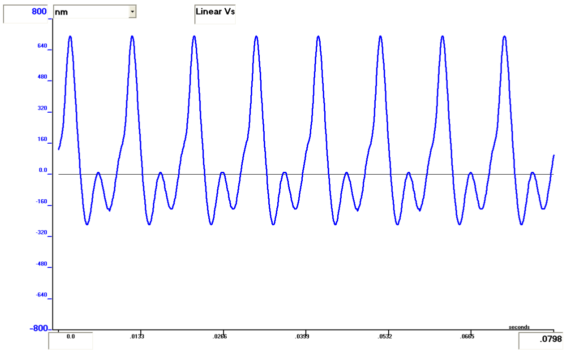

Figure 4.13: Piezoelectric thickness response with sine excitation at $200V$ at $100Hz$

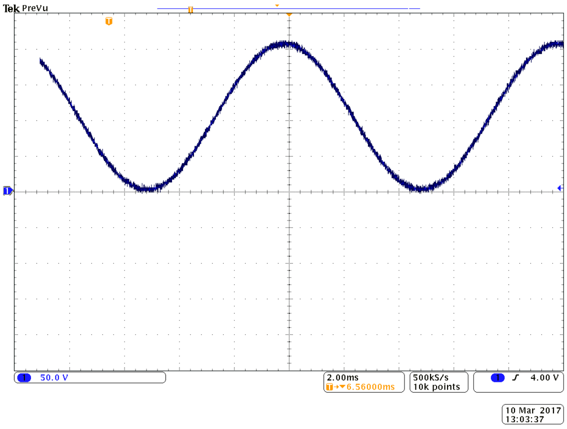

Figure 4.14: Excitation signal from the power amplifier at $200V$ at $100Hz$

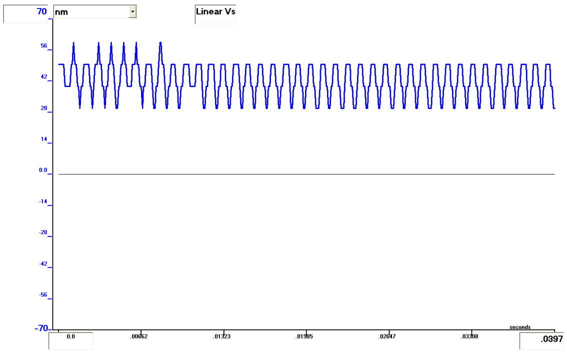

Figure 4.15: Piezoelectric thickness response with sine excitation at $200V$ at $1000Hz$

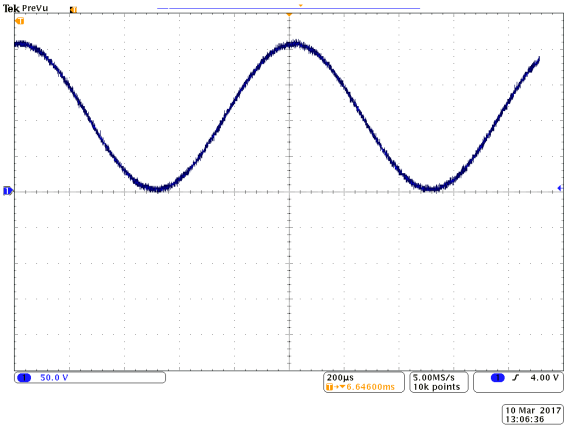

Figure 4.16: Excitation signal from the power amplifier at $200V$ at $1000Hz$

4.2.4.3 Triangle waveform

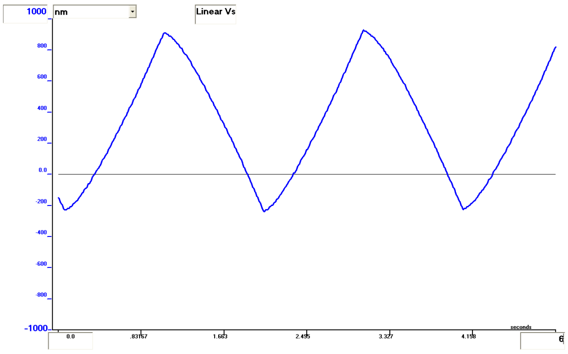

Figure 4.17: Piezoelectric thickness response with triangle excitation at $200V$ at $5Hz$

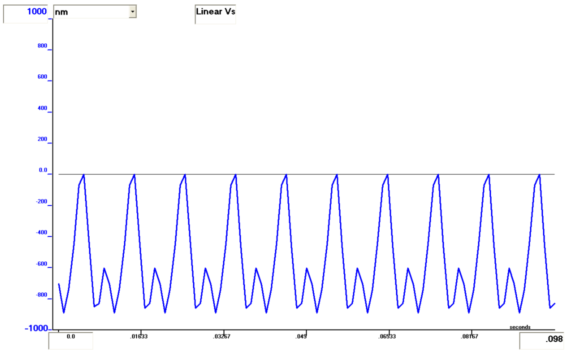

Figure 4.18: Piezoelectric thickness response with triangle excitation at $200V$ at $100Hz$

4.2.4.4 Ramp waveform

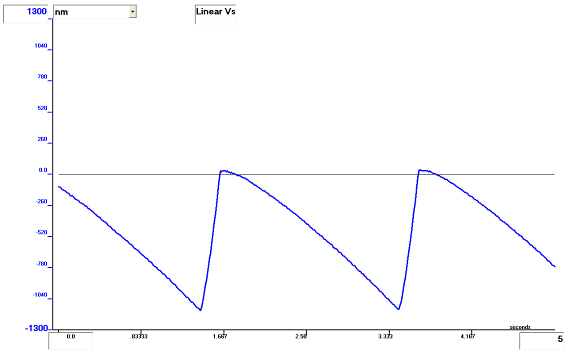

Figure 4.19: Piezoelectric thickness response with ramp excitation at $200V$, with duty cycle 10% at $5Hz$

4.2.5 Analysis of the results

The analysis of the results presented in the previous section is presented in this section. The static and the dynamic analysis of the experiments are presented separately. Furthermore, some of the experiments only present qualitative conclusions on the behavior of the piezoelectric patch.

The static results differ from the dynamic results in the fact that the piezoelectric patch is allowed to stabilize into a steady state before any changes in the input signal are introduced. This means that no quasi-static behavior needs to be assumed for the signal, at some periods of time is indeed stationary. The deformation reading of the actuator presents two distinguished phases for each of the different values of input voltage applied: a transitory response and a steady state response. These two phases are illustrated in Fig. 4.20 for one of the cases in which the steady state answer of the actuator was studied.

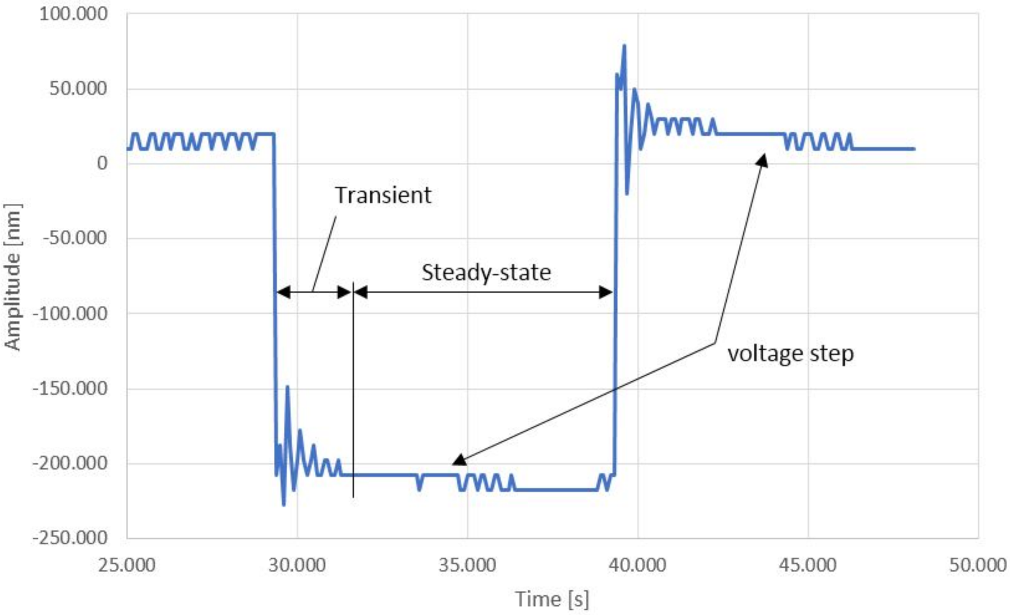

Figure 4.20: Representation of the deformation signal from the interferometer for a semi-period of the input voltage (square waveform of $200V$ at $0.5Hz$) showing the transitory and steady state responses occurring at every voltage change.

According to this definition of the transient and steady-state phenomenology in the deformation signal of the piezoelectric patch, a given experiment can be used to obtain data regarding static behavior if a steady-state answer exists. Otherwise, the inertial forces of the piezoelectric patch are too significant to extract reliable information on the static behavior of the actuator.

4.2.5.1 Static Results

The objective of this experiments is to determine the piezoelectric coefficient in the polarization direction (d_{33}). This coefficient, as detailed in the second report of this thesis (see [116]), relates the electric field in the direction in which the piezoelectric material is polarized with the deformation in the same direction. In the studied piezoelectric patch, d_{33} relates the thickness deformation with the applied voltage. The thickness deformation must be considered only in the steady-state regime of the movement as presented in Fig. 4.20.

For each of the measurements, the steady-state response has been isolated for each of the different voltage steps up to the frequency in which a steady state response does no longer exist in the acquired deformation signal. Such frequency marks the maximum frequency at which static results can be obtained and is found close to $2Hz$.

For each of the analyzed frequencies, the average value of the steady-state deformation has been obtained at 10 consecutive voltage steps in order to calculate 9 consecutive peak-to-peak amplitudes. The average of these values is represented in Fig. 4.21. The graphic shows the average amplitude of the steady-state regime in black together with the 95% confidence interval as well as the amplitude of the deformation for other frequencies that present no steady-state response.

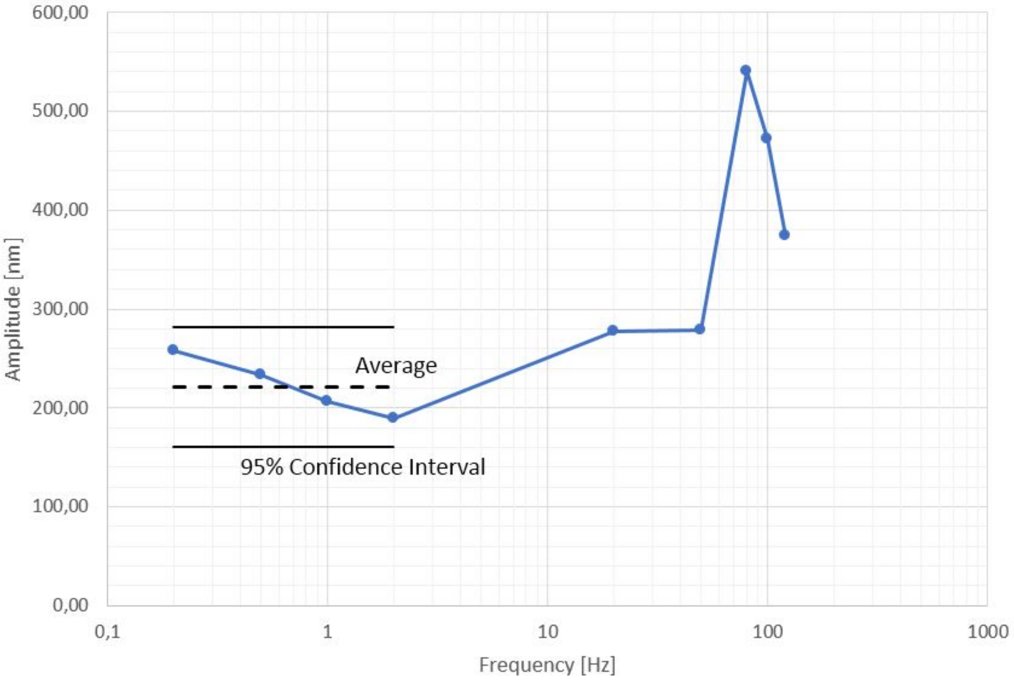

Figure 4.21: Amplitude of the thickness deformation on the piezoelectric patch for the different studied frequencies.

The average of the deformation for the steady-state response of the piezoelectric actuator is found at $221{,}52nm \pm 27{,}3\%$ (or $221{,}52nm \pm 60{,}42nm$). The graphic shows that the material does not present a constant amplitude behavior in the steady-state regime. This is consistent with the amplitude-frequency diagrams for the vibration of mechanical structures.

The integrity of the measures can be verified through the analysis of the results shown in Fig. 4.22. The standard deviation of the measures done throughout the static experiments does not surpass $7nm$ which means that the 95% confidence interval for these data is within $\pm 5\%$ of the respective value.

The simplification of the piezoelectric equations for the steady-state regime (considering that the piezoelectric deformation components do not present coupling between them) results in the equation presented in Eq. 4.2. In this equation Δ_z is the deformation in the thickness direction, V is the applied voltage, t the thickness of the piezoelectric layer, z the length of the piezoelectric patch in such direction.

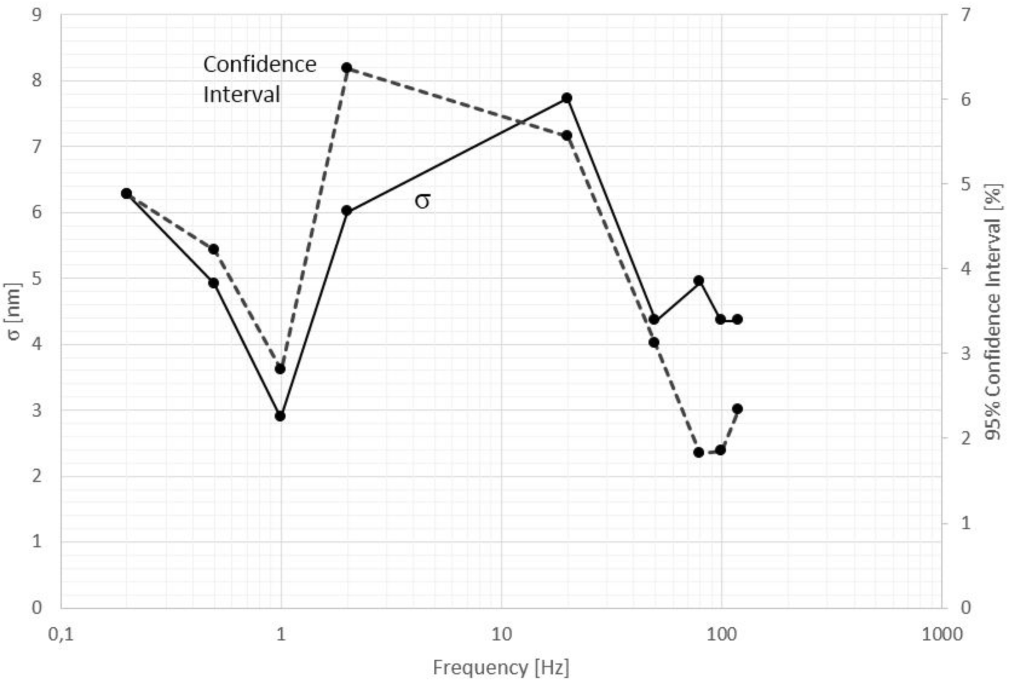

Figure 4.22: Standard deviation associated to the measures taken for each of the voltage steps for each of the studied frequencies.

$$\Delta_z = d_{33}\frac{V}{t}z \tag{4.2}$$

$$d_{33} = \frac{\Delta_z\, t}{V\, z} \tag{4.3}$$

The static deformation of the piezoelectric can be used together with the voltage to calculate the piezoelectric coefficient d_{33} as shown in Eq. 4.3. Table 4.2 presents the values for the calculated d_{33} coefficients for each of the studied frequencies.

Table 4.2: Obtained deformation values and calculated piezoelectric coefficients for the studied frequencies in steady-state regime.

Frequency $[Hz]$	**Amplitude** $[nm]$	d_{33} $\times 10^{-12}[C/N]$
0.2	$257.59 \pm 4.87\%$	515.2
0.5	$233.41 \pm 4.22\%$	466.8
1	$206.15 \pm 2.80\%$	412.3
2	$188,96 \pm 6.36\%$	377.9
Average	$221.52 \pm 27.28\%$	443.0

The results of Table 4.2 have been analyzed and compared with the piezoelectric patch manufacturer specifications. The piezoelectric obtains a performance higher than the expected published by the manufacturer at $0.2Hz$ (see Fig. 4.7). This can be explained because in that experiment the signal has a continuous temporal run-out of the signal in the data acquisition. For each of the voltage steps, the steady-state value of the signal is not constant. This generates significant distortions in the calculation of the piezoelectric properties. It has been possible to determine that the number of uncertainties that surround the readings of the piezoelectric thickness deformation in the steady-state regime diminishes as the frequency increases. This poses a compromise in the readings performed: a higher frequency means an increased reliability in the readings performed, but at the same time it results in a reduced number of valid measurements for each of the voltage steps (Fig. 4.9 illustrates how for a frequency of $2Hz$ the number of readings for each voltage step is inferior because the temporal length of the steady-state phase is shorter).

Attaining to this explanation, the most reliable reading performed are the $1Hz$ and the $2Hz$ readings, which result in deviations of 3.1% and 5.5% respectively from the manufacturer's specifications.

4.2.5.2 Dynamic Results

The second part of the analysis studies the dynamic behavior of the piezoelectric patch in terms of thickness deformation when it is excited at different frequencies with different waveforms. The scope of these tests is to analyze the capacity of the piezoelectric to deform according to different excitation waveforms and to study how does the deformation signal differ from the excitation in different cases. As detailed in Sec. 4.2.3, the piezoelectric patch has been excited with rectangular, triangular, sine and ramp waveforms.

Before any analysis of the results is to be attempted, it is interesting to observe how accurate is the excitation waveform to the intended excitation signal. In order to analyze this, the noise of the input signal has been analyzed through the oscilloscope captures like the one presented in Fig. 4.15. The parameter to analyze the influence of the noise on the overall signal is the signal-to-noise ratio commonly used in electrical engineering and as defined in Eq. 4.4.

$$SNR = \left(\frac{A_{signal}}{A_{noise}}\right)^2 \tag{4.4}$$

The analysis of the different input signals according to the presented formulation led to the conclusion that the signal-to-noise ratio is at all times greater than 200. Note than in Eq. 4.4, A_{signal} and A_{noise} are RMS values.

Once the quality of the excitation waveform can be verified, the results obtained can be analyzed with the certainty that the input signal is not a relevant agent in any distortion that may appear in the response.

The first tests performed have been the rectangular experiments with different duty cycles (20%, 40%, 50% and 70%). In these tests, it is important to notice, first of all, if the behavior of the piezoelectric patch presents or not a steady-state response as defined previously in Sec. 4.2.5.1. Fig. 4.8 and Fig. 4.9 present the response of the piezoelectric patch for a 50% duty cycle at the frequencies of $0.5Hz$ and $2Hz$ respectively. It is relevant to notice that the piezoelectric patch does reach a steady-state response only for the $0.5Hz$ frequency. At $2Hz$, the transient part of the response does not stabilize before the subsequent voltage step for all the different cycles and thus the results lose reliability. This answer is not only characteristic from the 50% duty cycle. This phenomenology is repeated for each of the studied duty cycles. This is an expected behavior given the fact that the frequency at which no more steady-state response appears is at $10Hz$ for a 20% duty cycle.

At a duty cycle of 20%, the shortest voltage step is 40% the length of the voltage step at a 50% duty cycle. This means that if the piezoelectric requires a frequency lower than $2Hz$ in order to present a steady-state answer when the duty cycle is 50%, it will require a frequency lower than $0.8Hz$ in order to present steady-state response at a duty cycle of 20% on the shortest voltage step. As this condition is verified, the 20% duty cycle square waveform response presents a steady-state. The 20% duty cycle waveform is the most demanding duty cycle in this aspect, as this condition is verified for the 20% duty cycle, all the rest of the cases studied are expected to present a steady-state part of the response at each voltage step.

On the other hand, this same criteria can be applied to the waveforms a $10Hz$. In such cases, as the excitation frequency is way higher than the calculated $2Hz$ limit, the signals are not expected to present steady-state response. The limiting case on this phenomenon is again the 20% duty cycle because it presents one of the voltage steps that is 60% longer than in the waveform of 50% duty cycle. This extended voltage step is, though, not long enough for the signal to reach a steady-state response. On the rest of the studied waveforms with different duty cycles, the response does not present any discrepancies from the expected behavior.

Quantitatively, the amplitude of the steady-state responses for the different duty cycle waveforms has been compared in order to determine the influence of the duty cycle in the piezoelectric patch response. This analysis compared, for the $0.5Hz$ frequency, the amplitude at 20%, 40%, 50% and 70% duty cycle. The conclusion that can be drawn is that no perceivable change in amplitude is observed as the duty cycle is modified as long as the signal presents a steady-state part of the response. At higher frequencies, where all the recorded response is transient, the differences in amplitude of deformation due to duty cycle are smaller than the confidence interval of the amplitude for each of the frequencies. This concludes that the difference of deformation amplitude that the piezoelectric presents in two consecutive periods of the same signal is higher than the difference between the averaged values of deformation for different duty cycles.

At higher frequencies than $10Hz$ only the 50% duty cycle square waveform has been studied because the amplitude of the deformation has been found to be independent of the duty cycle. It has been possible to characterize the thickness resonance frequency of the piezoelectric patch with a precision of $\pm 10Hz$. The resonance frequency has been determined through two separate methods:

The amplitude of the piezoelectric patch thickness deformation has been analyzed at different frequencies (shown in Fig. 4.21) and a maximum has been found in the graphic at a frequency around $80Hz$.

Once with the natural frequency detected, diverse frequency sweeps have been done. In each of the sweeps, the frequency has been changed at a constant rate, this allowed for an approximate correlation between the experiment time and the frequency at which the piezoelectric patch was being excited. The error in synchronization appeared due to the fact that the arbitrary waveform generator and the data acquisition software from the interferometer do not share a common time reference. The synchronization between both systems was performed manually. The delay in synchronization of both systems translates in the frequency uncertainty intrinsic of this method for determining the resonance frequency.

This second method is faster to determine the resonance frequency but presents a challenge that can introduce further uncertainty to the determined frequency. If the material is not linear, a high frequency sweep rate might derive in jump phenomena thus creating a displaced amplitude peak with a frequency offset. Moreover, this peak appears at different frequencies depending on the direction of frequency sweeping (increasing or decreasing frequency). [117]

Through these methods, the resonance frequency has been determined at $90Hz \pm 10Hz$ where this high uncertainty appears due to the lack of time synchronicity between excitation and sensing equipment. As the scope of the testing is not the determination of the resonance characteristics, no further testing has been done to isolate the resonance phenomenon with greater accuracy. Despite this, the approximate value of the piezoelectric resonance frequency is very important in the evaluation of the phenomenology that the piezoelectric patch presents.

The dynamic study continued with the analysis of the piezoelectric thickness deformation response to the sine excitation. The sine waveform presents milder voltage changes than the square waveform which allows the piezoelectric patch to follow the excitation waveform accurately up to higher frequencies. Due to this difference in the behavior of the piezoelectric, the amplitude of the resulting deformation is different from the square waveform tests. The magnitude of the compared deformation amplitudes is presented in Table 4.3. The amplitude of the piezoelectric thickness deformation subject to sine excitation is remarkably higher than for the 50% duty cycle square excitation (with a factor of around 3).

Table 4.3: Comparison between the steady-state amplitude and the sine amplitude of the piezoelectric patch deformation.

Frequency	**Amplitude [nm]**	
	Square	**Sine**
$10Hz$	-	1057
$50Hz$	279	753
$100Hz$	472	1463
$1000Hz$	-	30

At low frequencies (until around $50Hz$) the piezoelectric has accurately followed the excitation waveform (see Fig. 4.11). In this domain, the response of the piezoelectric presents small distortions close to the maximum amplitude points; this is consistent with a slight delay of the response in comparison with the excitation. At frequencies around the resonance frequency estimated during the testing with square waveform, the sine response presents periodical oscillations at the minimum of the response, representing a transient response due to the distribution of the piezoelectric layer thickness of the patch. Passed the resonance frequency, as frequency increases, this phenomenon fades as does the amplitude of the deformation and the signal becomes close to triangular. This happens due to inertial effects because the piezoelectric patch can no longer follow the excitation waveform and the voltage changes before the steady-state deformation amplitude can be reached. The higher the frequency, the more this phenomenon predominates and the resulting amplitude reduces.

The triangle waveform excitation led to interesting results that allowed for the study of the behavior of the piezoelectric patch in terms of deformation when subject to sudden voltage changes with slopes different than 0. In such case, no steady-state response appears and the phenomena around the maximums and minimums of the deformation signal become very relevant. As the amplitude of the exciting voltage is kept constant, the frequency of the input excitation controls the slope of the voltage changes, which is the same for the up-slope than for the down-slope for the waveform is symmetric. At low frequency (see Fig. 4.17) the piezoelectric follows the triangle signal accurately up to $10Hz$, from that point onward significant distortions appear on the response at the peaks of the signal. It is possible to observe a deviation in the deformation signal which is a combination of two factors: the inertial forces affecting the piezoelectric and the electrical behavior of the piezoelectric material as a capacitor. The magnitude of these deviations can be analyzed qualitatively but not quantitatively due to the impossibility to correlate the time scales of the interferometer and the arbitrary waveform generator given the available laboratory equipment.

Due to inertial effects, the deformation response in the piezoelectric presents a time lag in comparison to the excitation signal. This lag is more acute at higher frequencies because the piezoelectric materials cannot accelerate immediately to follow the change in voltage. The distortion effect due to the capacitor behavior of the piezoelectric is detailed in the paragraphs concerning the ramp excitation because the information provided by such a waveform is more relevant to study such phenomenon.

At frequencies higher than $10Hz$ and close to the resonance frequency, a transient coupling response appears analogue to the one studied in the sine waveform, on the lower peaks of the response (Fig. 4.18 illustrates this phenomenon for a frequency of $100Hz$).

In order to extend the understanding of the distortions that appear around the peaks of the triangle waveform, a ramp waveform has been used to excite the piezoelectric patch. This type of wave allows to analyze the effects of different slope changes in the piezoelectric response. The ramp waveform is particularly interesting at low frequencies (see Fig. 4.19) to study the distortions around the peaks of the deformation signal without any interference from the phenomena that appears close to the resonance frequency of the piezoelectric patch. At this low frequency it is possible to see that the lag that appears in the deformation response is higher when the slope change is milder; the abrupt voltage changes, the lagging of the signal is not that relevant in the signal. This behavior can be explained with the capacitor behavior that the piezoelectric materials present. In a capacitor, the rate of discharge is directly proportional to the negative voltage difference between the electrodes. In this case, this behavior explains why faster change in voltage results in a faster reaction of the piezoelectric patch. The ramp waveform has not been studied at higher frequencies because the focus of the interest for this waveform was precisely for low frequencies.

4.3 Tensometric experiments

The next step in the characterization of the piezoelectric patch when the thickness behavior is defined is the characterization of the in-plane behavior. This is the most important part of the characterization of the material as the intended application for the piezoelectric patch is not in the polarization direction but in the transverse direction.

The characterization transverse to the polarization direction is more complex than the interferometric tests performed as the change in dimension cannot directly be measured with the available equipment. The solution applied in order to evaluate the deformation of the patch has been to bond a strain gauge rosette on the top surface of the piezoelectric patch so any deformation occurring in the piezoelectric material can be measured by the gauge.

This methodology is detailed throughout this section and the results presented are used later on in the thesis to calibrate the numerical model of the piezoelectric patch in Sec. 5.3.

4.3.1 Instrumentation and experimental setting

This section details the different instruments and sensors that have been used during the experiments performed in the UPC in Terrassa.

The instrumentation for the different configurations has been done according to the necessities for each of the experiments to be performed. As the experiments have been designed only in static mode, none of the sensors and instruments used is expected to work in dynamic readings even though most of them do. The strain gauges, the laser and the data acquisition system are instruments that can work in dynamic regime if configured before the test but the multimeter used to measure voltage does not allow this type of experiments.

The instrumentation that has been used is presented in Table 4.4.

Table 4.4: Instruments used during the experiments.

	Manufacturer	**Model**	**Serial number**
Piezoelectric patch	PI Ceramic	P-876.A12	40/69
Strain gage rosette	HBM	350Ω rosette	
Laser meter	Riftek	RF603.2-125/500	829
Low voltage source	HQ Power	PS-920	
High voltage source	Advance electronics Ltd	PP13	304
Digital multimeter	Vitecom Electronic	75-MAS830L	1022477
Data acquisition system	HBM	Spider 8-30 600Hz	F04405
USB adaptor	HBM	USB-ADAPT	2561
Computer	HP Compaq	6910p HSTNN-C31C	

4.3.1.1 Arrangement of the experiment

Once the different equipment required for the experiment have been presented it is relevant to detail the general arrangement and connections performed between the different systems. The arrangement of the experiments is relevant in further modifications of the procedure and in the analysis of the results. Shall any perturbations in the results be detected, one of the most important aspects to consider is the adequacy of the experimental setting and any influence it may have on the results.

Tests 1 and 2 are designed to study the behavior of the piezoelectric patch when it actuates as a separate component. The tests performed in this experiment are done intending to compare them with the numerical simulations performed in the second report of the thesis in which the analysis of the piezoelectric material alone was simulated. This comparison should provide an insight in the distortion that the patch cover introduces on the behavior of the piezoelectric material. The configuration of the piezoelectric patch in comparison to the modelling done in the second report is presented in Fig. 4.23.

The numbering of the tests is the following: the first number indicates the configuration file for the Spider 8 DAQ system while the second number is the test number, running consecutively for configurations 1 and 2.

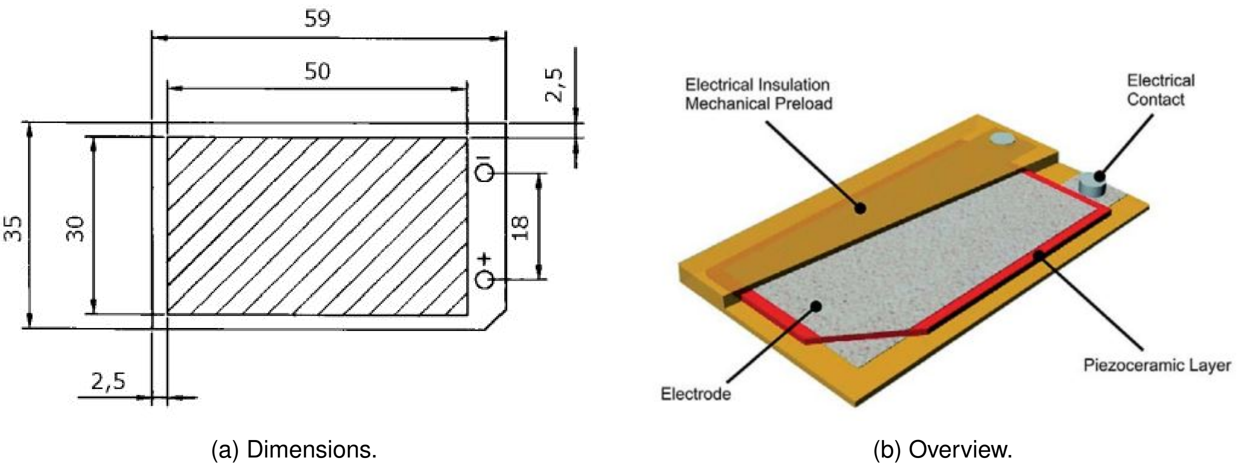

(a) Dimensions. (b) Overview.

Figure 4.23: Overview on the piezoelectric actuator used in the experiments as presented in the manufacturer's brochure.

With this target in mind, two configurations have been envisioned, a first configuration considers the piezoelectric patch fixed on the table on the side where the electrode cables are installed (tests 1-25 to 1-49). A second configuration also fixes with tape the opposite end of the piezoelectric (tests 2-05 to 1-14). Illustrations for the configuration of the piezoelectric actuator tapped at both ends is shown in Fig. 4.24.

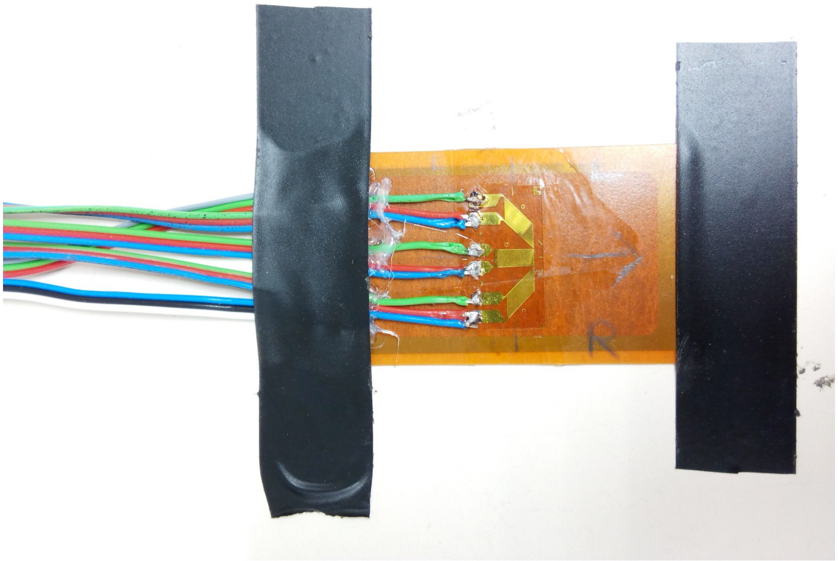

Figure 4.24: Experimental setting for tests 1 & 2 showing the configuration with the piezoelectric actuator tapped at both ends.

In this tests the piezoelectric had a strain gauge rosette installed on the upper surface. This rosette provides information on the strain in the longitudinal (X) direction of the piezoelectric and also in the two directions at $45deg$ of the X axis. The position of the strain gauge rosette on the piezoelectric patch can be seen in Fig. 4.24. In order to register data and perform the experiments, the following equipment has been required: piezoelectric patch, strain gauge rosette, low and high voltage sources (not simultaneously), multimeter, Spider 8 and computer. The architecture of this test is presented in Fig. 4.25.

The high voltage source powers the piezoelectric patch while the multimeter measures the actuation volt-

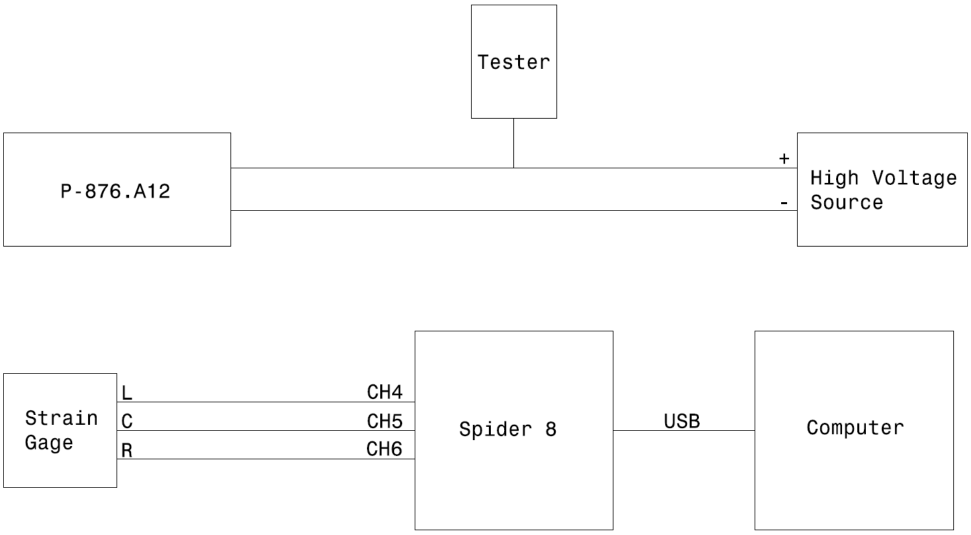

Figure 4.25: Architecture of the test in setup 1 and setup 2.

age. As the current in the piezoelectric is very low, the voltage drop in the cables is also very low and there is no effect on where the voltage is read along the cables. In a separate circuit, the strain gauge rosette is connected to channels 4 to 6 in the Spider 8 to read the deformations in the patch. Fig. 4.26 presents a general view on the test.

Test 2 presents exactly the same configuration as test 1 with a small difference on the channels to which the strain gauge rosette is connected to. This change in configuration is explained by some reading errors detected in the first tests (detailed in Sec. 4.3.2). Further tests abandon the procedure used in test 2 because no improvement was detected and and the methodology for connection was radically changed.

4.3.1.2 Cabling

The cabling details in the different experiments are significant in terms of how the data acquisition system has been set-up. A cable has been tailored for each of the different sensors used in the experimental phase either because the required cables did not exist or because errors have been experienced in the measurement with the existing cables. Integrity checks have been performed to determine whether the results are consistent. The unreliability of the initial integrity checks led to the conclusion that cables with more reliable connections were required.

The strain gauge cables connect individually each of the strain gauges that conform both rosettes with each of the six channels from the Spider 8 data acquisition system.

The connection with the Spider 8 has been done through a standard 15-pin connector (in two rows). The configuration of the pins has been done as indicated in the HBM manual. This configuration is depicted in Fig. 4.27. The configuration used in the data acquisition system has been the $1/4$ bridge configuration with three cables. For a 350Ω gauge, the connections to be done are in pins 5, 8 and 10; apart from a bridge between pins 6 and 13.

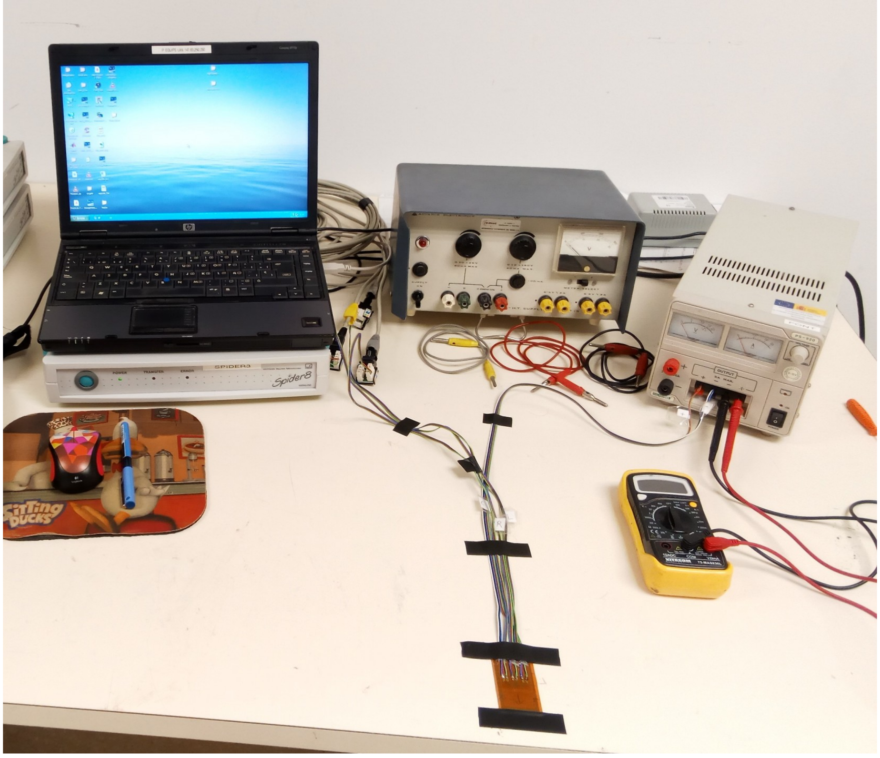

Figure 4.26: General arrangement for tests 1 and 2. Note that the image shows the setting with the low voltage source and the piezoelectric patch taped on both sides.

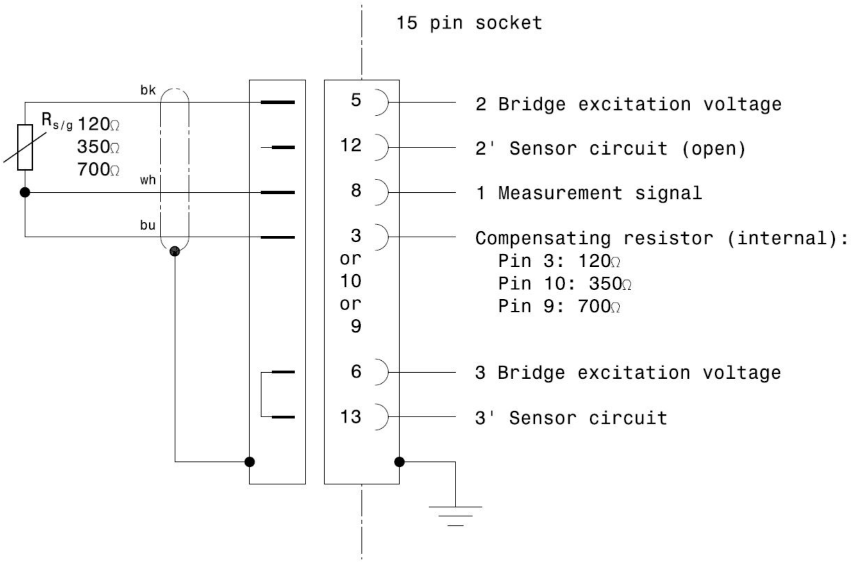

Figure 4.27: Configuration of the connections for the strain gauge channels in quarter bridge configuration with 3 cables per gauge.

4.3.1.3 Settings and configuration

With all the systems and cabling already detailed, the following step is the setting of the software part of the experiment. The DAQ system is the part of the measuring equipment which integrates all the software and digital processing of the measured data and, thus, is the only one that requires configuration through the specific software.

The Spider 8 is configured through the Catman AP program available at the UPC in Terrassa. The program configures the type of sensors to be connected, the type of bridge (in case of the strain gauges), the sensor adaptation (in case of other sensor types), the signal filter to be used and the data acquisition frequency among other parameters. The sampling frequency needs to be at least 2 times the bandwidth according to the Nyquist criteria so it does not present aliasing (usually if the DAQ system allows for it the sampling frequency is chosen at least 10 times the bandwidth). As the system used allows for high sampling frequencies and the phenomenon to study is static, a sampling frequency of $50Hz$ has been considered for all the tests. This means that any phenomenon detected at a frequency of more than $5Hz$ is not reliable and could be a sub-product of aliasing.

The filter for the different channels is left in automatic mode by the Catman. This mode allows for a program-chosen filter according to the signal to be analyzed and presents a good performance in static analyses.

Channels 0 to 6 (except from channel 3) have been set-up for strain gauges of 350Ω in a 3-wire quarter bridge configuration. A quarter bridge configuration has been chosen in order to be able to read independently all the strain gauges. A half bridge setting could have been used in the experiments with upper and lower strain gauge rosettes but would not have been correct due to the fact that the test specimen is not symmetrical (the piezoelectric patch is mounted only on one side). This aspect is later on corroborated in the results for the cantilever beam shown in Sec. 7.3 where the readings from both strain gauge rosettes are far from symmetrical.

4.3.1.4 Operating limits

It is relevant to set the maximum normal operation conditions for each of the aforementioned pieces of equipment. This limits are given by the different manufacturers. Hence, exceeding any of these magnitudes may inadvertently lead to failure of the component. These limits are presented in Table 4.5 below.

Table 4.5: Limiting values for the different equipment used in the experimental part of the research.

Equipment	Model	Limits
Piezoelectric patch	P-876.A12	-100/+400V
Strain gage rosette	HBM 350Ω	
Laser meter	Riftek	10-15V (power input)
Low voltage source	PS-920	0-15V
High voltage source	PP13	0-300V
Digital multimeter	75-MAS830L	0-400V
DAQ System	Spider 8-30	0-10V (input signal)

During the experiments, the limits stated have been further restricted in some of the equipment to account for any unforeseen problems during the experiments. This limits applied basically to the piezoelectric patch, where the actuation voltages admissible have been reduced to $-60/+200V$. During the final part of the testing, though, the piezoelectric patch has been excited up to $+250V$ with data not being saved during that test. As research advances and the piezoelectric patches are further controlled, the extended limits will be extended until the manufacturer's ones.

4.3.2 Experimental procedure

As the setting of the different experiments has been introduced already, this part presents the methodology followed during the different tests performed. This methodology can be synthesized in a generic test procedure that is introduced in the following sections. The inconveniences found during the testing phase are also presented in this section in chronological order together with images taken during the different tests.

4.3.2.1 Numbering of the tests performed

The tests performed have been numbered sequentially with a first index indicating the setting of the experiment. The generic numbering 1-28 indicates test 28 in the test configuration 1. Table 4.6 summarises the tests performed for tests 1 and 2.

Table 4.6: Numbering for the tests performed

Tests 1 and 2			
	Polarity	**Attached**	**Free**
Low voltage	Normal	05 - 09	(15 - 19)
	Inverse	10 - 14	(20 - 24)
High voltage	Normal	25 - 29	30 - 34 45 - 49
	Inverse	35 - 39	40 - 44

The first column in the test numbering table indicates the type of voltage source used to power the piezoelectric patch during the experiments. The low voltage source was able to produce an output of up to $15V$ while the high voltage source had a maximum voltage output of $300V$, all in continuous current. The polarity current refers on the direction of the electrical field across the piezoelectric patch, a positive or normal polarization indicates a contraction in the piezoelectric material while an inverse electric field causes the piezoelectric patch to expand. As the piezoelectric materials are ceramics, their mechanical strength in traction is almost 0. Hence, it would be expected for the material not to withstand any stress in traction. According to the piezoelectric manufacturer, the patch can resist up to $100V$ in traction because the piezoelectric material is surrounded by a resin cover that pre-stresses it.

The two following columns (attached and free) refer to the way in which the piezoelectric was fixed during the testing. During tests 1 and 2, two configurations have been experimented, a first configuration with the end of the piezoelectric patch further from the electrodes taped to the supporting surface, and another with that same end free. This comparison aims to see if the method for supporting the piezoelectric patch has a significant effect on the deformations it produces. The tapping of the piezoelectric imposes a small force in the direction on the deformation so no hypotheses are made on whether its effect on the results is significant.

4.3.2.2 Generic test procedure

The following is the generic step-by-step testing procedure used in the different experiments. This procedure is a product of the conclusions and experiences extracted from the different experiments.

- Power on: the Spider 8 is to be powered on first, followed by the computer, the laser sensor power source (for test 3 only) and the multimeter. The piezoelectric patch power source is not yet started in order to zero the voltages and the readings of the different sensors without any interference.
- Start Catman software and load the configuration file: the configuration file contains the information regarding the channel adaptations for the different sensors.
- Stabilization of the system: the whole testing system needs some stabilization time so the strain gauges can reach the equilibrium working temperature and their readings stabilize. This time can be up to 30min for the first power-up.
- Zeroing of the sensors: ensure that the readings are stabilized completely before zeroing in order to avoid reading run-out of the sensors during the experiment.
- Power-up of the piezoelectric patch power source: after power up the source takes up to 5 minutes to reach a voltage output equilibrium between $10V$ and $15V$.
- Start acquisition and testing: with the voltage source reading stabilized, the test can be started. Ensure that enough time passes for the voltage to stabilize after any change in voltage. If at any moment the strain readings stop being coherent (reading up to $8000\mu m/m$) the test must be restarted form the beginning.
- Finish of the test and remaining strains: after all the measuring points have been covered, the acquisition can be stopped and the results saved. The voltage source can be then stopped while maintaining the rest of the systems on. When the voltage source output discharges to $0V$, the readings of the strain gauges that can be read in the real-time display of the HBM Catman software are the remaining strains.

These steps constitute the generic procedure followed during the testing of the piezoelectric in all the experiments performed. Any particular situation encountered during the experiments is presented in the following section Sec. 4.3.2.3.

4.3.2.3 Development of the experiments

This section narrates chronologically the testing followed to detail the different problems found during the testing phase and to provide an insight to the adopted solutions. The previous section is constructed upon the conclusions presented throughout the development presented below.

The first test, 1-01, aimed to determine the order of magnitude of the deformations produced in the patch in order to qualitatively determine how far is the material according to the initial expectations. The voltage has been varied until $16V$ obtaining deformations up to $-6.4\mu m/m$. The current intensity has not been monitored. Until $15V$ severe fluctuations in the deformations have been recorded up to $\pm 1\mu m/m$. Moreover, significant hysteresis has been seen. It is important to note that the magnitude of the deformations measured falls well within the measuring error of the strain gauges so there is no telling if the fluctuation is a measurement error or has consistency with the physical system behavior.

The second test performed (1-02) aimed to study the origin of the fluctuations in the deformation readings detected in test 1-01. The test analyzed the fluctuation of the deformation readings throughout some time without voltage actuation of the patch. The measures showed a significant drift over time apart from the same fluctuations that in the previous test.

Test 1-03 allowed the gauges to stabilize over time for over $20min$ and then recorded different readings for the deformations until $15V$ at $2.5V$ intervals. The results of this test are presented in Table 4.7. The readings in gauges Left (L) and Center (C) show coherent values despite the fact that the remaining strains are quite high in terms of the values of deformation reached. Strain gauge (R), on the other hand, is completely off. The gauge recorded a positive drift during the whole experiment that did not allow for the recording of any significant information during the test.

Table 4.7: Deformations of Left, Center and Right strain gages mounted on the piezoelectric patch for test 1-03.

Voltage	**Left**	**Centre**	**Right**
$2.41V$	$-2.0\mu m/m$	$-1.9\mu m/m$	$2.1\mu m/m$
$5.15V$	$-3.8\mu m/m$	$-3.8\mu m/m$	$4.0\mu m/m$
$10.24V$	$-6.4\mu m/m$	$-6.7\mu m/m$	$1.6\mu m/m$
$15.02V$	$-8.7\mu m/m$	$-9.6\mu m/m$	$2.1\mu m/m$
$9.96V$	$-6.7\mu m/m$	$-7.6\mu m/m$	$6.0\mu m/m$
$4.97V$	$-4.3\mu m/m$	$-5.7\mu m/m$	$9.8\mu m/m$
$2.41V$	$-4.0\mu m/m$	$-4.8\mu m/m$	$-12.5\mu m/m$

As a conservative hypothesis, it has been assumed that the drift in R channel is a result of short period for the gauge to reach a stable reading. The system has been left for over $30min$ untouched in order to stabilize the readings once more. After a run-out of $10-15\mu m/m$, gauges L and C seem to have stabilized while R shows no signs of stabilization and read around $160\mu m/m$. A zeroing of the readings has been done and test 1-04 has been done regardless of gauge R drifting. The test followed the procedure of test 1-03, leaving a stabilization time between changes of voltage of more than $10s$ and allowing for an acquisition time of at least $30s$ to be able to provide averaged results for each of the voltages experimented; this allows also to analyze any run-out of the gauges. The results of this test are presented in Fig. 4.28. It can be seen that while gauges L and C follow the voltage, gauge R completely drifts in the opposite direction (positive sign). In less measure, gauge L also presents some drift in the measures as the readings end up well in the positive domain for strains. These drifts are not physically backed; any hysteresis would show a remaining effect in the opposite direction.

Test 2-05 followed and aimed to correct the drift of gauge R. Several hypotheses on where the problem

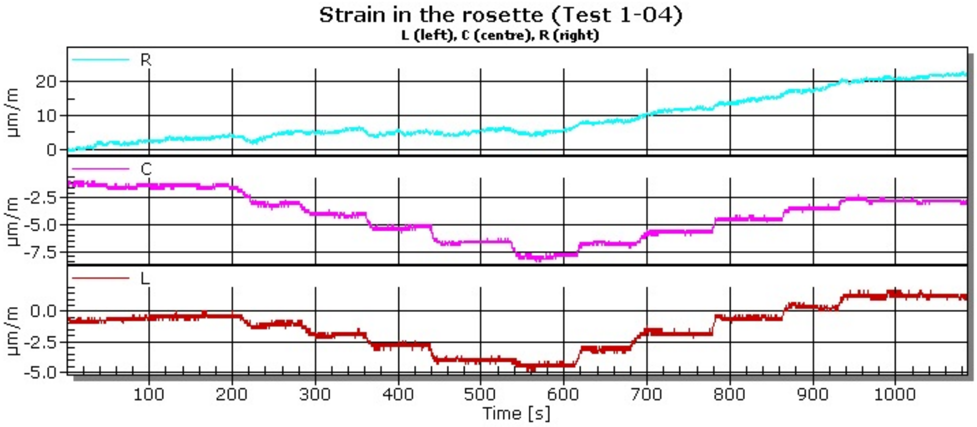

Figure 4.28: Deformation readings in the time domain for test 1-04.

could be located have been made, mostly regarding the cabling performed. For each of the cables the problems could be found in the connection with the Spider 8 or the Spider 8 channel itself, the intermediate connectors linking the channels and the strain gauge cables, and the welding of the strain gauge rosette. The first troubleshooting has been to change gauge R to CH6 in the Spider 8 due to the simplicity of this test. Channel 6 worked correctly given that gauge L had been connected there for the previous tests. An initial recording on deformations shows consistent reading for all the gages without any significant run-out of the readings after some setting time. Before the test could begin, gauge R started drifting again, being such deviation too significant not to be considered in the test (one order of magnitude higher than the previous tests). The following item that has been checked have been the intermediate connectors (see Fig. 4.29). A slight movement of the connector resulted in deviations of more than $1000\mu m/m$ in the readings. To correct this, 3 new cables have been done from 0 in order to bypass the intermediate connectors and link directly the gauges to the Spider 8 connectors. After the cables have been done, the Spider 8 did not recognize the sensors. The following has been checked according to the manual [118]:

- Check pins 5,8 and 10 of the connector
- Check continuity of cables
- Check that strain gauges have not been damaged
- Recheck all connections according to Spider 8 manual

A bridge between pins 6 and 13 of the Spider 8 15-pin connector had not been made causing the DAQ system not to recognize the sensor. After correcting the issue the sensors worked normally. After $30min$ of stabilization time of the system the readings of the gauges were: $-1.9\mu m/m$, $-3.4\mu m/m$ and $-3.8\mu m/m$ respectively for gauges L, C and R. Test 2-05 has then been performed in this configuration and new cabling.

The following tests 1-06 to 1-09 are a repetition of test 2-05 in which the only change has been that the cabling has been redone as in test 1-01. The repetitions of the tests are done in order to provide averaged results for each configuration. The remaining strains after the end of each of these tests is presented in Table 4.8.

The following tests performed, tests 1-10 to 1-14, invert the polarity of the actuating electric field on the piezoelectric field in order to determine the behavior of the patch with the opposite polarization of the

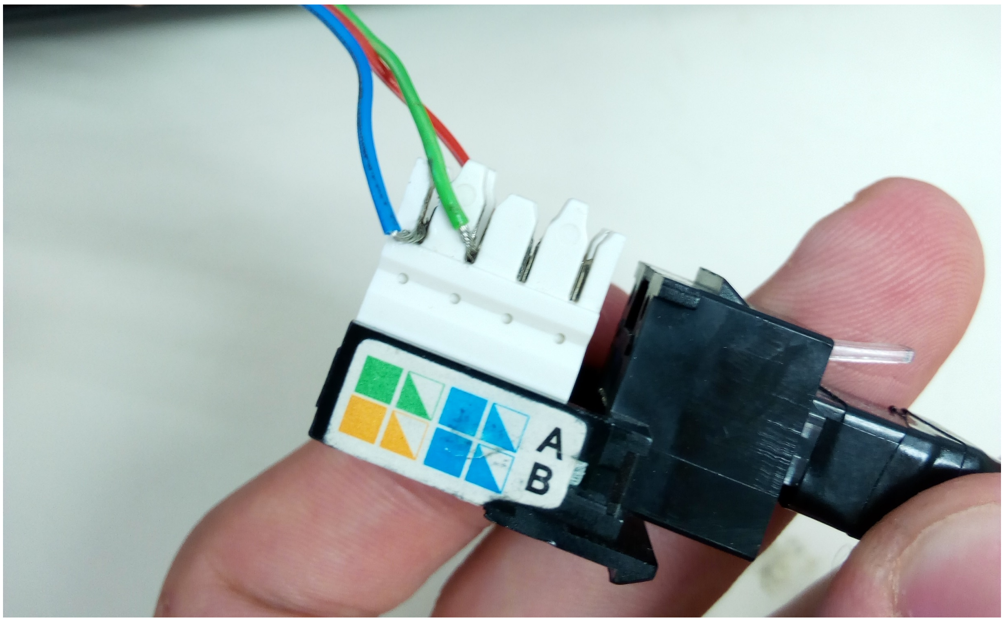

Figure 4.29: Intermediate connectors used between the Spider 8 cables and the strain gage cables in tests 1-01 to 1-04.

Table 4.8: Remaining strains for the tests 1-06 to 1-09.

	1-06	**1-07**	**1-08**	**1-09**
L	$-0.5\mu m/m$	$-1.7\mu m/m$	$-7.0\mu m/m$	$-5.8\mu m/m$
C	$-1.2\mu m/m$	$0.5\mu m/m$	$-3.4\mu m/m$	$-3.1\mu m/m$
R	$-1.2\mu m/m$	$-1.2\mu m/m$	$-4.1\mu m/m$	$-3.8\mu m/m$

piezoelectric material. The remaining strains at the end of each of the tests is presented in Table 4.9 for each of the strain gauges.

Table 4.9: Remaining strains for the tests 1-06 to 1-09.

	1-10	**1-11**	**1-12**	**1-13**	**1-14**
L	$2.9\mu m/m$	$2.4\mu m/m$	$2.2\mu m/m$	$3.6\mu m/m$	$2.4\mu m/m$
C	$-0.2\mu m/m$	$0.0\mu m/m$	$1.2\mu m/m$	$1.7\mu m/m$	$1.2\mu m/m$
R	$1.9\mu m/m$	$1.9\mu m/m$	$1.4\mu m/m$	$1.7\mu m/m$	$1.2\mu m/m$

After considering the results for these tests, the remaining strains are consistent, in sign, with the effects of hysteresis of the material. After test 1-14, the high voltage source has been connected to the piezoelectric for the second part of the tests with the piezoelectric patch. The first part of the high voltage tests has been with the positive electrical field (compression of the piezoelectric patch) up to a voltage of $200V$. The remaining strains for the patch are presented in Table 4.10. Note that the numbering of these tests is not consecutive to the previous ones following the scheme of Table 4.6.

The following Table 4.12 and Table 4.11 show the remaining strains for the configurations in which the polarization has been reversed in comparison to test 1-25 and in which the piezoelectric patch is free on the far end respectively.

Table 4.10: Remaining strains for the tests 1-25 to 1-29.

	1-25	**1-26**	**1-27**	**1-28**	**1-29**
L	$20.6\mu m/m$	$5.3\mu m/m$	$-1.9\mu m/m$	$-0.5\mu m/m$	$-0.2\mu m/m$
C	$24.5\mu m/m$	$3.8\mu m/m$	$1.7\mu m/m$	$3.1\mu m/m$	$-1.2\mu m/m$
R	$12.0\mu m/m$	$2.6\mu m/m$	$-6.0\mu m/m$	$-1.4\mu m/m$	$-0.5\mu m/m$

Table 4.11: Remaining strains for the tests 1-30 to 1-34.

	1-30	**1-31**	**1-32**	**1-33**	**1-34**
L	$-9.8\mu m/m$	$2.9\mu m/m$	$4.1\mu m/m$	$-3.4\mu m/m$	$-5.5\mu m/m$
C	$-4.3\mu m/m$	$3.6\mu m/m$	$4.1\mu m/m$	$0.7\mu m/m$	$-4.1\mu m/m$
R	$-12.7\mu m/m$	$1.0\mu m/m$	$1.7\mu m/m$	$0.5\mu m/m$	$-3.8\mu m/m$

Up to this point the experiments have been done with the multimeter existing battery that triggered the battery alert on the display. Once the battery has been changed, a close correlation between the source voltage indicator and the multimeter voltage reading has been detected. This correlation was non-existent before, leading to differences in the voltage reading of up to 40%. This information compromises the integrity of any test performed up to this point given the fact that the voltage readings can no longer be trusted to be correct.

With the new battery on the multimeter and good correlation between both voltage readings of the multimeter and the source, Table 4.13 shows the remaining strains for tests 1-40 to 1-44.

After the realization that the tests from before the multimeter battery change are not reliable the tests with the free far end of the piezoelectric, high voltage and normal polarity have been repeated and named 1-45 to 1-49. The remaining strains for these tests is presented in Table 4.14. Of the high voltage tests performed, the ones that are reliable in terms of measurement integrity are tests 1-45 to 1-49 in direct polarization and 1-40 to 1-44 in inverse polarization.

4.3.3 Experimental results and analysis

The results of the piezoelectric patch are presented in this section. Only the results of tests 1-40 to 1-49 are presented and discussed in this analysis because the rest of the testing presents problems in terms of reliability of the measures caused by the problems during the data acquisition presented in Sec. 4.3.2.3. The results presented are separated in two different parts, the tests in direct polarization and the tests in inverse polarization as shown in Table 4.6 and the electrical power supply has been the high power supply for all the tests.

The study of the strain gauge measurements has been performed at two different levels, a first level consisted in the analysis of the strain gauge readings for each test separately to determine the coherence of the results obtained and validate the experiments in question. The second level of analysis consisted in the comparison of the results obtained in each of the tests for a specific sensor. This analysis has the scope of determining the evolution of the results obtained by each of the sensors and isolating possible phenomenology related to non-linearity in the testing.

Table 4.12: Remaining strains for the tests 1-35 to 1-39.

	1-35	**1-36**	**1-37**	**1-38**	**1-39**
L	$10.8\mu m/m$	$1.9\mu m/m$	$-0.2\mu m/m$	$-0.2\mu m/m$	$0.7\mu m/m$
C	$7.4\mu m/m$	$1.7\mu m/m$	$-0.2\mu m/m$	$0.0\mu m/m$	$1.0\mu m/m$
R	$13.9\mu m/m$	$3.4\mu m/m$	$0.7\mu m/m$	$0.7\mu m/m$	$1.0\mu m/m$

Table 4.13: Remaining strains for the tests 1-40 to 1-44.

	1-40	**1-41**	**1-42**	**1-43**	**1-44**
L	$37.2\mu m/m$	$3.6\mu m/m$	$1.2\mu m/m$	$1.2\mu m/m$	$0.2\mu m/m$
C	$35.5\mu m/m$	$3.1\mu m/m$	$1.7\mu m/m$	$1.0\mu m/m$	$0.5\mu m/m$
R	$39.6\mu m/m$	$4.1\mu m/m$	$1.9\mu m/m$	$1.0\mu m/m$	$0.0\mu m/m$

Table 4.14: Remaining strains for the tests 1-45 to 1-49.

	1-45	**1-46**	**1-47**	**1-48**	**1-49**
L	$-3.1\mu m/m$	$-11.3\mu m/m$	$-10.3\mu m/m$	$-2.2\mu m/m$	$1.0\mu m/m$
C	$2.6\mu m/m$	$-9.1\mu m/m$	$-10.6\mu m/m$	$-2.2\mu m/m$	$1.4\mu m/m$
R	$-11.0\mu m/m$	$-13.4\mu m/m$	$-10.8\mu m/m$	$-4.6\mu m/m$	$-0.2\mu m/m$

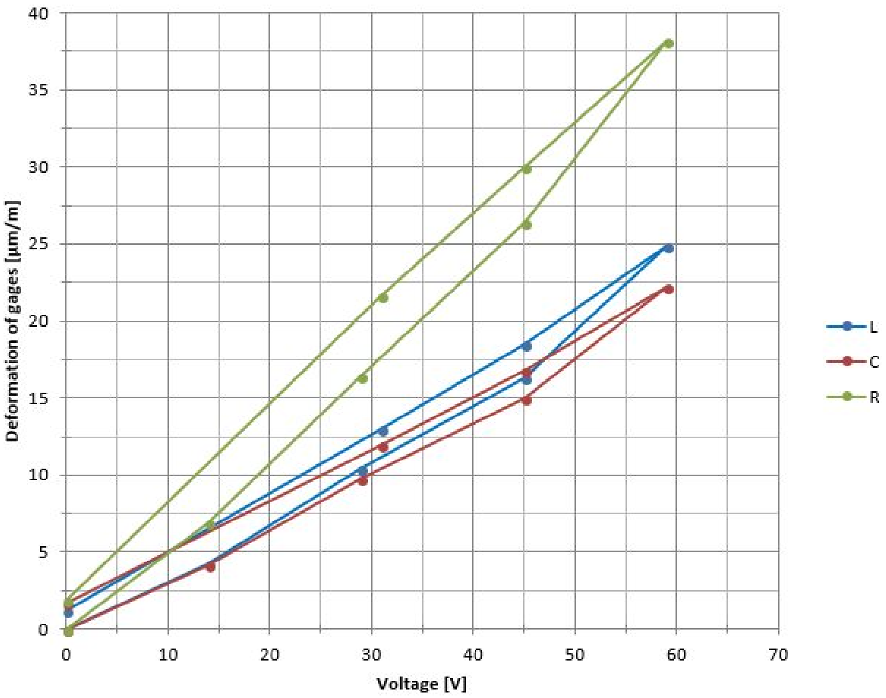

Figure 4.30: Strain results obtained in test 1-42.

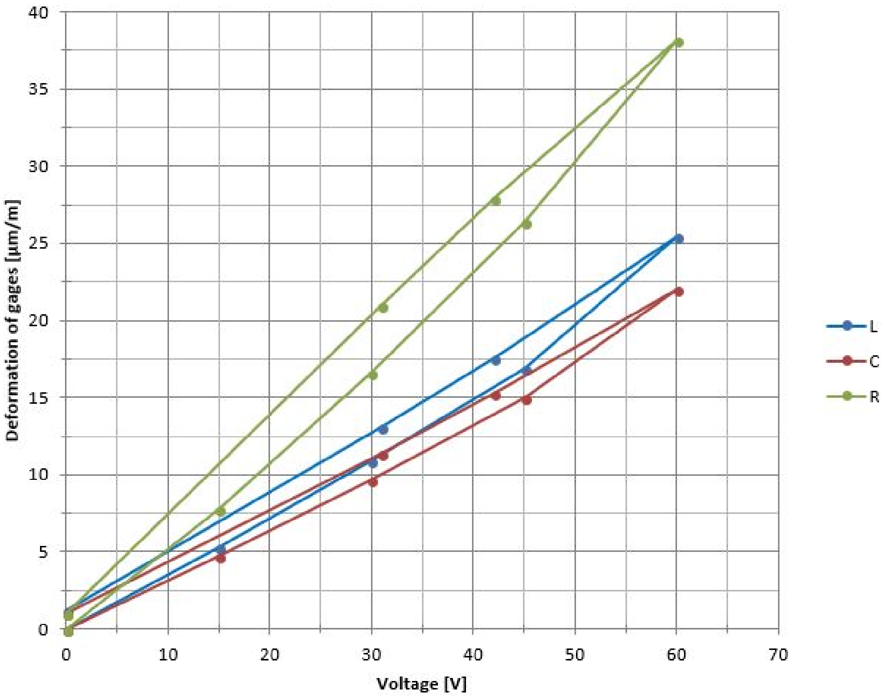

Figure 4.31: Strain results obtained in test 1-43.

The results for test 1-42 are shown in Fig. 4.30. The analysis of the results disregarded the results of the first two tests of the series because the magnitude of the obtained deformations is substantially higher than the results obtained in the subsequent tests. This could happen because the transitory response is happening in the first cycle of actuation of a system with hysteresis. The effect in such case stabilizes after the first cycle. As the system studied is not an ideal cycle, an extra loading cycle has been considered before the results are considered. This hypothesis is justified by the evolution of the strain gauge readings from test to test as shown in Fig. 4.36a and presented below.

The results in test 1-42 show a significant difference in the readings of the three strain gauges being gauge R (right) the gauge presenting the highest readings. The difference in the readings between gauges L (left) and C (center) is significantly smaller. Due to the piezoelectric properties of the material being homogeneous in the plane of interest the expected result would be for the readings of the three strain gauges to be equal (or at least close). In this case, though, the readings present a difference of about 39%. In the first test of the series (test 1-40, not presented in the figures) this difference is also present. Throughout the tests, the readings of strain gauge R have been higher than the rest of the sensors monitored.

The results of tests 1-43 (Fig. 4.31) and 1-44 (Fig. 4.32)show similar phenomenology than the results obtained in test 1-42. This allows for the verification of the fact that the results of test 1-40 are a product of a transitory response that stabilizes in subsequent testing. Moreover, it is possible to see that the magnitude of the hysteresis cycle amplitude for the presented experiments is very stable from test to test. In this aspect, the results of the first test in the series are completely different in all three gauges, where the amplitude of the hysteresis cycles for the three sensors is about 5 times larger.

The analysis has continued through the determination of the deformations transformation into the axis of the piezoelectric actuator from the system in the strain gauge rosette. This transformation expresses the

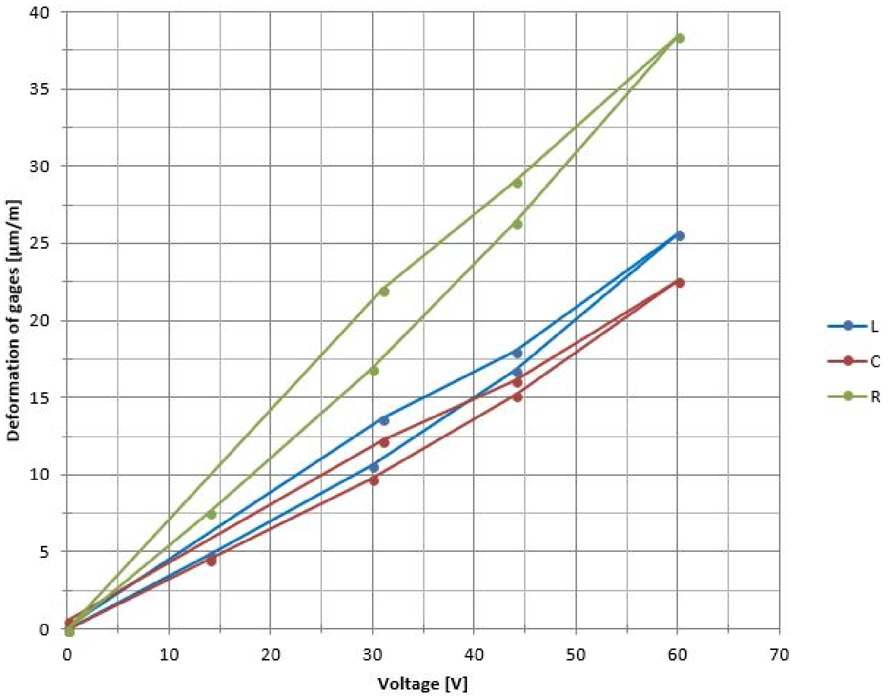

Figure 4.32: Strain results obtained in test 1-44.

deformations in the direction X along the longitudinal direction of the piezoelectric actuator and the direction Y transverse to such direction and in the plane of the strain gauge rosette. The Z axis is not relevant in this analysis because the strains caused by the piezoelectric actuator are studied only in plane in this report (the deformations in the Z direction are considered in Sec. 4.2). The results presented in the second part of the analysis show already the values of the deformation expressed in the axes X/Y.

The analysis of the test results in direct polarization 1-45 to 1-49 followed the same procedure as for the tests in inverse polarization. In this case and due to the reasons presented in Sec. 4.3.1.4 the maximum actuation voltage has been $200V$. This allows from the start for better quality results in terms of resolution of the sensors.

As the magnitude of the actuating voltages is significantly higher than in the inverse polarization tests, the resulting deformation in the actuator is also significantly higher and thus the amplitude of the hysteresis loops. A relevant effect worth noticing is the fact that after the tests, the remaining strain for all the gauges is very close to zero. This ensures the coherence of the readings because no run-out occurs but also is a certainty that the operation of the piezoelectric actuator is nominal and no plastic effects intervene during the testing.

As seen in Fig. 4.33, Fig. 4.34 and Fig. 4.35, the magnitudes for the maximum deformation are almost identical; this is a sign of the stability of the measurements through time. In this set of experiments the first test of the series did not present the difference in terms of magnitude of the readings or in the magnitude of the hysteresis cycle. Despite this fact, to perform that analysis of the results as close as possible to the one performed in the case with inverse polarization, the first two tests (1-45 and 1-46) are not considered in the analysis.

An aspect interesting to notice and relevant for all the tests in the series is the fact that the amplitude of

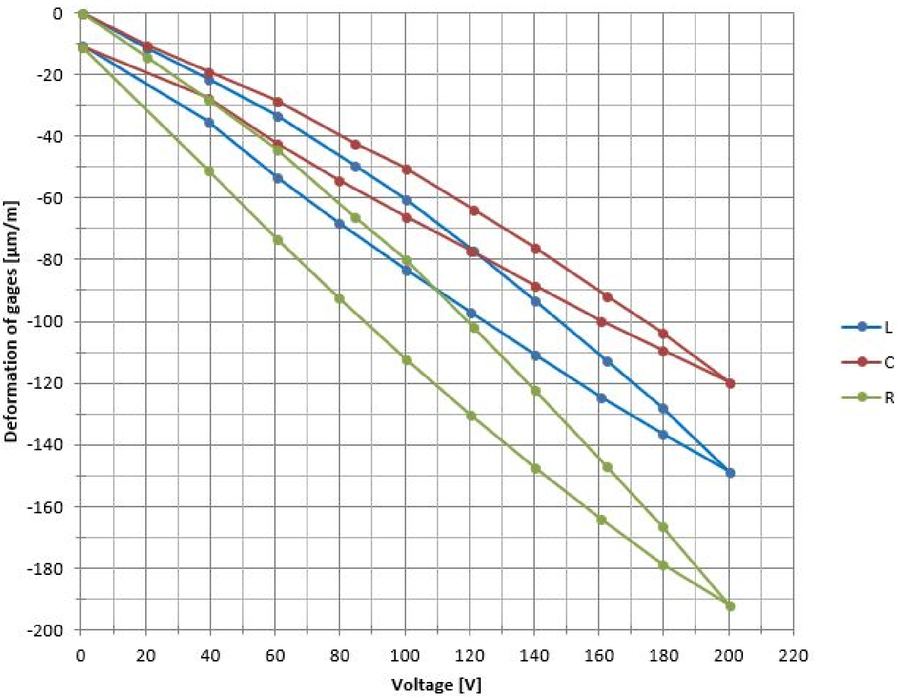

Figure 4.33: Strain results obtained in test 1-47.

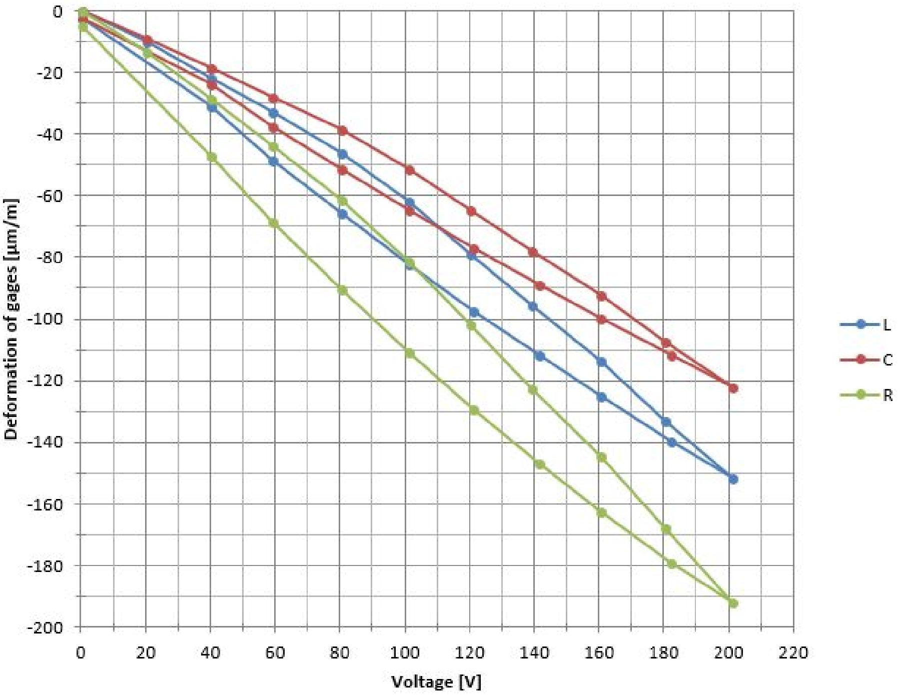

Figure 4.34: Strain results obtained in test 1-48.

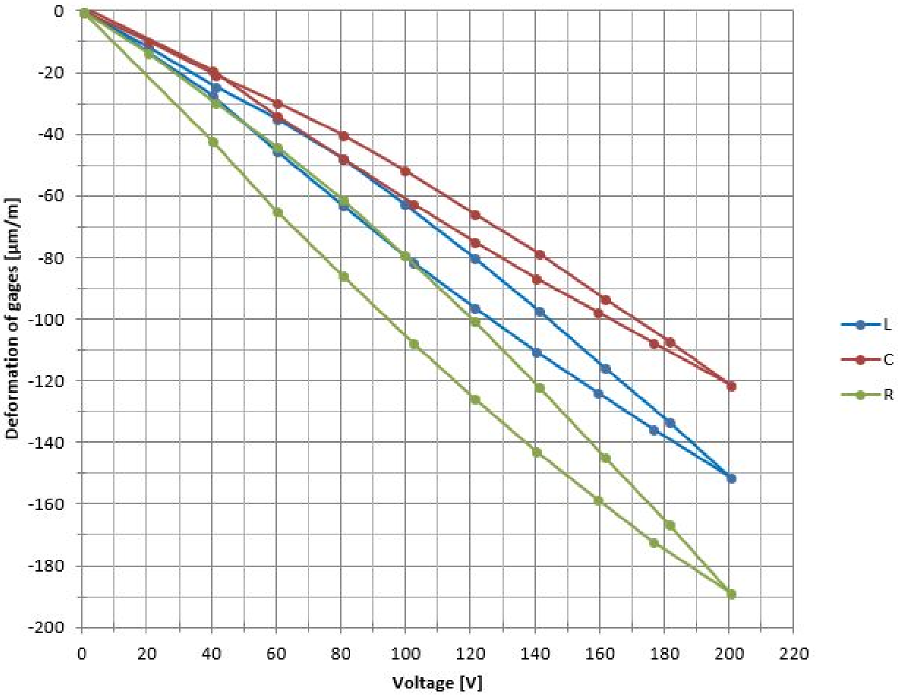

Figure 4.35: Strain results obtained in test 1-49.

the hysteresis cycle is not constant for each of the strain gauges; instead, the cycle increases in amplitude as the magnitude of the maximum deformation for a gauge increases. This behavior is expected from any system that presents hysteresis as for the limit case in which the maximum amplitude is 0, the hysteresis cycle amplitude would also be 0.

The second part of the analysis is the study of the results for all the tests performed separating by component of strain. The calculation of the components of strain in the X/Y axis system (piezoelectric actuator system) has been performed for each of the tests in the series and the results plot. Fig. 4.36 shows the strain in directions X and Y for the case with inverse polarization actuation (up to $60V$), Fig. 4.37 the equivalent results for the tests with direct polarization actuation and Fig. 4.38 the XY shear strains for both the direct and inverse polarization tests. The results have been structured in this manner because the shear strains are expected to be 0 given the fact that the piezoelectric actuator presents in-plane circular symmetry in the actuation.

In the analysis of the results for the inverse polarization tests shown in Fig. 4.36 it is possible to see the difference in the measurements of the first test of the series in relation to the subsequent tests. This difference can be attributed to the fact that the piezoelectric materials present a very significant hysteresis cycle and, as such, their behavior in the first loading cycle is different from any loading cycles to follow. The effect is visible in both the values of the strain in the X and Y direction. Is is remarkable that the strain in both directions is not equal in magnitude hence no circular symmetry can be assumed in the behavior of the actuator. Despite this there is a clear correlation between the results obtained for directions x and Y and in the involved phenomenology. This difference in the results is produced from the fact that the actuator is rectangular and not circular. The geometry of the actuator affects the response of the actuator in terms of deformation despite the in-plane circular symmetry of the material properties.

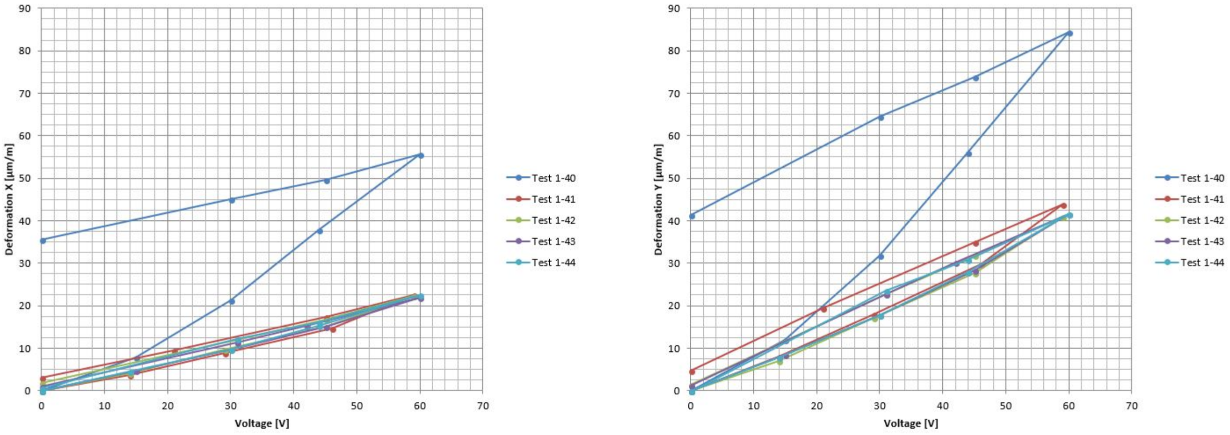

(a) X direction strain.

(b) Y direction strain.

Figure 4.36: Strain in the piezoelectric coordinates for tests in inverse polarization 1-40 to 1-44.

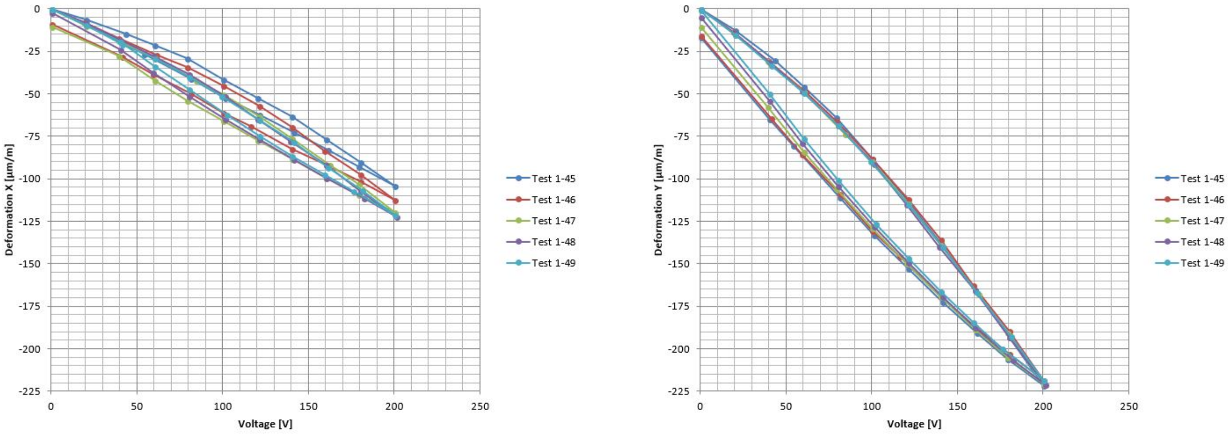

(a) X direction strain.

(b) Y direction strain.

Figure 4.37: Strain in the piezoelectric coordinates for tests in direct polarization 1-45 to 1-49.

The analysis of the results in the direct polarization tests is similar to the phenomenology described for the inverse polarization: the magnitude of the strain in the transverse direction is significantly higher than in the X direction (about 2 times), the magnitude of the hysteresis cycle is proportional to the maximum deformation registered. In this case, though, the first test of the series does not present the biased deformation as in the inverse polarization. The explanation for this fact is that before the tests in the series, an additional test was intended in which the DAQ system malfunctioned. The results of the test were similar to the first loading cycle although the results could not properly be stored.

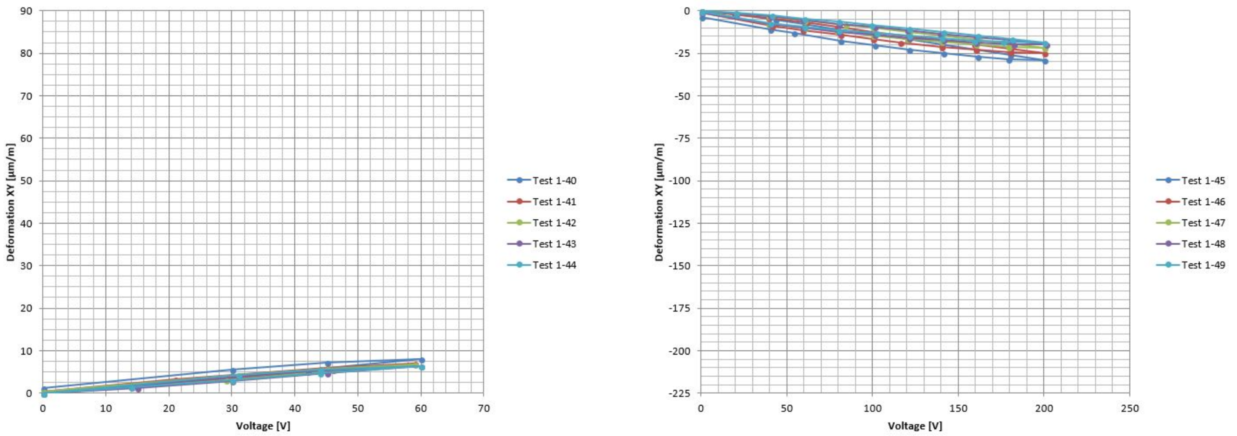

(a) Inverse polarization.

(b) Direct polarization.

Figure 4.38: Shear strain XY obtained from the deformations L, C, R in tests 1-40 to 1-49.

The results in Fig. 4.38 show the deviation of the piezoelectric actuator behavior from the circular symmetry behavior. In the ideal case where the geometry of the piezoelectric actuator did not affect the characteristics of the response of the material, the strain in the X direction would be equal to the strain in the Y direction and the shear strain XY would be 0 independently of the actuation voltage. As shown in the results this does not happen; the piezoelectric material geometry has an influence on the strain field and thus the XY shear strain is not 0. Note that the values of the shear strain are significantly lower than the values for the strain in X or Y directions (the graphics in Fig. 4.38a and Fig. 4.38b are in the same scale as Fig. 4.36 and Fig. 4.37 respectively). This means that the behavior of the piezoelectric actuator is not independent of the geometry but the geometrical influence is not the driving parameter in the deformation field produced.

5. Numerical prediction of structure morphing

In this chapter a numerical model for the piezoelectric material has been calibrated and implemented in some application cases with increasing complexity with the scope of determining the main objective of the thesis: the evaluation of the feasibility of application of piezoelectric material actuation in aeronautical structures morphing.

This chapter used all the information gathered in the thesis and integrates it into a concept for numerical testing that allows for the validation intended. It is important to reiterate that the resources of the thesis did not allow for the manufacturing and testing of the final prototype numerically analyzed. This is the main reason that justifies the testing on a simplified configuration tested in Sec. 7, where the investment necessary and the risk are smaller and the capacity of analysis of the phenomenology is significantly higher.

This part of the thesis represents the natural step in the process of developing any piezoelectric-actuated structure after the material has been characterized and its behavior on a simple structure has been evaluated. This thesis presents the development of the numerical models for the different configurations tested in the experiments already presented in this thesis in Sec. 4 and Sec. 7 together with the extrapolation of the model to a characteristic aeronautical structure. The structure considered in this chapter is a segment of a wing with constant geometry throughout the span.

To properly model the morphing wing profile configuration different steps of calibration of the numerical model have been defined. These steps are the following:

- Analysis of the piezoelectric material in comparison with the material characterization provided by the material manufacturer.
- Calibration of the piezoelectric patch model including the pre-stressing resin using experimental data.
- Calibration of the piezoelectric bending beam model including the aluminum bending bar using experimental results.
- Application case of the bending beam configuration in a complex geometry with multiple piezoelectric actuators in the shape of a generic wing profile trailing edge.
- Integration of the trailing edge geometry into a full wing profile and analysis of the suitability of the morphing obtained as control system for the wing.

These steps aim to provide a stepped and consistent approach to the problem of morphing flight control systems with piezoelectric actuators using as a starting point in the analysis currently available technology in terms of actuators.

5.1 Material definition

The calibration process of the numerical simulation is performed either though geometrical modifications or material property corrections. The geometrical modifications are considered in the following sections, where progressively more complex cases are analyzed to reach a configuration of model that can accurately predict the behavior of the studied experiment. The material properties, though, are adjusted in order for the phenomenology to match the experimental results.

The form of the matrices defining the mechanical and piezoelectric behavior of the different materials does not change depending on the calibration as the structure of the material is not dependent on the experiment itself. It is possible then to define the shape of the elastic, piezoelectric and dielectric matrices according to the material and identify the number of independent variables that define the behavior of each material.

5.1.1 Mechanical properties

The matrices defining the mechanical properties of the different materials simulated in the different experiments present a different number of independent coefficients depending on the behavior of the material in the different directions. In the present simulations only two types of materials are considered: isotropic materials and orthotropic materials. The reason for this is the fact that the piezoelectric material presents different mechanical properties in the polarization direction (Z) than in the other two directions (X,Y). The aluminium of the bar, the resin that embeds the piezoelectric material and the adhesive are considered isotropic.

5.1.1.1 Isotropic materials: aluminum, resins and adhesive

The isotropic materials require only two independent constants to define the elastic behavior of the material: the elastic modulus and the Poisson coefficient. The elastic modulus and Poisson coefficient for the aluminum are considered $69GPa$ and 0.3 respectively. The constants for the resin are $3GPa$ and 0.33 respectively and the ones for the adhesive $1.3GPa$ and 0.33. These constants fully define the behavior of the material as the rest of the non-zero coefficients of the elastic matrix can be derived from these two.

5.1.1.2 Transversely isotropic materials: piezoelectric PIC-255

The analysis of the piezoelectric material presents the particularity that the polarization direction has different mechanical properties that the directions perpendicular to it; this is known as a transversely isotropic behavior. Such materials present 5 independent constants that define the behavior of the material: E_x, E_z, ν_{xy}, ν_{yz} and G_{yz} (considering the direction z as the polarization direction).

The manufacturer of the piezoelectric provides the values of the compliance matrix $s_{11} = 16.1 \cdot 10^{-12} m^2/N$ and $s_{33} = 20.7 \cdot 10^{-12} m^2/N$ and the Poisson coefficient as 0.34 generic for all PZTs. According to the relation between the compliance matrix $[s]$ and the material constants presented in Eq. 5.1 it is possible to define all the 9 non-zero values of the compliance matrix to use as input in the numerical simulations.

$$[s_E] = \begin{bmatrix} S_{11} & S_{12} & S_{13} & 0 & 0 & 0 \\ S_{21} & S_{22} & S_{23} & 0 & 0 & 0 \\ S_{31} & S_{32} & S_{33} & 0 & 0 & 0 \\ 0 & 0 & 0 & S_{44} & 0 & 0 \\ 0 & 0 & 0 & 0 & S_{55} & 0 \\ 0 & 0 & 0 & 0 & 0 & S_{66} \end{bmatrix} = \begin{bmatrix} 1/E_x & -\nu_{xy}/E_y & -\nu_{xz}/E_z & 0 & 0 & 0 \\ -\nu_{xy}/E_y & 1/E_y & -\nu_{yz}/E_z & 0 & 0 & 0 \\ -\nu_{xz}/E_z & -\nu_{yz}/E_z & 1/E_z & 0 & 0 & 0 \\ 0 & 0 & 0 & 1/G_{xy} & 0 & 0 \\ 0 & 0 & 0 & 0 & 1/G_{yz} & 0 \\ 0 & 0 & 0 & 0 & 0 & 1/G_{xz} \end{bmatrix} \tag{5.1}$$

From these relations it is possible to obtain the remaining parameters excepting the shear modulus which is not given by the material manufacturer. The material has been compared with completely characterized piezoelectric materials in terms of mechanical and piezoelectric properties and found very similar to PZT-5A. Because of this similarity, the missing shear modulus has been assumed for the PIC-255 material as found for the PZT-5A. The complete constants are as follows:

$$\begin{array}{lll} E_x = 62.1GPa & \nu_{xy} = 0.34 & G_{xy} = E_x/(1-\nu_{xy}) \\ E_y = E_x & \nu_{yz} = 0.34 & G_{yz} = 21.1GPa \\ E_z = 48.3GPa & \nu_{xz} = \nu_{yz} & G_{xy} = G_{yz} \end{array}$$

These constants are sufficient input for the definition of the mechanical properties of the material in the simulation (where a transverse isotropic material is considered as a particular case of an orthotropic material, hence all 9 constants need to be introduced).

5.1.2 Piezoelectric properties

The only material in the simulations performed that has a non-zero piezoelectric matrix is the piezoelectric material PIC-255 found in the piezoelectric patches as the electroactive material producing the actuation. This matrix is the most relevant in all the simulations as determines directly the deformation produced in the material as a function of the applied voltage. The piezoelectric matrix can be expressed in two different formulations: as $[d]$ or as $[e]$ depending on the set of equations used. The relation between the two matrices is presented in Eq. 5.2 and allows to obtain one of the matrices when the other one is known. The units of $[d]$ are m/V or C/N while the units of $[e]$ are C/m^2.

$$[e] = [s_E]^{-1}[d] \tag{5.2}$$

The matrix $[s_E]$ is obtained previously in Sec. 5.1.1 and the piezoelectric matrix coefficients are privided by the piezoelectric patch manufacturer in the datasheet.[119] The form of the piezoelectric matrix can be obtained from the crystalline analysis of the material knowing it is a PZT type material; the detailed explanation on the shape of the piezoelectric matrix is presented in Sec. 3.1.2. According to this information, the piezoelectric matrices are obtained as presented in Eq. 5.3.

$$[d]=\begin{bmatrix}0 & 0 & -180\\ 0 & 0 & -180\\ 0 & 0 & 400\\ 0 & 550 & 0\\ 550 & 0 & 0\\ 0 & 0 & 0\end{bmatrix}\cdot 10^{-12}C/N \qquad [e]=\begin{bmatrix}0 & 0 & -7.526\\ 0 & 0 & -7.526\\ 0 & 0 & 14.205\\ 0 & 11.579 & 0\\ 11.579 & 0 & 0\\ 0 & 0 & 0\end{bmatrix}C/m^2 \tag{5.3}$$

These matrices provide a complete information for the simulation of the piezoelectric material. These coefficients will later on be adapted in order to calibrate the model created. The calibration will respect the proportionality between the different coefficients.

5.1.3 Dielectric properties

As for the piezoelectric properties, the only material whose dielectric properties are relevant to the simulations is the piezoelectric material. The piezoelectric material presents two independent dielectric coefficients in a diagonal 3x3 matrix as shown in Eq. 5.4. The coefficient in the direction of polarization is slightly higher than for the other two directions.

$$\varepsilon=\begin{bmatrix}\varepsilon_{11} & 0 & 0\\ 0 & \varepsilon_{11} & 0\\ 0 & 0 & \varepsilon_{33}\end{bmatrix} \tag{5.4}$$

The value for the dielectric coefficients has been obtained as $\varepsilon_{11} = 1650$ and $\varepsilon_{33} = 1750$ from the manufacturer datasheet.[119]

5.2 Calibration of the piezoelectric material

The first step in the modeling is the calibration of the piezoelectric material properties. This is performed through the simulation of a block of piezoelectric material of the same dimensions as the one that is embedded in the piezoelectric patch. The dimensions of the block are $50mm \times 30mm \times 0.2mm$. The analysis considers the results at an applied voltage of $100V$ and the material properties presented in the material definition in Sec. 5.1.

Under these conditions the maximum deformations obtained have been $\Delta x = 3.94 \cdot 10^{-6}m$ and $\Delta y = 2.37 \cdot 10^{-6}m$ with a constant strain in the XY plane of $\varepsilon_x = \varepsilon_y = 7.89 \cdot 10^{-5}m/m$. The deformed shape is presented in Fig. 5.1. It is possible to see that the constant in-plane strain produces a deformation with circular symmetry about a central point.

The numerical results are compared to the theoretical calculations for a material with the same properties. It

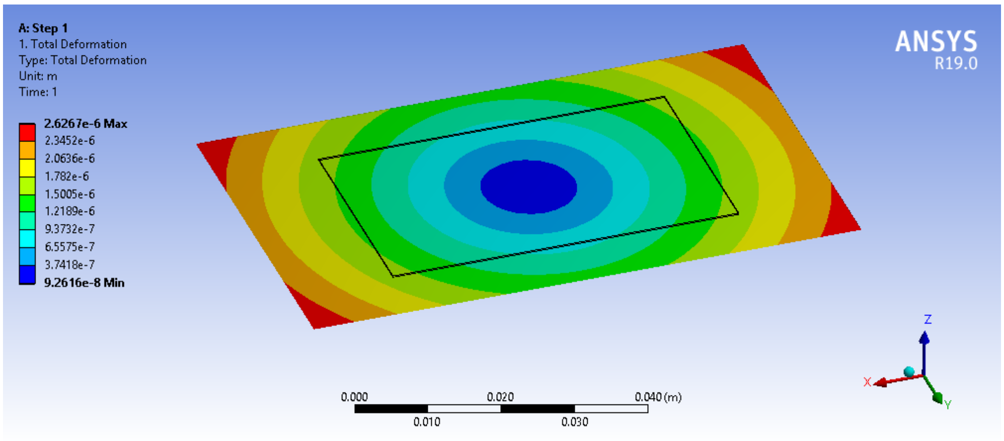

Figure 5.1: Results for the piezoelectric material simulation showing the sum of displacements of the deformed solution.

is possible to theoretically determine the deformation of a piezoelectric material through Eq. 5.5. According to this formulation the deformations in X and Y are $4.5 \cdot 10^{-6} m$ and $2.7 \cdot 10^{-6} m$ respectively.

$$\varepsilon_i = d_{ji} \frac{V_j}{t} \qquad \Delta_i = \varepsilon_i l_i \tag{5.5}$$

The comparison of the results leads to a 10% difference between theory and simulation. This deviation is consistent for the plane XY which is a validation of the phenomenology being correct. According to this deviation, the piezoelectric coefficient e_{31} (and by extension e_{32}) has been adjusted to $e_{31} = -8.596 C/m^2$. In order to keep the proportionality between the coefficients, e_{33} has been proportioned to $e_{33} = 16.224 C/m^2$ and $e_{24} = e_{15} = 13.225 C/m^2$. These piezoelectric coefficients lead to the following results: $4.5 \cdot 10^{-6} m$, $2.7 \cdot 10^{-6} m$ and $9.0 \cdot 10^{-5} m/m$. It is important to note that these piezoelectric constant corrected values do not imply that the experimental material presents these values, they are only corrected values to ensure that the simulations performed are calibrated.

5.3 Calibration of the patch

With the piezoelectric material calibrated, the following step in the simulation is the calibration of the model of the piezoelectric patch. The piezoelectric patch, show in Fig. 4.23 is modeled as the piezoelectric material block already calibrated surrounded by a resin block with the geometry presented. The geometry simulated disregarded the material of the electrodes and the electrical contacts for simplicity.

The material of the electrodes is not published in the datasheet or other information provided by the manufacturer which makes the geometrical modeling and the material determination a guess. On the other side, the influence of such a thin layer of material is disregarded as having negligible influence on the results. The non-consideration of the electrodes is accounted for in the corrections done in the material properties of the materials included in the simulation. The same applies to the electric contacts.

Different analysis have been performed both to calibrate the numerical model and to determine the influence of parameters in the solution of the simulations.

5.3.1 Analysis 1: resin thickness and boundary conditions influence

The first simulations performed in the patch geometry considered a $0.2mm$ thickness of the embedding matrix ($0.1mm$ on each side of the piezoelectric material). This geometry, although not the original one, allows to compare the results and to establish the influence of the matrix thickness on the results measured.

In order to consider the tests as close as possible to the experiments presented in Sec. 4.3 two cases of boundary conditions have been considered: free and with an end fixed on all displacements. The experimental case considered the piezoelectric material taped to the table; such condition should be between the assumptions of no boundary conditions (free) and fixed on one end. This analysis allows also to determine the influence of the boundary conditions in the measured results.

The results analyzed consist of the strain measured for the position of the strain gauge used in the experiments for the X and Y directions. The results obtained are the following:

Free boundary conditions:

$$\varepsilon_x = 49.8\mu m/m \qquad \Delta_x = 2.7\cdot 10^{-6}m$$
$$\varepsilon_y = 51.9\mu m/m \qquad \Delta_y = 1.6\cdot 10^{-6}m$$

Fixed end surface:

$$\varepsilon_x = 49.7\mu m/m \qquad \Delta_x = 2.5\cdot 10^{-6}m$$
$$\varepsilon_y = 52.0\mu m/m \qquad \Delta_y = 1.6\cdot 10^{-6}m$$

The simulations with different boundary conditions do not produce significant strain or displacement results being the biggest difference between results of 8% in the displacement in the x direction. The two deformed geometries, presented in Fig. 5.2 and Fig. 5.3.

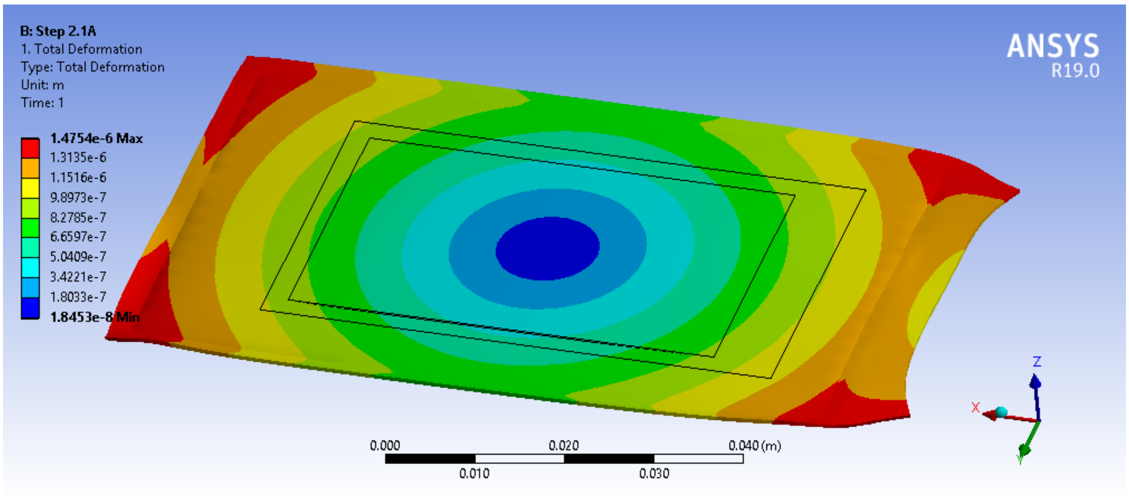

Figure 5.2: Total displacement of the piezoelectric patch for the analysis without applied displacement boundary conditions.

Despite the numerical results being very similar in the variables monitored the deformed geometries present significant qualitative differences. While the patch without displacement boundary conditions deforms in a manner similar to the piezoelectric material alone (analyzed in Sec. 5.2) the piezoelectric patch fixed on one end produces a deformation out of the plane in the corners opposite to the fixed side. This differences, as relevant as they are, cannot be contrasted to the experimental results as the overall deformed geometry

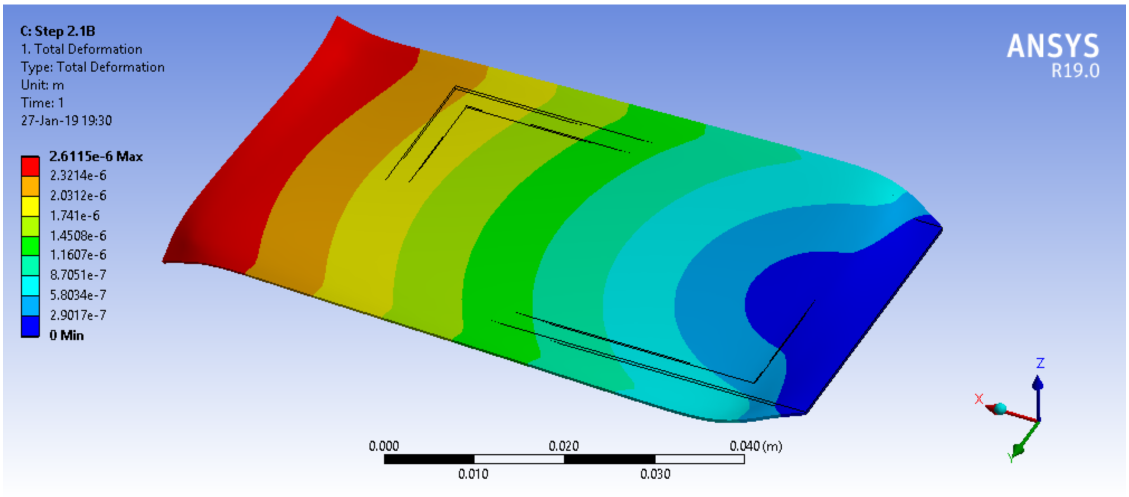

Figure 5.3: Total displacement of the piezoelectric patch for the analysis with a fixed side in all directions.

could not be measured due to the very small magnitude of the deformations.

Considering the small difference between results and without means to determine which of the deformed geometries is closer to the experiments both calculations are kept as plausible for further analysis.

5.3.2 Analysis 2: resin thickness influence and comparison to experiments

The second analysis performed considered the geometry with $0.3mm$ thick embedding matrix for the piezoelectric material ($0.15mm$ on each side of the piezoelectric material). This configuration is the geometry of the piezoelectric patch as published by the manufacturer.

The first purpose of this analysis is to determine how the thickness of the matrix influences the strain results measured in the actuated configuration. The configuration without mechanical boundary conditions is analyzed at an applied voltage of $60V$ and the results obtained as follows:

$$\varepsilon_x = 48.3\mu m/m \qquad \Delta_x = 2.6 \cdot 10^{-6} m$$
$$\varepsilon_y = 50.6\mu m/m \qquad \Delta_y = 1.5 \cdot 10^{-6} m$$

The results in this configuration have been compared to the experimental results. The experimental results have been obtained with a strain gauge rosette of ± 45 degrees. The strains measured by the rosette (denoted L, C, R) are the following:

$$\text{L: } 25.5\mu m/m \qquad \varepsilon_x = 22.5\mu m/m$$
$$\text{C: } 22.5\mu m/m \qquad \varepsilon_y = 41.0\mu m/m$$
$$\text{R: } 38.0\mu m/m \qquad \gamma_{xy} = -12.5\mu m/m$$

The transformation equations for a generic strain gauge rosette measurements to X and Y axes are presented in Eq. 5.6. In these equations, the angles that the three gauges form with the X axis are denoted with Θ_1, Θ_2 and Θ_3.

$$\begin{aligned}
\varepsilon_1 &= \varepsilon_x \cos^2\theta_1 + \varepsilon_y \sin^2\theta_1 + \gamma_{xy}\sin\theta_1\cos\theta_1 \\
\varepsilon_2 &= \varepsilon_x \cos^2\theta_1 + \varepsilon_y \sin^2\theta_2 + \gamma_{xy}\sin\theta_2\cos\theta_2 \\
\varepsilon_3 &= \varepsilon_x \cos^2\theta_1 + \varepsilon_y \sin^2\theta_3 + \gamma_{xy}\sin\theta_3\cos\theta_3
\end{aligned} \tag{5.6}$$

In the comparison of the simulation results with the numerical simulations it is possible to see that the numerical results are mostly symmetrical about the X axis while the strain gauge readings in the experiments are noticeably not symmetric (notice the high relative value of the shear strain and the difference between the readings of ε_L and ε_R). The only contribution for the non-symmetry in the numerical analysis is the contribution of the e_{24} and e_{15} constants, which does not have such influence in the solution as the experiments indicate. The deviations in the experiments can be explained by a deviation in the positioning of the strain gauge rosette (in terms of angular positioning) or by an asymmetry of the boundary conditions.

5.3.3 Analysis 3: model calibration

The calibration of the model is performed by modifying the elastic constants of the matrix. As the material properties are not provided by the manufacturer of the piezoelectric patch, the calibration of the model can be performed adjusting this parameter. The calibration of the model through the adjustment of the elastic constants of the matrix.

Different values of the elastic modulus have been considered in different analysis the results of whose are presented below:

Elastic modulus 3GPa:

$$\varepsilon_x = 49.0\mu m/m$$
$$\varepsilon_y = 51.1\mu m/m$$

Elastic modulus 10GPa:

$$\varepsilon_x = 40.5\mu m/m$$
$$\varepsilon_y = 45.0\mu m/m$$

Elastic modulus 15GPa:

$$\varepsilon_x = 36.1\mu m/m$$
$$\varepsilon_y = 41.4\mu m/m$$

These results are compared with the experimental data presented in the Analysis 2. It is significant to note that the isotropic modeling of the matrix cannot account for the X and Y strain results at the same time. In such condition two possibilities have been identified:

Orthotropic matrix consideration:

$$E^x_{resin} = 42GPa \quad \varepsilon_x = 22.5\mu m/m$$
$$E^y_{resin} = 22GPa \quad \varepsilon_y = 40.8\mu m/m$$

Isotropic matrix:

$$E_{resin} = 42GPa \quad \varepsilon_x = 22.5\mu m/m$$
$$\varepsilon_y = 28.4\mu m/m$$

Neither of the two solutions presents a fully desirable approach as the more accurate model presents orthotropic behavior which increases the complexity of the calibration and even though such behavior is possible, most of the resins do not present anisotropic behavior. On the other hand, the consideration of isotropic matrix reproduces properly the behavior in the X direction while resulting in some error in the Y direction. The image depicting the deformed shape in this situation is shown in Fig. 5.4.

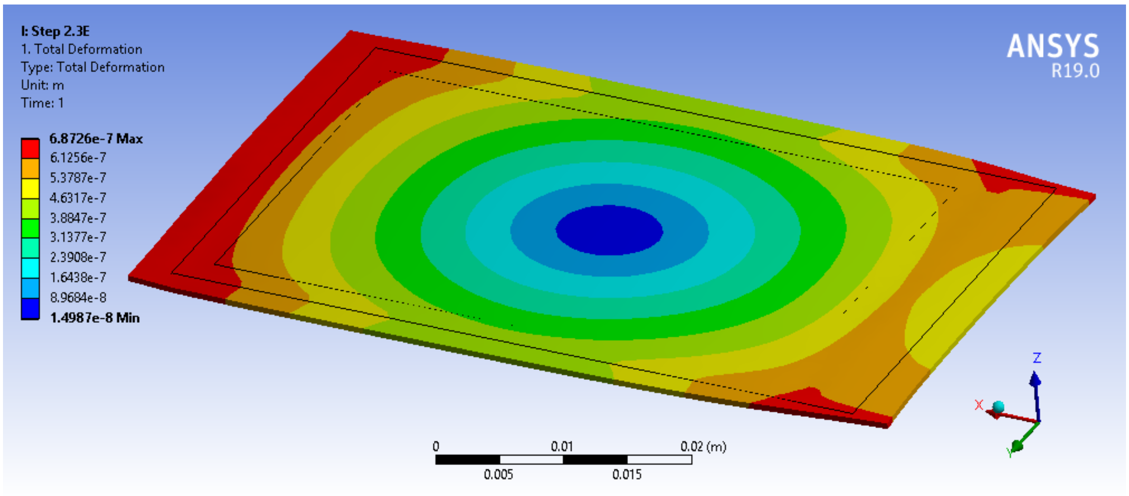

Figure 5.4: Total displacement of the piezoelectric patch in the configuration used with an isotropic matrix and elastic modulus of 42GPa.

As inaccurate this model is, the advantage of having a simpler model in terms of characterization compensates for the lack of accuracy in the Y direction of the deformation. This error will be considered assumable as for all the problems modeled in this thesis the principal direction is X and any distortion of the model in the Y direction will not significantly affect the relevant results.

Considering the large influence of the elastic modulus of the matrix in the deformation produced by the piezoelectric actuator, this parameter is a very good way of calibrating the results of the numerical simulations.

5.4 Calibration of the bending beam

The following (and last) step used in the calibration of the piezoelectric patch behavior is the analysis of the configuration in which the patch is bonded to a piezoelectric beam. In this set of numerical simulations two main geometric configurations have been analyzed: a configuration in which the piezoelectric patch is directly bonded to the beam and a geometry in which an adhesive layer is modeled between the piezoelectric patch and the beam.

The aim of these analyses is to determine the influence of the adhesive layer between the patch and the beam in the strain results and the deformation of the bar. Also to verify whether it is possible to model the geometry of the piezoelectric patch accurately (through a calibrated model) without considering the adhesive layer at all in the simulation. This hypothesis significantly reduces the complexity of the model as disregards the material properties of an unknown material as not relevant while simplifying the geometry.

The experimental results obtained during the bending beam testing (see Sec. 7.3) are shown below:

L: $-338\mu m/m$ $\varepsilon_x = -345\mu m/m$
C: $-345\mu m/m$ $\varepsilon_y = -330\mu m/m$
R: $-338\mu m/m$ $\gamma_{xy} = 0\mu m/m$
$defl. = 5mm$

It is relevant to note that the position of the strain gauge in this set of experimental results is positioned exactly at the same location in the patch as for the patch set of experiments. The strains in the X and Y directions are obtained through the planar transformation presented in Eq. 5.6. The experimental results show, in this results, a symmetry about the X axis in the deformed solution as the measured shear strain is 0.

5.4.1 Full geometry (adhesive) simulations

The first simulation considered a complex geometry including the piezoelectric patch, aluminum bending beam and adhesive interface between them. This model is the most accurate and its calibration serves as a reference for the validation of further simplifications aimed at reducing the complexity of the numerical model.

The main disadvantages of this model are the mechanical unknowns that the addition in the modeling of a layer of adhesive presents. This material presents the disadvantage that is not linear throughout the elastic domain. This poses a very significant added complexity to the model as the solution type needs to be adjusted accordingly. The main inconvenient though, relates to the elastic mechanical properties of the adhesive (Z70 as used in the experimental part in Sec. 7.1) which are not provided by the manufacturer and are, hence, unknown at the time of the simulation.

Considering that in previous experiments the stress levels reached throughout the structure have been very low, the hypothesis has been made for the materials to be considered linear in the intended domain. This hypothesis is done to simplify the calculation algorithm of the simulations but also to reduce to a single parameter the unknowns related to adhesive material characterization. As the adhesive is a type of cyanoacrylate, similar material elastic modules have been used to define the material properties in the simulation.

The initial simulation has been performed considering the adhesive as a $1.8GPa$ elastic modulus elastic material. This value is taken from similar materials. The results of this simulation considering the input parameters calculated in the patch simulations in Sec. 5.3 are illustrated in Fig. 5.5. In this consideration a value for the adhesive layer thickness is taken exaggeratedly large ($0.2mm$) in order to analyze the effect of this parameter in the results.

The numerical results for the strain at the strain gauge location and the deformation at the tip of the bar are obtained as follows:

$$\varepsilon_x = -221.9\mu m/m$$
$$\varepsilon_y = -218.6\mu m/m$$
$$defl. = 2.4mm$$

In this results it is clear to see that the addition of the adhesive produces a deformation in this configuration

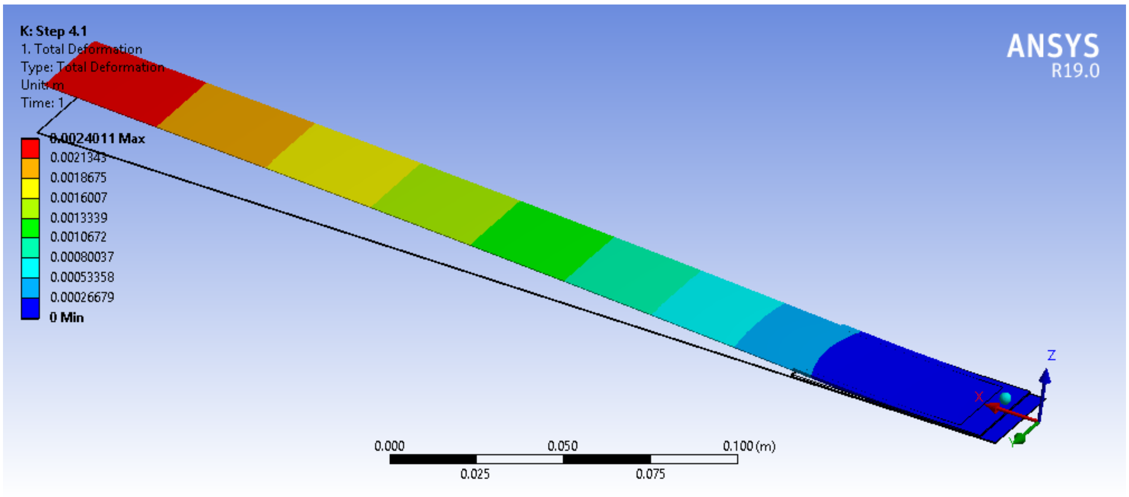

Figure 5.5: Deformation of the bending bar for the $0.2mm$ adhesive thickness case.

significantly lower that the experimental results which leads to the fact that a calibration of the model is required.

A second analysis evaluated the effect of the elastic modulus of the adhesive in the results. The elastic modulus has been considered at $3GPa$, same as for the embedding matrix of the piezoelectric material. In this manner, there is no mechanical discontinuity of the materials and the results can be evaluated without the influence of any distortions that may appear in the bonding between piezoelectric patch and adhesive. In these conditions the measure strains and deflection are presented below:

$$\varepsilon_x = -219.7\mu m/m$$
$$\varepsilon_y = -216.4\mu m/m$$
$$defl. = 2.4mm$$

As it is possible to see, the results are almost insensitive to the elastic modulus of the adhesive for the range of values relevant to the particular problem. Because of this, the elastic modulus of the adhesive has been returned to the initial original value of $1.3GPa$ as obtained from similar materials.

A second simulation aimed at the evaluation on the change in the results as a consequence of the modification of the thickness of the adhesive layer between the beam and the piezoelectric material. In this geometry the layer has been considered to be $0.05mm$ thick. This value represents a common order of magnitude for adhesive layers with this type of adhesives. As mentioned before, though, the thickness of the adhesive layer cannot be obtained with high precision due to the very small order of magnitude of the dimensions in the thickness direction. The values of the obtained strains at the strain gauge location are the following:

$$\varepsilon_x = -236.2\mu m/m$$
$$\varepsilon_y = -229.5\mu m/m$$
$$defl. = 3.0mm$$

The reduction of the thickness of the adhesive layer has a very significant effect in the deformation of the bar although the measured strains do not present significant variations. In this analysis, the strains measured tend to homogenize in comparison to previous analysis.

A calibration has been performed for this geometrical model varying the piezoelectric properties of the patch and considering the mechanical properties of the adhesive as in the non-calibrated tests. The results for this, calibrated, configuration are shown in Fig. 5.6. Notice that the deformation obtained at the end of the bending beam does not reach $5mm$; the reason for this is that the strains already surpass the experimental ones for this set of results so the piezoelectric properties are calibrated at an intermediate point.

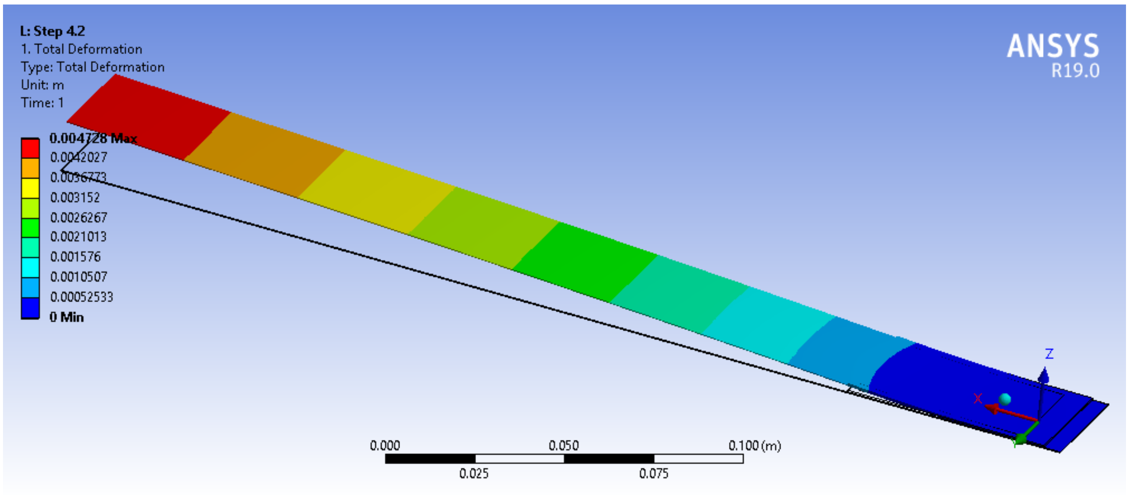

Figure 5.6: Deformation of the bending bar for the calibrated $0.05mm$ adhesive thickness case.

The strain results for this configuration are show below:

$$\begin{aligned} \varepsilon_x &= -364.1 \mu m/m \\ \varepsilon_y &= -359.7 \mu m/m \\ defl. &= 4.7mm \end{aligned}$$

Note that the model for this configuration is not properly adjusted in terms of proportion between the different magnitudes measured as the strain measured at the strain gauge location increases faster than the deflection of the bar leading to the present results in which neither of the results realistically represent the experimental results.

In these conditions, the adhesive layer separates the piezoelectric actuator away from the elastic axis of the beam section thus increasing the curvature produced in the affected sections. The layer is thin enough, though, not to absorb this extra deformation (as in the case for a thickness of $0.2mm$ of the layer) due to its low elastic modulus compared to the surrounding materials. It is relevant to point out that there is an optimal thickness of the adhesive that produces a maximum deflection in the bar when all the other parameters are kept constant.

In this analysis case, different configurations have been analyzed in which the elastic modulus of the aluminum has been varied from $60GPa$ to $75GPa$ resulting in a negligible influence in the results.

5.4.2 Simplified (no adhesive) simulations

Given the results obtained in the simulations that considered an adhesive layer, the hypothesis was made that a properly calibrated model could simulate the deflections of the piezoelectric beam without considering the particular mechanics of the adhesive explicitly. This simulations considered that an adjustment of the rest of the parameters of the problem can lead to similar results that the modeling of the adhesive but significantly reducing the geometric and parametric complexity of the problem.

The simulation that considered no adhesive between the piezoelectric patch and the beam has also been simulated at $200V$ in order to be able to compare the obtained results with the experimental data presented in Sec. 7.3.

Using the materials definition from the piezoelectric patch calibrated model in Sec. 5.3 the results obtained for the simulation are the following:

$$\begin{aligned}\varepsilon_x &= -198\mu m/m\\ \varepsilon_y &= -182\mu m/m\\ defl. &= 2.9mm\end{aligned}$$

The presented displacement is the deformation of the tip of the bar in the direction Z. This value presents a good reliability as the repetitivity of the values obtained during the experiments is very good.

As the results obtained in the simulation are far from the experimental results the analysis of the elastic modulus of the embedding matrix in the piezoelectric material has been revisited to analyze the influence of this parameter on the overall results in this particular configuration. A value of $3GPa$ for the resin has been considered as this value is common for resins. Notice that this hypothesis has already been considered in the patch analysis and disregarded only as calibration means for the particular model, not because of the accuracy of the assumption. In this configuration the strain results have been obtained as follows:

$$\begin{aligned}\varepsilon_x &= -242\mu m/m\\ \varepsilon_y &= -224\mu m/m\\ defl. &= 3.5mm\end{aligned}$$

These results show the significant influence of the matrix in the overall results. The values obtained are mostly proportional to the experimental results leading to the conclusion that the elastic moduli proportion of the different materials of the numerical model is properly calibrated. Because of this the elastic modulus of the embedding matrix is considered at 3GPa throughout the beam simulations and the piezoelectric coefficient e_{24} (and hence e_{15}) adjusted so the deflection of the bar matches the $5mm$ experimentally obtained.

In this configuration the deformation of the beam is presented graphically in Fig. 5.7. In the simulation performed it is possible to see the symmetry of the results about the X axis (as presented in the simulation results for the Y direction displacement) as the strains produced closely resemble the experimental ones.

The simulation values at $200V$ are presented together with the experimental values and the relative deviations in Table 5.1 for the calibrated piezoelectric coefficients shown below:

$$\begin{aligned}e_{31} = e_{32} &= -12.4C/m^2\\ e_{33} &= 23.43C/m^2\\ e_{24} &= 18.07C/m^2\end{aligned}$$

The comparison of the simulated results with the simulation presented in Table 5.1 demonstrates that is

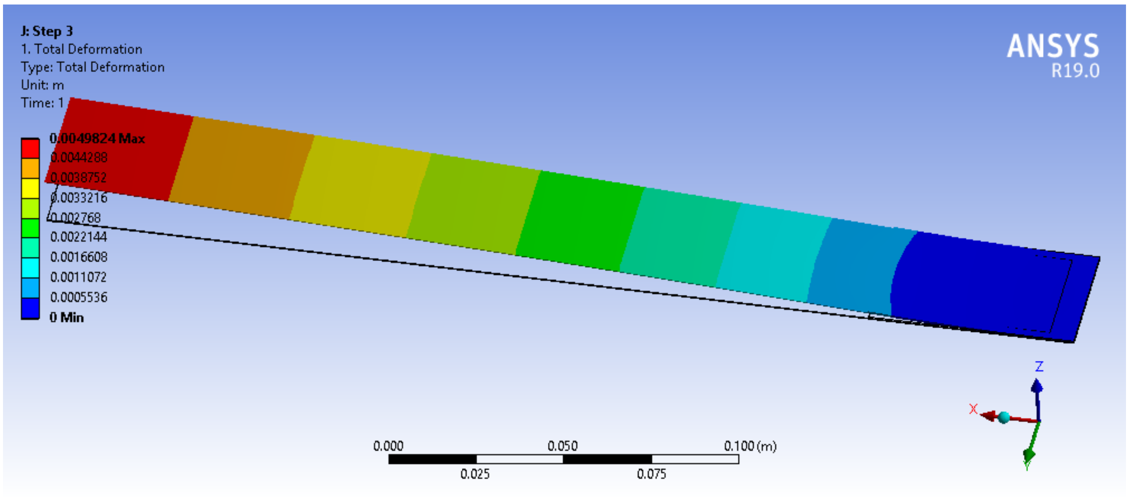

Figure 5.7: Deformation of the bending beam at $200V$ with material characteristics adjusted to match the experimental results.

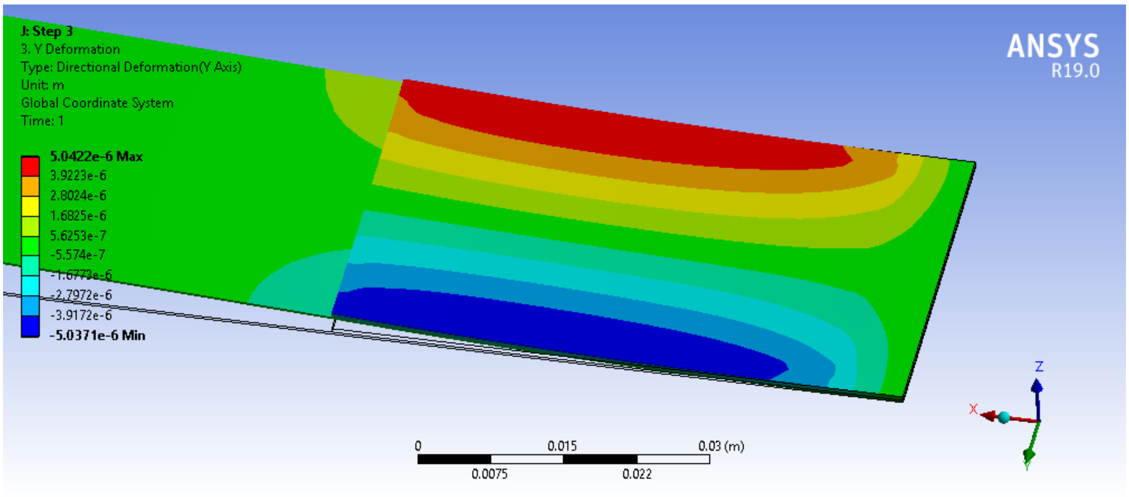

Figure 5.8: Y direction displacement for the bar shown in Fig. 5.7 depicting the symmetry of the results.

possible to obtain a calibrated model for the piezoelectric-actuated beam without including the adhesive between the patch and the beam in the model.

Table 5.1: Simulated strain and deflection results at $200V$ compared to the experimental values.

	Simulated	Experimental	Deviation
ε_x	$-347.9\mu m/m$	$-345\mu m/m$	0.85%
ε_y	$-325.2\mu m/m$	$-330\mu m/m$	1.45%
$defl.$	$4.98mm$	$5.0mm$	0.4%

The conclusion of this simulation is that it has been possible to obtain simulation results very close to the experimental ones while keeping a simple geometrical model that avoids the complexity of adding a material for which no information has been available during the simulations performed.

5.4.3 Comparison of calibrated model to experimental results

The results obtained for the no adhesive configuration are very close to the experimental results at the $200V$ point. This section compares the results obtained for the rest of the envelope of experimented voltages with the experimental results in the same boundary conditions.

The simulation results are presented in Table 5.2 while the experimental results are shown in Table 5.3 averaged for the representative tests applying the zeroing correction presented in the experimental results processing in Sec. 7.3.

Table 5.2: Simulated results of strain and deflection for the beam with calibrated actuator piezoelectric constants.

Voltage	ε_x $[\mu m/m]$	ε_y $[\mu m/m]$	d $[mm]$	ε_x^b $[\mu m/m]$	ε_y^b $[\mu m/m]$
$20V$	-34.8	-32.5	0.5	6.8	4.1
$40V$	-69.6	-65.0	1.0	13.6	8.3
$60V$	-104.4	-97.5	1.5	20.5	12.4
$80V$	-139.2	-130.1	2.0	27.3	16.6
$100V$	-174.0	-162.6	2.5	34.1	20.7
$120V$	-208.8	-195.1	3.0	40.9	24.9
$140V$	-243.6	-227.6	3.5	47.7	29.0
$160V$	-278.4	-260.1	4.0	54.6	33.2
$180V$	-313.1	-292.6	4.5	61.4	37.3
$200V$	-347.9	-325.2	5.0	68.2	41.5

Table 5.3: Averaged experimental results for the direct polarization tests applying zeroing correction.

Voltage	ε_x $[\mu m/m]$	ε_y $[\mu m/m]$	d $[mm]$
$20V$	-27.8	-26.6	0.38
$40V$	-52.4	-50.1	0.86
$60V$	-82.3	-78.8	1.35
$80V$	-119.1	-113.4	1.95
$100V$	-154.2	-146.0	2.44
$120V$	-192.2	-181.4	3.04
$140V$	-232.1	-218.9	3.67
$160V$	-268.3	-253.2	4.28
$180V$	-308.7	-292.3	4.89
$200V$	-346.6	-329.9	5.37

The comparison between the experimental and simulated results is presented graphically in Fig. 5.9 with an indication of the relative error between experimental and numerical results. It is important to note that the numerical simulations performed only consider the linear phenomenon so no hysteresis loop is modeled. Because of this, only the voltage ramp-up readings for the experimental results are considered in the analysis.

The main difference that appears when comparing the experimental and numerical results comes from the fact that the physical phenomenon is not linear. This causes that even though the model is calibrated at $200V$ some errors appear which are maximum in the area close to $100V$. In this case the maximum deviation is obtained at a value of $-22.1\mu m/m$ representing a relative deviation of 26.9%. At higher voltages, due to the characteristic hysteresis curve, the absolute and relative deviations decrease until the values calculated for the $200V$ point, where the maximum relative deviation is 3.8% which implied a good calibration of the numerical model.

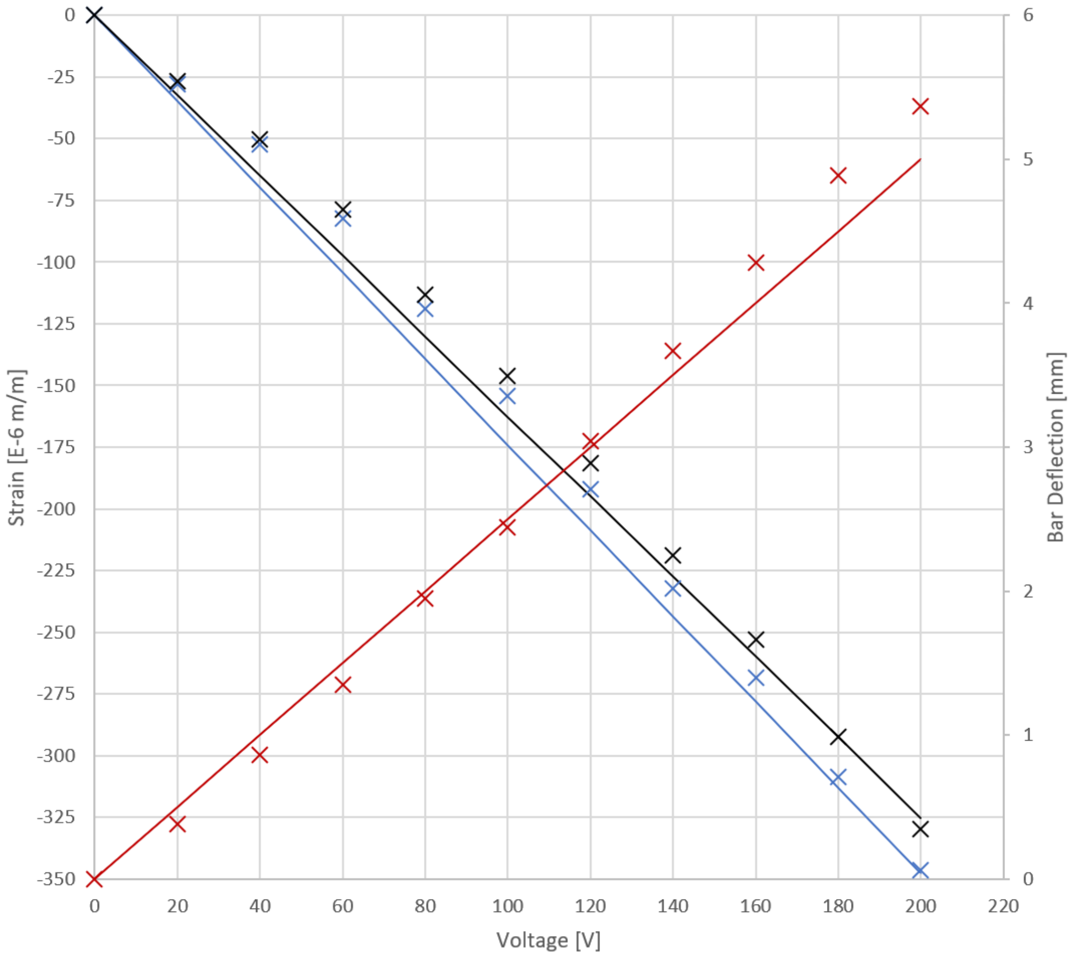

Figure 5.9: Comparison between experimental (cross) and numerical (line) results for the piezoelectric-actuated bending beam. The stain in X and Y are represented in blue and black respectively and the bar deflection in red.

The non-linear behavior of the system has other contributors apart from the piezoelectric material as the adhesive used to bond the piezoelectric patch presents a non-linear strain-stress characteristic curve. These effects have been considered not relevant to the present analysis, though, because of the presence of a small stress domain in the areas where non-linear materials are found.

As a conclusion, the developed model presents accurate results for the area about which the model has been calibrated, at lower voltages than the calibration, the model tends to overestimate the strain effects of the piezoelectric material. On the other hand, the deflection of the bar is properly modeled throughout the voltage domain analyzed, being the high voltage area the one that presents higher discrepancies with the experiments. At $200V$ the deviation reaches $0.37mm$ and a relative value of 6.9%. At lower voltages the model is more accurate. This is not problematic in the high voltage area because the model slightly underestimates the effect of the actuator and the value for this deviation is small (under 10%).

5.5 Application case: wing profile trailing edge

With the model of the piezoelectric patch calibrated for the bending application with the geometry of the beam as presented it is possible to attempt more daring configurations of morphing applications for the piezoelectric actuator. The configuration analyzed considers an aerodynamic profile trailing edge characteristic geometry in which both the upper and lower skins are actuated by a piezoelectric patch bonded on the outer side of the geometry as shown in Fig. 5.10.

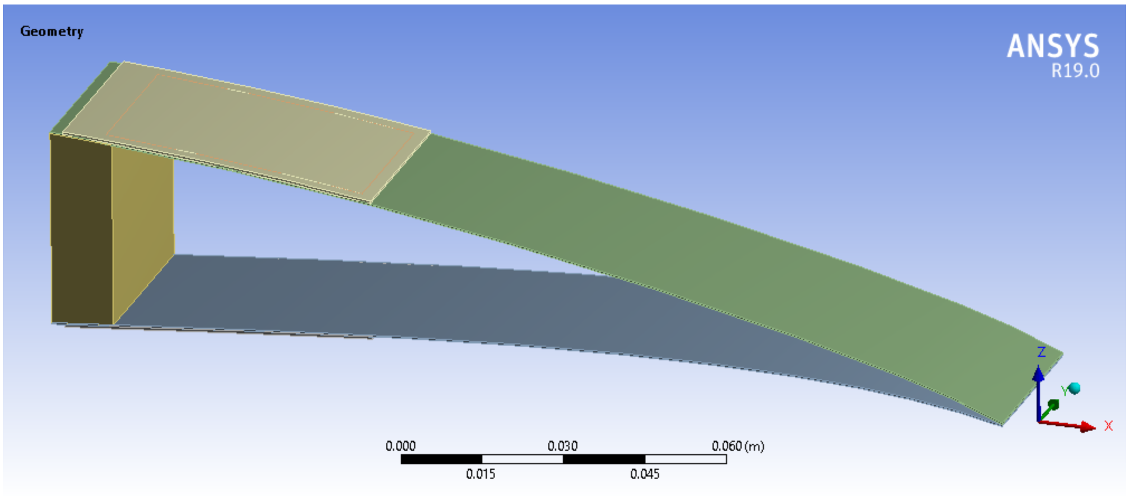

Figure 5.10: Trailing edge geometry used in the analysis of a more advanced morphing configuration.

This configuration aims to analyze the deflection of the trailing edge of the profile to determine whether it is feasible to produce aerodynamic changes on a wing profile with this type of actuation. In order for the feasibility analysis to be complete the calculations must include overall effect on geometry which, for aerodynamic purposes, is usually referred to as a base aerodynamic profile. Because of this, the analysis presented in this section is completed with the results obtained in Sec. 5.6.

It is important to note that the external forces that would normally act on a wing profile during a flight are not considered in the simulation and such an analysis is out of the scope of this thesis, as it would require recurring aerodynamic analysis of the deformed geometry as input for the aerodynamic forces in the mechanical model. Also, such an implementation would require also dynamic validation of the systems characteristics which this analysis does not provide.

The simulations have been performed in different boundary condition cases for the trailing edge, which has been found to greatly influence the results obtained.

5.5.1 Independent upper and lower surfaces

The first analysis case considered the upper and lower surfaces of the profile independent at the trailing edge location. This allows for each of the surfaces to move independently and even intersect each other if it was the case. Because of this condition being the most optimistic in terms of lowest restrictions, the displacements obtained in these simulations represent a best-case scenario (highest deflection values) for the behavior of the system.

Considering the characteristics of the piezoelectric patch used in the calibration of the simulations (see Sec. 5.4), the experiments considered a maximum direct voltage of $400V$ and a maximum inverse voltage of $-100V$; this leads to significantly higher deflections of the structure than the ones obtained in the experimental part. On the other side, the overall chord chosen for the profile to be analyzed has been taken similar to the dimension of the bending bar studied which makes the free length of the beams considered as upper and lower surfaces in this experiment considerably shorter than previous experiments resulting in lower deflection per voltage unit than the bending beam experiments. The trailing edge deflections obtained in this analysis for a voltage of $400V$ is shown in Fig. 5.11.

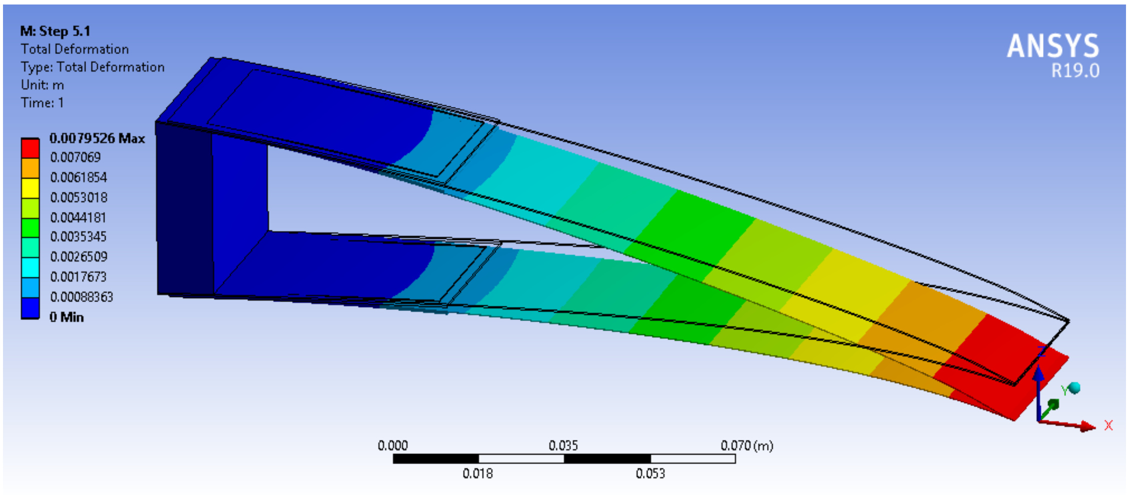

Figure 5.11: Deflection of the trailing edge geometry for a voltage of $400V$.

The results at $400V$ are very promising with an obtained deformation of $7.98mm$ and a free distance for the bending skins of approximately $175mm$ (the exact measure is difficult to evaluate as the skins are curved). It is important to note that is possible to obtain this deformation with a very low stress in the materials; the maximum stress in the model is found at $30.9MPa$ as seen in Fig. 5.12. This value is well under any elastic limit of the materials simulated in the geometry which means that not only does the model withstand the deflection but also makes it a good candidate for resistance to fatigue.

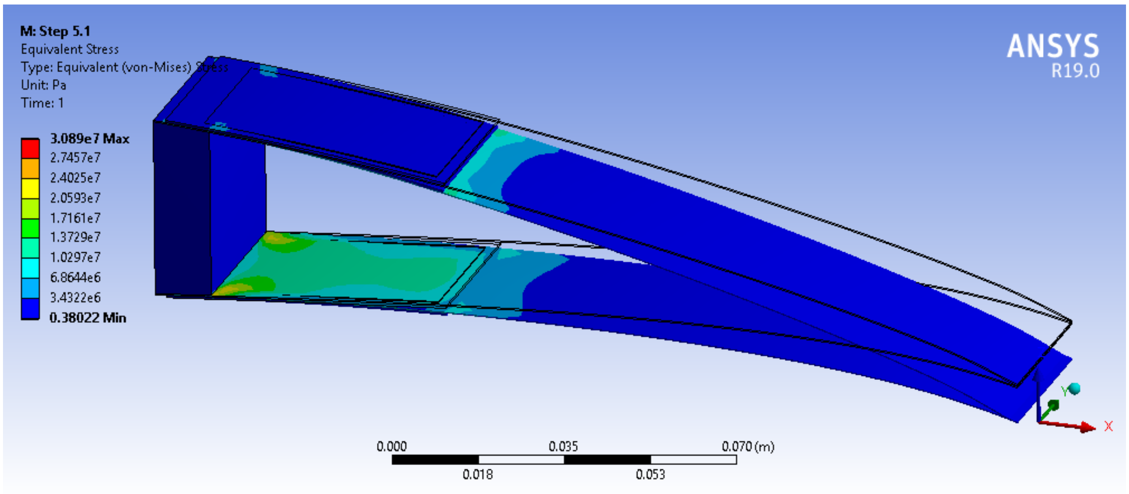

Figure 5.12: Mechanical Von Misses equivalent stress for a voltage of $400V$.

This presents advantages when compared to conventional actuation as mechanisms currently used in aviation are usually designed to work at the highest permissible stress to reduce weight, which means that the fatigue life for these systems is reduced.

A simulation has also been performed for the actuation in the opposite direction at a voltage of $-100V$. The simulation obtained a displacement of the trailing edge of $1.99mm$ and the results are shown in Fig. 5.13.

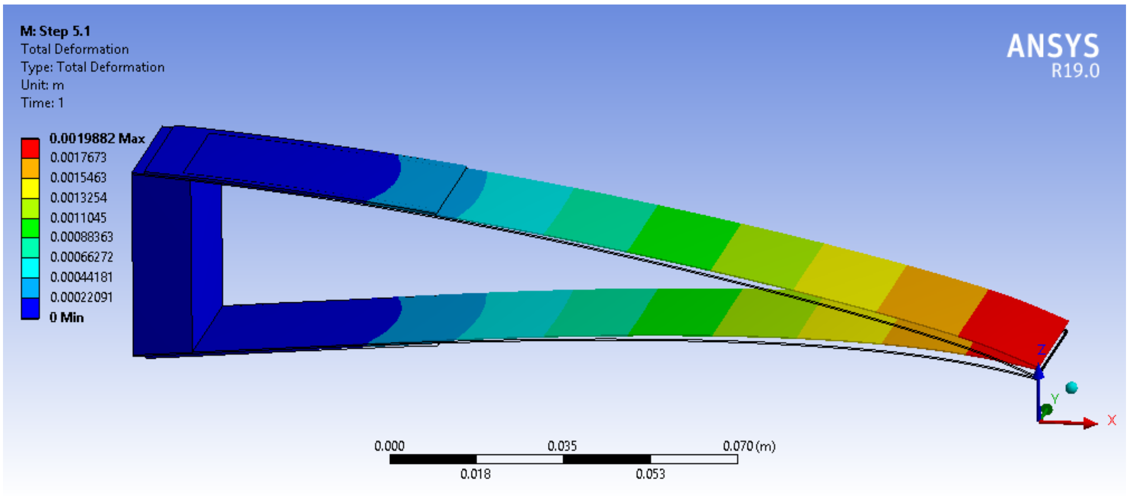

Figure 5.13: Deflection of the trailing edge geometry for a voltage of $-100V$.

This means that the range of deflection for the piezoelectric actuated trailing edge is between $-1.98mm$ and $7.98mm$ for the operational range of the piezoelectric material. This operational range is limited by the maximum electric field that the material can withstand without depolarizing and by the mechanical pre-stressing imposed by the embedding matrix.

It is important to note in this set of analysis that the problem has been simulated using two main hypotheses that reduce the accuracy of the solution underestimating the effects of the piezoelectric actuator.

- Planar piezoelectric patch: to simplify the modeling of the piezoelectric elements a single coordinate system has been considered to define the piezoelectric, mechanical and dielectric properties of the piezoelectric patch (the only anisotropic material in the model). The coordinate system has been positioned in the middle of the piezoelectric patch and with the Z direction perpendicular to the patch surface at that point. This introduces small deviations in the properties of the rest of the point of the patch, which should be defined on local coordinate systems element to element in order to avoid the hypothesis. As the angular deviation of the normal vectors of the piezoelectric patch elements with respect to the central point is under $1deg$ a common normal has been considered for all the piezoelectric element.

- Small deformations hypothesis: the simulations have been performed considering that the change in geometry in the deformed model does not have an influence on the forces acting on the system. This is commonly known as the small deformations hypothesis. This significantly reduces the computation cost of the simulation as it allows for a single iteration calculation instead of an iterative cycle that redefines the boundary conditions for the deformed shape after every iteration. This hypothesis has been considered as the deformations expected in the results are small in comparison to the characteristic dimensions of the problem. As seen in the results, the maximum deflection in the problem is about $8mm$ while the characteristic dimension for such deformation is about $175mm$; the ration between these magnitudes is 4.6% which makes the hypothesis reasonable.

These hypotheses are considered adequate in this specific problem as the curvatures in the non-deformed and deformed geometries are small and the errors of these assumptions are small. These hypotheses need further consideration nevertheless if simulations are to be attempted in which the deflections obtained cannot be assumed in the small-deflections hypothesis. A result that is very sensitive to these hypotheses is the electric field value in the piezoelectric actuator (see Fig. 5.14).

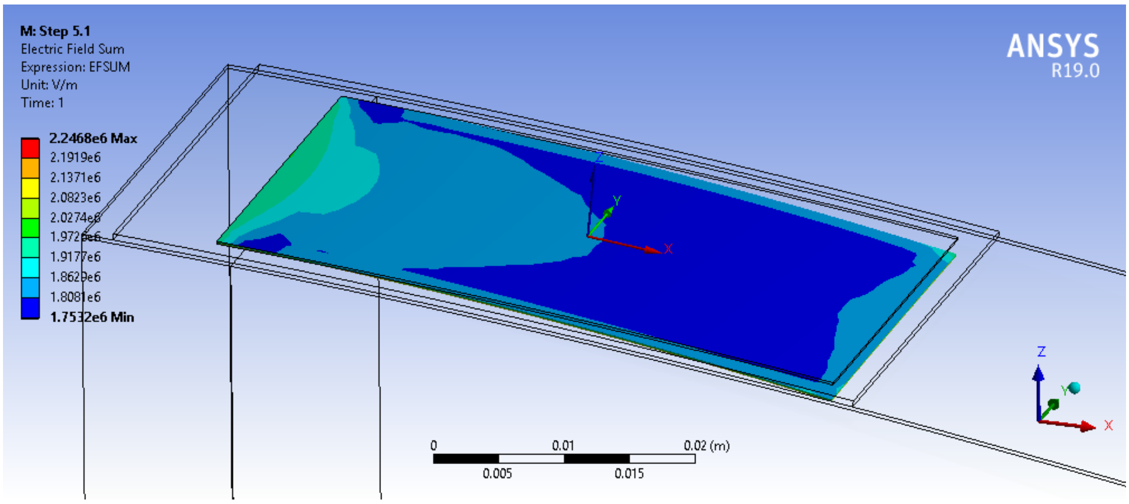

Figure 5.14: Electric field in the upper piezoelectric patch for a voltage of $400V$.

As the voltage at each of the electrodes of the piezoelectric material is constant, the electric field to which the piezoelectric material is constant. This is only true, though, if one does not consider that the piezoelectric material deforms in the polarization (and electric field) direction which reduces the distance between electrodes in a non-uniform manner (because of the boundary conditions to which the piezoelectric material is subject). This non-uniform deformation produces on its own non-uniformity in the electric field to which the material is subject. If no geometrical distortions that affected the relative angle between the polarization direction and the electric field direction occurred, the non-uniformity in the electric field would follow the same pattern as the non-uniformity in the deformation of the piezoelectric material in the polarization direction. This means that any other distortion in the uniformity of the electrical field in the piezoelectric material must be caused by the hypotheses assumed in the numerical solution of the problem.

5.5.2 Contact between upper and lower surfaces

A second analysis case has been simulated considering that the upper and lower skins of the profile trailing edge had a contact constraint that allowed them to slide without friction. This condition restricts the movement of the morphing structure as the results of the free simulation case previously presented showed a small intersection between the deformations of the upper and lower skins.

The results obtained at $400V$ show a deflection of the trailing edge of $5.94mm$ and the displacement field shown in Fig. 5.15.

The introduction of the contact between the two skins reduces significantly the deflection of the trailing edge and maintains qualitatively the same geometry as the one without any boundary conditions in the trailing edge. This is also valid for the results at a voltage of $-100V$ shown in Fig. 5.16 where the deflection is obtained at $1.49mm$. This results represent a reduction in deflection of 25% from the free simulations for

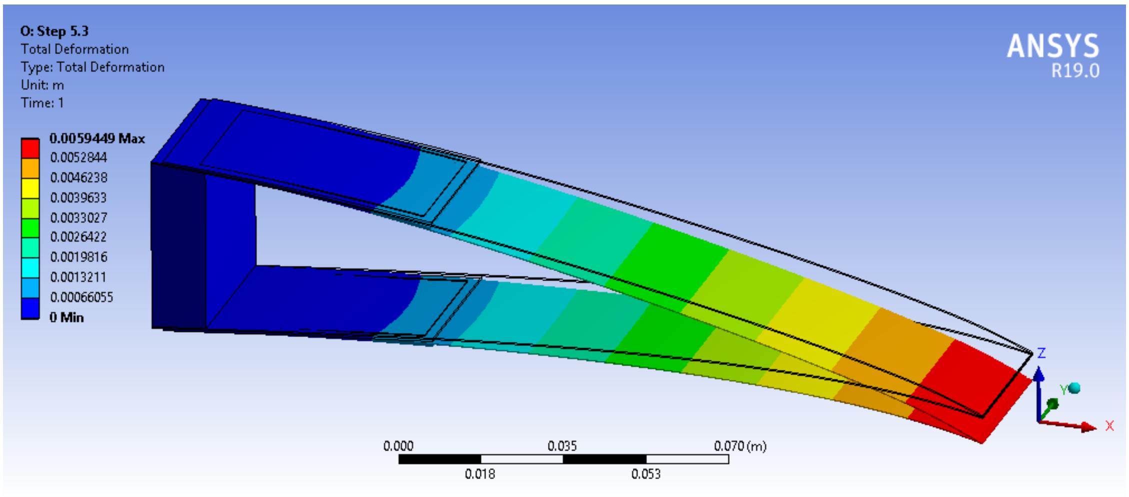

Figure 5.15: Deformation of the trailing edge model with contact boundary condition for a voltage of $400V$.

both loading cases.

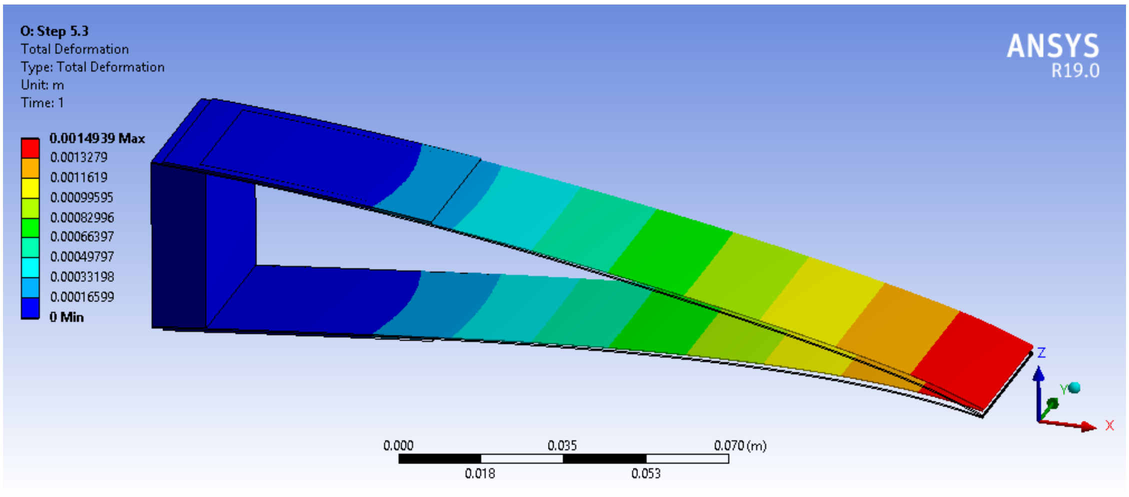

Figure 5.16: Deformation of the trailing edge model with contact boundary condition for a voltage of $-100V$.

Despite this reduction in the performance of the geometry in terms of deflection, the boundary conditions in this case reflect a real case more accurately than the free simulation.

5.5.3 Bonded upper and lower surfaces

A third simulation case has been analyzed in which the end of the upper and lower surfaces has been considered bonded at the trailing edge. This bonding boundary condition has been considered in two different situations: a case in which the relative rotation between bodies is restricted at the contact point and a case in which the relative rotation is allowed.

The results of the simulations for both cases showed no significant difference depending on the condition of fixed relative rotation between the profile skins so only the results for the case in which the bonding between the skins does not allow relative rotation is presented. The results at $400V$ are presented in Fig. 5.17.

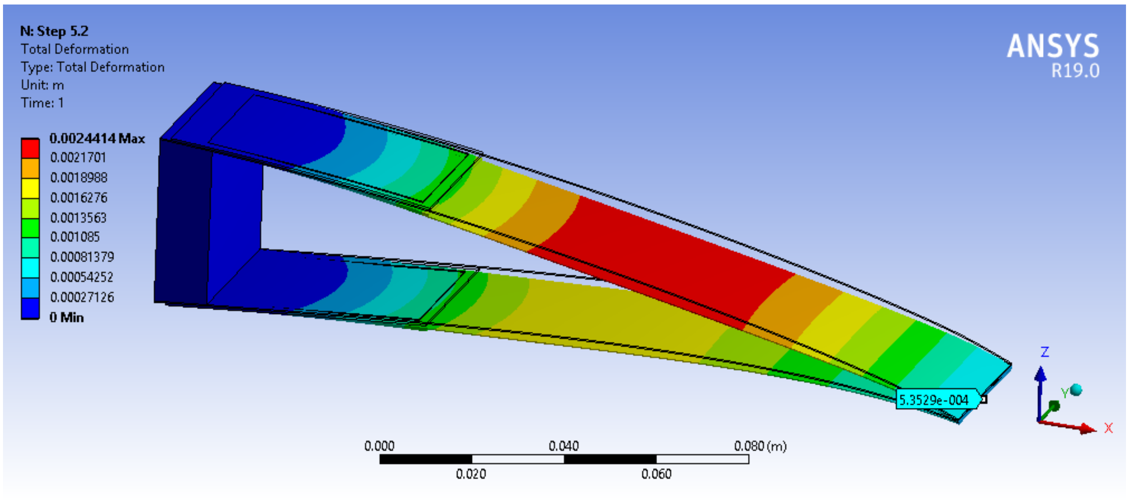

Figure 5.17: Deformation of the trailing edge model with bonded boundary condition for a voltage of $400V$.

It is possible to see that the form of deformation of the profile trailing edge, in this case, is completely different than any of the previous analysis cases due to the fact that the geometry to be deformed is a closed profile. This closed profile geometry presents a torsional stiffness completely different than any of the previous cases which restricts the deflection motion of the trailing edge to a deflection of $0.54mm$ in comparison to the $7.95mm$ and $5.94mm$ obtained in previous analyses. Qualitatively, the deformation mode of the structure is also completely different as the maximum deformation is produced somewhere in the middle between the actuation point and trailing edge for both the upper and lower skins.

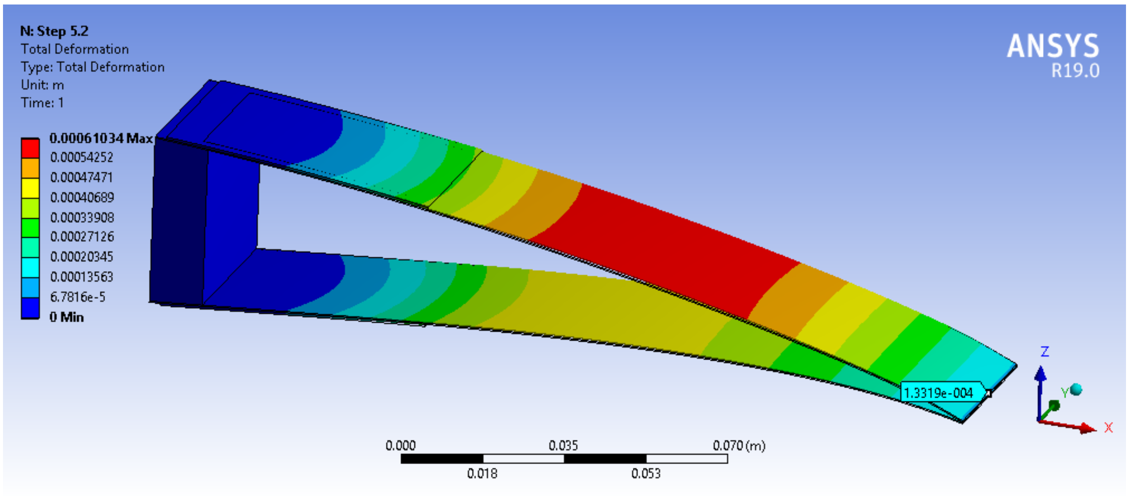

Figure 5.18: Deformation of the trailing edge model with bonded boundary condition for a voltage of $-100V$.

These results are analogue but opposite in sign for the analysis at an actuation voltage of $-100V$ shown in Fig. 5.18. The behavior of the structure under this analysis condition leads to the conclusion that an effective morphing trailing edge must provide as much as possible freedom of independent deformation to the upper and lower skins of the profile in order to maximize the deflection regardless of the actuation direction.

5.6 Application case: complete wing profile

The last part of the numerical simulations of the thesis considers the full geometry of a wing profile in the scale relevant to the UAV industry. The chord of the full profile has been taken similar to the bending beam experiments from Sec. 7.3 and the trailing edge section is common to the simulations in Sec. 5.5. This allows to evaluating the effect that the integration in a wing has on the deflection of the trailing edge.

The scope of these analyses is to determine whether the implementation of commercially available piezoelectric materials on a representative UAV wing produces an effect relevant enough to produce changes in the aircraft equilibrium and thus making it controllable. This would imply the feasibility of piezoelectric actuated morphing flight controls.

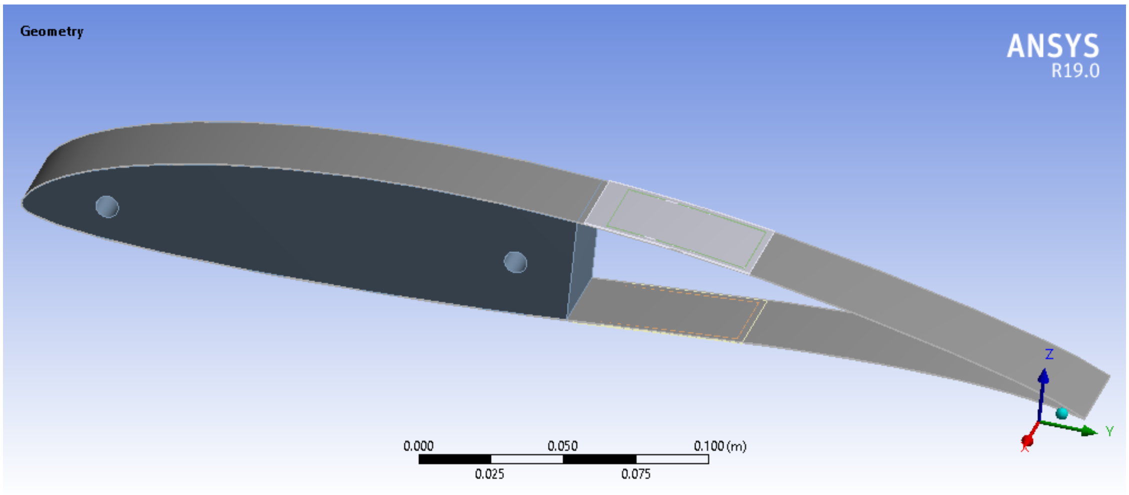

Figure 5.19: Geometry of the simulated wing profile with morphing trailing edge.

The simulations considered the geometry shown in Fig. 5.19. The aerodynamic shape is considered as a $0.3mm$ thick aluminum sheet with two piezoelectric patches on the upper and lower surfaces in the same position as the trailing edge simulations. The filling of the wing is considered in the area between aluminum skins until a point about $5mm$ in chord before the piezoelectric patches are bonded and the material considered is epoxy resin with an elastic modulus of $3GPa$. This geometry is expected to slightly increase the deflection produced in the trailing edge as it slightly increases the part of the skin that can be subject to bending.

The results in this configuration for an actuation voltage of $400V$ are shown in Fig. 5.20 where it is possible to see that the deflection of the trailing edge of the profile is, indeed, slightly higher than for the case analyzed in Sec. 5.5.1 ($8.23mm$ in comparison to $7.98mm$).

The analysis has also been performed for the case in which the actuation voltage is $-100V$ and the deflection of the trailing edge of the profile simulated at $2.06mm$ (in comparison to $1.98mm$). The solution is illustrated in Fig. 5.21.

These results on itself provide no information from which the feasibility analysis for morphing of a wing can be done. To determine whether the produced deflection is enough for the system to be used as a flight control the movement of the trailing edge is expressed as a variation in the angle of attack of the profile in comparison to the non-deformed geometry.

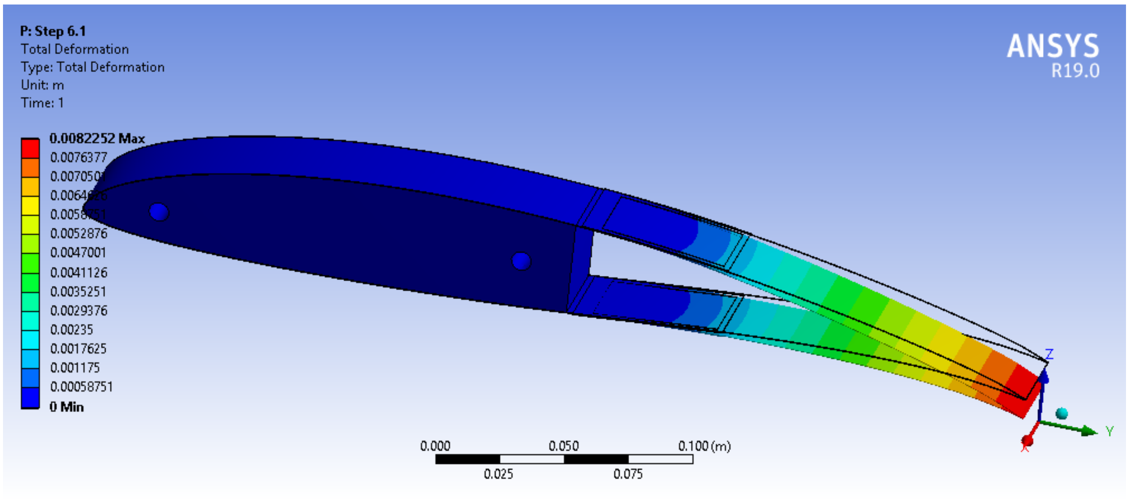

Figure 5.20: Displacement results for the analyzed wing profile configuration at a voltage of $400V$.

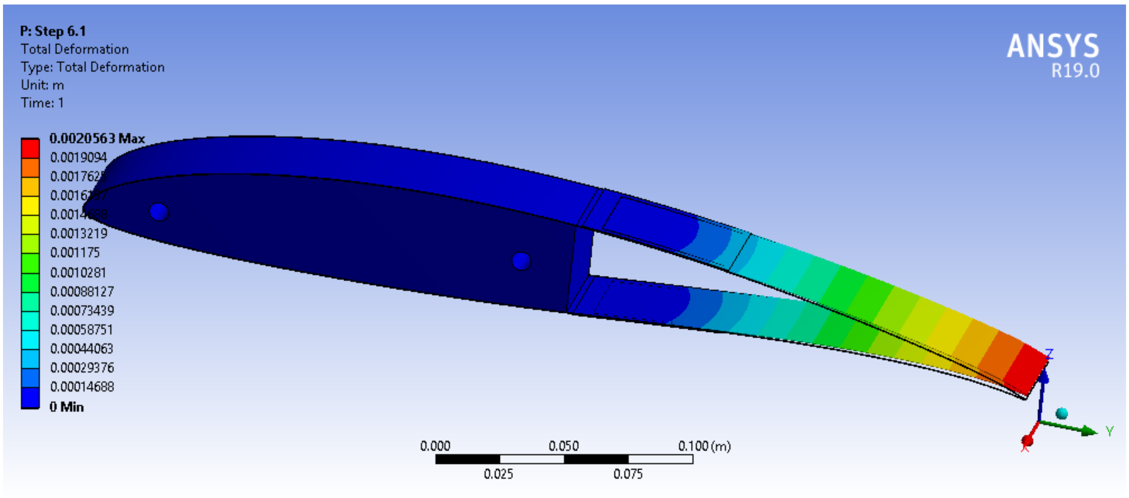

Figure 5.21: Displacement results for the analyzed wing profile configuration at a voltage of $-100V$.

The increase in angle of attack by the morphing system can be easily obtained through the formula:

$$\Delta AOA = \arctan\left(\frac{defl}{chord}\right)$$

The results for this particular case at the analyzed actuation voltages are $1.2deg$ and $-0.3deg$. On its own, these values provide not enough information for comparison as conventional control surfaces do not use this type of analysis to determine its efficiency. To provide a proper term of comparison the increase in the angle of attack definition has been applied to different UAVs. At full deflection, the primary control surfaces have an increase in angle of attack of about $7deg$ to $10deg$ depending on if they are ailerons or elevators (the rudder has not been considered in this analysis).

The comparison of the control surfaces for a representative UAV in comparison to the morphing concept presented in this thesis leads to the conclusion that the use of morphing structures as primary flight control systems is not feasible in the form analyzed. Even though the increases in angle of attack for the morphing case and the conventional actuators are in the same order of magnitude, the deflections still need to be significantly higher for this type of actuation to be suitable for primary control.

This technology can be used as secondary control of the aerodynamic characteristics of small UAVs, for example in optimization of flight envelope through the adjustment of the curvature of the profile. This application is suitable for this type of technology due to the low energetic consumption it requires, the versatility of the geometries where it can be implemented and the low weight.

6. Piezoelectrically actuated conventional control surfaces

The experimental part of the research presented in this thesis is covered in two complementary ways, the piezoelectric actuation in the application of aircraft control can be performed, as mentioned in the state of the art, in different manners from which, conventional actuation and piezoelectric morphing out-stand. Conventional actuation is the technology for aircraft control most developed as all commercial airliners use it. Because of this, this technology has been incorporated into this research.

The application of piezoelectric materials in the actuation of conventional control surfaces is conceptually simpler than the integration of piezoelectric materials in the aircraft structure as it only requires the replacement of an existing mechanic, hydraulic or electric actuation system with a piezoelectric one, without any influence in the architecture of the system. This simplicity and architecture commonality with current technology is very attractive from the reduced implementation risk it presents but sets a limit to the performance of the control system. This limit is the one presented by the control surface itself: independently of how efficient the actuator is, the system will aerodynamically be as efficient as the control system actuated by any means other than piezoelectric.

Another way of stating this is: a piezoelectric-actuated conventional control surface may present advantages in terms of weight saving, actuation performance and energy savings but will not result in the increase of the aerodynamic performance of the control system itself, as the aerodynamic element of the system remains unchanged.

This restriction is not critical at this level of research as the increase in the performance of the control system may be enough to justify a piezoelectric-actuated control system without evaluating aerodynamic performance. The increase of actuation capabilities in the high-frequency field (inaccessible through mechanical and hydraulic actuation systems) opens a wide spectrum of possibilities in the control of dynamic aeroelastic effects such as flutter thus presenting potential breakthroughs in terms of flight envelope capabilities without significant modifications in the current aircraft configurations and architectures.

This chapter aims to explore the possibilities of piezoelectric actuation in the field of flutter control with the scope of proving that it is possible to safely fly (in terms of structural integrity) at speeds higher than the flutter velocity without modifications in the structural properties of an aircraft.

Secondly, the research aims at evaluating if piezoelectric actuation is suitable as a substitute for conventional control surface actuation systems, particularized to the requirements that the anti-flutter system implies.

6.1 Project overview

The research presented in this chapter has been performed as part of a research project in which diverse research organizations have been involved, the name of the project is AFDPA: Anti-Flutter Demonstrator using Piezoelectric Actuators.

The project developments are included in the thesis because the objectives of the project are analogue to the objectives of this chapter as presented in Sec. 6. The main goal of the project is to determine whether it is possible to avoid the aeroelastic phenomenon of flutter through the careful application of commands in a conventional control surface of an aerodynamic body.

To determine this, the project proposed the construction of a test specimen shaped with an aerodynamic profile simulating an aircraft wing carefully designed to suffer from flutter at low speeds. The wing is instrumented with accelerometers to measure the dynamic behavior of the structure during testing and incorporates a control surface at the tip of the span simulating an aileron. The control surface is actuated by a piezoelectric actuator controlled by an active control system designed to avoid flutter.

The project implementation is divided into four stages in which the different elements of the system are designed, manufactured and tested providing a robust methodology for the determination of the performance of the system. The different stages of the project are detailed in Sec. 6.2.

The project started in 2014 and finished in 2017 with the completion of the wind tunnel testing of the system. The general results obtained are presented as part of the last stage of the project in Sec. 6.2.4 and the analysis of the results was considered as one of the activities within the project.

The project was coordinated by Dr. I. Ursu from INCAS (National Institute for Aerospace Research) in cooperation with investigators from the University “Politehnica" of Bucharest, S.C. STRAERO S.A. and other partners.

6.1.1 Description of the project

Flutter is an aeroelastic phenomenon that occurs whenever the torsion and bending vibration frequencies of a body moving through a fluid converge. In such case, the body starts vibrating in such a way in which the force that causes the vibration is amplified by the motion itself. This rapidly leads to a point in which the strength limits of the body are surpassed and structural failure occurs.

As bodies moving through fluids, aircraft present susceptibility to flutter, particularly on the areas in which the fluid-structure interaction forces significantly change the stress state of the structure as the velocity of the body increases. These areas are mainly aerodynamic surfaces (wings and horizontal and vertical tail planes).

The most commonly encountered aerodynamic structures present very differentiated bending and torsional resonance frequencies when there is no external load on the structure. In this condition flutter phenomenon does not exist. As the loads on the structure increase, however, the resonance frequencies change so there is a point in which they overlap. The velocity at which this occurs is called flutter velocity. Fig. 6.1 presents a characteristic example of such behavior for an airplane wing. The complete study presenting the condition of the measurement is found in [120].

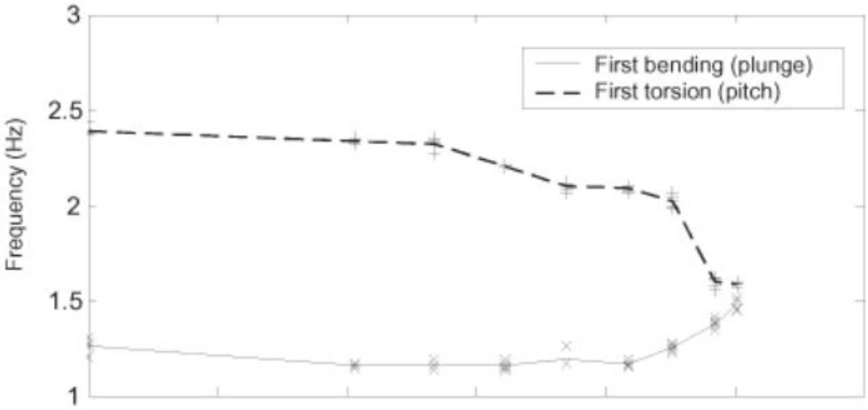

Figure 6.1: Evolution of bending and torsional frequencies of a characteristic wing as a function of velocity during wind tunnel testing (measured points) and numerical simulation (lines). [120]

In conventional aircraft structures, the wing presents a dynamic behavior changing with loading. In flight, this loading occurs due to aerodynamic loading. However, it is possible to obtain changes in the dynamic behavior of the structure with static loads applied mechanically while on ground obtaining analogue results. [117] This allows for a simplification in the mechanical characterization of the structure as in the first stages of the research, wind tunnel testing is not required in order to obtain a first approximation of the structure's dynamic behavior.

The AFDPA project (Anti-Flutter Demonstrator using Piezoelectric Actuators) aims to create an integrated solution for flutter avoidance that allows for aerodynamic surfaces to fly at speeds higher than flutter velocity without encountering the phenomenon.

The solution proposed in the project consists of two basic elements: a wing-like structure designed to experience flutter at very low speeds and a control system designed to avoid such phenomenon. The wing specimen consists of a flexible structure with an aerodynamic shape resembling an aircraft wing. The structure, though, is segmented as to provide for a very low torsional resonance frequency, which ensures a low flutter velocity. The wing implements an integrated control system integrated by four different elements: a control and command unit, a sensing subsystem, a control subsystem and a control surface to introduce the commands on the aero-elastic system.

The control and command unit consists of a computer with a DAQ (Data Acquisition System) capable of both: reading realtime the parameters by the different sensors instrumenting the test specimen and capable of issuing control signals to the actuator.

The actuator is a piezoelectric-based system that takes a pre-amplified electric signal from the control unit and transforms it into a mechanical movement. In the AFDPA project the movement produced by the actuator is a rotary movement which is directly transmitted to the control surface. The actuator uses piezoelectric material as active elements because of the excellent frequency characteristics that this type of materials present when compared to electric motors. The main challenge of these materials is the amplification of the small motions they produce (as presented in Sec. 1.4.5.3).

The control surface is a conventional aileron located at the tip of the wing which can deflect symmetrically to provide control on the forces acting on the specimen during wind tunnel tests. It is interesting to note that the forces produced by the aileron are proportional to the square of the wind velocity so the control characteristics of the specimen increase as the wind velocity increases.

Lastly, the sensing elements used are piezoelectric accelerometers used to measure the motion of the test specimen. This data is processed by the control unit and used as feedback in the closed-loop control algorithm implemented.

The design and implementation of the different elements are proposed in different phases according to the planning proposed in the following sections in terms of definition of tasks and distribution of tasks between the different project members.

6.1.2 Organization of the project

The organization of the project is proposed at two different levels, a first classification distributes the work included in the project in stages. These stages, due to administrative reasons, are designed to converge with the reporting phases that the financing program requires. A deeper classification split the workload of the project into tasks assigned to the different project members according to their experience and capacity to perform them.

In the majority of projects, this classification of tasks is referred to as the work breakdown structure (WBS) and this allows for simpler planning of the project. The planning of the project is addressed to in Sec. 6.1.3 together with the project management considerations.

The project is organized in four different stages (commonly referred to as Work Packages in the European Commission funded projects such as the Clean Sky 2 or the Horizon H2020 projects, in the present project the same terminology has been kept in the reports and project documentation) which address the following topics:

- **Stage 1 - Base concepts:** in this phase the preliminary definition of the system is performed, detailing the requirements for each of the major subsystems, relations and preliminary interfaces. The wing specimen is designed, the actuator concept is developed and the control algorithm is defined at a preliminary design level.
- **Stage 2 - Detailed design and manufacturing:** in this stage the design is further defined and completed for the different hardware systems, the actuator and the wing specimen are built and tested in static conditions.
- **Stage 3 - Preliminary testing of the complete system:** in this stage the systems integration are performed and static and dynamic tests are performed to check the behavior of the control algorithm of the fully assembled system, and the structural behavior of the wing (from integrity checks to dynamic verification of the modes of vibration).
- **Stage 4 - Final systems testing:** the final test campaign includes the wind tunnel testing as the main activity. The wind tunnel tests are designed to determine the functioning of the system in a real dynamic environment. The dissemination activities, very important in any research project, are also included in this stage of the project.

The presentation of the work performed during the project is done in Sec. 6.2 according to these stages presented here.

6.1.3 Project planning and management

The planning of the project consists in organizing all the activities to be performed in the project according to the relations between them, their duration and the available resources for each of the activities. The objective is to fit the activities to be performed in the time frame of the project without exceeding the available resources and considering the order in which the different tasks need to be performed.

The planning of the AFDPA project is presented in Fig. 6.2 in the form of a Gantt diagram. Each of the tasks presented has a appointed task coordinator (a partner in the consortium responsible for the progress of that task). Apart from the task coordinator, other partners can be involved in each of the tasks of the project.

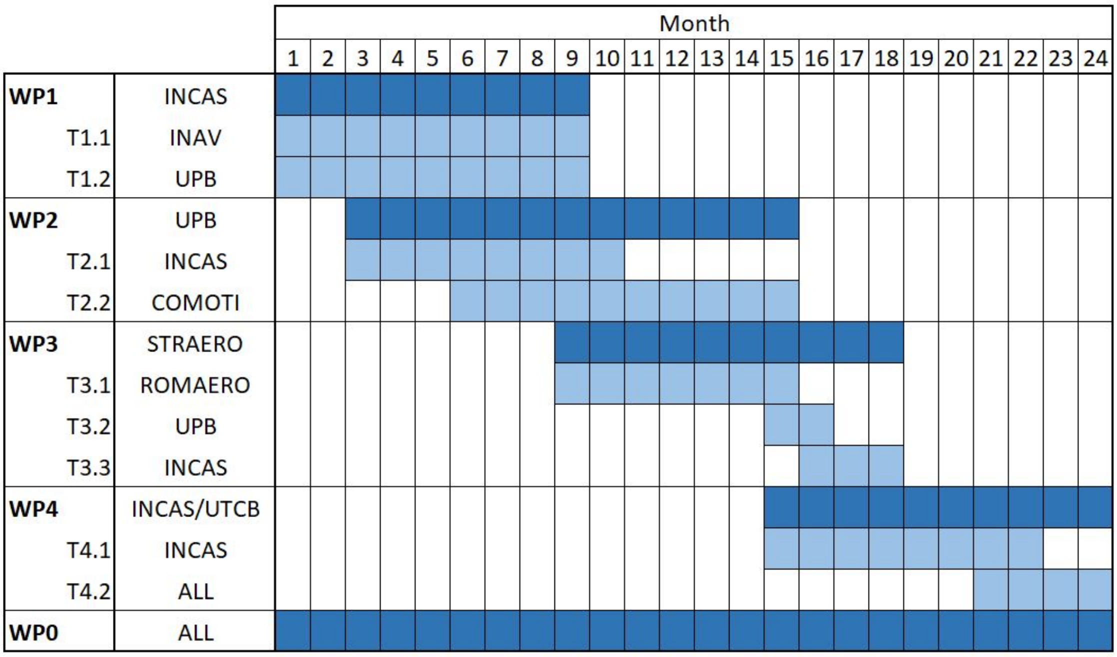

		Month																							
		1	2	3	4	5	6	7	8	9	10	11	12	13	14	15	16	17	18	19	20	21	22	23	24
WP1	INCAS	■	■	■	■	■	■	■	■	■															
T1.1	INAV	▨	▨	▨	▨	▨	▨	▨	▨	▨															
T1.2	UPB	▨	▨	▨	▨	▨	▨	▨	▨	▨															
WP2	UPB			■	■	■	■	■	■	■	■	■	■	■	■	■									
T2.1	INCAS			▨	▨	▨	▨	▨	▨	▨	▨														
T2.2	COMOTI						▨	▨	▨	▨	▨	▨	▨	▨	▨	▨									
WP3	STRAERO									■	■	■	■	■	■	■	■	■	■						
T3.1	ROMAERO									▨	▨	▨	▨	▨	▨	▨									
T3.2	UPB															▨	▨								
T3.3	INCAS																▨	▨	▨						
WP4	INCAS/UTCB															■	■	■	■	■	■	■	■	■	■
T4.1	INCAS															▨	▨	▨	▨	▨	▨	▨	▨		
T4.2	ALL																					▨	▨	▨	▨
WP0	ALL	■	■	■	■	■	■	■	■	■	■	■	■	■	■	■	■	■	■	■	■	■	■	■	■

Figure 6.2: Gantt diagram of the AFDPA project.

The management of the project is the set of activities that are not directly linked technically to the research but that organize the work, such as progress reports preparation or dissemination activities.

In any publicly funded research project there is a great emphasis on the dissemination activities that will make the research performed in the project known to other researchers in the field. This project is not an exception, the activities are considered in the last stage of the project even if they were performed throughout the duration of the project.

6.2 Project development

This section presents the activities related to the development of the piezoelectric-actuated anti-flutter system. The work is presented as the project has been performed and divided by the different stages presented in Sec. 6.1.2.

The explanations focus on the aspects relevant to the thesis: the piezoelectric actuator, its mechanical amplification system, the implementation of the actuator in the wing and the performance of the actuator in the particular application. It is important to present a global view on the project, however, to present other activities that complete the development of the project and that play an important role in the justification of the different trade-off decisions considered during the project.

6.2.1 Base concepts

The conceptual design of the high aspect ratio wing requires the study of the constraints and operational requirements. In order to perform such a study it is important to consider a model for the prediction of the non-linear wing dynamics which in turn allows for a prediction of the aeroelastic behavior present during flutter.

The aeroelastic analysis of an aeronautical structure requires a coupling between two different sub-problems: the structural dynamics of the wing and the aerodynamic analysis, which considers the forces actuating on the deformed wing. To study both sub-problems simultaneously, the Theodorsen model can be applied in the present problem with the hypotheses of incompressible, harmonic, non-stationary flow. The problem then reduces to the application of a formulation in which the structure displacement and its derivatives as a function of time appear explicit.

In order to study flutter, the calculation model represents the wing as a typical section with three degrees of freedom (angle of attack, vertical displacement of the section and deflection of a generic control surface). The model allows for the calculation of the flutter conditions (speed and frequency) for an elastic wing with constant characteristics throughout the wingspan. The elastic modeling in terms of vertical deformation is done through a spring of elastic constant K_h and the modeling of the torsional elasticity through a torsional spring of constant K_t. The generic control surface is considered articulated at a point located at a distance c_b from the center of the chord and is elastically linked to the profile through a spring of torsional rigidity K_b.

Table 6.1: Geometrical characteristics of the conceptual wing analyzed.

Profile	NACA 0012
Chord	$0.3m$
Span	$1m$

Three calculation methods of the flutter conditions have been considered applying this model, called the typical sections model: the V-g method, the PK method and the root locus method. The first two methods present an analysis only in terms of frequency while the third method presents it in terms of time also. A Matlab mathematical model has been developed for each of the methods leading to the following results of flutter conditions for a first estimation geometry. The conceptual analysis performed considered the initial data presented in Table 6.1.

- **V-g method:** $89.4 - 90.9 m/s$
- **PK method:** $95.1 - 95.4 m/s$
- **Root locus method:** $91.4 m/s$

The obtained flutter speed for all three methods used is very similar, thus proving the robustness of the calculation methodology. The results obtained in this conceptual approach are not usable in the preliminary design of the test specimen because the obtained flutter speed is too high in relation to the available wind tunnel performance.

At this conceptual stage it is important to set the aerodynamic considerations that the physical model needs to verify for the proper development of the testing. As the testing of the AFDPA system is performed in a wind tunnel, the similarity criteria for aerodynamics, solid mechanics and elasticity needs to be verified. The first condition is the dimensional homogeneity of the equations used in the modeling of the problem. This verification can be performed through the Pi theorem (Buckingham). This theorem defines the minimum number of non-dimensional variables to be kept constant in order for the model to be dimensionally homogeneous. The dimensional analysis of the equations relevant to the aeroelastic phenomena of interest in this project are presented in [121].

The physical model built to evident the flutter phenomena during the wind tunnel testing phase of the project is shown in Fig. 6.3. It is composed of a longeron and an aerodynamic skin profiling a NACA 0012. The wing features an aileron and a servotab in one of the ends and it is fixed rigidly in the wind tunnel in the opposite end.

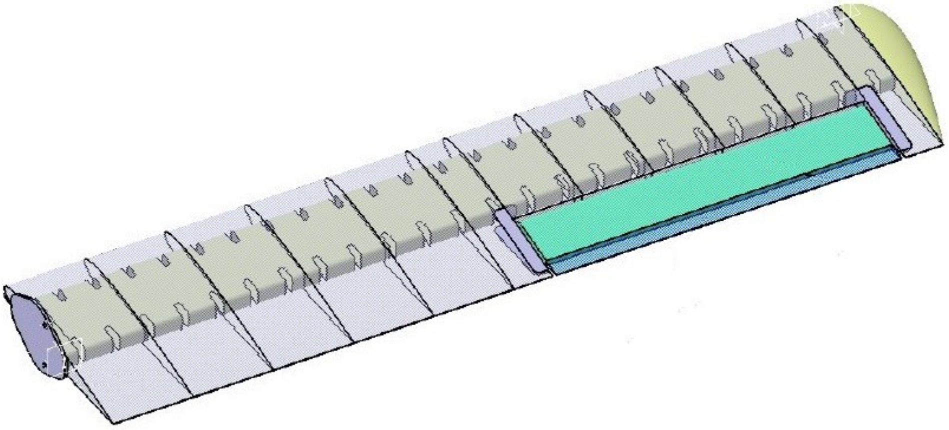

Figure 6.3: Concept geometry of the AFDPA wing showing the structural spar, the aerodynamic skin, the fixing interface, the aileron and the servotab.

On the concept of the wing design the natural frequencies have been calculated in order to verify that the flutter condition is attained within the wind tunnel operational range. The calculation has considered only the spar of the wing because the aerodynamic skin is designed not to influence significantly the rigidity of the structure. The calculation has been performed using Patran and a model with shell type elements. The material considered in the spar is aluminum, with the mechanical properties presented in Table 6.2. The boundary conditions reflect the future operating conditions of the wing prototype. One of the ends has been fixed through the constraining of the 6 degrees of freedom in the relevant nodes.

The obtained results show the first bending frequency at $10.2 Hz$ (see Fig. 6.4) and the second vibration

Table 6.2: Mechanical properties for the aluminum used in the conceptual design of the wing spar.

Elasticity modulus	$71GPa$
Poisson coefficient	0.3
Density	$2700kg/m^3$

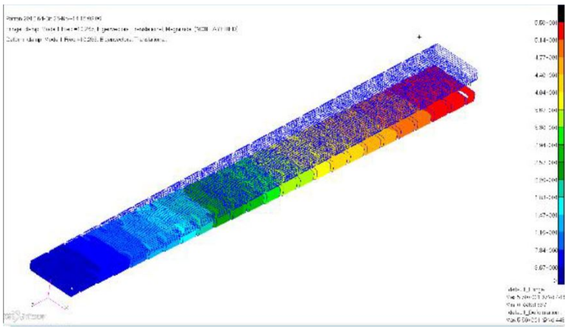

Figure 6.4: 1^{st} vibration mode of the wing structure proposed.

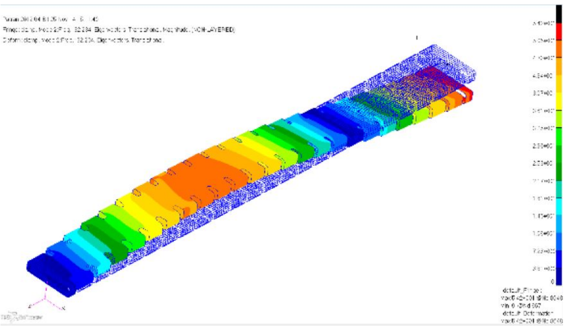

Figure 6.5: 2^{nd} vibration mode of the wing structure proposed.

mode at a frequency at $32.2Hz$ (see Fig. 6.5). These two frequencies are the ones involved in flutter phenomena so the rest of the calculated vibration modes are neglected in this analysis. The prediction of the flutter condition apparition with the considered geometry and structural characteristics can be done with the validation method presented in [122] according to the following formulation shown in Eq. 6.1.

$$k_{cr} = \frac{\omega c}{2U} \tag{6.1}$$

In this formulation ω is the first bending vibration frequency, c is the chord of the wing section and U the free stream velocity. Considering the proposed model magnitudes, $k_{cr} = 0.32$. According to the referenced bibliography the flutter phenomenon appears for values of $k_{cr} < 0.9 \pm 0.12$ so in the calculated wing the flutter condition will be attained.

The design of the piezoelectric actuation system is a very complex aspect of the project and the relevant part for the present thesis. The use of piezoelectric actuators as means of actuating the control surface of the anti-flutter system implies a mechanical amplification of the displacement produced by the piezoelectric actuator before its introduction to the servotab. This amplification is justified because of two aspects of the system:

- The necessity to transform the linear movement produced by the piezoelectric actuators into a rotational movement necessary in the servotab.
- The magnitude of the required movement cannot be attained by the piezoelectric deformation without a previous step of amplification.

The present technology in PZT-type piezoelectric materials does not allow for a displacement of enough magnitude so the servotab can be actuated by the piezoelectric material without an intermediate amplification stage. [123, 124] To overcome this necessities, two solutions have been proposed and implemented at a conceptual stage: the use of piezoelectric stack actuators and the design of an amplification mechanism.

Piezoelectric stack actuators have been selected for this particular application due to the main advantage they offer in terms of the magnitude of the produced linear displacement and actuating force. Other types of actuators such as bending actuators produce larger deformations at the cost of lower actuating force. [116] In the present application, the stack-type piezoelectric actuator offers a good compromise in its performance.

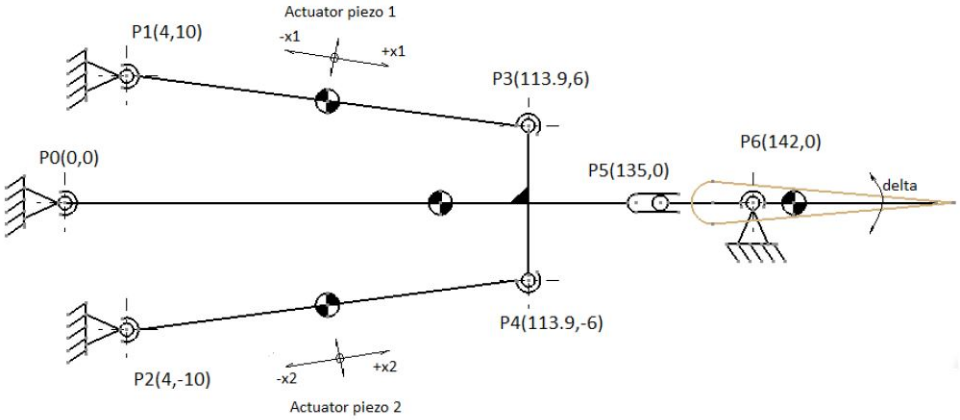

Figure 6.6: Proposed mechanism for force amplification and linear to rotational motion transformation based on two stack piezoelectric actuators working in tandem.

The mechanism proposed (shown in Fig. 6.6) is designed to perform both functions of amplification and transformation of movement from linear to rotational. In order to verify the suitability of the mechanism, a dynamic analysis has been performed. The scope of this analysis is to verify that the concept proposed is able to produce the required $\pm 10deg$ turn in the servotab with the maximum dynamic conditions: a maximum piezoelectric actuator force of $4200N$, a maximum actuation frequency of $30Hz$ and a maximum linear displacement of the piezoelectric actuator of $\pm 0.1mm$. The restrictions in terms of piezoelectric actuator capabilities are defined considering a specific model of actuator that has been proposed.

A dynamic simulation of the proposed amplification mechanism has been performed using Matlab / SimMechanics with the following simulation network parameters: the deformation is imposed by the piezoelectric actuator with a frequency in the range $f = 1..30Hz$ and a constant amplitude of $a = 0.1mm$, mass of the aileron $100g$, mass of the mobile support $40g$, mass of the piezoelectric actuator $80g$, dry friction coefficient[1] $\mu = 0.05..0.25$, hinge moment calculated through the formula:

$$c_h = c_h^{\alpha}\alpha + c_h^{\delta}\delta \tag{6.2}$$

where α and δ are the angle of attack of the wing and the deflection angle of the aileron respectively, $c_h^{\alpha} = -0.254$ and $c_h^{\delta} = -0.613$ for a free stream velocity of $30m/s$ and the wing dimensions as defined in Table 6.1. The block diagram of the simulation model used is shown in Fig. 6.7.

The simulations are performed for a diversity of cases for the following input conditions:

- Dynamic simulation without simulated aerodynamic hinge moment (test A)
- Dynamic simulation with aerodynamic hinge moment (test B)
- Influence of the friction coefficient

---

[1] Obtained from SKF documentation

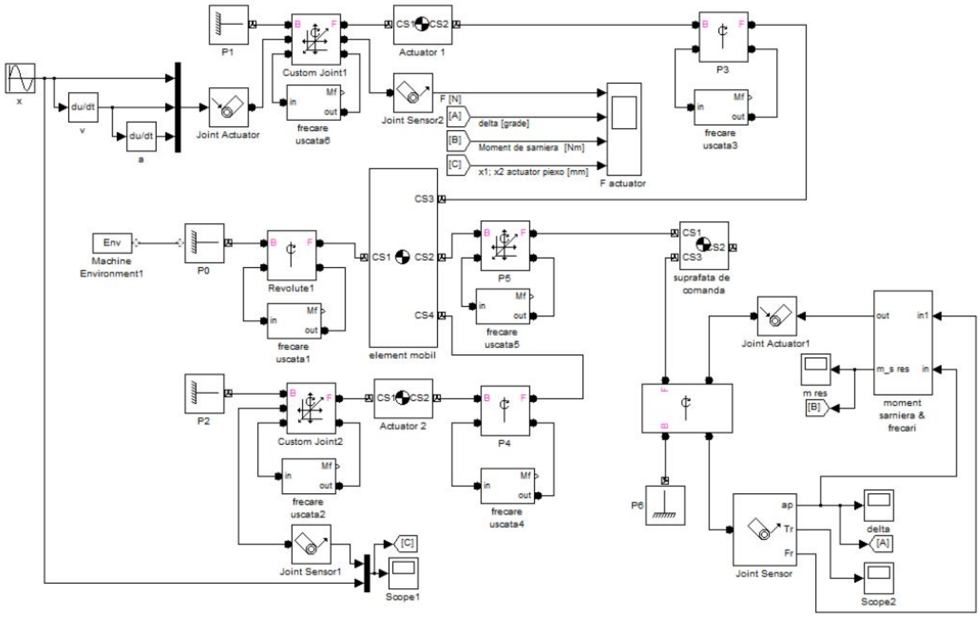

Figure 6.7: Diagram of the simulation block structure performed to analyze the dynamics of the proposed mechanism presented in Fig. 6.6.

- Influence of the position of the center of gravity of the aileron
- Dynamic simulation of an averaged case (test C)

The results of the simulations show that the required force by the actuator is approximately proportional to the square of the frequency at which the actuator operates. The most restrictive case is, then, the case in which the actuation frequency is $30Hz$. Considering only this restrictive case, the results in terms of the required actuation force are presented for the different simulations in Table 6.3. For the chosen design and according to the presented results, the piezoelectric actuator is capable of producing the required force for the actuation of the AFDPA system considering the presented operational restrictions.

Table 6.3: Results of the required force simulations for the preliminary piezoelectric amplifier mechanism performed in Matlab.

Freq.	**Test A**	**Test B**	**Test C**
5Hz	102	670	N/A
10Hz	260	835	940
15Hz	570	1100	1370
20Hz	980	1490	1970
25Hz	1512	1980	2750
30Hz	2160	2580	3700

The design concept is validated with the results of the simulations and a first 3D conceptual model can be done for the geometry of the selected piezoelectric actuators. The 3D design has been done using Catia V5 software and is presented in Fig. 6.8.

The piezoelectric actuators selected for acquisition are the following: Micromechatronics, Inc. MMech NAC2022 (Noliac plate actuator stack). The piezoelectric actuators are combined with piezoelectric drivers in order to provide an integrated solution for the actuation problem. Because the piezoelectric actuators operate at high voltages, the acquisition of an actuator is accompanied by the acquisition of an electric

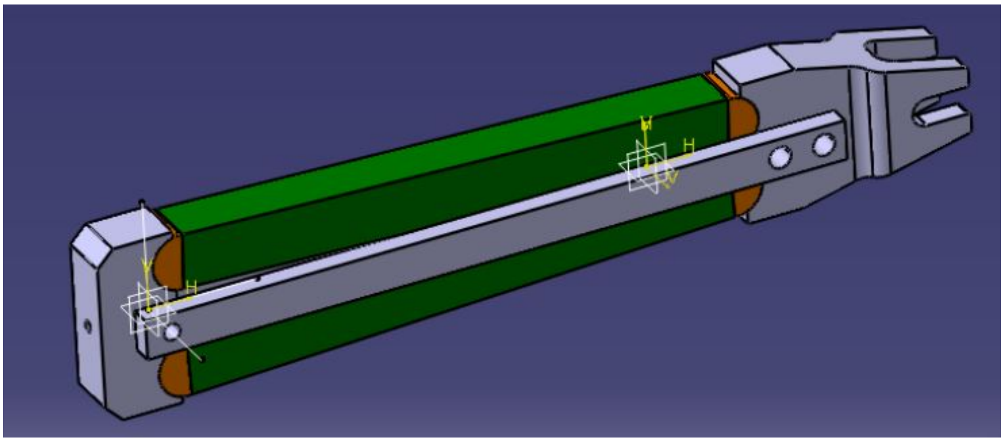

Figure 6.8: 3D conceptual model of the piezoelectric actuator tandem configuration and the mechanical amplification mechanism.

driver of the required power. The calculation of the power required is performed through the results of the performed simulations.

6.2.2 Detailed design and manufacturing

In terms of control synthesis, a preliminary characterization of the piezoelectric actuator is necessary before any control law can be designed. The characterization has been performed at the laboratory of the lead partner of the project INCAS. The actuator has been manufactured by one of the project partners (S.C. Energoreparatii Serv S.A.) and can be seen in Fig. 6.9. The tests performed are preliminary behavior determination tests that aim to verify the proper operation of the actuator and validate the mathematical model of the actuator.

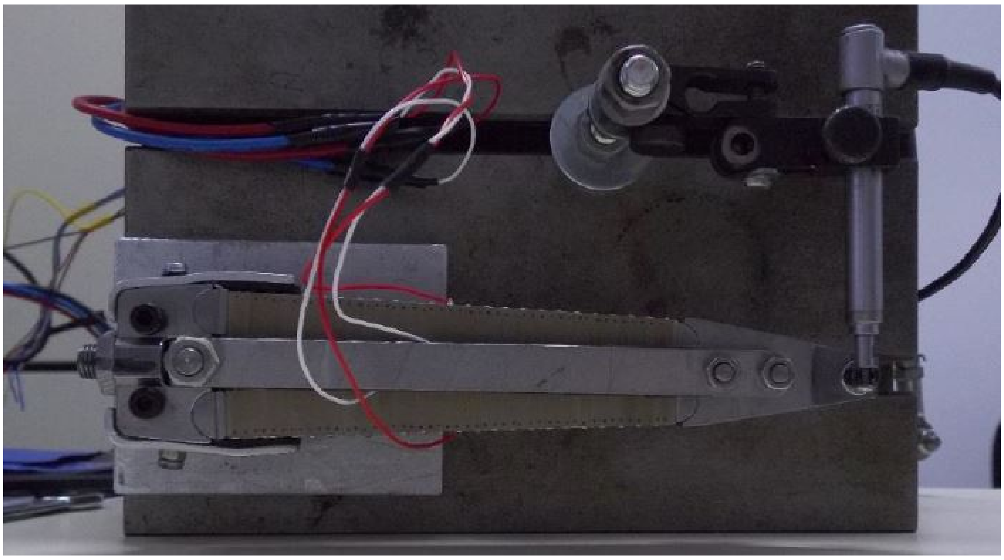

Figure 6.9: Setting of the piezoelectric actuator preliminary characterization experiments at the laboratory.

The testing consists in the actuation of the piezoelectric actuator and the monitoring of the electric parameters and the displacement output through a LVDT[2] sensor. The tests are performed without any external

---

[2] Linear Variable Differential Transformer. Precision of $1\mu m$ at a frequency of $50Hz$.

opposing force on the actuator to determine the cutout frequency of the actuator without loading. A second type of tests is designed to determine the maximum force and torque that the actuator is able to develop. After the bench tests, the mathematical model of the actuator has been developed as a control means through LabVIEW software (see Fig. 6.10).

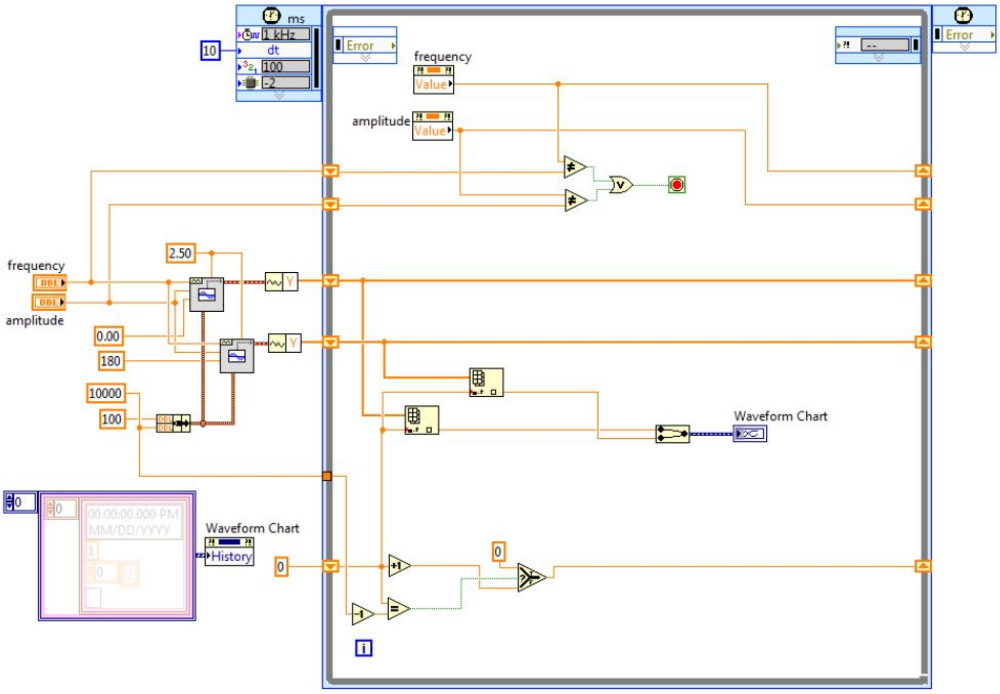

Figure 6.10: LabVIEW software model of the piezoelectric actuator system developed from the testing performed in work package 2.

The piezoelectric actuator characterization tests are continued with the synthesis of the control algorithm. The methodology used in the development of the control law is based on the receptance method. The receptance-based antifluter control algorithm implies the identification of the model while simultaneously determining the closed-loop amplification of the different sensors installed on the prototype. In the present case, the experimental model identification implies identifying the open-loop natural frequencies of the wing. In order to perform the development of the control system, given the unavailability of the prototype wing at this stage, the system shown in Fig. 6.11 has been used as an analogue system.

Figure 6.11: Equivalent system used in the development of the receptance-based control algorithm.

The used system has been a wing model mounted cantilever on the laboratory bench with two pairs of piezoelectric actuators attached to inner and outer surfaces close to the wing root. The actuators used have been of the type MFC (Macro Fiber Composite). An accelerometer has been used at the tip of the wing, in the vertical direction, as the vibration sensing system for the closed loop configuration. The system has a different actuator than the AFDPA system but the mathematical model is analogue for both systems.

The analysis of the natural frequencies of the laboratory specimen is done with frequency sweep signals that cover the interest frequency domain. A signal generator connected to a control computer generates a low power signal that is later amplified through a high voltage amplifier to the different actuators. In terms of sensing, the accelerometer registers the vibration of the structure and the signal is amplified through a pre-amplifier. The signal is later on processed by an oscilloscope.

In the determination of the natural frequencies both sweep and impulse signals are used. The natural frequencies obtained are the following: $21Hz$, $108Hz$ and $128Hz$ as can be seen in the spectrum diagram shown in Fig. 6.12.

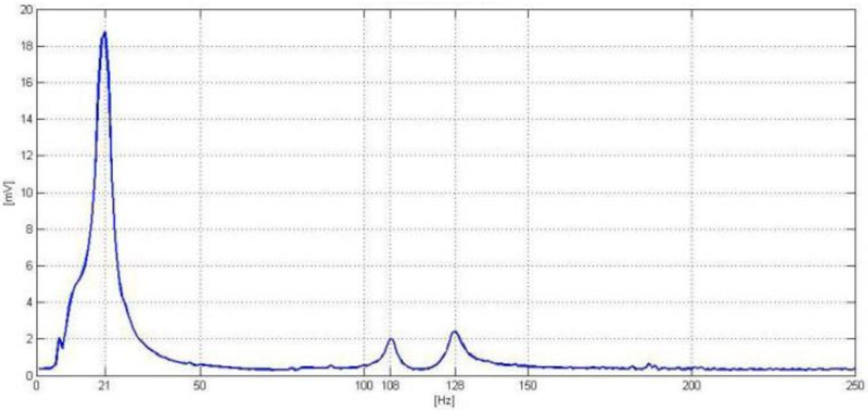

Figure 6.12: Frequency spectrum of the laboratory specimen.

The method consists of elaborating the control through laboratory measurements in progress, as opposed to theoretical calculations. Practically, the methodology implies measuring the frequency response of the structure, thus avoiding the calculation of the M, C, K matrices (mass, damping and elasticity) and B, C matrices (influence and measure). No order reduction is necessary on the model using this method nor any estimation of the non-measured states of the system. Theoretically, the control can be corrected and adjusted while the testing is performed thus increasing the anti-flutter performance and reducing the development time of the control system.

For a single input control case, the second order system model in the matrix form and in the Laplace space is shown in Eq. 6.3 where the control is expressed in $u(s)$ and its expression is shown in Eq. 6.4, $\mathbf{p}(s)$ represents the external perturbation matrix and $\mathbf{b}(s)$ the influence vector through which the control is expressed.

$$(\mathbf{M}s^2+\mathbf{C}s+\mathbf{K})\mathbf{x}(s)=\mathbf{b}(s)u(s)+\mathbf{p}(s) \tag{6.3}$$

$$u(s)=-(s\mathbf{f}+\mathbf{g})^T x \tag{6.4}$$

The closed-loop characteristic polynomial of the problem can be obtained as shown in Eq. 6.5 where $\mathbf{H}(s)$

represents the transfer function of the system defined as $\mathbf{H}(s) = (\mathbf{M}s^2 + \mathbf{C}s + \mathbf{K})^{-1}$. The pole allocation problem of the system with values $\{\mu_1\, \mu_2\, K\, \mu_{2n}\}$ can be solved. Let us note $\mathbf{r}_k(\mu_k) = \mathbf{H}(\mu_k)\mathbf{b}(\mu_k)$. The characteristic equation then becomes of the form shown in Eq. 6.6.

$$1 + (\mathbf{g} + s\mathbf{f})^T \mathbf{H}(s)\mathbf{b}(s) \tag{6.5}$$

$$\mathbf{r}_k^T(\mu_k) \times (\mathbf{g} + \mu_k \mathbf{f}) = -1,\ \ k = 1, K, 2n \tag{6.6}$$

The matrix representation of the system allows for the determination of **g** and **f** through Eq. 6.7. This relation is essential in the control synthesis through the receptance method.

$$\mathbf{G}\left(\frac{\mathbf{g}}{\mathbf{f}}\right) = \begin{pmatrix} -1 \\ -1 \\ M \\ -1 \end{pmatrix},\ G \begin{bmatrix} \mathbf{r}_1^T & \mu_1 \mathbf{r}_1^T \\ \mathbf{r}_2^T & \mu_2 \mathbf{r}_2^T \\ M & M \\ \mathbf{r}_{2n}^T & \mu_{2n} \mathbf{r}_{2n}^T \end{bmatrix} \tag{6.7}$$

During the preliminary design phase of the wing structure geometry, the shape of the spar changed significantly. The main reasons for the change are the optimization (decrease) of the natural frequencies and the simplification of the manufacturing process. The design presented significantly reduced the bending and torsional stiffness without compromising the structural integrity of the system and is shown in Fig. 6.13. The other significant change in the geometry of the wing involves the skin design. While in the conceptual model, though not structural, the skin was continuous, in the redesigned model the skin is considered in segments along the span. This allows for a significantly reduced torsional natural frequency which drastically reduces the velocity at which the wing encounters flutter phenomena. Moreover, the skin elements increase the mass of the wing without a significant modification of the stiffness, this further reduces the values of the natural vibration frequencies, tightly related to the ratio between stiffness and mass. [125]

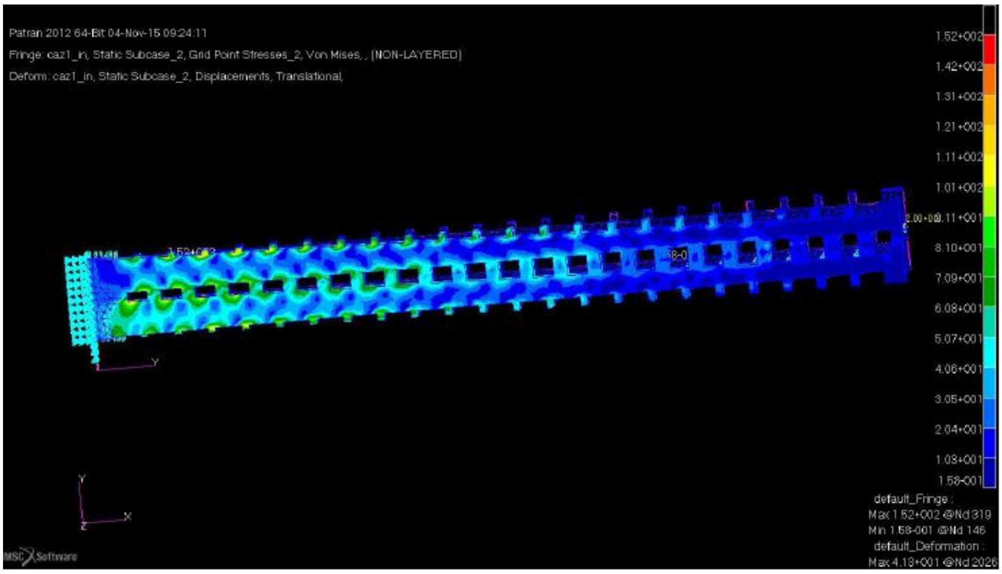

Figure 6.13: Redesigned wing spar and simulation on the static stress field during normal operation.

The validation of the preliminary design is offered by the aeroelastic calculations that certify the flutter apparition of the wing within the wind tunnel operational range. This validation has been performed through a custom made software tailored to this specific problem. The software is called Aeroel (222SG5) and allows for the determination of the aerodynamic forces for stationary and transient conditions.

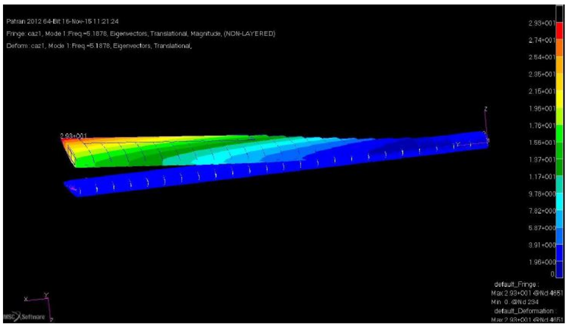

Figure 6.14: 1^{st} vibration mode of the redesigned wing structure.

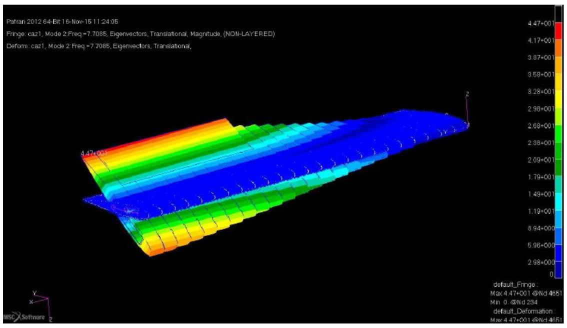

Figure 6.15: 2^{nd} vibration mode of the redesigned wing structure.

As part of the input data for the Aeroel calculations, the natural frequencies are analyzed through Patran-Nastran software. The first and second natural vibration frequencies for the condition of no flow around the wing are presented in Fig. 6.14 and Fig. 6.15 respectively. The calculation considered the aluminum redesigned spar and the skin elements not interconnected and machined out of wood. Higher order natural frequencies do not directly influence the flutter apparition so are not presented in the report even though they have been calculated during the simulations.

The validation of the structural numerical simulations is performed through laboratory testing of a first manufactured prototype. The tests consist of impulse excitation analysis. The wing has been instrumented with two low-frequency accelerometers and excited through an impact hammer impulse. The structure is then let vibrate naturally; the resulting vibration is a superposition of all the vibration modes of the structure which can then be isolated through the post-processing of the accelerometer signals. [126]

The general arrangement used in the wing spar vibration tests is shown in Fig. 6.16. The configuration tested has been chosen as a cantilever configuration with the spar in the vertical direction. This configuration presents two main advantages: the bending and torsional deformations, which are the most significant effects to be considered in the flutter analysis, are not influenced by the gravitational field and the test arrangement is analogue to the configuration to be used during the wind tunnel testing.

The laboratory equipment used includes 2 charge accelerometers, a signal conditioner, a data acquisition board (HBM Spider 8) and a data acquisition software (HBM Catman 5.0). The configuration of the accelerometers used has been modified in each test to capture different modes of vibration[3]. The position of the accelerometers is shown in Fig. 6.17 for a configuration optimized to capture the 2^{nd} bending and the 1^{st} lagging modes of vibration. The isolated modes of vibration and their respective frequencies for the tests performed is shown in Table 6.4.

The results obtained in the first batch of experiments shows a deviation of the simulations towards lower frequencies and a distinct order in the apparition of the natural modes of vibration. In order to adapt the tests closer to the real model to be build, the mass of the piezoelectric actuator assembly is simulated at

---

[3] Depending on the natural vibration mode shape, some of the modes may not be captured from all the points in the structure. The points in the structure that are not excited by a particular mode of vibration are called nodal points of the respective mode of vibration. [127]

Figure 6.16: General arrangement of the wing spar vibration tests.

the tip of the spar. The test results for the second batch with the piezoelectric equivalent mass (also shown in Table 6.4) are very close to the simulations thus validating the suitability of the numerical simulations in the aeroelastic calculations.

With the validation of the laboratory experiments for the numerical simulations of the dynamic behavior of the wing structure, the aeroelastic calculations can be performed. The Aeroel software has been checked throughout its development with various theoretical and experimental problems available in the literature that present a well known and corroborated solution. With the confidence that the software produces coherent results the calculations on the aeroelastic performance of the designed wing are done in the following situations:

- Binary flutter model with stationary aerodynamic forces
- Binary flutter model with non-stationary aerodynamic forces (Theodorsen model)

Figure 6.17: Detail of the positioning of the accelerometers for one of the tested configurations.

- Binary flutter model with non-stationary forces considering the wing as a rectangular plate fixed on one end
- Tridimensional flutter model with non-stationary aerodynamic forces

The results obtained all show close results in terms of calculated velocities for flutter apparition and divergence of the structure. The hypotheses considered in the aeroelastic calculations are in line with the ones used in the structural numerical simulations in the fact that the wooden aerodynamic elements are considered not to influence the stiffness of the structure and the gaps between them have been considered negligible. The averaged results are the following:

- **Flutter velocity:** $17-21m/s$
- **Divergence velocity:** $47m/s$

It is very significant to note two aspects in the obtained averaged results: that the flutter velocity has reduced in comparison to the calculated in the conceptual design of the system and that the divergence velocity is significantly higher than the flutter velocity and out of range of the wind tunnel characteristics. These conclusions are very welcome in the present project: a lower flutter velocity is easier to attain thus simplifying the testing and reducing the uncertainty level of the experiments and a clear separation between flutter and divergence velocities ensures that no coupling exists between the phenomena during testing.

6.2.3 Preliminary testing of the complete system

The manufacturing of the system presents several challenges regarding the condition of dynamic similarity with the laboratory specimen used for the spar ground vibration tests (see Sec. 6.2.2) and the integration

Table 6.4: Isolated natural vibration modes and respective frequencies for each of the impact hammer experiments performed on the redesigned wing spar structure without (Tests 1-12) and with (Tests 13-15) piezoelectric actuator equivalent mass.

	1^{st} **Mode** 1^{st} **Bending**	2^{nd} **Mode** 2^{nd} **Bending**	3^{rd} **Mode** 1^{st} **Torsion**	4^{th} **Mode** 1^{st} **Lagging**	5^{th} **Mode** 3^{rd} **Bending**
Test 1	$12.78Hz$	$43.31Hz$			$81.79Hz$
Test 2	$12.78Hz$	$43.31Hz$			$81.77Hz$
Test 3	$12.74Hz$	$43.35Hz$	$44.96Hz$		$81.59Hz$
Test 4	$12.74Hz$	$43.39Hz$	$45.55Hz$		$81.66Hz$
Test 5	$12.74Hz$	$43.28Hz$	$46.54Hz$		$81.84Hz$
Test 6	$12.74Hz$	$43.28Hz$			$81.84Hz$
Test 7	$13.00Hz$	$43.61Hz$	$46.65Hz$		$81.50Hz$
Test 8			$46.65Hz$		
Test 9				$60.05Hz$	
Test 10				$60.01Hz$	
Test 11				$60.05Hz$	
Test 12	$12.96Hz$	$43.86Hz$			$81.25Hz$
	1^{st} **Mode** 1^{st} **Bending**	2^{nd} **Mode** 1^{st} **Torsion**	3^{rd} **Mode** 1^{st} **Lagging**	4^{th} **Mode** 2^{nd} **Bending**	5^{th} **Mode** 3^{rd} **Bending**
Test 13	$7.58Hz$			$35.63Hz$	$71.40Hz$
Test 14	$7.58Hz$	$29.29Hz$		$35.55Hz$	
Test 15			$33.76Hz$		

of the piezoelectric actuator among others. The design for manufacturing of the components that are not manufactured as part of previous activities (i.e. spar manufacturing or actuator mechanism manufacturing and integration) is also presented in this activity.

A new spar has been manufactured to ensure that the manufactured AFDPA system is not compromised structurally. The spar previously manufactured and used in the ground vibration testing phase is not used in the first prototype of the assembled system because there is no guarantee that the structure did not suffer any damage during testing. The newly manufactured spar presents the added difficulty that its dynamic behavior needs to be as close as possible to the ground testing specimen to ensure that the calculation model is still valid.

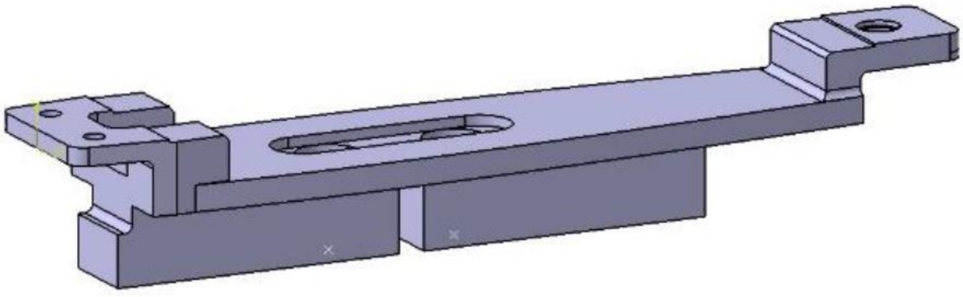

Figure 6.18: Interface plates designed to integrate the aileron and piezoelectric actuator into the wing structure.

The manufactured wing presents an important challenge in the integration of the piezoelectric actuation system in the structure. Two interfaces have been designed as shown in Fig. 6.18 and mounted at the ends of the aileron. The interface at the wingtip is used as the mounting point for the actuator as shown in Fig.

6.19. A third interface is used to support the wing root into the wind tunnel. The design of this last interface has not suffered any changes from the preliminary design stage and its concept is validated through the spar vibration tests conducted.

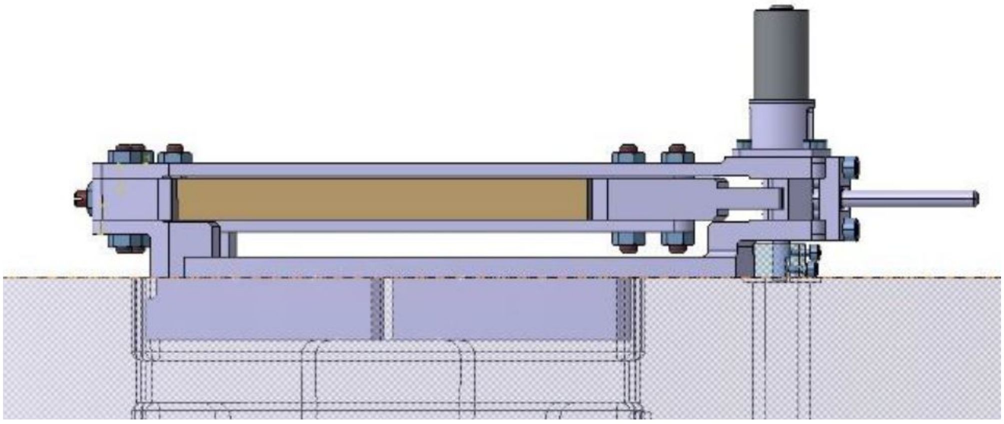

Figure 6.19: Integration of the piezoelectric actuator in the wingtip aileron interface plate.

A significant modification in the manufacturing technology from the preliminary design is the construction technology for the aileron. The aileron (designed in wood in the preliminary design) has been redesigned and manufactured in CFRP (Carbon Fiber Reinforced Plastic) laminate. This technology presents a significant saving in weight which drastically reduces the loading on the piezoelectric actuator. The dependence between the required force of the actuator and the weight of the aileron is studied in Sec. 6.2.1.

The static checks comprise the final verification of the manufactured structure to ensure that it can withstand the loading of the flutter testing in the wind tunnel. The performed tests include the verification of the natural frequencies of the structure in order to validate the final structural simulations of the system, the functional testing of the actuator to ensure that no damage is sustained during the vibration tests and the refinement of the control laws developed in Sec. 6.2.2 adapting them to the manufactured wing mounted in an out-of-wind-tunnel stand.

The validation harmonic testing aims at the precise determination of the natural vibration frequencies of the structure in a configuration as close as possible to the wind tunnel arrangement in a no-loading configuration. The tested wing includes all the elements necessary in the normal operation of the AFDPA system. The testing used the same testing procedure and measuring equipment as presented in Sec. 6.2.2. The arrangement of the tests can be seen in Fig. 6.20. Note the root interface is used during the test to provide a boundary condition as close as possible to the one to be used during wind tunnel testing.

The testing has been performed in two different configurations: with free aileron and with the aileron blocked. In order not to damage the piezoelectric actuator, the mechanical link between actuator and aileron has been interrupted during the vibration testing. This modification introduces a small uncertainty during testing because the dynamic behavior of the actuator is not present during the experiments. In order to better simulate the conditions of the vibration in flutter testing two different configurations are used: one in which the aileron can be moved freely and one in which the aileron is rigidly attached to the wingtip interface plane. The behavior of the piezoelectric actuator linked to the aileron falls between these two conditions so the qualification of the structure in these conditions is a good hypothesis for the real behavior of the system with the coupled actuator. The results of the testing are presented in Table 6.5 and an example of the post-processing of the results shown in Fig. 6.21. The effect of the condition of the aileron on the

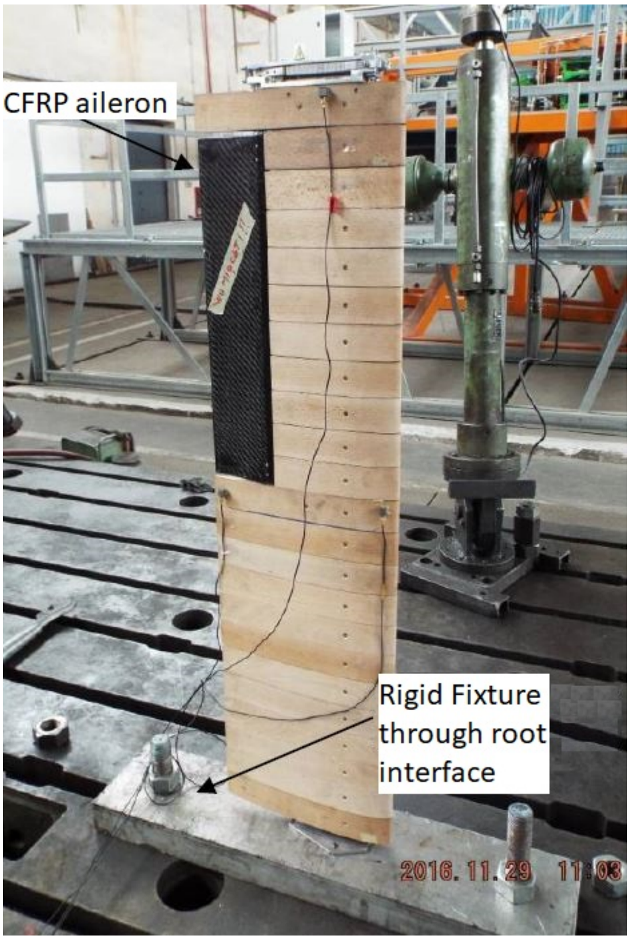

Figure 6.20: General arrangement of the vibration validation testing performed before wind tunnel testing.

bending frequency is negligible while the change in the torsional mode is small. The results of the testing validate the results of the numerical modeling thus qualifying the wing for further testing from the dynamic point of view.

Table 6.5: Results of the vibration testing on the integrated AFDPA system for the configuration with the aileron free and fixed.

	Bending Mode	**Torsion Mode**
Free aileron	$6.37Hz$	$14.94Hz$
Fixed aileron	$6.37Hz$	$16.63Hz$

The implementation of the control law developed on the laboratory specimen in Sec. 6.2.2 can be done on the AFDPA system prototype. This procedure ensures that the piezoelectric actuator is responding as designed and the sensing and control loop performs as expected.

One of the chosen methods for the anti-flutter control system within the AFDPA project is the pole allocation method through the receptance method. The preliminary results obtained through this method in the laboratory tests are presented in Sec. 6.2.2. This section presents the adaptation of the obtained control law to the manufactured prototype. The tests have been conducted at the Mechatronics laboratory of INCAS using the wing specimen. The scope of these tests is to validate the control methodology prior to wind tunnel testing.

The receptance method in active control of elastic structures is developed to avoid analytic models which

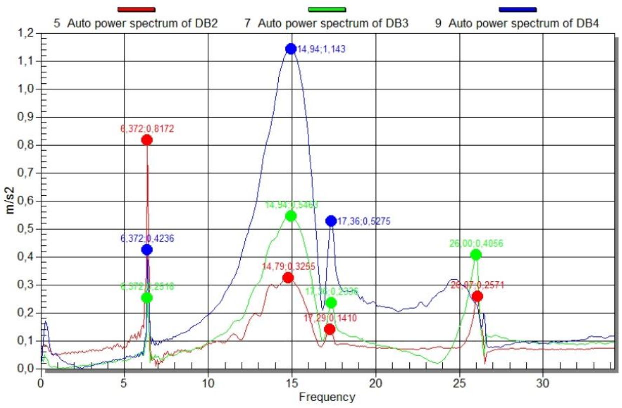

Figure 6.21: Power spectrum results obtained in the ground vibration testing of the fixed aileron configuration through HBM Catman software post-processing of the acceleration data.

need to be obtained through analysis techniques such as FEM. The main advantage of this methodology is the utilization of experimental data instead of mass, damping and elasticity matrices. Likewise, the damping of the structure is considered through an experimentally measured modal data set. The acquired data leads to the control law parameters in a way in which state-space allocation and estimation of non-measured states are not required thus simplifying the control development process. The application of the receptance method involves the proper determination of the receptance matrices: the transfer functions between the control variable and the measured output parameter.

In the present case, the measured output parameter is the displacement of the wingtip which has been indirectly measured through an accelerometer and the related sensing equipment. The steps in the pole allocation process are the following:

1. **Experimental data recording and determination of the frequency response function in open-loop configuration**

   The experimental test specimen has been excited with a chirp-time signal with a 10 second length sweeping linearly frequencies from $0.001Hz$ to $200Hz$ and with an amplitude of $400V$. The limits of the signal in terms of frequency have been established considering that the natural vibration frequencies of interest are well within the considered range. The sampling frequency has been considered at $1000Hz$, verifying the Nyquist criteria for the highest input signal frequency. The response of the prototype wing to the chirp excitation is shown in Fig. 6.22 as acquired by the data acquisition system and after being post-processed.

   The frequency response has been experimentally measured and determined using the MatLab system Identification Toolbox function (etfe). This function calculates the discrete Fourier transformation of two signals (u and y) and determines the transfer function as the ratio between the output Fourier transformation and the input Fourier transfer function. The calculation is performed in the frequency domain and for a sampling frequency that verifies the Nyquist criteria. The results of this calculation determine the behavior of the system and are shown in Fig. 6.23 for the absolute value of the FRF. The real and imaginary parts of the FRF are shown in Fig. 6.24 and Fig. 6.25 respectively.

   The analysis of the results of the MatLab calculation shows a pseudo-resonance at the frequency of $1Hz$. The amplitude-frequency characteristics of this resonance are the ones of a double integrator which can be a product of the spectrum capturing not only the dynamic system but all the measurement chain. As the measurement chain contains a double integrator in the processing of

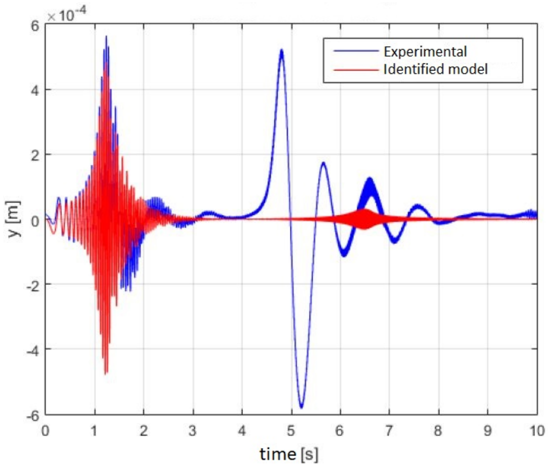

Figure 6.22: System response to the chirp excitation.

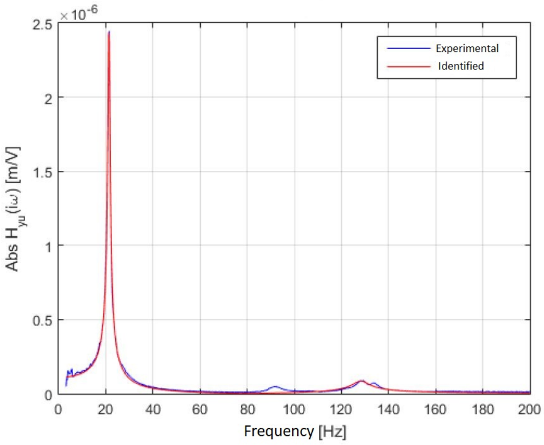

Figure 6.23: Absolute value of the system FRF.

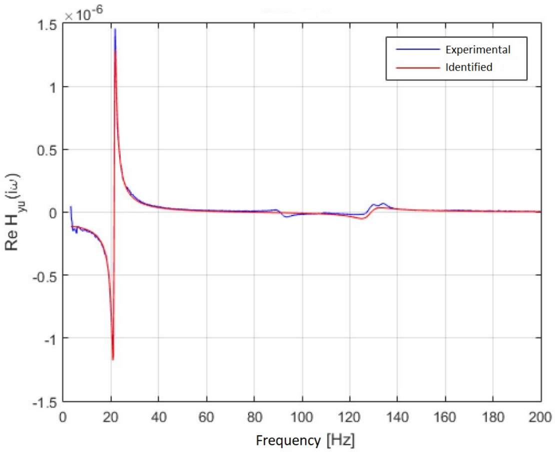

Figure 6.24: Real part of the open-loop FRF.

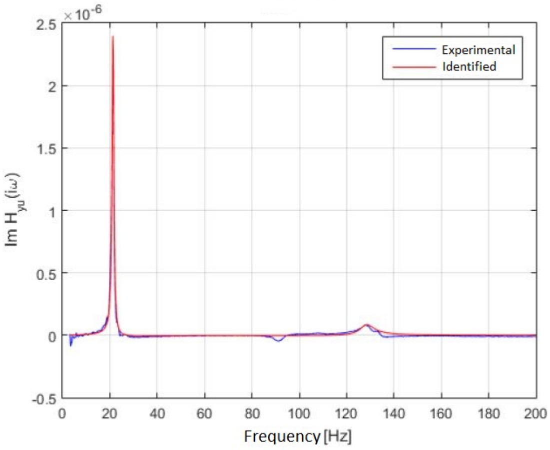

Figure 6.25: Imaginary part of the open-loop FRF.

the accelerator signal, such processing causes the pseudo-resonance that does not correspond to a dynamic behavior of the wing specimen. As this pseudo-resonance disrupts the control law that is to be obtained from the transfer function, the interest domain is changed to $3-200Hz$.

The analysis of the rest of the spectrum $(3-200Hz)$ shows the resonance frequencies at $21.5Hz$, at $92Hz$, at $128.4Hz$ and at $133.8Hz$. Because of the particular interest that the first resonance frequency presents in the present problem, manual fine tuning has been used to determine more accurately the frequency at which the resonance occurs. This methodology determined the first resonance frequency at $21.3Hz$.

2. **Identification of the transfer function in open-loop and calculation of the frequency response**
The identification of the transfer function consists in establishing the number of poles and zeros and the determination of the numerator and denominator coefficients in a way in which the response matches as close as possible the experimental frequency response of the system. As mentioned, this has been done through the "$etfe$" function of MatLab and the results presented in the images under point 1 of this process.

From the experiments performed, it is established that a function with 4 poles and 2 zeros approximates properly the first 2 resonance frequencies behavior. The expression of this transfer function is presented in Eq. 6.8 and the coefficients present the values shown in Table 6.6.

$$H_{yu}(s) = \frac{b_2 s^2 + b_1 s + b_0}{s^4 + a_3 s^3 + a_2 s^2 + a_1 s + a_0} \tag{6.8}$$

Table 6.6: Values for the coefficients of the correlated transfer function of the prototype wing.

b_0	-1286.223
b_1	0.4461
b_2	5164×10^{-2}
a_0	$1.1685147884 \times 10^{10}$
a_1	4547234.6774
a_2	667560.9391
a_3	54.4176

The identification precision of the transfer function, as obtained with MatLab function *tfest* (fit to estimation data), has been $87,4\%$ which is a close approximation to the behavior of the system in the domain of interest. The behavior of the structure is compared with the real and imaginary parts of the correlated transfer function in Fig. 6.24 and Fig. 6.25 where the identified transfer function is presented in the red line.

3. **Pole allocation with receptance method**
   The pole allocation method through the receptance method is performed for the case in which the system is excited at the input with a perturbation of the frequency of the dominant vibration frequency of the structure. In these conditions, the modes of the model represented by the transfer function $H_{yu}(s)$ shown in Eq. 6.8 are the following:

   (a) Mode 1:

   - Corresponding poles of the transfer function: $p_{1,2} = -2.8258 \pm 134.1266i$
   - Resonance frequency: $f_1 = 21.35Hz$
   - Damping factor: $\zeta_1 = 0.021$

   (b) Mode 2:

   - Corresponding poles of the transfer function: $p_{3,4} = -24.383 \pm 805.41i$
   - Resonance frequency: $f_2 = 128.24Hz$
   - Damping factor: $\zeta_2 = 0.03$

   In order to attenuate the dominant mode of vibration (mode 1), the damping needs to be increased to a value of $\zeta_1^0 = 0.0855$. When effectuating this change, the poles change to the following values:

$$p_{1,2}^0 = -11.47 \pm 133.66i$$

The amplification factors for the control law in closed-loop configuration ($u = K_p y + K_v$), which allocates the modified poles through the receptance method, result from Eq. 6.9.

$$\begin{bmatrix} H_{yu}(p_1^0) & p_1^0 H_{yu}(p_1^0) \\ H_{yu}(p_2^0) & p_2^0 H_{yu}(p_2^0) \end{bmatrix} \begin{bmatrix} K_p \\ K_v \end{bmatrix} = \begin{bmatrix} -1 \\ -1 \end{bmatrix} \tag{6.9}$$

The amplification factors resulting from the solution of the equation are $K_p = -83171$ and $K_v = 9000$. It is important to note, though, that the pole allocation allows for the exact location for the poles of the considered mode; the poles of the other modes are also modified. The poles and parameters characterizing the second vibration mode are verified as follows:

- Corresponding poles of the transfer function: $p_{3,4} = -39 \pm 801i$
- Resonance frequency: $f_2 = 127.65Hz$
- Damping factor: $\zeta_2 = 0.048$

Through the used model, the dynamic characteristics for the second mode have also improved, deeming the modification positive for the control of the considered system.

4. **Pole allocation verification through the receptance method**

   Considering the previous pole allocation method, the verification of the obtained solution is done through the experimental identification of the transfer function in the closed-loop system. This implies implementing the control law and applying the first steps in the method. In this case, though, the used input signal amplitude has been $200V$.

   After the validation testing, a conclusion has been reached that a transfer function with 4 poles and 1 zero describes better the behavior of the system than the function previously used. The newly identified transfer function is presented in Eq. 6.10 with the values presented in Table 6.7.

$$H_{yu}(s) = \frac{b_1 s + b_0}{s^4 + a_3 s^3 + a_2 s^2 + a_1 s + a_0} \tag{6.10}$$

Table 6.7: Values for the coefficients of the recalculated transfer function of the prototype wing.

b_0	-935.58
b_1	-0.49021
a_0	$1.3163945324 \times 10^{10}$
a_1	20323037
a_2	744006
a_3	40.15

After this adaptation and validation of the control law for the AFDPA system the prototype is operating nominally in terms of the actuation and control system. Also, the structural integrity of the wing has been verified.

Numerical simulations have been performed in order to determine the pressure and velocity fields around the wing in the non-stationary flow characteristic of the flutter phenomenon. These simulations are the validation of the flutter prediction model developed throughout the activities in Sec. 6.2.2 and Sec. 6.2.3. The CFD simulations require extensive input information to be defined for its results to be accurate: model geometry, elastic information and control dynamics. This information has been previously calculated and defined in previous sections and validated in the testing prototype.

The CFD simulations performed considered the 3D wing geometry split into two domains in order to perform separate meshes of these domains with different levels of refinement. The domains used are shown in Fig. 6.26. The outer domain is shown on the left and represents the wind tunnel test section, the element size in this area is coarse while the elements in the inner cylinder, modeling the vicinity of the wing geometry,

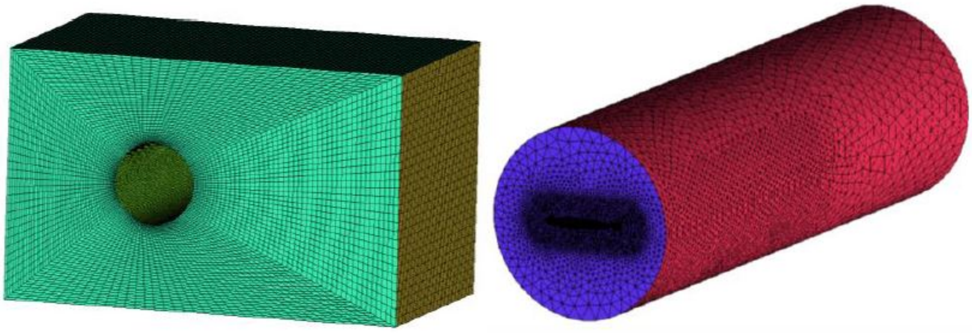

Figure 6.26: Mesh domains used in the CFD simulations of the AFDPA wing.

are significantly more refined. This compound geometry allows for the simulation of the wing in different angles of attack without modification of the wing and reduces the required computational power through the reduction of the number of elements modeled.

The boundary conditions used in the model are the following:

- Inlet air velocity: $41 m/s$
- Outlet pressure: $101325 Pa$
- The wind tunnel walls are considered without drag

According to these conditions the simulations have been performed using a second order upwind discretization scheme and a DES (Detached Eddy Simulation) as turbulence model. The results of the flow simulations are presented in Fig. 6.27 and Fig. 6.28 for the velocity field and in Fig. 6.29 and Fig. 6.30 for the pressure distribution.

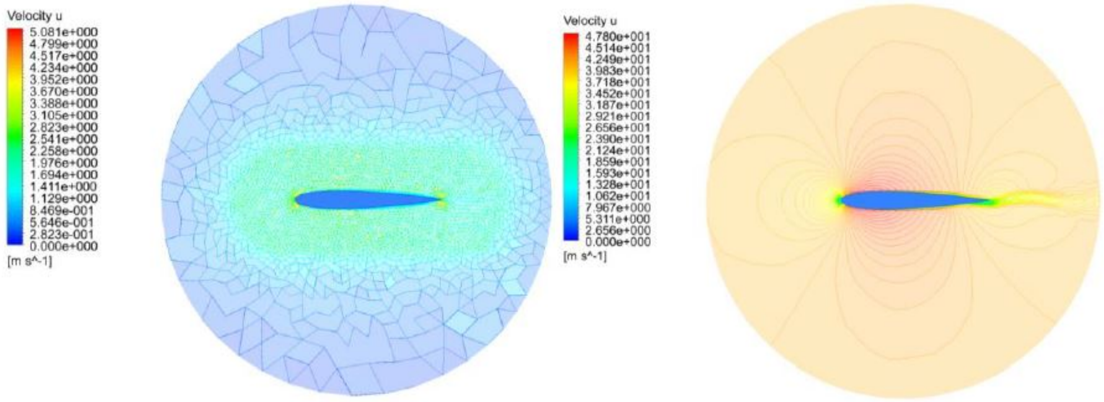

Figure 6.27: Velocity contours at the wing root and at a middle section inboard of the aileron.

It is relevant to note that due to the high aspect ratio of the wing and the symmetric wing profile, Von Karman vortexes [128] appear close to the root of the wing. These vortexes are transient and alternating and produce an oscillating force that helps initiate the flutter phenomenon without any external input. This effect can be seen at the wake of the profile in the sections that are far enough from the wing root not to be influenced by the boundary layer of the ground but also far enough from the wingtip so the outboard and

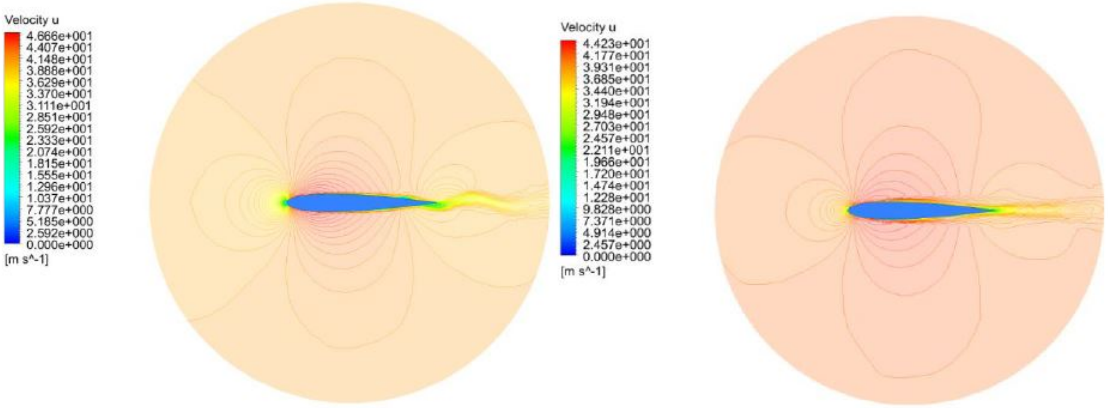

Figure 6.28: Velocity contours at a section outboard of the aileron and at the wingtip.

inboard surfaces of the wing profile can be considered isolated in terms of pressure. The phenomenon is seen with most intensity in the section outboard of the aileron as seen in Fig. 6.28. Apart from the Von Karman vortexes, the flow behaves symmetrically around the wing as expected in any symmetrical profile at a zero incidence angle.

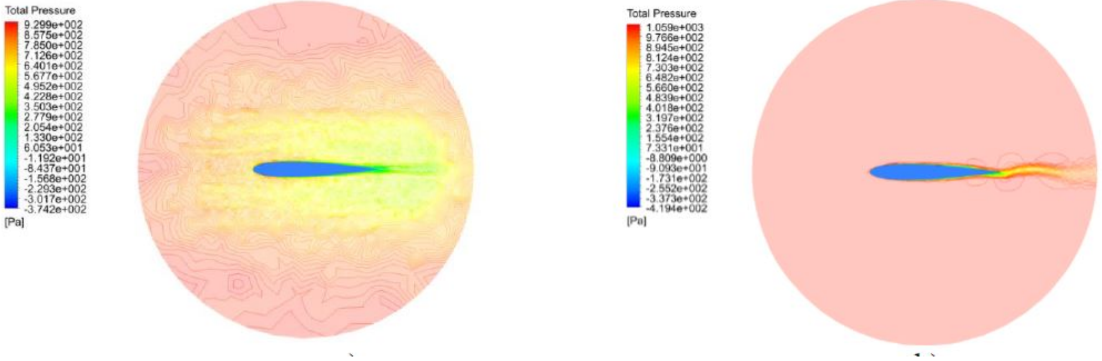

Figure 6.29: Pressure distribution at the wing root and at a middle section inboard of the aileron.

In the analysis of the pressure field results the same phenomenology can be observed as with the velocity analysis. The Von Karman vortex street at the trailing edge of the profile is strongest at the section where it is most intense in terms of velocity also. Apart from this effect, the area of influence of the ground boundary layer can be seen in the section close to the root (see Fig. 6.29) as a turbulent region. Note that the interference between the ground boundary layer and the profile local pressure field produces a higher intensity turbulent region close to the profile (seen in yellow tone in the figure). Any phenomenology occurring in this area is very hard to predict because of the high-intensity turbulence.

On the rest of the regions throughout the spar, no significant degree of turbulence is to be expected outside of the wake and the boundary layer areas. In these areas, the turbulence model used in the calculations is able to predict to a good extent the phenomenology involved. Because of this the numerical results present a significant reliability that certifies that the built prototype will not encounter any aerodynamic disturbance before reaching the flutter condition and no interference exist between the wing and other elements of the testing environment.

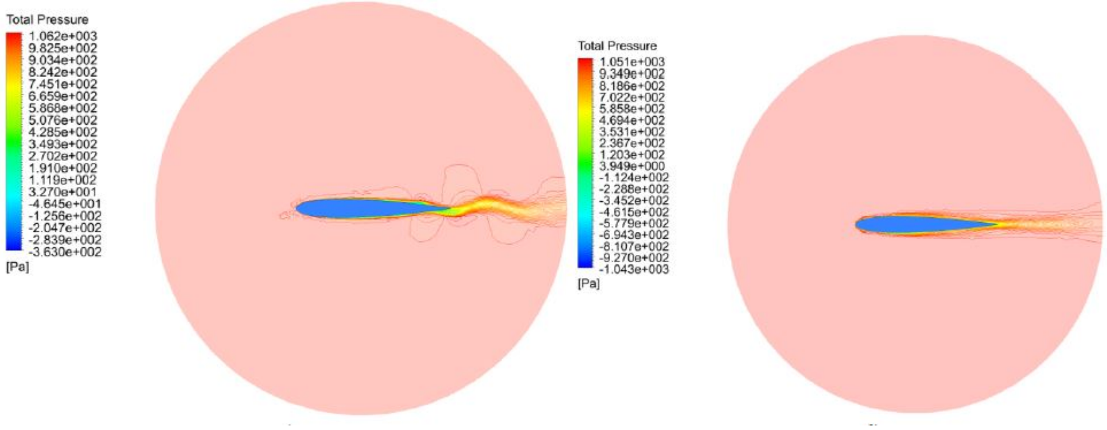

Figure 6.30: Pressure distribution at a section outboard of the aileron and at the wingtip.

6.2.4 Final systems testing

The experimental validation of the performance of the AFDPA system has been performed in the subsonic wind tunnel within INCAS facilities. The wind tunnel presents restrictions in terms of maximum speed it can simulate and cross-section dimensions of the test section. These restrictions have already been considered during the conceptual and preliminary design of the hardware part of the system.

Initial considerations in wind tunnel testing operation prior to the experimental part, even though included in previous stages of the project, are presented in this section in order to provide a more comprehensive understanding of the testing phase. An important operational consideration during the design of the system, which has direct implications on the design, is the safety measures of the wing in case a structural failure occurs during testing. It is important to ensure that, in such case, all the components of the system remain contained so they do not fly off to the wind tunnel fan. In order to ensure this requirement, the wing spar is fit with a kevlar wire that runs along its span ensuring that in case of structure failure the different elements integrating the structure remain attached. Another important operational consideration is the capacity of the system to develop flutter within the wind tunnel operational range; this has been considered as a design objective throughout the project.

The system is set vertically on the wind tunnel test section as shown in Fig. 6.31 and mounted through the wing root interface which can be seen in Fig. 6.16 in the wind tunnel balance, which is located under the wind tunnel test section floor. The instrumentation of the system consisted of two accelerometers positioned at the tip section of the wing in the horizontal direction, perpendicular to the airflow in such manner throughout the chord o the wing so the first bending and first torsional modes can be properly identified. The control of the piezoelectric actuator uses the input data from the accelerometers in the control loop.

The experiments in the wind tunnel are divided in two main subcategories, having different objectives and presenting different setups in terms of the equipment used in each test:

- **Aeroelastic behavior validation tests:**
  A preliminary set of experiments is performed in which the control is not powered to determine the flutter velocity of the produced wing. In this configuration, as the control is not active, the appropriation to the flutter point needs to be very careful and progressive so the structure is not damaged during

Figure 6.31: Positioning of the AFDPA system in INCAS's subsonic wind tunnel.

the testing. At the point of flutter apparition the experiment needs to cease immediately.

- **Aeroelastic vibration attenuation experiments:**
  These experiments are the validation of the proper functioning of the AFDPA system. They are meant to ensure that given an external perturbation of the system which results in the starting point of flutter phenomenon the amplitude of the resulting motion can be controlled and attenuated with the control system. The validation is done in three steps:

  1. Root locus: is performed for different velocities ($5m/s$, $10m/s$,..., $25m/s$) through the identification of the transfer functions. The analysis of the imaginary part of the transfer functions allows for the determination of the evolution of the instability (the resonance occurs when the imaginary part of the transfer function reaches 0).
  2. Closed loop: wind tunnel tests in closed-loop control configuration are performed in which the wing is subject to airspeed higher than the experimentally determined flutter point. The capacity of the system to attenuate vibrations and stabilize the structure past the flutter velocity is studied.
  3. Optimization: low and high-frequency filtering is used to minimize sample rate effects and to eliminate accelerometer bias respectively in order to increase the obtained performance of the system.

The identification of the transfer functions in open loop configuration (seen in Fig. 6.32 and Fig. 6.33 for the absolute value and the phase respectively) allowed for the determination of the vibration frequencies and the modal parameters. According to the control law developed during the bench testing of the wing, the poles have been allocated in the open loop configuration so the damping factor of the bending frequency is

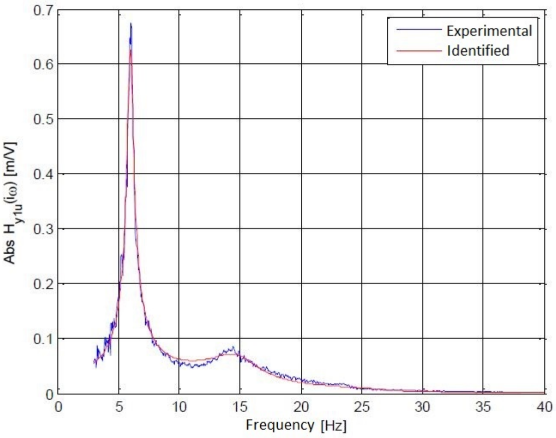

Figure 6.32: Open loop FTF magnitude.

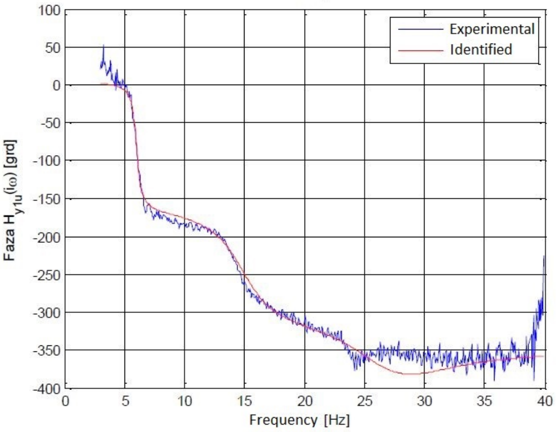

Figure 6.33: Open loop FTF phase.

doubled and the resonance value for the torsional frequency increases with $2Hz$. The obtained values for the poles are the following:

$$\begin{array}{c} -0.03369 \pm 0.37630i \\ -0.15168 \pm 1.05517i \end{array} \tag{6.11}$$

The root locus law for the poles selected is shown in Eq. 6.12 where y_1 and y_2 are the measured response of the accelerometers and the factors K_n are the amplification parameters as follows: $K_1 = 13.5530$, $K_2 = -12.6195$, $K_3 = -0.0228$ and $K_4 = -0.0787$.

$$u = K_1 y_1 + K_2 y_2 + K_3 \dot{y}_1 + K_4 \dot{y}_2 \tag{6.12}$$

With the presented closed loop control law, the experiments performed in an open loop configuration have been repeated. In this new configuration, the performance of the system presents a significant improvement in terms of damping the external perturbations. This capability is shown as the capacity to reduce the amplitude of the vibration in the areas close to resonance modes of the structure as can be seen in Fig. 6.34. The graphic presents the results of the FTF for one of the accelerometers; the results for the second accelerometer are analogue to the ones presented.

The difference between the open-loop and closed-loop control is very clear in the low-frequency band. That is precisely the interest of the control because flutter phenomenon, as well as most aeroelastic phenomena, occur in such area. It is significant to evaluate also the evolution of the magnitude of the transfer functions of the system in the closed loop configuration for the different velocities. Such analysis is important because it presents the evolution of the control capacity of the system as a function of airspeed. The analysis is presented in Fig. 6.35.

Two different phenomena are expected to show in the analysis: the low amplitude of the resonance at low speed and the high controllability of the system at high speeds. At low speeds the dynamic forces actuating on the wing are of low intensity because they are roughly proportional to the square of the velocity; the magnitude of the resonance amplitude is hence expected to be low. At higher airspeed, the forces actuating on the wing are higher but such is the aileron force. As the aileron is designed to control the dynamic

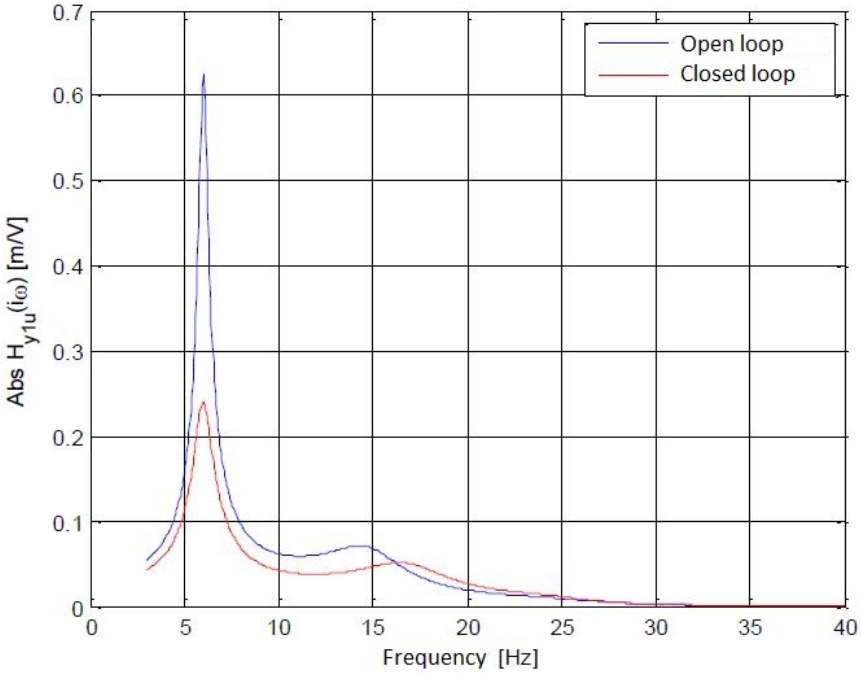

Figure 6.34: Comparison of the FRF magnitude for open and closed-loop control.

behavior of the wing, the control capacity of the aileron is greater than the perturbation forces on the wing, hence the high controllability. Both phenomena combined explain the increase and then decrease of FTF amplitude in Fig. 6.35 as the air velocity increases.

The fact that the high controllability phase is reached before the flutter velocity is confirmation that the phenomenon can be controlled and the associated perturbations damped.

The dissemination of the project is an important part in any research project together with the analysis on the completion of the goals of the project as defined in the objectives at the stage of the project proposal (Sec. 6.1.1). Different means have been foreseen in the dissemination of the research performed and the results obtained to provide visibility on the original contributions of the project.

The completion of the project is evaluated through the level of completion of the proposed objectives through the activities performed in each of the project four stages:

The first stage of the project obtained several results concerning the objectives regarding prediction methodology for the anti-flutter system as well as the preliminary definition of the characteristics required for the piezoelectric actuator. The advances of this stage in the project concern mainly preliminary definition required for further development of the system and are not at a sufficient maturity level as to be disseminated as original research. This part of the research is, though, very necessary in any research project and the later stages of the project depend strongly on the outcome of this first stage.

The second stage concerned the design of the elastic wind tunnel wing upon which the AFDPA system is implemented. The determination of the control system parameters and the control laws to be used as well as the design of the piezoelectric actuator system are considered as a consequence of this design. Because of this, the wing has been designed considering a target set of dynamic behavior parameters to ensure the testing can be performed simulating the desired phenomena. Different dynamic behavior has been obtained through the simulations and preliminary structural testing of the wing which posed challenges

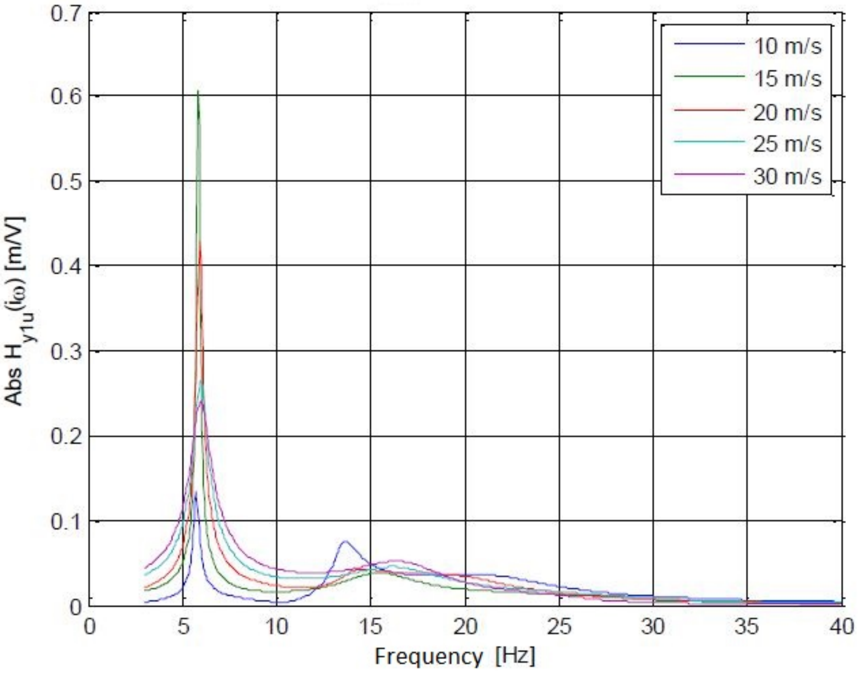

Figure 6.35: Comparison of the FRF magnitude for the different airflow velocities tested.

in terms of data correlation.

The third stage of the project consisted of the manufacturing of the system, the component testing and the system integration. The objectives concerning the functionality of the different AFDPA sub-systems and the assembled system outside of the wind tunnel showed very promising behavior and performance similar to the calculations and numerical determinations performed.

The final stage of the project comprised the wind-tunnel testing of the system and the final calibration of the control laws and the synthesis of these control laws itself. Despite the difficulties encountered during the testing of the system, the synthesis method was validated and implemented with success. The project then closed the development circle of the proposed system starting with the conceptual definition and ending with a mature test-specimen validating the intended technologies and methodologies.

In terms of publications and events organized to maximize the visibility of the project in the scientific community, the project presented publications on the different aspects of the research advanced. Some of the published articles and conferences are presented:

- Mathematical modeling of a V-stack piezoelectric aileron actuation. [129] The article presents the mathematical model of the used piezoelectric actuator and the laboratory simulations performed. The correlation between simulations and laboratory results is presented.
- Surface Pressure Sensitivities for the Measurement of the Mach Number and Angle of Attack of unsteady Flows. [130] The article presents a sensitivity analysis on the positioning of pressure sensors on the surface of an aerodynamic body to determine its attitude.
- Aeroelastic investigations of disc wing UAV. [131] Presents a non-stationary aeroelastic analysis for a disc-shaped wing.
- A Local Sensitivity Analysis of Some Performances of Reactive Projectiles, Rockets and Missiles.

[132] The article presents a reduction of the order of the aeroelasticity analysis matrix to a model of 6 degrees of freedom.

- Piezo active sensors and piezo actuators for space and aerospace applications. [133]
- A V-stack piezoelectric actuator for active mitigation of flutter – design and laboratory tests. [134]
- Study of the Instability due the Different Position of an Aileron. [135]
- System and method for flight envelope expansion via piezoelectric actuation. [136]

Apart from the presented articles, the developed AFDPA system has been displayed in the 2017 edition of the Romanian Research fair and at the end of the project, also in 2017, a workshop has been organized in INCAS with the title “AFDPA: Accomplishments and difficulties 2014-2017".

7. Piezoelectric actuated surface morphing

This chapter aims to implement the results of the characterization of the piezoelectric patch actuator characterized in Sec. 4.3 in order to produce a more complex test specimen. This specimen is used to demonstrate the feasibility of morphing simple structures with piezoelectric actuators.

One of the most significant challenges encountered in this part of the research is that the motion of the piezoelectric match cannot be measured further than local deformation through strain gauges (as already seen in Sec. 4.3). In this situation it is impossible to directly measure the change of shape of a morphing structure without implementing, in some form, a system that amplifies the motion of the actuator. This amplification is the second main objective of the research in this chapter.

An amplification system, as already seen in Sec. 6.2, presents very significant problems in terms or dynamic actuation, especially when the actuation frequencies increase. As frequency increases, the inertial effects of the different elements of the amplifier start influencing the output (in terms of motion) of the actuation system. An example of this phenomenon would occur when the actuator reaches a resonance frequency for the amplifier, in this condition, the amplifier would introduce an amplitude of motion that is not linear with the displacement that the actuator is producing.

When, on the other hand, the actuation is only considered in the static or quasi-static domain, these effects can be neglected and the design of the amplifier simplifies.

In this chapter, only the static part of the structure morphing subject is attained. This happens due to the complexity of accounting for the dynamic behavior of the structure, actuator and mechanical amplifier in the problem in terms of available equipment.

The experiments in this part of the research are then focused on the static analysis of the actuator implemented in an amplification system and representative morphing structure. This morphing structure is analyzed in the experiments in terms of the magnitude of deformations, force output and linearity of the response. All these elements are very relevant in the design of morphing structures in order to characterize how the structure will react to an input of the actuator.

7.1 Development of the test specimen

The development and preparation of the test specimen is the most complex part of the research presented in this chapter. The main objective has been to find a system that allows for enough displacement for the available sensing equipment to measure it, that does not require more force to be actuated than the available piezoelectric can produce, that produces a displacement in the structure perpendicular to the length of the actuator and that is simple enough that can be built using the tools available in the laboratory.

All this preparation is has been done in the laboratory of aerospace structures of the “Universitat Politècnica de Catalunya" as part of the experiments performed there under direct supervision of one of the tutors of the thesis Prof. Lluís Gil Espert and with the help of a master student which did the master project on a similar project.

The concept of the test specimen chosen for implementation is a cantilever bending bar. The piezoelectric actuator can be mounted in one of the sides of the bar, close to the root. In such configuration the actuator produces an in-plane extension or contraction in one of the sides of the bar forcing it to curve. This local curvature, is translated into a bending deformation at the tip of the bar.

This configuration is both a morphed structure and an amplification system for the deformation produced by the actuator as the magnitude of the bending of the bar increases linearly as the measured point gets further away from the actuator. The concept for the specimen is similar to the one presented in Fig. 1.9.

7.1.1 Material selection

Because of the simplicity it presents and the advantages in terms of test specimen preparation simplification and further characterization of the structure (presented in Sec. 5.4), the specimen has been considered with constant transverse section and made of aluminum.

The material selection considered in the first stage the use of composite materials which presented several major disadvantages:

- The materials are expensive to acquire, especially in very small quantities as required for the experiments to be performed.
- The process of manufacturing of composite materials does not guarantee the homogeneity of the mechanical properties throughout the component. A very well adjusted manufacturing process is required to ensure that components can be manufactured without defects (for example: air pockets, delamination or contaminants in the material).
- The manufacturing process requires specialized equipment such as vacuum system or oven not available where the preparation of the materials has been performed.
- The increased stiffness of composite materials, when compared to an equivalent metallic structure, implies a reduction in the deformations generated by an actuator with the same actuating force. This is counterproductive for the considered application.

On the other hand, the main advantages of composite materials relied on the following points:

- Composite materials allow for complex geometries and specimens with variable section without changes in the manufacturing process.

- The specimen can easily be tailored to fit the different sensors during the manufacturing process allowing for better geometrical control on the position of the different elements embedded in the specimen.

- The specific mechanical properties are significantly higher than aluminum which allows for lighter components with the same characteristics.

The metallic approach for the test specimen presents the advantage that the material necessary for the preform can be bought in the required thickness. Furthermore, the material can be considered as isotropic in the analysis.

7.1.2 Geometry definition

With the material defined, the geometry can be defined in a simple manner. The section has been considered constant in order to simplify the numerical calculations as a structured mesh can be readily used without deformation in the shape of the elements throughout the length of the specimen. This is further developed in Sec. 5.

The constant section in the test specimen presents also the advantage of being the simplest form to manufacture. As the manufacturing of the specimen is performed manually, the tolerances that can be obtained in the manufacturing are best in simple geometries.

Accounting for this fact, the geometry of the substrate has been defined as a rectangle with constant thickness. The length of the bar has been considered at $300mm$ due to the difficulties to produce a straight bar longer than that. The length of the bar is expected to be proportional with the displacement at the tip as the actuator produces a warp of the bar only at its root. The width has been designed to be $35mm$ which is the same as the actuator width. In this manner, the inertia of the section where the actuator is mounted is minimal and the deformation produced by the actuator is maximum.

The thickness of the bar needs to be as thin as possible because of the following phenomena. As the thickness is reduced the area inertia of the bar is reduced as it depends on the 3^{rd} power of the thickness for a rectangular section. The smaller the area inertia of the section the higher the stresses produced in the bar and hence the deformation. On the other hand, as the piezoelectric actuator imposes a constant deformation on the substrate where it is integrated, the closer this imposed displacement is to the neutral fiber of the section of the beam, the resulting warping angle will be larger. It is the objective then to use the minimum thickness possible of the beam without compromising the structural integrity of the specimen (both during manufacturing and testing). The chosen thickness of the specimen is $0.3mm$.

Sec. 5 presents a numerical optimization of the geometry to maximize the output displacement at the tip of the bar.

7.1.3 Manufacturing of the test specimen

With the geometry of the test specimen defined, the manufacturing process of the test specimen has followed the different stages presented below.

7.1.3.1 Manufacturing of the aluminum beam

The manufacturing of the aluminum beam is done starting from a $0.3mm$ laminated aluminum sheet. The sheet is cut in a metal guillotine into smaller parts roughly of the dimension of 4 specimens. The specimens have not been directly cut with this guillotine because of the roughness obtained in the cut.

The smaller sheets are cut in a higher precision guillotine to final dimensions as this method presented the advantages of being fast, simple and capable of achieving the desired clean cut. Four specimens have been produced and measured in order to select the one presenting the best tolerance. The lamination direction of the aluminum has been considered perpendicular to the longitudinal direction to the bar in order to provide for the minimum flexural stiffness and maximize any deformations occurring during the experiments. The dimensions of the 4 specimens are presented in Table 7.1 where A and B are the ends of the bar.

Table 7.1: Dimensions of the 4 aluminum bar specimens cut. A and B are the ends of the bar. The length was not a critical parameter because only $30cm$ are free beam, leaving the remaining length for clamping.

Specimen	Width A	Width B	Length
I	$34.2mm$	$35.0mm$	$40.5mm$
II	$34.8mm$	$35.1mm$	$41.0mm$
III	$34.9mm$	$34.9mm$	$41.0mm$
IV	$34.9mm$	$34.9mm$	$41.0mm$

7.1.3.2 Preparation of the piezoelectric patch

In parallel to the production of the aluminum specimen, the piezoelectric patch cables are installed. This operation presents no difficulty as it only consists in welding a cable to each electrode in the patch. This operation has already been performed once for the preparation of the patch actuator in Sec. 4.3.1. In this phase a strain gauge rosette is bonded to the piezoelectric patch surface that is not in contact with the beam.

7.1.3.3 Integration of the specimen

The piezoelectric patch has been glued into the aluminum bar on one side while after the integration of the piezoelectric patch, a second strain gauge has been installed in the opposing side of the beam but in the same location of the bar like the one mounted on the piezoelectric patch. The final configuration of the instrumented bar is as shown in Fig. 7.1.

The adhesive that has been used to glue the piezoelectric patch to the aluminum bar has been the same

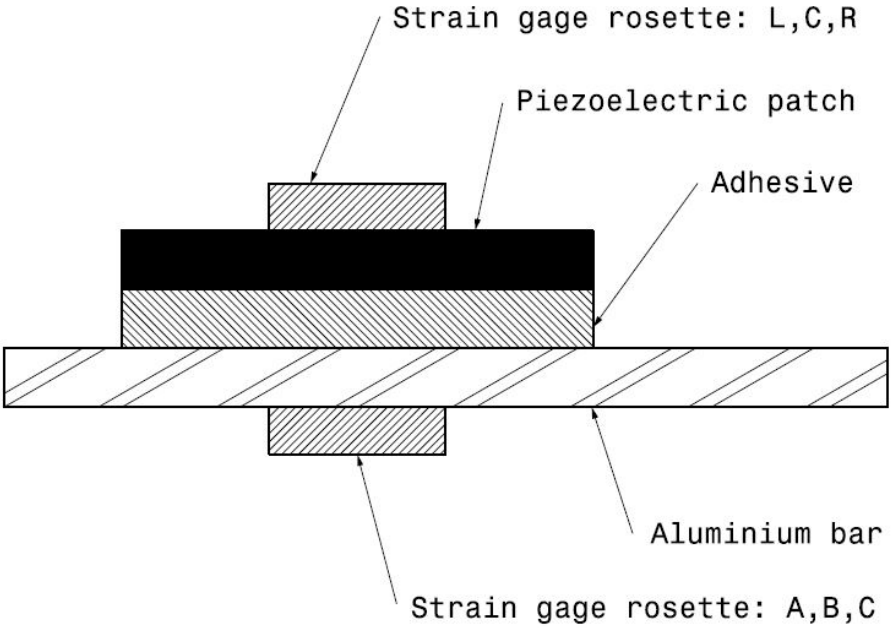

Figure 7.1: Arrangement of the aluminum bar prepared for testing. Note the two strain rosettes positioned opposite on the bar. Figure is not to scale.

used for the strain gauges: HBM Z70 cyanoacrilate-based adhesive. The procedure for gluing was to clean the surfaces with acid (M-Prep conditioner 6557) and then neutralize the acid effect with a neutralizer (M-Prep neutralizer 5A 12833). After the preparation of the surfaces, the piezoelectric was placed in its position and taped to the aluminum in a way in which it can be lifted to insert the adhesive underneath without losing the alignment. After the adhesive was introduced, pressure needed to be applied for at least 5min. The curing process for the adhesive was around 12h.

7.2 Instrumentation and experimental setting

The different instruments used in the testing setup 3 are presented in this section. As most of the equipment used in this experiment is the same as the equipment already used in the previous tests, only the aspects where a difference exist in terms either of equipment or experiment architecture are presented. The conditions in which this experiment has been designed are almost the same as the philosophy used in tests 1 and 2. As the testing in this part is also static, the equipment and the setting are not restricted by the velocity in the acquisition response.

The main difference in terms of the equipment used is the addition o the laser sensor to the experiment architecture, the laser used can be found in Table 4.4.

7.2.1 Arrangement of the experiment

The arrangement of the experiment is completely different than the experiments performed in tests 1 and 2. The main difference is the fact that the piezoelectric actuator is embedded in an aluminum cantilever bar supported sideways so the actuator produces a deflection of the bar in the horizontal direction. The configuration of the experiment can be seen in Fig. 7.2.

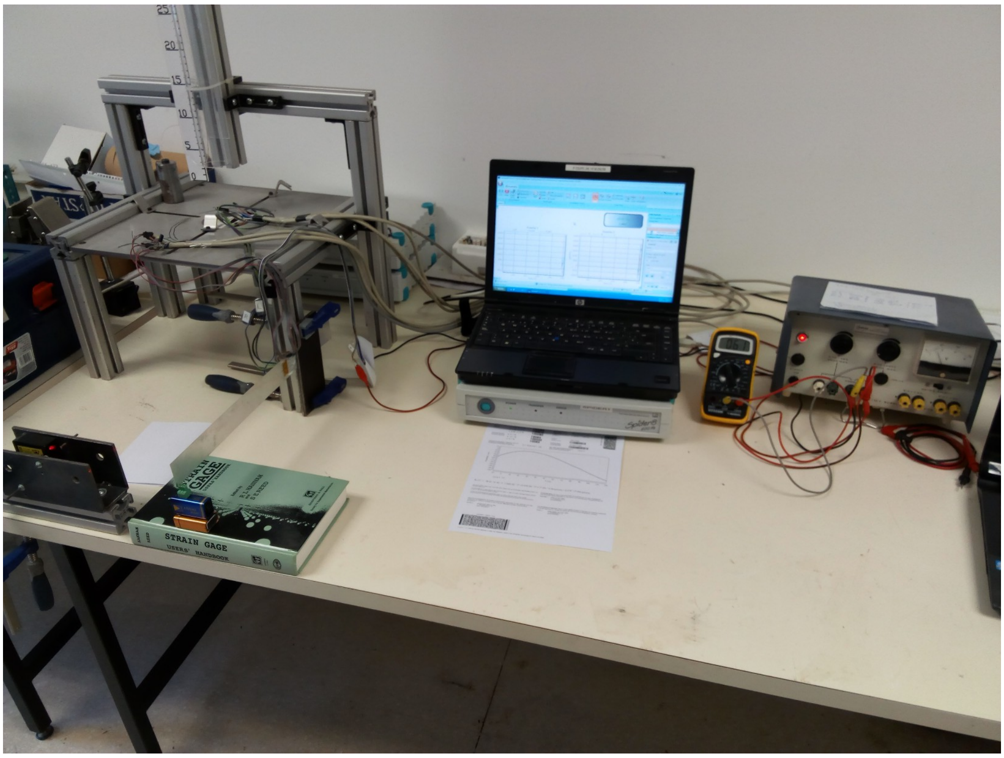

Figure 7.2: Test 3 setup showing the aluminum bar mounted sideways, the laser and the DAQ system.

This configuration has been chosen to avoid the effects of gravity on the bar deflection. In order to obtain a maximum amplification of the deflection of the aluminum bar, its length has been chosen as long as possible given the restrictions in terms of manufacturing and difficulties of measurement stability (vibrations). As lengthening the aluminum bar increases the deflection created by the piezoelectric actuator, it also increases the deflection due to gravity (if the cantilever bar is mounted facing up). In order to avoid this the bar has been mounted sideways so the deflection of the aluminum bar due to gravity is perpendicular to the deflection due to the piezoelectric actuation. Apart from decoupling the effects, as the section inertia of the aluminum bar is four orders of magnitude higher in the lateral direction than in the vertical direction (the thickness of the bar is $0.2mm$ while the width is $35mm$) the deflection due to gravity becomes negligible.

In terms of architecture there are no significant differences from the test setting presented in Sec. 4.3. The main difference is the addition of the laser, which introduces its own low power electric source. In addition, the 4 extra measurement channels (3 for gauges and 1 for the laser) are introduced. The architecture is shown in Fig. 7.3.

7.2.2 Cabling

The cabling used in this tests is the same used in tests 1 and 2 with some differences appearing as the number of strain gauges was doubled and the laser sensor was used to measure the bar deflection. The cables added in this test are detailed below, the rest of the cables used has already been presented in Sec. 4.3.1.

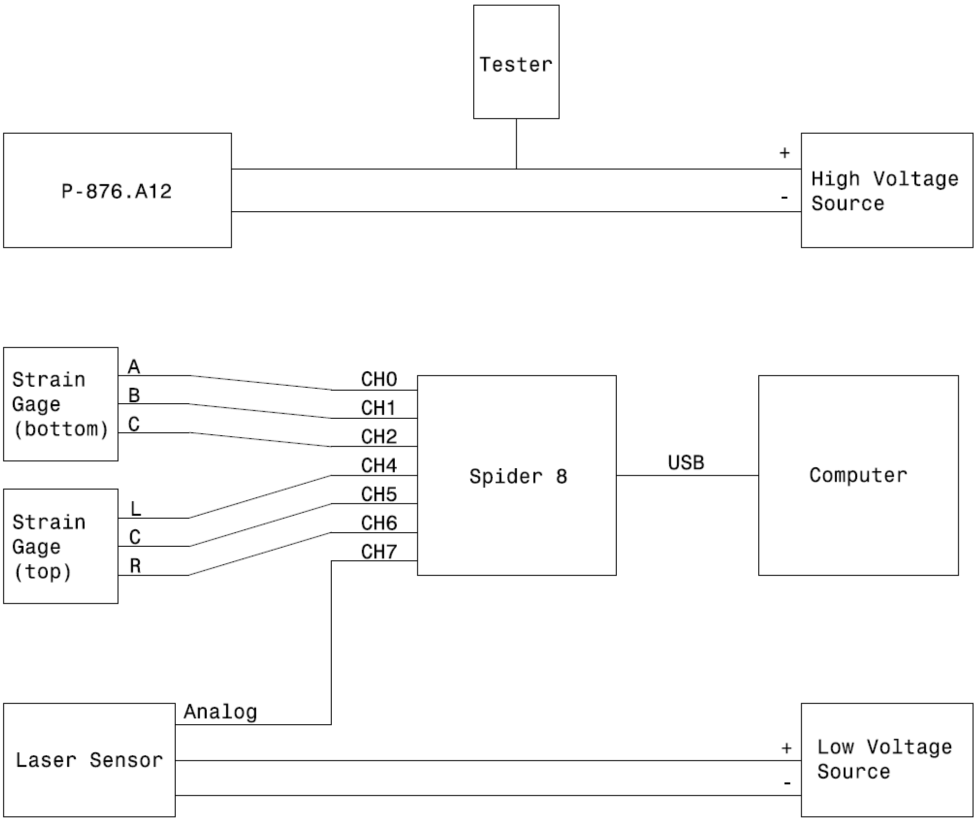

Figure 7.3: Architecture of the test in setup 3.

7.2.2.1 Laser analogue data cable

The laser sensor has been connected in the Spider 8 through the analogue output of the sensor. The connector in the Spider 8 used also a standard 15-pin connector, the connections of the pins followed the arrangement for a voltage reading from 0 to 10V as indicated in the HBM manual [118]. This connection arrangement is shown in Fig. 7.4

7.2.2.2 Laser power cable

Apart from the data cable, the laser requires separate power at a voltage of $5-12V$. The voltage has been supplied through the low voltage power source. The cable connection presents no complexity at all because it is a simple continuous power connection. The integrity of the cable was checked nonetheless with the multimeter to avoid disruptions in the laser power supply during testing.

7.2.2.3 Laser digital data cable

The laser features also a digital I/O (Input/Output) port that can be connected to a computer through an RS-232 interface. This allows for the laser to be connected to the software provided by the manufacturer. Through this connection, the laser has been configured to reduce the full-scale of the measurement area thus increasing the precision of the readings. The cable for the digital interface was already prepared at the

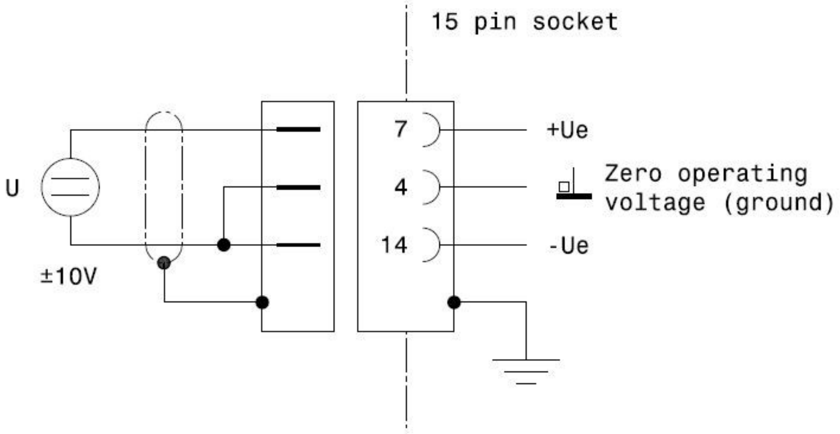

Figure 7.4: Configuration of the connections for the laser sensor in the connection with the HBM Spider 8 through the $10V$ analog in port.

beginning of the experimental phase so the connectivity in terms of pins is not relevant to this report.

7.2.3 Settings and configuration

In terms of configuration of the software related to the experimental setting, test 3 presents basically two differences: the configuration of the Catmap AP DAQ software for an additional 3 strain gauge measurement channels and the laser sensor, and the set-up of the laser configuration through the manufacturer software.

7.2.3.1 Configuration of the laser

The configuration of the laser needs to be done through the RS-232 digital interface; a computer with such interface is required. As the computer available for the testing did not incorporate the required port, a separate computer has been used for the set-up of the laser. The laser used has an embedded flash memory to save the configuration file created by the computer so the laser can be configured with a computer and then operate through a different connection, even when the laser has been powered down.

The first step is to connect the laser through the RS-232 to the computer that will be used for set-up and execute the program by the manufacturer of the laser (RF60x setup software). The program will recognize the laser model and then the laser can be configured. When all the required options have been selected, it is necessary to run the option to save data into the flash memory of the laser. When the baud rate or the communication port are changed only in the computer and not in the laser flash memory, the program loses the connection and the laser needs to be disconnected and restarted.

Through this procedure the analogue output has been configured in the following manner. The laser has a full scale of $500mm$ with a $0-10V$ analogue output. This analogue output signal is generated with a digital-analogue converter because the laser sensor is integrated into a digital signal. As the default full scale is not important in the tests to be performed, it has been reduced to 5% of the original one. The main implication of this is that for the same output of $0-10V$, the reading is not $500mm$ but $25mm$ so the precision of the digital-analogue converter is enhanced and so the quality of the analogue system. This analogue signal can then e introduced in the Spider 8 to synchronize it with the strain readings.

Once the laser configuration is finished, the laser is disconnected from the RS-232 computer and connected to the Spider 8 as shown in Sec. 7.2.2.1 for the testing.

The laser meter (connected in channel 7) is configured in the Spider 8 as a $0-10V$ sensor with the sensor adaptation presented in Sec. 7.2.4 together with the calibration procedure used. Channel 3 and the digital input channel 8 of the Spider have been closed so no superfluous signal is recorded in the data files.

7.2.4 Experimental procedure

With the setting of the experiment and the different parts of the testing specimen already introduced, the present section introduces the methodology followed during the different tests performed. The different tests have been performed following a generic test procedure introduced below similar to the tests already performed in Sec. 4.3.

The tests have been performed for direct and inverse polarization to determine the asymmetry of the specimen behavior. It is relevant to note that one of the points of interest of the testing is precisely the study of the behavior of an asymmetrically-actuated specimen, in contrast with the majority of experiments presented in the state of the art (Sec. 1.5).

Other considerations such as the notation for test numbering and the different difficulties encountered during the development of the experiments are also presented in this section in chronological order. The results are thoroughly presented in Sec. 7.3.

7.2.4.1 Numbering of the tests performed

The experiments performed with the bending bar are grouped into the 3^{rd} set of experiments, numbered sequentially and divided in to groups: the tests in direct polarization and the tests in inverse polarization. The numbering of the experiments associated to each of the groups is shown in Table 7.2.

Table 7.2: Numbering for the tests performed

Test 3		
	Polarity	**Bending bar**
High voltage	Normal	01 - 05
	Inverse	06 - 10

The structure of the test numbering has followed the same logic as the testing performed in the patch characterization tests. In this set, though, the power source used has been exclusively the high voltage one $(0-300V)$ already used in the test sets 1 & 2.

Following the same logic, the tests are divided into direct and inverse polarization tests depending on the direction of the difference of potential between the actuator electrodes. The direct polarization tests create a contraction in the piezoelectric actuator while the inverse polarization tests expand it.

The tests have not been performed with a symmetric voltage actuator as the limits of voltage for direct and inverse polarization are not equal ($400V$ vs $100V$). This happens because the piezoelectric material, like any other ceramic, cannot withstand the tensile strength associated with inverse polarization. In order for the material to withstand inverse polarization, the material is embedded in a pre-stressing resin in a way in which when the actuation reaches the limit inverse polarization voltage, the stress state in the piezoelectric ceramic is neutral. Passed that point the material enters a tensile state with the associated risk of mechanical failure.

7.2.4.2 Calibration of the laser meter sensor

As mentioned in Sec. 7.2 a laser sensor has been used to obtain the deflection of the tip of the bending bar. The laser provides a digital and analogue reading of the distance which can be used simultaneously.

The sensor has been digitally set through the producer's software to a narrow range of measurement of interest for the particular application, this allowed for increased accuracy in the region of measurement. This modification in the range of measure has as impact in the analogue (unprocessed) readings provided by the laser, which are the base for further test laser readings.

In order to calibrate the readings of the analogue output of the laser sensor, the setting from Fig. 7.5 was used. Both readings from the laser sensor were used, the digital through an auxiliary computer with RS-232 port; and the analogue through the Spider 8 data acquisition system. The spider was set to show voltage reading. The purpose of this experiment was to correlate the digital reading of the RS-232 port (which showed distance in mm) with the voltage output from the sensor.

The results of the calibration are presented in Table 7.3. The setting used a vertical plate as a measurement reference in order to avoid vibrations of the measured distance. The calibration resulted in a linear function that linked the distance measured with the voltage output. The function is the following:

$$d = 4.9862V + 25.452$$

with the distance measured in millimeters an the voltage in volts.

This calibration was later introduced in the Spider 8 configuration for CH7 (where the analogue laser sensor reading was recorded) in order to dispose of real-time deflection readings in the same time reference as the deformation readings.

7.2.4.3 Generic test procedure

The procedure for the testing procedure used in the experiments in this set 3 follows the same logic and shares almost entirely the steps presented for the tests of the piezoelectric patch characterization in Sec. 4.3.2. The only difference in the testing procedure appears in terms of the equipment used related to the introduction of the laser transducer.

The procedure differs only in the phase of initial setup of the DAQ due to the integration of the data from the laser. This data is read through channel 7 of the Spider 8 DAQ used. The channel has been configured

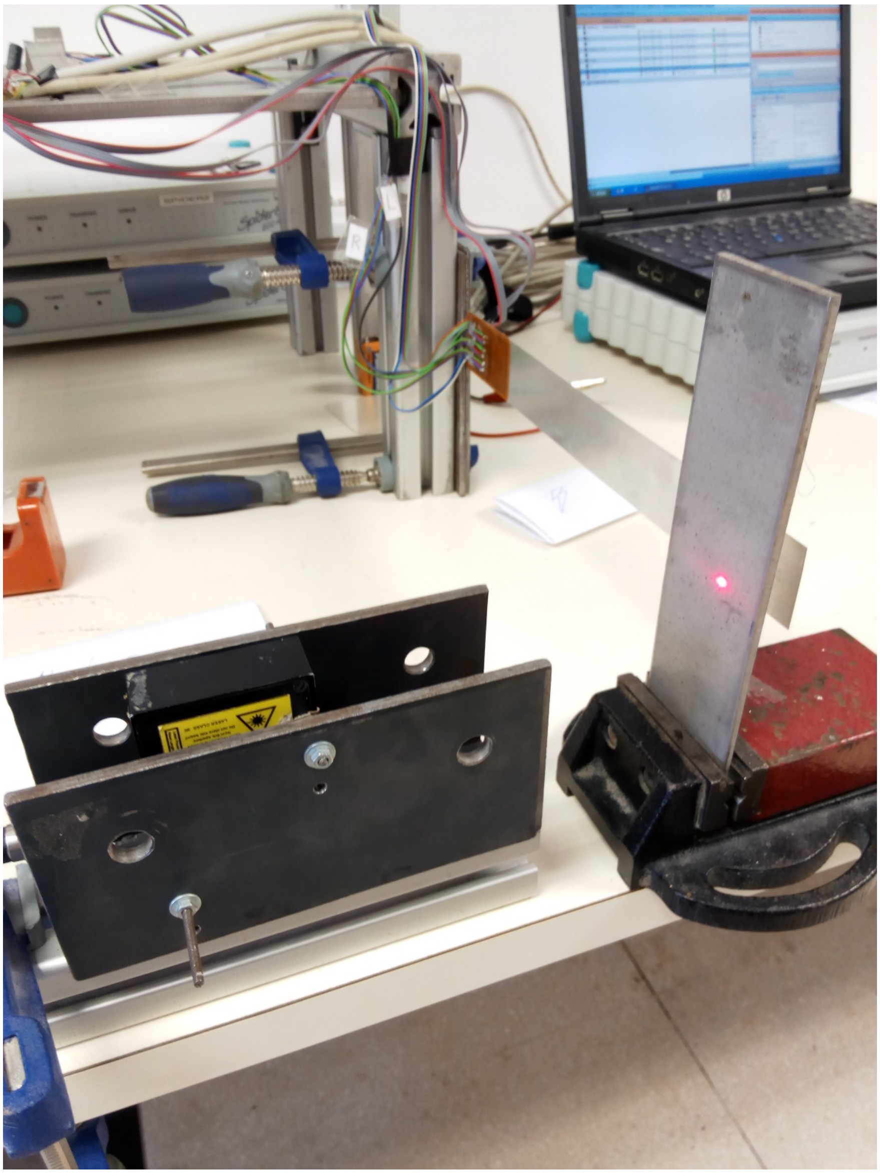

Figure 7.5: Arrangement during the calibration of the laser sensor.

Table 7.3: Calibration values for the Riftek RF603 laser sensor.

Digital distance reading	**Analogue voltage output**
$25.97mm$	$0.1256V$
$30.43mm$	$1.010V$
$35.98mm$	$2.090V$
$40.95mm$	$3.066V$
$45.56mm$	$4.044V$
$50.84mm$	$5.121V$
$55.54mm$	$6.006V$
$60.82mm$	$7.083V$
$65.52mm$	$8.064V$
$70.83mm$	$9.134V$
$75.07mm$	$9.919V$

in the DAQ software with the laser calibration function obtained in Sec. 7.2.4.2.

The rest of the procedure for testing is the same as presented in the patch characterization tests. The situations that have deviated from the procedure are presented below in Sec. 7.2.4.4.

7.2.4.4 Development of the experiments

The instrumented aluminum bending bar has been positioned using the clamping mechanism shown in Fig. 7.6 in order to provide the most homogeneous possible clamping stresses on the bar. The bar has been fixed in a manner so any deformation of the bar happens in the horizontal direction in order to be able to disregard gravitational effects in the experiment. This hypothesis has later been validated in Sec. 5.

The configuration of the spider has been saved under test 3 nomenclature and includes the 6 strain gauges connected individually in $1/4$ bridge and the laser sensor, whose calibration is detailed in Sec. 7.2.4.2.

The tests use an actuating voltage on the piezoelectric patch as input and measure the strain on both rosettes installed together with the deflection of the aluminum bar at the free end. The first tests done (3-01 to 3-05) input a positive voltage on the piezoelectric patch of up to $200V$. During these tests the DAQ software has given some problems during the powering of the high voltage source. This forced to repeat test 3-02 three times and to restart the DAQ program after every experiment. The remaining strains for the first set of tests are presented in Table 7.4.

Provided that restarting the DAQ system implies powering down the strain gauges, the downtime of the system has been minimized in order to affect as few as possible the electrical and thermal equilibrium on the gauges; hence reducing the strain gauge run-out in the consequent tests. After every power up of the system, a long stabilization time has been considered to minimize reading run-out effects in the strain gauges.

The following tests analyzed the inverse polarity configuration up to an actuating voltage of $60V$. The num-

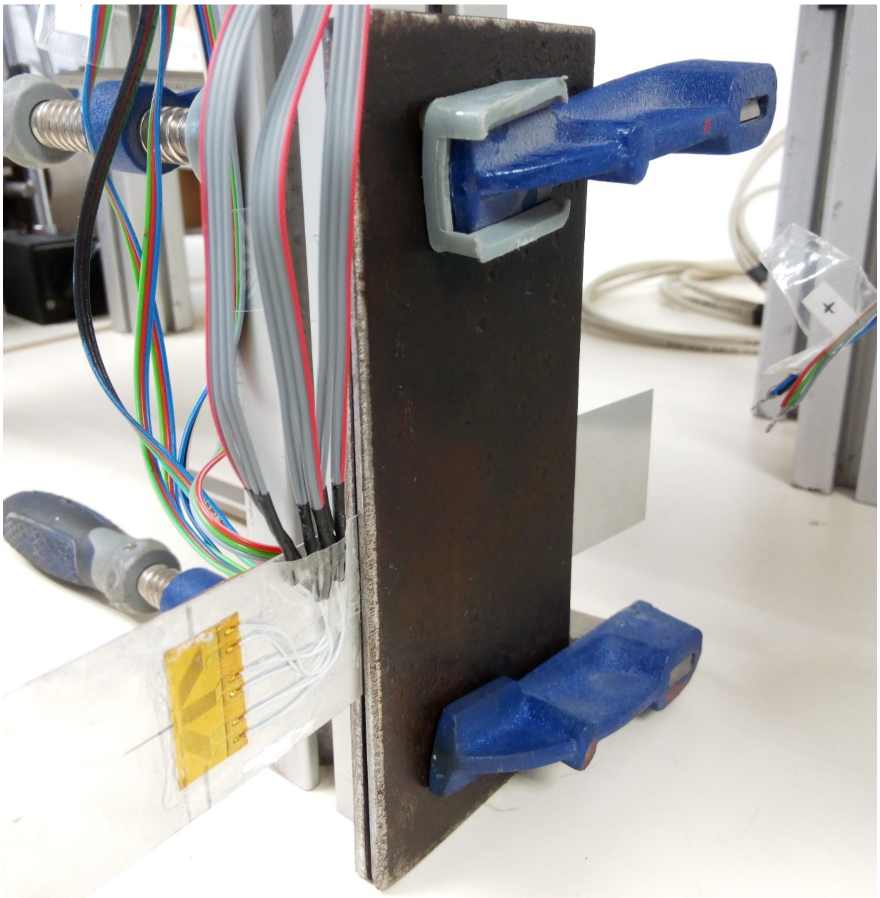

Figure 7.6: Detail of the clamping system used in the bending bar tests.

bering of these tests is 3-06 to 3-10 and the remaining readings for the different sensors are presented in Table 7.5. These tests presented problems in the low voltage readings during the slope down measurements due to the high electrical inertia of the system at values lower than $20V$.

At this point, all the experimental phase has been centered in analyzing the converse piezoelectric effect, which is of special interest on the structure morphing applications. It has been considered of relevance though, to study the electrical behavior of the piezoelectric patch when subject to mechanical stress (direct piezoelectric effect). Test 3-11 tried to study this phenomenon. The methodology intended was to impose a displacement at the free end of the aluminum bar and try to correlate the deflection with the output voltage of the piezoelectric patch.

It has not been possible to perform this analysis in test 3-11. Although the data has been saved, not being able to dynamically record and integrate the output voltage data with the other sensors made the recorded data incomplete. The voltage output of the piezoelectric has been observed to be qualitatively as presented in Fig. 7.7 being the output voltage of the piezoelectric material proportional to the strain derivative rather than the the strain itself.

In the light of this phenomenon two main hypotheses arise that could explain this behavior:

- The first hypothesis considers that the voltage output is directly proportional to the derivative of the strain produced.

Table 7.4: Remaining strains and laser meter reading for the tests 3-01 to 3-05.

	3-01	**3-02**	**3-03**	**3-04**	**3-05**
A	$5.2\mu m/m$	$10.9\mu m/m$	$0.7\mu m/m$	$0.7\mu m/m$	$1.9\mu m/m$
B	$11.0\mu m/m$	$12.2\mu m/m$	$2.6\mu m/m$	$1.9\mu m/m$	$2.3\mu m/m$
C	$6.4\mu m/m$	$10.9\mu m/m$	$1.2\mu m/m$	$1.4\mu m/m$	$1.0\mu m/m$
Left	$-19.9\mu m/m$	$-14.2\mu m/m$	$-5.3\mu m/m$	$0.7\mu m/m$	$-2.4\mu m/m$
Centre	$-36.2\mu m/m$	$-14.2\mu m/m$	$-6.5\mu m/m$	$0.2\mu m/m$	$-3.1\mu m/m$
Right	$-22.6\mu m/m$	$-14.6\mu m/m$	$-6.7\mu m/m$	$0.5\mu m/m$	$-2.9\mu m/m$
Laser	$-0.973\mu m/m$	$-0.484\mu m/m$	$0.0\mu m/m$	$0.002\mu m/m$	$-0.002\mu m/m$

Table 7.5: Remaining strains and laser meter reading for the tests 3-06 to 3-10.

	3-06	**3-07**	**3-08**	**3-09**	**3-10**
A	$-7.6\mu m/m$	$-1.0\mu m/m$	$-0.2\mu m/m$	$0.2\mu m/m$	$0.7\mu m/m$
B	$-11.0\mu m/m$	$-1.2\mu m/m$	$-0.2\mu m/m$	$-0.2\mu m/m$	$0.9\mu m/m$
C	$-8.6\mu m/m$	$-1.0\mu m/m$	$-0.2\mu m/m$	$0.0\mu m/m$	$0.5\mu m/m$
Left	$41.8\mu m/m$	$6.5\mu m/m$	$4.3\mu m/m$	$2.6\mu m/m$	$2.2\mu m/m$
Centre	$41.8\mu m/m$	$6.2\mu m/m$	$3.8\mu m/m$	$6.5\mu m/m$	$1.9\mu m/m$
Right	$41.5\mu m/m$	$7.0\mu m/m$	$4.3\mu m/m$	$2.4\mu m/m$	$1.9\mu m/m$
Laser	$0.4867\mu m/m$	$0.481\mu m/m$	$0.00\mu m/m$	$0.00\mu m/m$	$0.00\mu m/m$

- Secondly, the phenomenon can be explained if the voltage output is proportional to the strain but there is an electrical dissipation in the material that rapidly reduces the voltage when the mechanical stress stabilizes.

Proving or disproving these hypotheses have not been possible due to the lack of capability of integrating the actuation/output voltage to the DAQ system. The voltage readings could not be dynamically measured or referenced to the time frame of the strain readings thus forcing the experiments to be static.

In order to integrate the voltage readings in the Spider 8 it would be necessary to proportionally reduce the voltage from a range of $0-200V$ to a range of $0-10V$ so the voltage can be read by the spider. This can be readily done with a voltage divider, with the configuration as follows in Fig. 7.8.

The formulation of the reduction offered by the voltage divider is as follows:

$$V_{out} = \frac{R_2}{R_1 + R_2} V_{in}$$

The voltage divide presents on its own problems in electric charge inertia that may affect dynamic readings passed a certain frequency. As the experiments performed do not include the analysis of the dynamic behavior of the system the concept is left as an idea to be studied in future testing. Other issues arising from the implementation of such a system like measurement noise or distortions due to the added element are too complex to be analyzed in such an experiment and are considered to be out of the scope of the

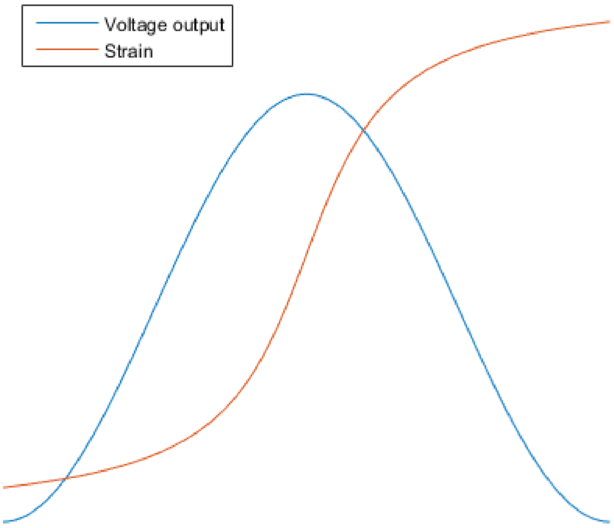

Figure 7.7: Qualitative diagram of the behavior of the piezoelectric patch during direct piezoelectric effect test 3-11.

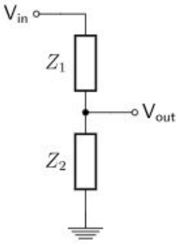

Figure 7.8: Example of a voltage divider.

experiments presented in this thesis.

7.3 Experimental results and analysis

The results for the cantilever beam experiments are presented in this section together with the comments on the results obtained in terms of phenomenology and in terms of quantitative values.

The experiments are divided in two sets: the experiments in direct polarization (3-01 to 3-05) and the experiments in inverse polarization (3-06 to 3-10). The experiments in direct polarization excited the piezoelectric patch with a voltage in the direction of the material polarization vector. In this case the material presents an expansion in the direction of polarization (thickness) and a contraction in the in-plane directions. In the inverse polarization experiments the results are opposite.

The results of the experiments performed in this section are used to study the phenomenology of the piezoelectric-actuated beam and in the performed numerical modeling of the beam.

7.3.1 Direct polarization experiments

The experiments performed in direct polarization consist in a stepped ramp-up of the excitation voltage while reading deformation at two points close to the root of the bar and deflection at the tip of the bar. In this situation the voltage has been increased at intervals of $20V$ up to $200V$ and then reduced in the same manner to 0 (as detailed in Sec. 7.2.4).

The results obtained consist of a data file in the format as presented in Fig. 7.9. The format is exported directly from the data acquisition software (HBM Catman) into an Excel table for post-processing. Automated post-processing in a specialized software was not considered an advantage for the volume of tests to be analyzed.

File comment:							
Time 1 - default sample	A	B	C	Left	Center	Right	Laser
s	µm/m	µm/m	µm/m	µm/m	µm/m	µm/m	mm
13.05.16 10:58:02	13.05.16 10:58:02	13.05.16 10:58:02	13.05.16 10:58:02	13.05.16 10:58:02	13.05.16 10:58:02	13.05.16 10:58:02	13.05.16 10:58:02
20.00 ms (50 Hz)	20.00 ms (50 Hz)	20.00 ms (50 Hz)	20.00 ms (50 Hz)	20.00 ms (50 Hz)	20.00 ms (50 Hz)	20.00 ms (50 Hz)	20.00 ms (50 Hz)
Hardware channel:0	Hardware channel:0	Hardware channel:1	Hardware channel:2	Hardware channel:4	Hardware channel:5	Hardware channel:6	Hardware channel:7
Serial No. (Electronics / (	Serial No. (Electronics / CP): N.A.	Serial No. (Electronics / CP): N.A.	Serial No. (Electronics / CP): N.A.	Serial No. (Electronics / CP): N.A.	Serial No. (Electronics / CP): N.A.	Serial No. (Electronics / CP): N.A.	Serial No. (Electronics / CP): N.A.
Sensor:	Sensor: SG 3 wire 350 Ohms	Sensor: SG 3 wire 350 Ohms	Sensor: SG 3 wire 350 Ohms	Sensor: SG 3 wire 350 Ohms	Sensor: SG 3 wire 350 Ohms	Sensor: SG 3 wire 350 Ohms	Sensor: DC voltage 10 V
Sensor T-ID:	Sensor T-ID: DMS_1_3_350	Sensor T-ID: DMS_1_3_350	Sensor T-ID: DMS_1_3_350	Sensor T-ID: DMS_1_3_350	Sensor T-ID: DMS_1_3_350	Sensor T-ID: DMS_1_3_350	Sensor T-ID: DC_10V
Amplifier typeN.A.	Amplifier typeSR30 600 Hz (base)	Amplifier typeSR30 600 Hz (base)	Amplifier typeSR30 600 Hz (base)	Amplifier typeSR30 600 Hz (extensio	Amplifier typeSR30 600 Hz (extension)	Amplifier typeSR30 600 Hz (extension)	Amplifier typeSR30 600 Hz (extension)
Connector plate:N.A.	Connector plate:N.A.	Connector plate:N.A.	Connector plate:N.A.	Connector plate:N.A.	Connector plate:N.A.	Connector plate:N.A.	Connector plate:N.A.
Transducer type:N.A.	Transducer type:Quarter bridge	Transducer type:Quarter bridge	Transducer type:Quarter bridge	Transducer type:Quarter bridge	Transducer type:Quarter bridge	Transducer type:Quarter bridge	Transducer type:DC Voltage
Measuring range:N.A.	Measuring range:700	Measuring range:700	Measuring range:700	Measuring range:700	Measuring range:700	Measuring range:700	Measuring range:712
Native unit	Native unitmV/V	Native unitmV/V	Native unitmV/V	Native unitmV/V	Native unitmV/V	Native unitmV/V	Native unitV
Engineering unit:	Engineering unit:	Engineering unit:	Engineering unit:	Engineering unit:	Engineering unit:	Engineering unit:	Engineering unit:
Nominal range: 0	Nominal range: 4000	Nominal range: 4000	Nominal range: 4000	Nominal range: 4000	Nominal range: 4000	Nominal range: 4000	Nominal range: 75.314
catman Scaling:None	catman Scaling:Strain gage wiring	catman Scaling:Strain gage wiring	catman Scaling:Strain gage wiring	catman Scaling:Strain gage wiring	catman Scaling:Strain gage wiring	catman Scaling:Strain gage wiring	catman Scaling:Linearization table
Excitation:N.A.	Gage factor:2.01999998092651	Gage factor:2.04999995231628	Gage factor:2.01999998092651	Gage factor:2	Gage factor:2	Gage factor:2	x(1) = 0 y(1) = 25.4519996643066
Filter characteristics:N.A	Bridge factor:1	Bridge factor:1	Bridge factor:1	Bridge factor:1	Bridge factor:1	Bridge factor:1	x(2) = 10 y(2) = 75.3140029907227
Filter frequency:N.A.	Shunt correction factor1	Shunt correction factor1	Shunt correction factor1	Shunt correction factor1	Shunt correction factor1	Shunt correction factor1	Excitation:Unknown
Zero balancing:0 s	Excitation:Unknown	Excitation:Unknown	Excitation:Unknown	Excitation:Unknown	Excitation:Unknown	Excitation:Unknown	Filter characteristics:Bessel lowpass
Tare value:0 s	Filter characteristics:Bessel lowpas	Filter characteristics:Bessel lowpas	Filter characteristics:Bessel lowpass	Filter characteristics:Bessel lowpass	Filter characteristics:Bessel lowpass	Filter characteristics:Bessel lowpass	Filter frequency:5 Hz
Software zero: 0 s	Filter frequency:5 Hz	Filter frequency:5 Hz	Filter frequency:5 Hz	Filter frequency:5 Hz	Filter frequency:5 Hz	Filter frequency:5 Hz	Zero balancing:45.81763 mm
Signal measured:N.A.	Zero balancing:343.3663 µm/m	Zero balancing:422.6342 µm/m	Zero balancing:576.7129 µm/m	Zero balancing:-471.84 µm/m	Zero balancing:-58.32 µm/m	Zero balancing:-182.88 µm/m	Tare value:45.81763 mm
Amplifier input:N.A.	Tare value:343.3663 µm/m	Tare value:422.6342 µm/m	Tare value:576.7129 µm/m	Tare value:-471.84 µm/m	Tare value:-58.32 µm/m	Tare value:-182.88 µm/m	Software zero: 45.81763 mm
Gage factor:0.00000	Software zero: 343.3663 µm/m	Software zero: 422.6342 µm/m	Software zero: 576.7129 µm/m	Software zero: -471.84 µm/m	Software zero: -58.32 µm/m	Software zero: -182.88 µm/m	Signal measured:N.A.
Bridge factor:0.00000	Signal measured:N.A.	Signal measured:N.A.	Signal measured:N.A.	Signal measured:N.A.	Signal measured:N.A.	Signal measured:N.A.	Amplifier input:N.A.
N.A.	Amplifier input:N.A.	Amplifier input:N.A.	Amplifier input:N.A.	Amplifier input:N.A.	Amplifier input:N.A.	Amplifier input:N.A.	Gage factor:0.00000
	Gage factor:0.00000	Gage factor:0.00000	Gage factor:0.00000	Gage factor:0.00000	Gage factor:0.00000	Gage factor:0.00000	Bridge factor:0.00000
	Bridge factor:0.00000	Bridge factor:0.00000	Bridge factor:0.00000	Bridge factor:0.00000	Bridge factor:0.00000	Bridge factor:0.00000	N.A.
	N.A.	N.A.	N.A.	N.A.	N.A.	N.A.	
0	0.475247529	1.90681E-14	0.475247529	-6.66134E-15	-3.66374E-15	0.24	0.00199448
0.020000001	0.475247529	1.90681E-14	0.475247529	-6.66134E-15	-0.24	0.24	0.00199448
0.040000002	0.475247529	0.234146347	0.475247529	-6.66134E-15	-0.24	0.24	0.00199448
0.060000003	0.475247529	0.234146347	0.475247529	-6.66134E-15	-0.24	0.24	0.00199448
0.080000004	0.712871294	0.234146347	0.475247529	-6.66134E-15	-3.66374E-15	0.24	0.00199448
0.100000005	0.712871294	0.234146347	0.475247529	-6.66134E-15	-3.66374E-15	0.24	0.00199448

Figure 7.9: Extract of the raw data obtained from HBM Catman DAQ software. The first column indicates the measurement time.

The post-processing of the results takes into consideration the intervals set during testing for data acquisition which account for a stabilization time of the read values after any voltage change. After the stabilization of the measured values has taken place, the measured parameters are constant. The interest intervals are averaged for each channel and the standard deviation calculated. If the value of the standard deviation is high, the measure presented oscillations during the reading and its value may be compromised.

The results obtained for each of the tests includes readings from 2 strain gauge rosettes, with 3 strain channels each, and a laser sensor. The results obtained from test 3-01, combined into a single figure are shown in Fig. 7.10. The qualitative analysis of these results shows strain-voltage relations with significant hysteresis cycles for both strain gauge rosettes (the one instrumenting the piezoelectric patch and the one instrumenting the same location of the opposite side). The deflection measurements also show hysteresis.

Quantitatively, the magnitude of the deformation of the strain gauges mounted on the piezoelectric patch (Left, Center and Right) is kept almost homogeneous. There are no measurement differences more significant than the strain gauge measurement error. In a conventional cantilever bending bar, the readings of strain in the direction longitudinal of the bar are expected to be significantly higher than the readings at $\pm 45deg$. In this situation this does not happen due to the behavior of the piezoelectric material.

The piezoelectric material presents in-plane isotropy in the mechanical, electric and piezoelectric behavior. In a strain-imposed problem (as the present one) the material expands with circular symmetry thus gener-

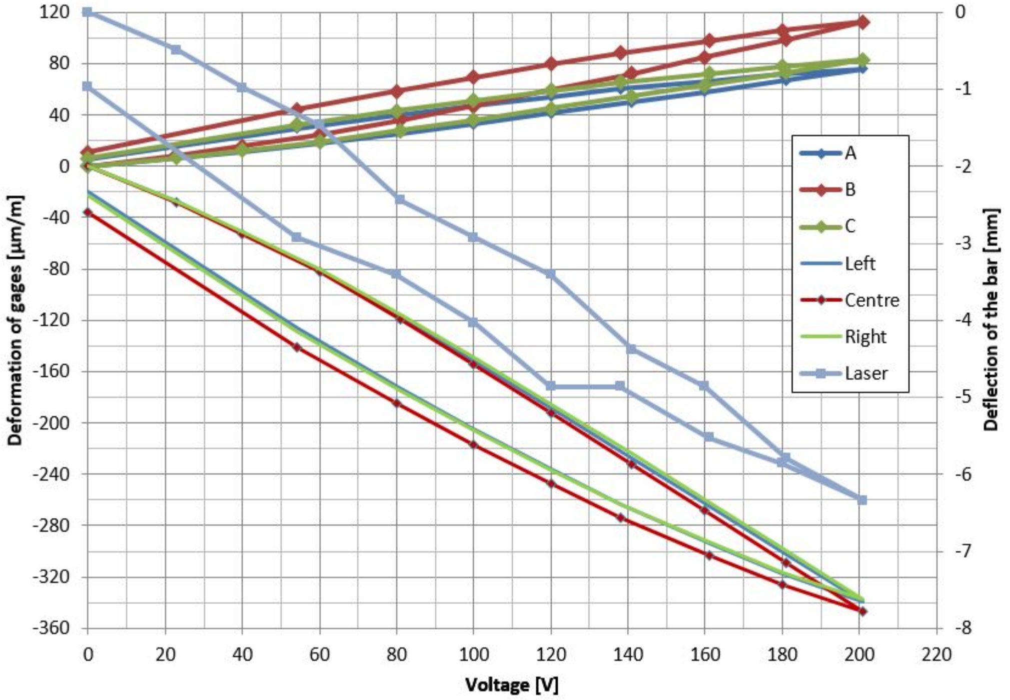

Figure 7.10: Results obtained after signal post-processing for test 3-01.

ating a homogeneous strain field in any in-plane direction. This phenomenon causes the strain readings for Left, Center and Right strain gauges to be of equal magnitude.

On the strain gauges mounted on the aluminum bar (opposite to the ones instrumenting the patch) the phenomenology is radically different. In this case, gauge B (longitudinal gauge) presents a value of deformation proportionally higher to the readings of A and C. The analysis of this aspect is performed later on together with the comparison of the results between tests.

The analysis of the results for the rest of the experiments in direct polarization presents very similar results qualitatively to the first experiment. The hysteresis phenomenon appears in all the tests the amplitude of which is not readily comparable without an analysis of the results one against another (performed below). Also, the different slopes of the strain readings can be seen. The strain magnitude decreases for points further away from the piezoelectric actuator.

In terms of deflection bar readings with the laser measurement, the readings in the ramp-up are significantly more consistent than the down-slope. The readings present oscillations in the voltage decreasing paths for most of the tests. One of the causes for the oscillations is the resolution of the laser sensor equipment. The laser used has a measuring range of more than $200mm$. Although the measuring domain can be reduced to as much as 10% of the full scale, this still implies that the domain used in the measures is lower than 30% of the maximum value the sensor can read. In this conditions and considering that the measuring error of the transducer consists of a constant and a proportional error, the error for the used domain is proportionally 3 times higher than for a reading in the full scale of the transducer. This fact reduces the confidence in the local oscillations of the deflection readings.

The analysis of the results in the direct polarization tests is continued through an analysis that compares the readings of a particular sensor for the different tests. This allows for the determination of the variations

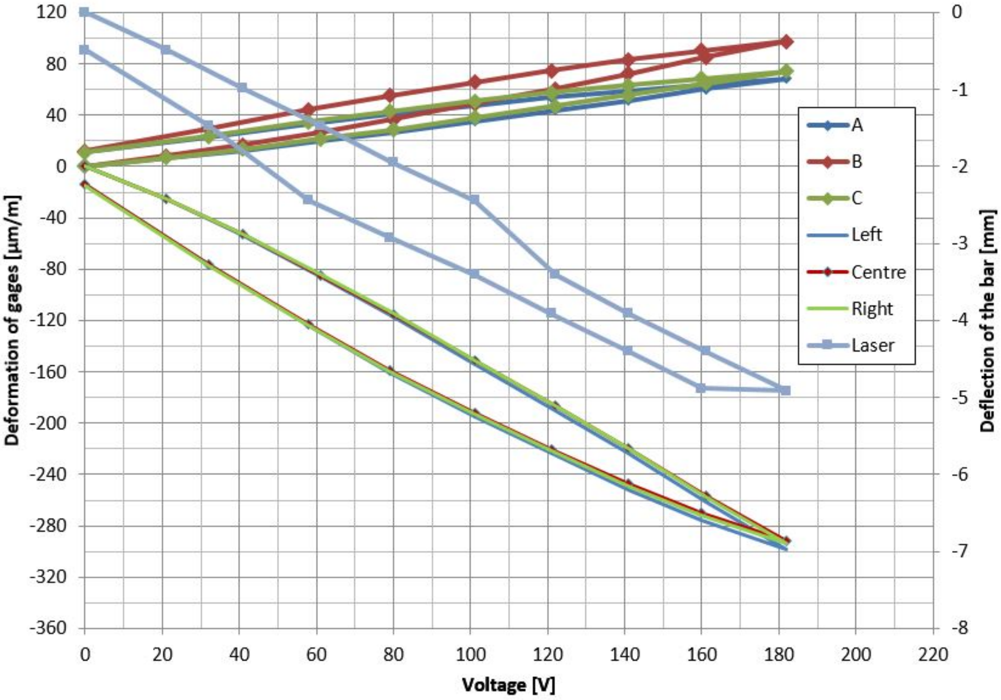

Figure 7.11: Results obtained after signal post-processing for test 3-02.

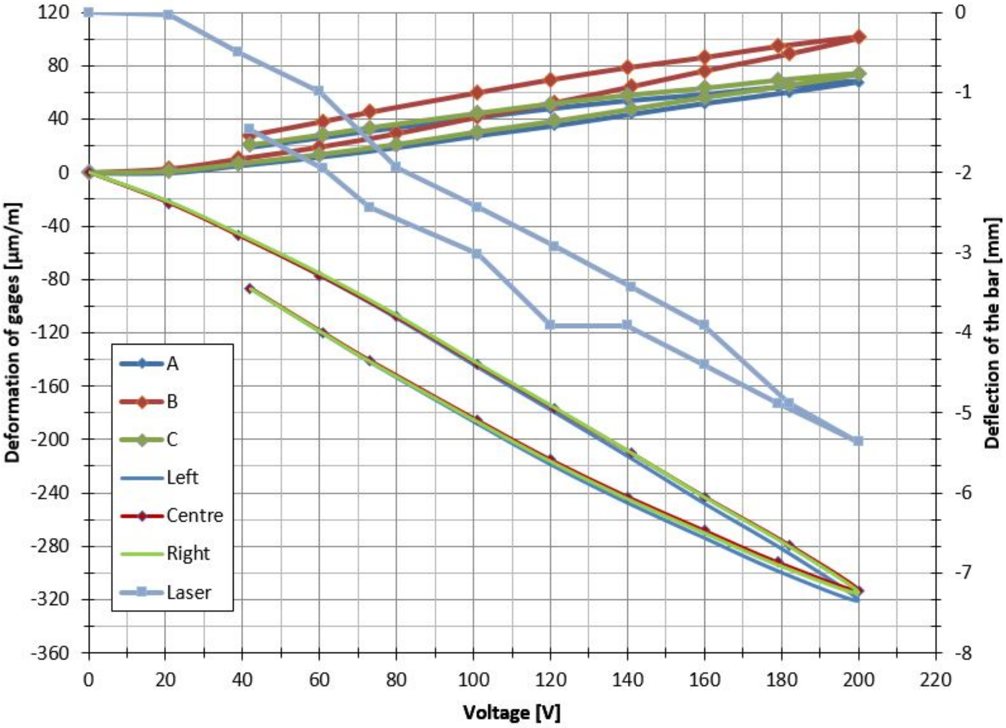

Figure 7.12: Results obtained after signal post-processing for test 3-03.

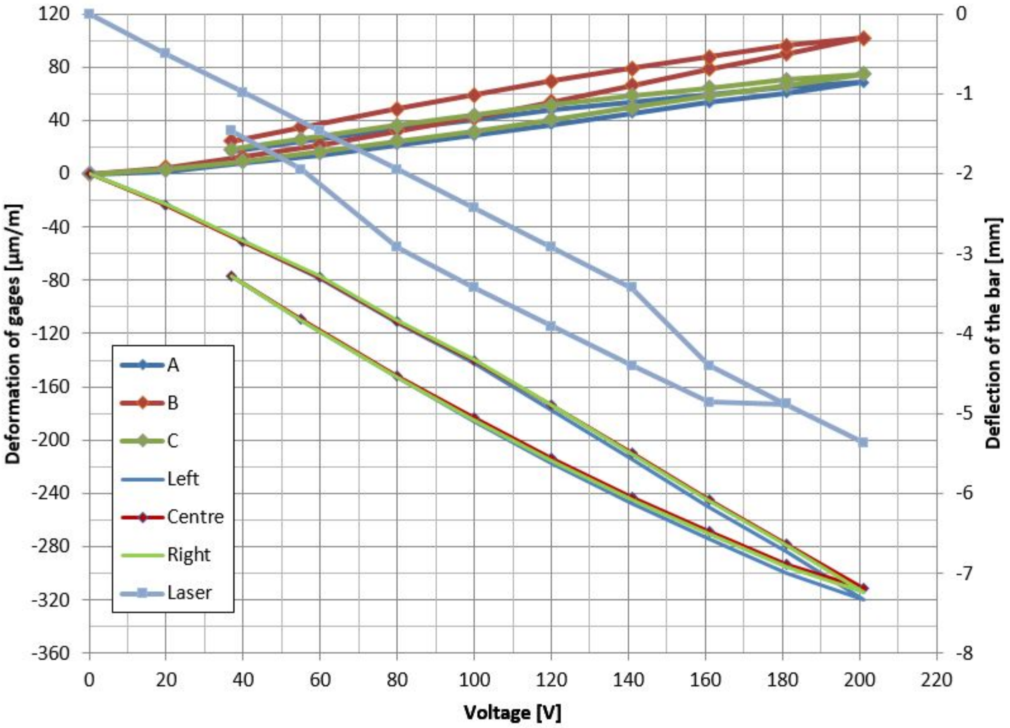

Figure 7.13: Results obtained after signal post-processing for test 3-04.

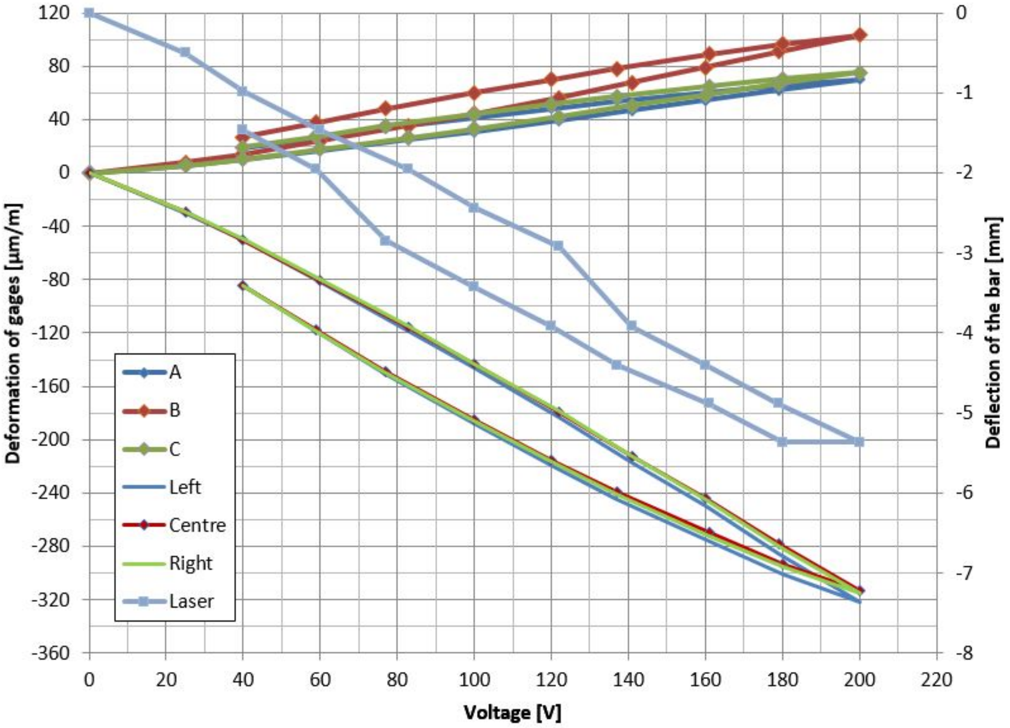

Figure 7.14: Results obtained after signal post-processing for test 3-05.

in the results from test to test and the study of the evolution of the results.

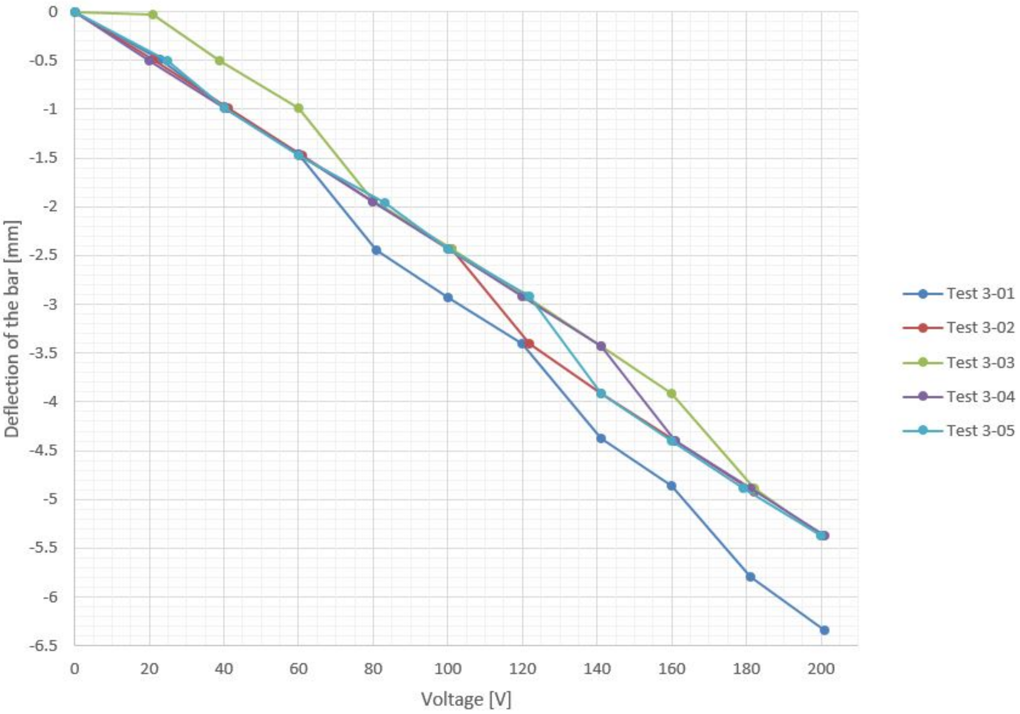

Figure 7.15: Deflection readings on the voltage ramp-up for the direct polarization tests.

The first analysis is performed on the deflection readings performed with the laser. The comparison of the readings for the different tests is presented in Fig. 7.15. It is readily observable that the results are consistent from test to test, the general trend is the same for all the tests except for test 3-01 which presents a slightly lower slope leading to a higher deflection of the bar. The analysis of the sloped for the deflection readings is presented in Fig. 7.16.

In the analysis of the slopes plotted in Fig. 7.16 the discrete measurement performance of the laser deflection sensor is evidenced. The value for the slope “jumps" from one value to another, showing that the reading of the sensor is not continuous (analogical) but discrete. The poor resolution of the sensor, although is not that significant in the measurement of the deflection itself is very relevant when the deflection readings are derived to determine the slope. In this context the points of measurement cannot be considered as reliable individually but a statistical approach to their behavior leads to a more credible result.

The correlation between the strain gauge readings for the rosette that instruments the piezoelectric patch and the deflection at the tip of the bar is presented in Fig. 7.17. The results show a behavior very close to linear between these two magnitudes, it is relevant to note that the hysteresis does not significantly alter the linearity of the graphic. This happens because a relation of proportionality exists between the hysteresis of the piezoelectric and the hysteresis shown at the tip of the bar; most importantly, the factor of proportionality is kept constant throughout the testing.

Another aspect that can be studied from the strain results is the magnitude of the hysteresis cycle, this can be seen in Fig. 7.14 although this phenomenon appears throughout the tests. Strain gauges L, C, R present a hysteresis cycle significantly more pronounced than the one shown by gauges A, B, C. This phenomenon can be explained by the fact that the only non-linear material in the structure is the piezoelectric patch.

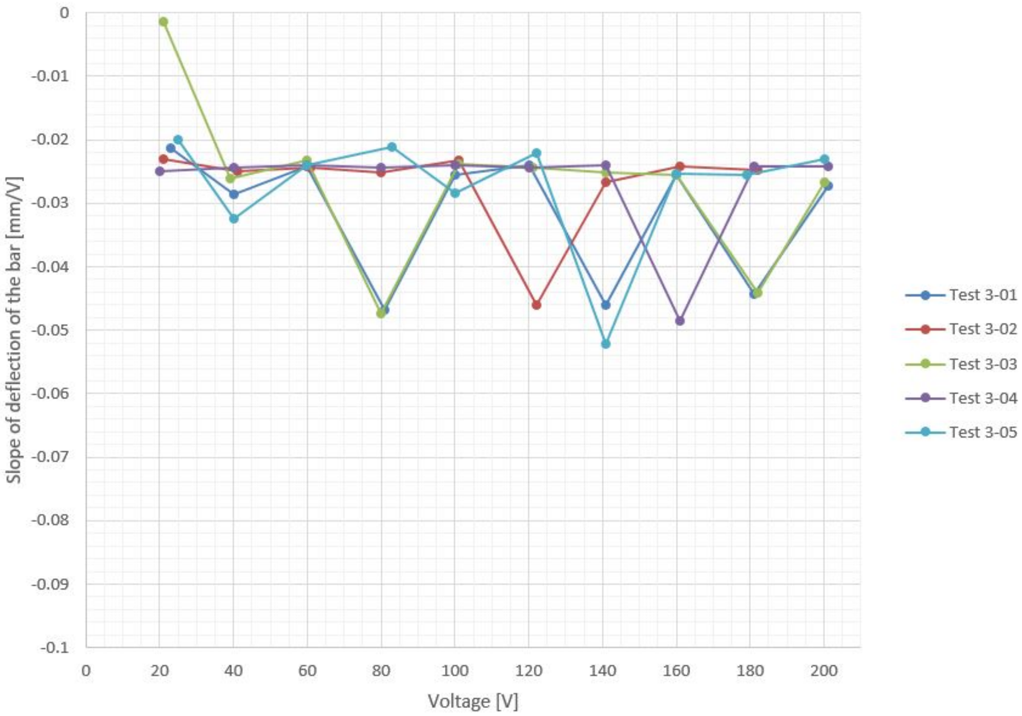

Figure 7.16: Deflection slopes for the direct polarization tests.

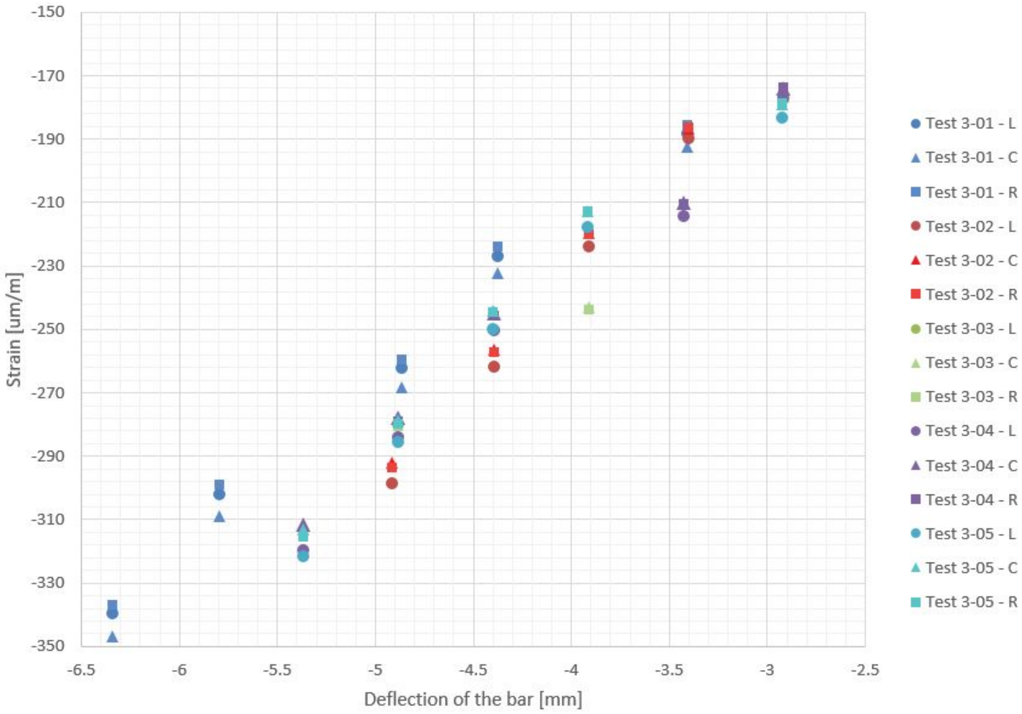

Figure 7.17: Correlation between bar deflection and strain readings for the rosette instrumenting the piezoelectric patch.

Because of this, any hysteresis present in the structure will increase its magnitude as the measurement point gets closer to the piezoelectric. Points A, B, C, being on the side of the cantilever bar furthest to the piezoelectric patch, present a magnitude of the hysteresis cycle significantly lower than the strain gauges on the piezoelectric.

It is notable to mention that the piezoelectric material is the only element in the experimental setting that introduces a factor of non-linearity. Hence, any non-linear behavior in any other point of the structure other than the actuator, as introduced by the piezoelectric patch, is expected to be proportional to the behavior of the piezoelectric.

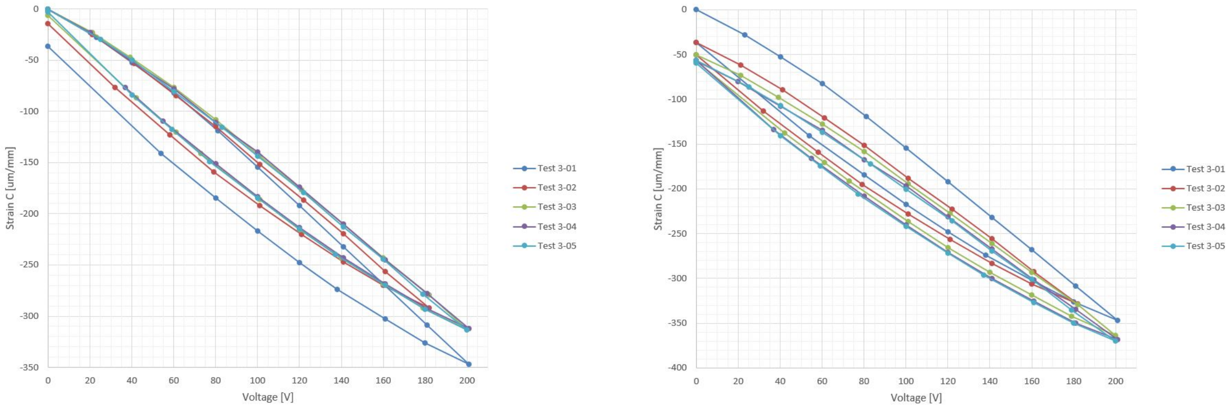

(a) With zeroing.

(b) Without zeroing.

Figure 7.18: Strain gauge C readings during direct polarization testing: comparison of the results for the case in which a zero was performed after each test and the case it was not.

The results for each of the strain gauges have been analyzed through different representations. A first representation (presented in Fig. 7.18) is the analysis of the strain as a function of the voltage for both the ramp-up and the slope-down and for the consecutive tests.

A first aspect identified is the difference in strain magnitude between the first test of the series and the consecutive tests. The first test presents a maximum amplitude (corresponding to the voltage of $200V$) around 10% higher than the rest of the tests. The analysis of the standard deviation is presented in Table 7.6. The table analyzes how the average and the 95% confidence interval change as different combinations of tests are considered.

Table 7.6: Standard deviation analysis for different combinations of results for tests 3-01 to 3-05.

Tests considered	**Average**	**St. Dev.**	95% **Int.**
Zeroing after each test			
Tests 3-01 to 3-05	$-315.4\mu m/m$	$19.6\mu m/m$	12.5%
Tests 3-02 to 3-05	$-307.5\mu m/m$	$10.3\mu m/m$	6.7%
Tests 3-03 to 3-05	$-312.7\mu m/m$	$0.83\mu m/m$	0.5%
No zeroing after each test			
Tests 3-01 to 3-05	$-355.4\mu m/m$	$17.7\mu m/m$	10.0%
Tests 3-02 to 3-05	$-357.6\mu m/m$	$19.7\mu m/m$	11.0%
Tests 3-03 to 3-05	$-367.3\mu m/m$	$3.4\mu m/m$	1.9%

The rapid increase in the consistency of the obtained results as the first tests of the series are excluded from the analysis is clear in the analysis. The 12.5% confidence interval when all the tests are considered rapidly decreases to 6.7% when the first test is excluded and to 0.5% when the second test is also excluded.

The analysis leads to the conclusion that for the same stabilization time in all the test in the series, the non-linearity of the piezoelectric material affects the behavior of the system in a way in which more than one load cycle is required before the results start being repeatable.

A cause for this could be that the piezoelectric material retains part of the deformation after it has been electrically unloaded. This remaining strain has been noted after each test in order to provide a magnitude of the phenomenon and the results can be seen in Fig. 7.18a. During testing, in order to ensure the proper calibration of the sensors, the data acquisition system has been electronically zeroed after each test, this implying that the reading of strain at the beginning of each test is always $0\mu m/m$. It is interesting, though, to study the behavior of the system cumulatively throughout the tests in order to determine the stabilization of the strain readings in conditions closer to the actual behavior of the system. The behavior of the structure has been corrected applying cumulatively the read remaining strains after each test. The results of this analysis are presented in Fig. 7.18b.

In the application of the “no-zeroing" correction the results substantially change qualitatively because the readings for tests 3-03 to 3-05 are actually higher than for test 3-01 (as occurred before the correction). In this case, the difference between tests is significantly reduced as presented also in Table 7.6. The results in the zeroing correction present an average maximum deformation significantly higher than the non-corrected case. Also, the confidence interval for the results is increased, even when only the last 3 tests are considered. This can be explained because the non-zeroing between tests causes not only the correction of the results but also the addition of any previous deviation.

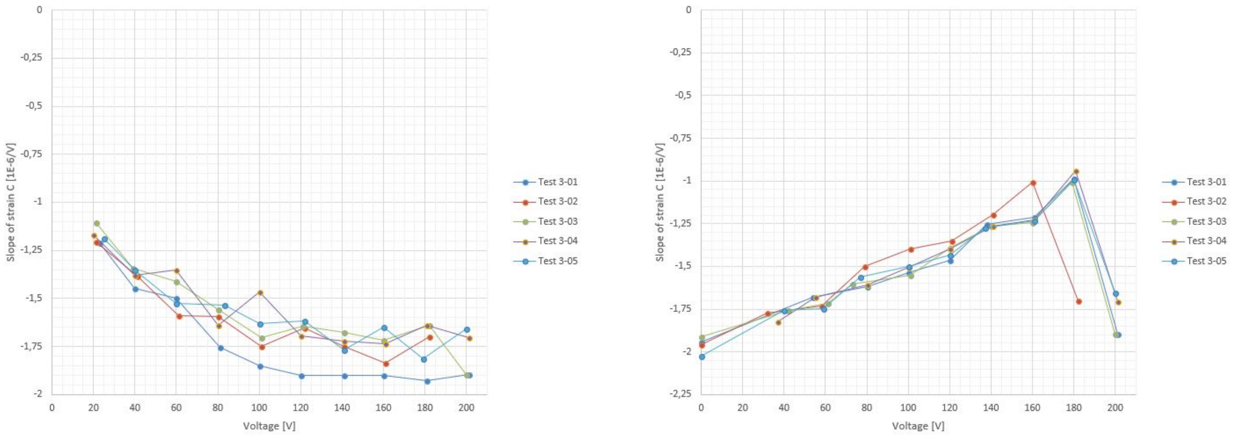

(a) Ramp up.

(b) Slope down.

Figure 7.19: Slope calculations for the strain readings of gauge C.

In order to determine the linearity of the results obtained the derivatives of the strains as a function of the actuation voltage have been studied. The closer the values of the derivative are to a constant value, the closer the results are from linearity. The analysis has been performed separately for the voltage ramp up and for the slope down and the results are presented in Fig. 7.19.

The analysis shows that the behavior in the ramp-up and the slope down during the testing are completely different. The behavior during ramp up tends to stabilize to a value about $1.75\mu m/V$. The results of test

3-01 are significantly higher than the results of the following tests. This can be associated with the fact that, in the other aspects, the results also present similar deviations in the first test of the series. On the contrary, on the slope down the results do not stabilize to a constant value and the slope consistently decreases as the voltage also decreases. In this situation, the way of reading Fig. 7.19b would be from right to left in accordance to the passing of time.

The slope stabilization value of $1.75\mu m/V$ when the voltage increase is not directly comparable to the specifications of the piezoelectric material as supplied by the manufacturer and presented in [116]. The piezoelectric specifications define the piezoelectric properties in terms of the piezoelectric coefficients matrix (see [116]) which is represented in C/N or m/V. Even though the derivative of the deformation read is the strain gauges during the experiments presents the same units as the piezoelectric coefficient, the magnitude they represent is not the same.

7.3.2 Inverse polarization

The experiments have been performed also in inverse polarization, meaning that the polarization vector and the electric field vector in the piezoelectric material had opposite directions (in the same manner as in the piezoelectric patch experiments). The testing in inverse polarization implies an extension in the piezoelectric material. In these conditions, due to the fact that the material is ceramic, the strength of the material is greatly reduced in comparison to the compression case present in direct polarization. This has a direct effect on the maximum voltage for actuation of the piezoelectric (which reduces to a maximum value of $100V$). This actuation voltage is influenced mainly by the existing pre-stress in the material imposed by the polymeric cover of the patch. This pre-stress allows for the piezoelectric material to expand while still working in the compression side of the stress-strain graphic. Throughout the testing and in order to avoid actuating the piezoelectric material over the pre-stress value, the maximum actuation voltage has been considered a $60V$.

As in the tests for direct polarization, a first part of the analysis of the results consists of the analysis of the results test by test comparing all the data channels acquired during the testing in the same graphic. The results of the first test for the inverse polarization series of experiments are presented in Fig. 7.20. This test presents qualitatively the best results of the series despite the fact that the magnitude of the read values is almost twice the magnitudes presented in any subsequent testing. This difference in the magnitude presents an advantage if the qualitative aspect of the results is analyzed using this test: the error associated to the resolution of the measurements is significantly lower than in any other test (for a given DAQ resolution, as the read magnitudes increase the relative error reduces).

The hysteresis results are very significant in this experiment. A very significant difference exists between the hysteresis loops of gauges A, B, C and L, C, R which can be explained, as for the phenomenon detected in the direct polarization tests, by the location of the two strain gauge rosettes used in the experiment. As gauges L, C, R are positioned on the piezoelectric patch, their behavior in terms of hysteresis is very close to the hysteresis behavior of the piezoelectric material thus presenting such a difference between the strain readings between the voltage ramp-up and the slope-down. On the other rosette, located on the other side of the aluminum bar, the preponderating behavior is the one of the bar in terms of strain. The hysteresis phenomenon is then less present in these gauges due to the linear behavior of the material. The behavior of the material is still, though, influenced to some extent by the hysteresis of the piezoelectric patch.

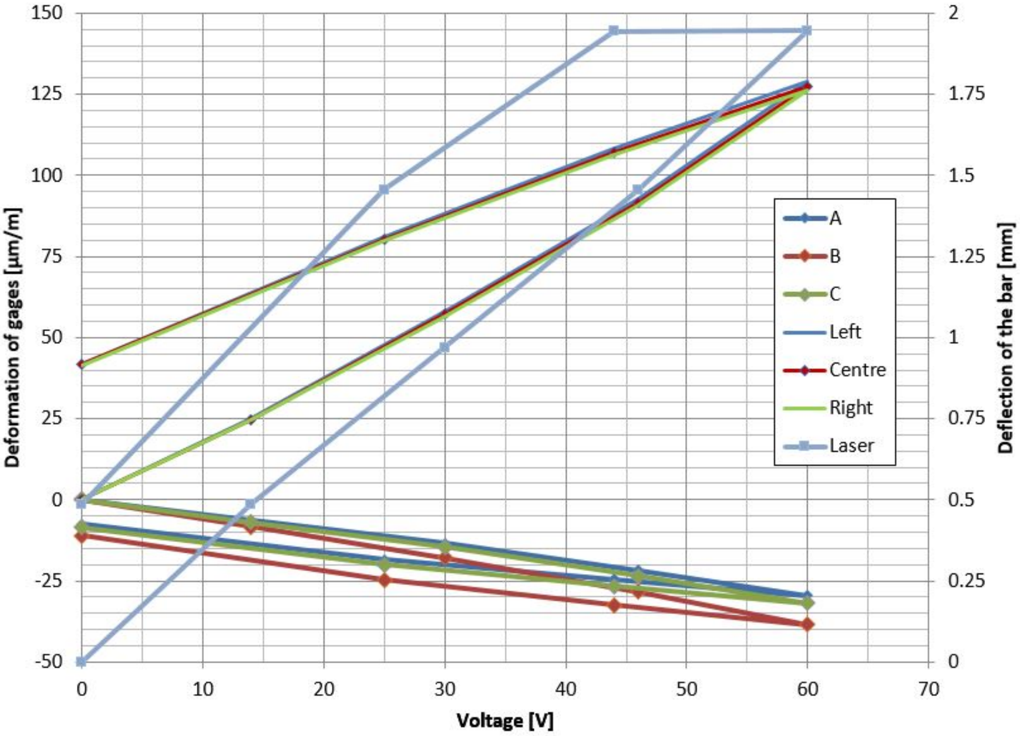

Figure 7.20: Results obtained after signal post-processing for test 3-06.

In terms of bar deflection, the hysteresis introduced by the piezoelectric material is the only source of non-linearity in the system. As the deflection of the bar is the integral of the strain field throughout the bar, a component that introduces hysteresis at some point in the structure will result in a deflection that presents the same hysteresis even if the rest of the material is linear.

The results for the second test of the series (shown in Fig. 7.21) present a deflection reading significantly deviated from the linear behavior during the voltage ramp-up and a linear behavior in the slope-down with a noticeable hysteresis although not as prominent as in test 3-06. As in the tests in direct polarization the readings of gauges L,C,R present almost identical readings throughout the test while on the readings of A,B,C, gauge B presents slightly higher strain readings. The reason for this difference in the readings between both rosettes is the fact that gauges L,C,R instrument the piezoelectric material where the in-plane strain is homogeneous in any direction (as presented in Sec. 7.3.1).

The results of test 3-08 as presented in Fig. 7.22 show a phenomenology very similar to test 3-07 (shown in Fig. 7.21). One notable difference though is the inaccuracy of the bar deflection readings and the almost nonexistent hysteresis in the measure of this parameter. We can observe that in comparison to the two previous tests of the series the amplitude of the hysteresis cycle has reduced.

Test 3-09 (the results of which are presented in Fig. 7.23) presents results almost identical to test 3-08 both qualitatively and quantitatively with only slight differences in the voltage at which the measurements have been performed (remember that the voltage was manually selected during the testing and that any overshoot on the selection of the voltage was not corrected backwards so the hysteresis did not compromise the reading. In this aspect the voltage-function is a strictly growing one).

The repetition of the non-linear shape of the bar deflection readings leads to the conclusion that the resolu-

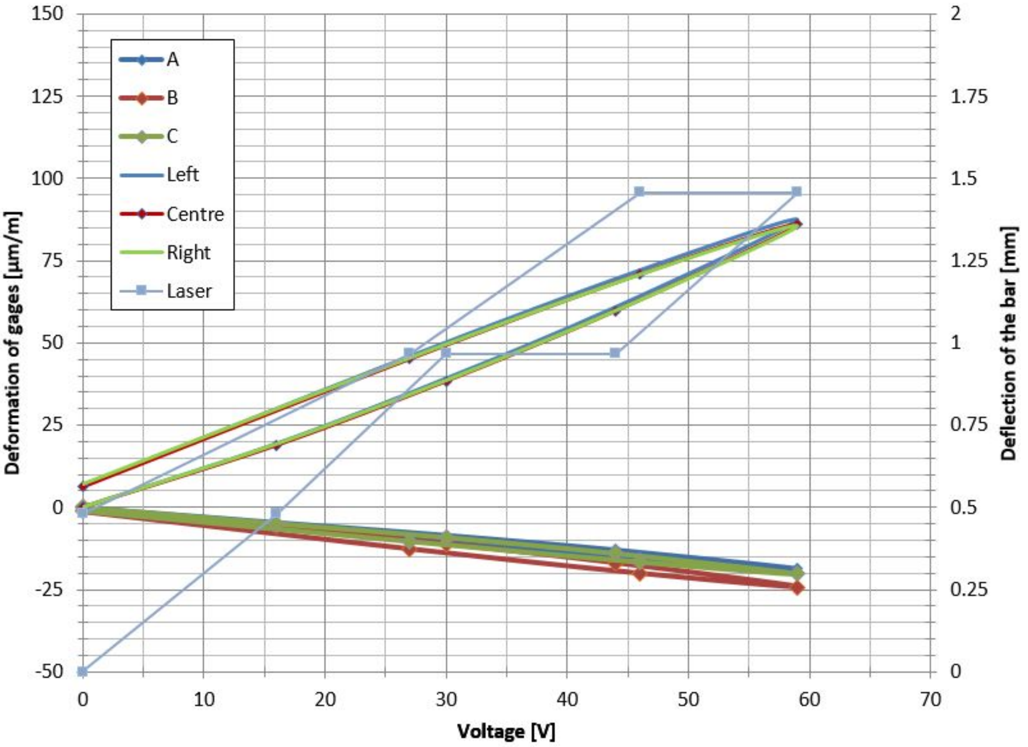

Figure 7.21: Results obtained after signal post-processing for test 3-07.

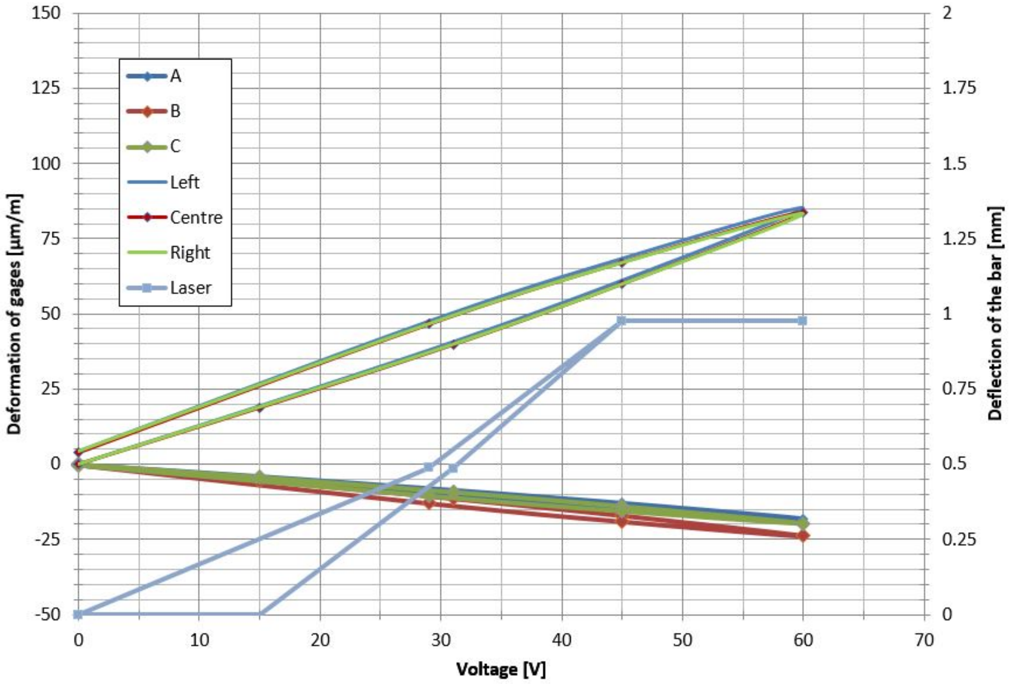

Figure 7.22: Results obtained after signal post-processing for test 3-08.

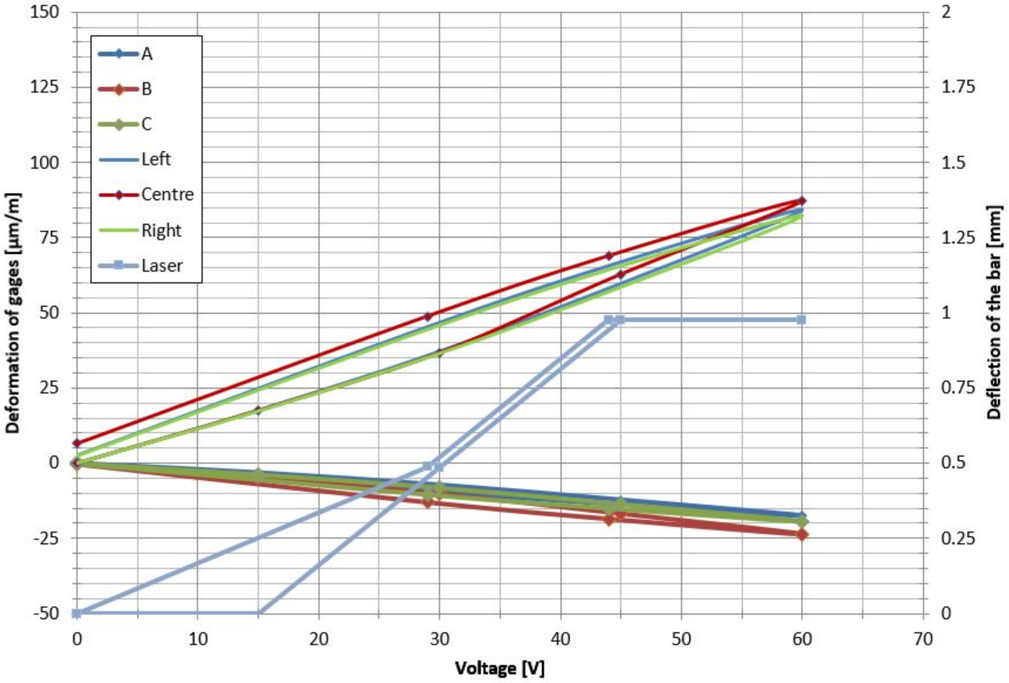

Figure 7.23: Results obtained after signal post-processing for test 3-09.

tion of the laser sensor was not accurate enough to provide for a continuous-like reading of the deflection. The sensitivity of the laser sensor was adjusted at the beginning of the testing (test 3-01) to the maximum expected deflection. This allowed for an acceptable resolution throughout the direct polarization testing where the full-scale of the sensor was close to the maximum deflection; in this series of tests, as the maximum deflection is about 6 times lower than in the direct polarization, the resolution that the sensor is capable of producing is also about 6 times worse thus causing the jumps in the readings of deflection.

The results of test 3-10 shown in Fig. 7.24 present no differences from tests 3-08 and 3-09 in this series corroborating the consistency of the obtained results.

As in the direct polarization testing, the analysis is then continued by analyzing the results of the different tests in relation to each other parameter by parameter. This comparison brings some conclusions regarding the repeatability of the results and the dispersion of the measures. The first magnitude to be analyzed is the deflection of the bar during the voltage ramp up the results of which are presented in Fig. 7.25. It is possible to see that the dispersion on the readings between tests is significantly higher than in the direct polarization testing (see Fig. 7.15). As mentioned before, this occurs due to the fact that the sensitivity of the laser sensor was the same for both sets of tests and as the measures of deflection in the inverse polarization tests are significantly lower, the relative error is significantly higher. The sensor presents a resolution of $0.49mm$.

Despite the lack of resolution in the deflection results, the difference in the maximum deflection between the first test and the subsequent ones is visible. Test 3-06 presents a maximum deflection of approximately $2mm$, test 3-07 of approximately $1.5mm$ and the subsequent 3 tests of $1mm$. Even though the accuracy of the results is more than debatable considering the resolution of the sensor, a trend can be observed in which the first tests present a significantly higher deflection, which tends to stabilize to a significantly lower value.

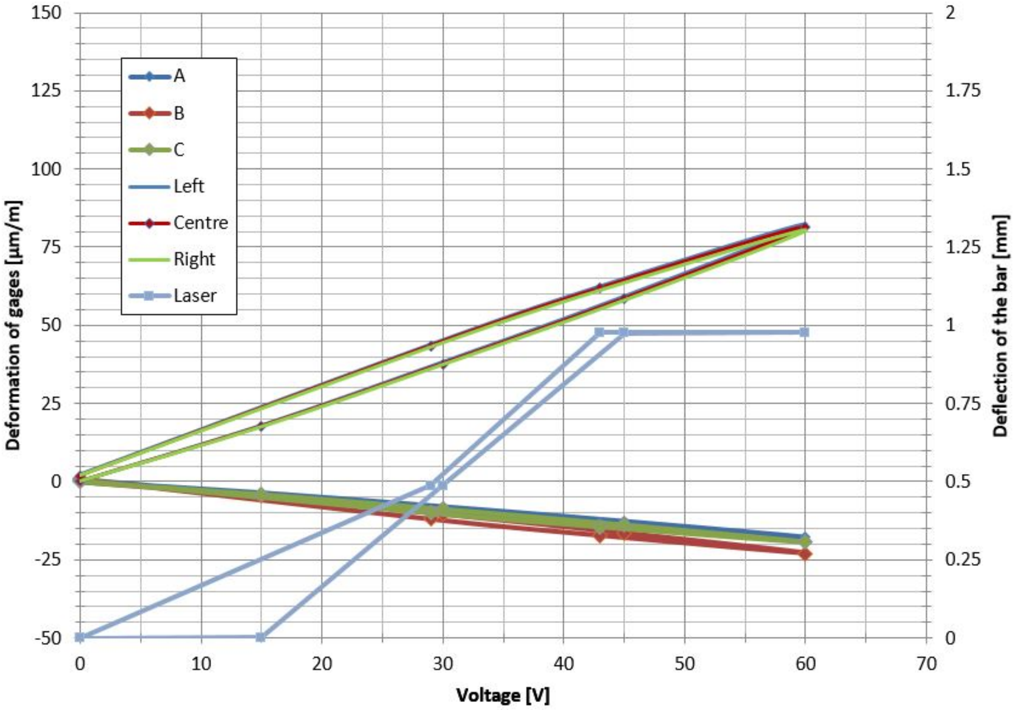

Figure 7.24: Results obtained after signal post-processing for test 3-10.

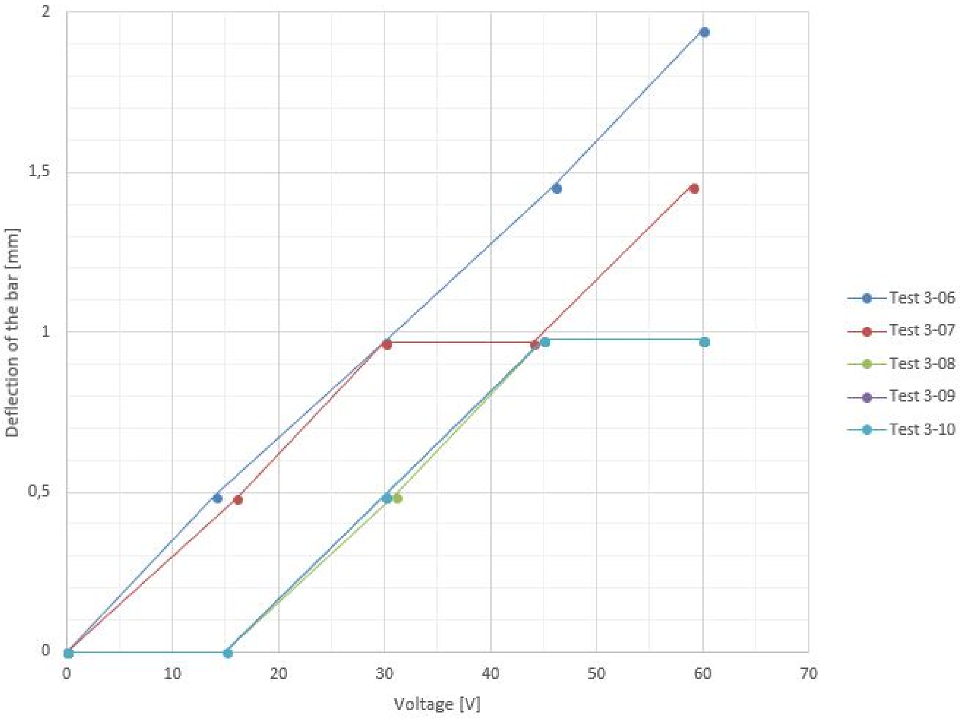

Figure 7.25: Deflection readings on the voltage ramp-up for the inverse polarization tests.

In this case the results are shown to verify the following formulation (also within the error introduced by the resolution of the laser sensor):

$$D_1 = D_N + \sum_{N-1} R_i$$

where D is the deflection and R the remaining deflection reading after each test. The obtained results basically show the behavior presented in the direct polarization results for the strain gauge readings: once no zeroing is performed between tests, the maximum value for each of the tests is practically kept constant, the sum of the remaining strains (or deflections in the present case) adds to the reduction of amplitude in subsequent tests.

The strain for the gauges is analyzed individually for each of the gauges and represented for the different tests together. Fig. 7.26a shows this analysis for gauge C (L,C,R rosette) (mounted on the piezoelectric patch). It is possible to see that the maximum strain decreases throughout the test succession while the hysteresis cycle becomes stationary after the first test (3-06). A similar analysis to the one performed in the direct polarization tests is performed and shown in Fig. 7.26. The representation of the results of the testing when the zeroing after each test is not considered shows a stabilization of the maximum strain the strain gauge from the first test of the series within an error of 9% of the stabilization result. It is possible to see also that the maximum stress of each consecutive test does not decrease but even slightly increases until the stabilization value is reached at test 3-09.

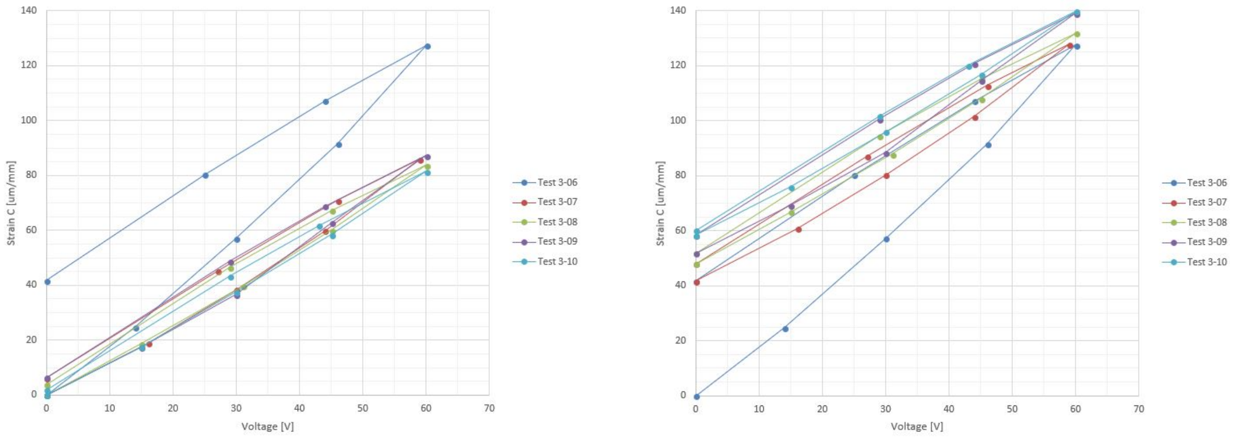

(a) With zeroing.

(b) Without zeroing.

Figure 7.26: Strain gauge C readings during inverse polarization testing: comparison of the results for the case in which a zero was performed after each test and the case it was not.

The analysis of the linearity of the experimental results is performed as in the direct polarization tests through the analysis of the derivative of the strain readings for both the ramp-up and the slope-down. The graphics showing these calculations are shown in Fig. 7.27a and Fig. 7.27b. In this case it possible to see that the behavior is completely different from the direct polarization tests in the fact that during the ramp-up there is no stabilization of the slope for any of the tests. On the other hand these results are in line with the general trend identified in the direct polarization tests, where the stabilization of the strain slope was reached at about $120V$. As the inverse polarization tests only reach $60V$ the slopes do not reach the stabilization. This implies that at no point the material behaves linearly during this set of tests.

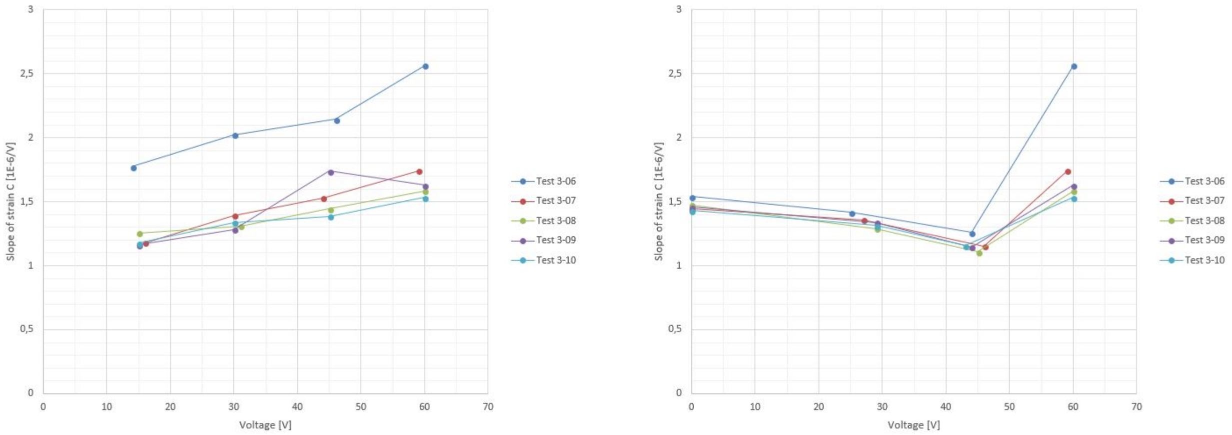

(a) Ramp up.

(b) Slope down.

Figure 7.27: Slope calculations for the strain readings of gauge C (L,C,R rosette).

In the comparison of the slope magnitude between the direct and inverse polarization tests during the ramp-up the values of the slope are very similar (when compared in absolute value) but differ significantly in the slope down. This occurs due to the hysteresis cycle differences between both series. The system presented as shown in the previous results a hysteresis cycle rather different in the magnitude of the difference between ramp-up and slope down values of strain.

8. Conclusions

The aim of the thesis was the evaluation of the capacity of piezoelectric actuation technology to morph a wing profile enough to provide control of the flight vehicle. This capacity is considered with a major restriction: the possibility of integrating the used technology in the aerodynamic shape of the system. This restriction has been imposed at this early level of maturity to ensure the applicability of the research performed.

The main advantages of the technology in its present development status are the weight of the overall system being lower than the conventional hydraulic or mechanic control systems and the dynamic response presented by the system is significantly faster than the present systems. Moreover, the electrification of the actuation of the control systems is aligned with the strategic development of aerospace technology worldwide, which pushes towards the concept of "more electric aircraft" aiming at further optimization of air transport. These advantages can only be precisely quantified when a real-size application is considered where the advantages (or disadvantages) of piezoelectric actuation can be directly compared with an existing reference control system. In the present thesis the analysis performed has been more fundamental analyzing the capability of a representative small-scale actuation system to perform the actuation of conventional actuation technology.

The capacity to provide control of the vehicle is assessed using current control surfaces technology as a reference(regardless of the actuation system used). The criteria used in the determination of the capacity of piezoelectric actuators to perform the actuation functions of conventional control surface has been evaluated using different evaluation criteria for the two applications analyzed: static and dynamic. The static case has used a typical value for the deflection of conventional control surfaces as a reference while the dynamic analysis has used the frequency response as a baseline for determining whether piezoelectric actuators are advantageous in comparison with current technology.

The static and dynamic areas of investigation have been covered in the thesis through different perspectives as follows:

- The research performed as part of the AFDPA project together with the interferometric characterization experiments aimed at studying the dynamic domain of piezoelectric actuators. The selected application case is a characteristic wing designed to present flutter phenomenon at low speeds. Using the piezoelectric actuators as anti-flutter actuators allow for the high-frequency characterization of the actuator given the frequency domain characteristic of flutter.
- The tensometric experiments and the numerical simulations had as a goal the analysis of the static behavior of the actuators. The application case for this study has been a morphing wing concept with a system capable of producing a chord-wise deflection of the trailing edge of a wing.

The static and dynamic experiments with the piezoelectric actuators led to a series of different conclusions presented below:

In terms of the dynamic applications, the piezoelectric actuators present clear advantages over conventional actuation systems due to their excellent dynamic response. The two types of actuators analyzed (stack and patch) reacted accurately to the sinus waveform excitation signals up to frequencies of over $50Hz$ and presented considerable response in amplitude at frequencies up to $1000Hz$. At such frequencies, though, the output signal presented significant distortion.

When analyzing the response of the actuators to a square waveform the response presented a significantly lower bandwidth where the actuator reached a stabilization of the response for each of the voltage steps. As the square signal is a succession of step signals, the response of the piezoelectric actuator presented a characteristic under-damped second order response which stabilized only at very low frequencies of actuation. This second order response is proportional to the inertial effects present in each of the actuators. The actuation response was accurate in this excitation mode up to frequencies of about $2Hz$. At higher than that frequency the actuator did not present a stationary response before the subsequent change of actuation step and the response rapidly resembled such of the sinus excitation as the frequency increased.

In the anti-flutter dynamic applications, given the nature of the behavior of the aeroelastic phenomena, the input signals used for the actuation were sinus waveform. The flutter phenomenon was studied and modeled as having apparition frequencies well below the operational limits of the piezoelectric actuator, this makes piezoelectric systems well suited for this type of applications. Because the piezoelectric actuator outputs very small displacements, a mechanical amplifier has been designed considering inertia and dynamic response as main priorities. The control surface used in the anti-flutter system was built in composite materials to reduce its inertia about the hinge axis thus improving the dynamic response of the system. The combination of all these measures resulted in a system capable of continuous operation at frequencies up to $35-40Hz$ (significantly higher than the $6Hz$ up to which the flutter phenomenon was identified). The dynamic capability demonstrated by the system developed is achievable only with sophisticated conventional control systems which are not suitable for aerospace applications due to their weight and complexity. This happens because of the high inertia throughout the actuation chain, which makes it impossible for the system to respond that fast.

In terms of static applications, a morphing wing concept with a system capable of producing chord-wise deflection of the trailing edge of a wing was studied. The research performed was conducted in parallel numerically and experimentally with the aim of producing a numerical model that can accurately predict the behavior of piezoelectric-actuated morphing structures.

The end structure analyzed has been a wing profile with a rigid leading edge section and flexible upper and lower skins at the trailing edge section aiming to produce changes in the camber of the wing profile chord-wise.

The analysis of the morphing of such structure was too complex to be attempted without the certainty that the different elements of the system were properly calibrated so a methodology of testing was defined to calibrate the numerical model step by step. Different analyses have been conducted in parallel with laboratory experiments to develop a simulation model capable of accurately representing the piezoelectric material, the piezoelectric actuator used and the piezoelectric actuator - bending beam configuration. These elements increasingly complicate the problem and allow for the calibration of the final model in multiple, simpler steps. Throughout the calibration process, the numerical model was calibrated using experimental data on the deformation of the test specimen (obtained through tensometry) and laser deformation indications.

The final step of this calibration process was the simulation of the morphing wing profile. This simulation included elements simulated and calibrated using laboratory experiments. The aim of the simulations of the complete profile was to determine whether the deformation of the trailing edge produced by the actuators was significant enough to act as a control surface.

The results obtained for the wing morphing configuration are promising and the deflections obtained are relevant to consider the design a success. The magnitude of the deformations obtained allows for the application of the technology in cases where small deformations are required and the dynamic response is critical. An example of such application is the optimization of the aerodynamic performance of a configuration throughout the flight envelope.

Despite this, the deformations obtained as the results of the experiments and the numerical simulations are not significant enough for the technology to be applied in larger-scale demonstrators. The scalability of the technology is one of the major challenges that piezoelectric-actuated morphing technology faces.

According to the results obtained in this thesis, a diversity of factors must be taken into consideration to properly evaluate whether the piezoelectric actuation technology is suitable as an alternative for actuation of control surfaces in aircraft. The main challenge that piezoelectric actuation poses is scalability. The voltages required for actuation of piezoelectric materials are proportional to the thickness of the material in the polarization direction. Hence, if the actuator is bigger, the actuating voltage needs to be scaled by the same proportion. When considering actuators for large aircraft this effect would lead to very high voltages.

The second main challenge for the piezoelectric-actuated control systems is integration. The design of the aerodynamic surface to be controlled needs to be considered in designing the type of actuator to be used. This means that the control surface needs to adapt to the low actuation range of the piezoelectric actuators and/or allow for the integration of a mechanical amplifier.

Moreover, the current manufacturing technologies would need to be adapted to be able to cope with the production of piezoelectric materials that are more than an order of magnitude thicker than currently used.

Having these challenges in mind, piezoelectric actuators can be currently used in aeronautical applications such as UAVs and helicopter blade morphing. These applications present geometries one order of magnitude smaller than thus of aircraft wings thus reducing the problems associated to scalability to a manageable level. Moreover, the optimization of parameters in UAV wings and rotor blades does not require the amplitude of motion that aircraft control surfaces do, which makes the operation of such elements feasible through the technology researched in this thesis.

9. Personal contributions and future work

The research performed throughout the thesis presents different aspects of novelty into the subject of morphing of aeronautical structures through the integration of piezoelectric actuators. These main areas of innovation are found mainly in the experimental part of the thesis.

The characterization of the piezoelectric actuators presents two main areas of innovation: the determination of the dynamic behavior of actuators to different waveform signals and the use of tensometry as means of characterization of the piezoelectric patch actuator. The interferometric experiments present a detailed analysis of the thickness response of the actuator throughout a range of frequencies $(0-1000Hz)$ for a variety of input signals (square, sinus, triangular and ramp) leading to a comprehensive study on the phenomenology involved in piezoelectric transient response both qualitatively and quantitatively.

The tensometric analysis of the piezoelectric patch introduced elements of novelty in the methodology used throughout the experiments. One of the important points of the research was the simplicity in the testing while maintaining the consistency of the obtained results; because of this, the utilization of simple and inexpensive sensor configurations was prioritized.

The AFDPA project introduced several aspects of novelty which are integrated in the final demonstrator produced in the project. The design and characterization of the piezoelectric actuator in a V-stack configuration is the element of novelty of most interest to the present thesis. Other elements of innovation of the research performed such as the design of the wing demonstrator are not relevant to the subject of piezoelectricity.

The analysis of the bending beam configuration is, experimentally, the main element of relevance to the problem of structural morphing of aerostructures. A main element of innovation was introduced in this thesis: the analysis of non-symmetrical actuation of the cantilever beam. The main scope of the research was to determine the feasibility of producing relevant deformations in the beam through the use of a non-symmetrical actuator configuration.

Lastly, the numerical simulations performed throughout the research aimed at validating the configuration analyzed for wing morphing. The configuration analyzed, on its own, is the main element of innovation of the research in this chapter of the thesis. The utilization of tandem patch actuators, each in a non-symmetrical configuration on the skins of the trailing edge, led to promising results which encourage the continuation of the research.

The research presented in this thesis presents several possibilities of continuation throughout the different aspects studied. The main relevant aspect to the continuation of the research is the completion of the morphing wing profile demonstrator and its subsequent static and dynamic testing.

The natural continuation of this research is the coupling of the piezoelectric problem with the aerodynamic problem, both statically and dynamically. This is justified in the scope of determining the capacity of the designed system to produced the required forced throughout the morphed skin. This continuation of the research is a necessary study before the technology can be deemed suitable for airborne research.

Bibliography

[1] Helmi Zaini and Noor Iswadi Ismail. “A Review of Morphing Wing”. In: (2016).

[2] Silvestro Barbarino et al. “A review of morphing aircraft”. In: *Journal of intelligent material systems and structures* 22.9 (2011), pp. 823–877.

[3] Kenneth Cheung et al. “Development of Mission Adaptive Digital Composite Aerostructure Technologies (MADCAT)”. In: *17th AIAA Aviation Technology, Integration, and Operations Conference*. 2017, p. 4273.

[4] David L Chandler. “A new twist on airplane wing design”. In: *MIT News* (2016).

[5] Yasuhiro Tani et al. “Experimental study of the morphing flap as a low noise high lift device for aircraft wing”. In: *ICAS2012-9.11* 3 (2012).

[6] R Pecora et al. “Experimental validation of a true-scale morphing flap for large civil aircraft applications”. In: *Industrial and Commercial Applications of Smart Structures Technologies 2017*. Vol. 10166. International Society for Optics and Photonics. 2017, p. 101660L.

[7] Seung-Hee Ko, Jae-Sung Bae, and Jin-Ho Rho. “Development of a morphing flap using shape memory alloy actuators: the aerodynamic characteristics of a morphing flap”. In: *Smart Materials and Structures* 23.7 (2014), p. 074015.

[8] Roelof Vos et al. “Morphing wing flight control via postbuckled precompressed piezoelectric actuators”. In: *Journal of Aircraft* 44.4 (2007), pp. 1060–1068.

[9] Benjamin K Woods and Michael I Friswell. “Structural characterization of the fish bone active camber morphing airfoil”. In: *22nd AIAA/ASME/AHS Adaptive Structures Conference*. 2014, p. 1122.

[10] Giulio Molinari et al. “Aero-structural optimization of morphing airfoils for adaptive wings”. In: *Journal of Intelligent Material Systems and Structures* 22.10 (2011), pp. 1075–1089.

[11] Terrence A Weisshaar. *Morphing aircraft technology-new shapes for aircraft design*. Tech. rep. PURDUE University Lafayette IN, 2006.

[12] EARLE R Caley and JFC Richards. “Theophrastus on Stones: Introduction Greek Text”. In: *English Translation, and Commentary, Columbus, Ohio* (1956).

[13] C Linnaeus. “Flora Zeylanica”. In: *Sumtu & Literis Laurentii Salvii [Lars Salvius], Holmiae [Stockholm], Sweden* (1747).

[14] Franz Ulrich Theodosius Aepinus. “Mémoire concernant quelques nouvelles expériences électriques remarquables”. In: *Histoire de l’Academie Royale deas Sciences et Belles Lettres* (1756), pp. 105–121.

[15] Sidney B. Lang. "The history of pyroelectricity: From ancient greece to space missions". In: *Ferroelectrics* 230.1 (1999), pp. 99–108. DOI: `10.1080/00150199908214903`. eprint: `https://doi.org/10.1080/00150199908214903`. URL: `https://doi.org/10.1080/00150199908214903`.

[16] René Just Haüy. *Traité de minéralogie*. Vol. 1. Chez Louis, 1801.

[17] Antoine César Becquerel. *Expériences sur le développement de l'électricité par la pression: lois de ce développement*. 1823.

[18] Gustav Gautschi. "Piezoelectric sensors". In: *Piezoelectric Sensorics*. Springer, 2002, pp. 73–91.

[19] Jiří Erhart, Petr Půlpán, and Martin Pustka. *Piezoelectric Ceramic Resonators*. Springer, 2017.

[20] Jacques Curie. "Développement par compression de l'électricité polaire dans les cristaux hémièdres à faces inclinées". In: *Bull. Soc. Fr. Mineral.* 3 (1880), p. 90.

[21] J Curie and P Curie. *Comptes Rendus Academie de Science 91*. 1880.

[22] W G Hankel. "Uber die aktinound piezoelektrischen eigenschaften des bergkrystalles und ihre beziehung zu den thermoelektrischen". In: *Abh. Sachs* 12 (1881), p. 457.

[23] Gabriel Lippmann. "Principe de la conservation de l'électricité, ou second principe de la théorie des phénomènes électriques". In: *J. Phys. Theor. Appl.* 10.1 (1881), pp. 381–394.

[24] W Voigt. "General theory of the piezo-and pyroelectric properties of crystals". In: *Abh. Gott* 36.1 (1890).

[25] Woldemar Voigt. "Beiträge zur molecularen Theorie der Piëzoelectricität". In: *Annalen der Physik* 287.4 (1894), pp. 638–660.

[26] W Voigt. *Kristallphysik*. 1910.

[27] Warren P Mason. "Piezoelectricity, its history and applications". In: *The Journal of the Acoustical Society of America* 70.6 (1981), pp. 1561–1566.

[28] Angela D'Amico and Richard Pittenger. *A brief history of active sonar*. Tech. rep. SPpace and Naval Warfare Systems Center San Diego, CA, 2009.

[29] Pavel Mokry. "100 years of piezoelectric materials in acoustics: from a sonar to active metasurfaces". In: *Proceedings of meetings on acoustics 22ICA*. Vol. 28. 1. ASA. 2016, p. 045008.

[30] Joseph Valasek. "Piezo-electric and allied phenomena in Rochelle salt". In: *Physical review* 17.4 (1921), p. 475.

[31] Jan Fousek. "Joseph valasek and the discovery of ferroelectricity". In: *Applications of Ferroelectrics, 1994. ISAF'94., Proceedings of the Ninth IEEE International Symposium on*. IEEE. 1991, pp. 1–5.

[32] E Schrödinger. "Studien über Kinetik der Dielektrika, den Schmelzpunkt, Pyro-und Piezoelektrizität". In: *Wien. Ber.-1912.-Abt. A* 2 (1912), pp. 1937–1973.

[33] Walter-G Cady. "The piezo-electric resonator". In: *Proceedings of the Institute of Radio Engineers* 10.2 (1922), pp. 83–114.

[34] Don Berlincourt. "Piezoelectric ceramics: Characteristics and applications". In: *The Journal of the Acoustical Society of America* 70.6 (1981), pp. 1586–1595.

[35] Albert Frederick Devonshire. "XCVI. Theory of barium titanate: Part I". In: *The London, Edinburgh, and Dublin Philosophical Magazine and Journal of Science* 40.309 (1949), pp. 1040–1063.

[36] AF Devonshire. "CIX. Theory of barium titanate—Part II". In: *The London, Edinburgh, and Dublin Philosophical Magazine and Journal of Science* 42.333 (1951), pp. 1065–1079.

[37] B Jaffe, RS Roth, and S Marzullo. "Piezoelectric properties of lead zirconate-lead titanate solid-solution ceramics". In: *Journal of Applied Physics* 25.6 (1954), pp. 809–810.

[38] Dragan Damjanovic. "Ferroelectric, dielectric and piezoelectric properties of ferroelectric thin films and ceramics". In: *Reports on Progress in Physics* 61.9 (1998), p. 1267.

[39] A Meitzler et al. *IEEE standard on piezoelectricity*. 1988.

[40] Piezo Institute. *Standards*. 2015. URL: `http://www.piezoinstitute.com/resources/standards/` (visited on 11/25/2015).

[41] Military Standard. "Piezoelectric ceramic material and measurements guidelines for sonar transducers". In: *MILSTD-1376B, February* 24 (1995).

[42] Victor Giurgiutiu. "Piezoelectricity principles and materials". In: *Encyclopedia of structural health monitoring* (2009).

[43] British Standard. "Piezoelectric properties of ceramic materials and components-Part 2: Methods of measurement–Low power". In: *BS EN* (2002), pp. 50324–2.

[44] Markys G Cain and Mark Stewart. "Standards for Piezoelectric and Ferroelectric Ceramics". In: *Characterisation of Ferroelectric Bulk Materials and Thin Films*. Springer, 2014, pp. 267–275.

[45] TC 49. *Guide to dynamic measurements of piezoelectric ceramics with high electromechanical coupling*. 1979.

[46] M Kadota et al. "EMAS-6100, Standard of Electronic Materials Manufacturers Association of Japan". In: *Tokyo: Piezoelectric Ceramics Technical Committee* (1993).

[47] Gene H Haertling. "Ferroelectric ceramics: history and technology". In: *Journal of the American Ceramic Society* 82.4 (1999), pp. 797–818.

[48] GH Kwei et al. "Structures of the ferroelectric phases of barium titanate". In: *The Journal of Physical Chemistry* 97.10 (1993), pp. 2368–2377.

[49] DW Robertson. "Lead titanate". In: *Industrial & Engineering Chemistry* 28.2 (1936), pp. 216–218.

[50] B Jaffe, RS Roth, and S Marzullo. "Properties of piezoelectric ceramics in the solid-solution series lead titanate-lead zirconate-lead oxide: tin oxide and lead titanate-lead hafnate". In: *Journal of research of the National Bureau of Standards* 55.5 (1955), pp. 239–254.

[51] Edward D Palik. *Handbook of optical constants of solids*. Vol. 3. Academic press, 1998.

[52] *INRAD Lithium Niobate Datashet*. Lambda Photometrics Ltd. 2014.

[53] Isaak D Mayergoyz and Göran Engdahl. *Handbook of giant magnetostrictive materials*. Elsevier, 1999.

[54] Elena Aksel and Jacob L Jones. "Advances in lead-free piezoelectric materials for sensors and actuators". In: *Sensors* 10.3 (2010), pp. 1935–1954.

[55] Shinichiro Kawada et al. "(K, Na) NbO3-based multilayer piezoelectric ceramics with nickel inner electrodes". In: *Applied Physics Express* 2.11 (2009), p. 111401.

[56] T Takenaka. "Lead-free piezo-ceramics". In: *Advanced Piezoelectric Materials*. Elsevier, 2010, pp. 130–170.

[57] Victor Giurgiutiu and Sergey Edward Lyshevski. *Micromechatronics: Modeling, analysis, and design with MATLAB*. CRC Press, 2009.

[58] Manhal Souleiman et al. “Hydrothermal growth of large piezoelectric single crystals of GaAsO 4”. In: *Journal of Crystal Growth* 397 (2014), pp. 29–38.

[59] Il Hyoung Jung et al. “Ca 3 Ga 2 Ge 4 O 14 (CGG)-type Sr 3 Nb 0.95 Ga 3.083 Si 2 O 14 single crystal grown by the Czochralski method for piezoelectric applications”. In: *Materials Letters* 51.2 (2001), pp. 129–134.

[60] Hiroshi Maiwa et al. “Electromechanical properties of Nd-doped Bi4Ti3O12 films: A candidate for lead-free thin-film piezoelectrics”. In: *Applied physics letters* 82.11 (2003), pp. 1760–1762.

[61] Jin-Ho Choy, Yang-Su Han, and Jin-Tai Kim. “Hydroxide coprecipitation route to the piezoelectric oxide Pb (Zr, Ti) O3 (PZT)”. In: *J. Mater. Chem.* 5.1 (1995), pp. 65–69.

[62] Moon-Ho Lee, Arvind Halliyal, and Robert E Newnham. “Poling studies of piezoelectric composites prepared by coprecipitated PbTiO3 powder”. In: *Ferroelectrics* 87.1 (1988), pp. 71–80.

[63] Marin Cernea et al. “Sol-gel synthesis and characterization of BaTiO 3-doped (Bi 0.5 Na 0.5) TiO 3 piezoelectric ceramics”. In: *Journal of Alloys and Compounds* 490.1 (2010), pp. 690–694.

[64] Kui Yao et al. “Screen-printed piezoelectric ceramic thick films with sintering additives introduced through a liquid-phase approach”. In: *Sensors and Actuators A: Physical* 118.2 (2005), pp. 342–348.

[65] Ya-dan Li et al. “The influence of heat treatments on the thermoelectric properties of copper selenide thin films prepared by ion beam sputtering deposition”. In: *Journal of Alloys and Compounds* 658 (2016), pp. 880–884.

[66] CM Foster et al. “Single-crystal Pb (ZrxTi1- x) O3 thin films prepared by metal-organic chemical vapor deposition: Systematic compositional variation of electronic and optical properties”. In: *Journal of Applied Physics* 81.5 (1997), pp. 2349–2357.

[67] Hideaki Adachi et al. “Ferroelectric (Pb, La)(Zr, Ti) O3 epitaxial thin films on sapphire grown by rf-planar magnetron sputtering”. In: *Journal of applied physics* 60.2 (1986), pp. 736–741.

[68] Robert Eason. *Pulsed laser deposition of thin films: applications-led growth of functional materials*. John Wiley & Sons, 2007.

[69] James Mulling et al. “Load characterization of high displacement piezoelectric actuators with various end conditions”. In: *Sensors and Actuators A: Physical* 94.1 (2001), pp. 19–24.

[70] Stephanie A Wise. “Displacement properties of RAINBOW and THUNDER piezoelectric actuators”. In: *Sensors and Actuators A: Physical* 69.1 (1998), pp. 33–38.

[71] JW Waanders. *Piezoelectric ceramics: properties and applications*. NV Philips’ Gloeilampenfabrieken, 1991.

[72] *Antiflutter Demonstrator with Piezoelectric Actuators (AFDPA)*. 2013.

[73] Michael Sinapius et al. “DLR’s Morphing Wing Activities within the European Network”. In: *Procedia IUTAM* 10 (2014), pp. 416–426.

[74] Troy Anthony Probst. “Evaluating the aerodynamic performance of MFC-actuated morphing wings to control a small UAV”. PhD thesis. Virginia Tech, 2012.

[75] Onur Bilgen. “Aerodynamic and electromechanical design, modeling and implementation of piezocomposite airfoils”. PhD thesis. Virginia Tech, 2010.

[76] Peter L Bishay et al. “Development of a New Span-Morphing Wing Core Design”. In: *Designs* 3.1 (2019), p. 12.

[77] Jesee Kimaru and Abdessalem Bouferrouk. “Design, manufacture and test of a camber morphing wing using MFC actuated mart rib”. In: *2017 8th International Conference on Mechanical and Aerospace Engineering (ICMAE)*. IEEE. 2017, pp. 791–796.

[78] Lauren Butt et al. “Wing morphing design utilizing macro fiber composite smart materials”. In: *69th Annual Conference of The Society of Allied Weight Engineers, Virginia Beach, Virginia*. 2010.

[79] Onur Bilgen et al. “Morphing wing aerodynamic control via macro-fiber-composite actuators in an unmanned aircraft”. In: *AIAA Infotech@ Aerospace 2007 Conference and Exhibit*. 2007, p. 2741.

[80] AF Devonshire. “Theory of ferroelectrics”. In: *Advances in physics* 3.10 (1954), pp. 85–130.

[81] John Grindlay. *An Introduction to the Phenomenological Theory of Ferroelectricity: International Series of Monographs In: Natural Philosophy*. Vol. 26. Elsevier, 2013.

[82] John Frederick Nye. *Physical properties of crystals: their representation by tensors and matrices*. Oxford university press, 1985.

[83] Nikhil Shelke. *Ferroelectric Materials – Theory, Properties and applications*. 2010. URL: `http://www.indiastudychannel.com/resources/117961-Ferroelectric-Materials-Theory-Properties-and-applications.aspx` (visited on 10/28/2015).

[84] Karin M Rabe. “Antiferroelectricity in oxides: a reexamination”. In: *Department of Physics and Astronomy* (2012).

[85] N Srivastava and GJ Weng. “A theory of double hysteresis for ferroelectric crystals”. In: *Journal of applied physics* 99.5 (2006), p. 054103.

[86] Phil Jeffrey. *X-ray Data Collection Course*. 2006. URL: `http://xray0.princeton.edu/~phil/Facility/Guides/XrayDataCollection.html` (visited on 12/03/2015).

[87] William D Callister, David G Rethwisch, et al. *Materials science and engineering: an introduction*. Vol. 7. Wiley New York, 2007.

[88] Shao-Liang Zheng. *Introduction of Chemical Crystallography*. 2014. URL: `http://chemistry.fas.nyu.edu/docs/IO/32861/Shaoliang_Zheng1.pdf` (visited on 12/03/2015).

[89] C Klein and CS Hurlbut. *Manual of Mineralogy*. John Wiley: New York, 1985.

[90] Rocks in my head too. *Crystal systems*. 2009. URL: `http://www.rocksinmyheadtoo.com/Systems.htm` (visited on 12/04/2015).

[91] Donald Clark. *What are Crystal Systems and Mineral Habits?* 2016. URL: `https://www.gemsociety.org/article/mineral-habits/` (visited on 12/08/2015).

[92] Australian museum desin unit. *Crystal group 7: Tetragonal - Prism and Pyramid*. 2009. URL: `http://australianmuseum.net.au/image/crystal-group-7-tetragonal-prism-pyramid` (visited on 12/08/2015).

[93] Gemology online. *Crystal systems*. URL: `http://www.gemologyonline.com/crystal_systems.html` (visited on 12/10/2015).

[94] Teravolt. *Pyrite cubes*. 2010. URL: `https://commons.wikimedia.org/wiki/File:Pyrite_Cubes.JPG` (visited on 12/08/2015).

[95] Edward Prince et al. *International tables for crystallography*. International Union of Crystallography, 1999.

[96] Salvador Galí Medina. *Cristal·lografia: teoria reticular, grups puntuals i grups espacials*. Promociones y Publicaciones Universitarias, PPU, 1993.

[97] Donald E Sands. *Introduction to crystallography*. Courier Corporation, 2012.

[98] B Jaffe and WR Cook. *H. Jaffe, Piezoelectric Ceramics*. 1971.

[99] Hammad Nazeer et al. “Compositional dependence of the Young’s modulus and piezoelectric coefficient of (110)-oriented pulsed laser deposited PZT thin films”. In: *Journal of microelectromechanical systems* 24.1 (2015), pp. 166–173.

[100] Wei Qiu and Huey Hoon Hng. “Effects of dopants on the microstructure and properties of PZT ceramics”. In: *Materials chemistry and physics* 75.1-3 (2002), pp. 151–156.

[101] RA Pferner, G Thurn, and F Aldinger. “Mechanical properties of PZT ceramics with tailored microstructure”. In: *Materials chemistry and physics* 61.1 (1999), pp. 24–30.

[102] C Tănăsoiu, E Dimitriu, and C Miclea. “Effect of Nb, Li doping on structure and piezoelectric properties of PZT type ceramics”. In: *Journal of the European Ceramic Society* 19.6-7 (1999), pp. 1187–1190.

[103] Sergey Edward Lyshevski and Victor Giurgiutiu. *Micromechatronics: Modeling, analysis, and design with MATLAB*. CRC Press, 2003.

[104] Martin H Sadd. *Elasticity: theory, applications, and numerics*. Academic Press, 2009.

[105] Saleem Hashmi. *Comprehensive materials processing*. Newnes, 2014.

[106] Jiří Erhart. *Piezoelectricity and ferroelectricity: phenomena and properties*. 2014.

[107] Kenji Uchino. *Introduction to piezoelectric actuators and transducers*. Tech. rep. Pennsylvania State University Park, 2003.

[108] Shiv P Joshi. “Non-linear constitutive relations for piezoceramic materials”. In: *Smart Materials and Structures* 1.1 (1992), p. 80.

[109] Yaowen Yang and Deepesh Upadrashta. “Modeling of geometric, material and damping nonlinearities in piezoelectric energy harvesters”. In: *Nonlinear Dynamics* 84.4 (2016), pp. 2487–2504.

[110] Jose-Manuel Rodriguez-Fortun et al. “Hysteresis in piezoelectric actuators: Modeling and compensation”. In: *IFAC Proceedings Volumes* 44.1 (2011), pp. 5237–5242.

[111] Ping Ge and Musa Jouaneh. “Modeling hysteresis in piezoceramic actuators”. In: *Precision engineering* 17.3 (1995), pp. 211–221.

[112] CV Newcomb and I Flinn. “Improving the linearity of piezoelectric ceramic actuators”. In: *Electronics Letters* 18.11 (1982), pp. 442–444.

[113] Isaak D Mayergoyz. *Mathematical models of hysteresis*. Springer Science & Business Media, 2012.

[114] Peter J Chen and Stephen T Montgomery. “A macroscopic theory for the existence of the hysteresis and butterfly loops in ferroelectricity”. In: *Ferroelectrics* 23.1 (1980), pp. 199–207.

[115] Gordon E Martin. “Dielectric, elastic and piezoelectric losses in piezoelectric materials”. In: *1974 Ultrasonics Symposium*. IEEE. 1974, pp. 613–617.

[116] Albert Arnau Cubillo. “Considerations on piezoelectricity: mathematical models, crystallography and numerical simulations”. In: (2016).

[117] Lica Flore and Albert Arnau Cubillo. “Dynamic Mechanical Analysis of an Aircraft Wing with emphasis on vibration modes change with loading”. In: *Scientific Research & Education in the Air Force-AFASES* 2 (2015).

[118] *Spider 8-30 Operating manual*. B0405-7.0. Hottinger Baldwin Messtechnick - HBM.

[119] *Material data. Specific parameters of the standard materials.* 2015.

[120] Carlos De Marqui Junior et al. “Identification of flutter parameters for a wing model”. In: *Journal of the Brazilian Society of Mechanical Sciences and Engineering* 28.3 (2006), pp. 339–346.

[121] Project Coordinator: Ioan Ursu. “Raport stiinţific si tehnic in extenso privind implementarea proiectului in perioada septembrie – decembrie 2014”. In: (2014).

[122] Yuan Cheng Fung. *An introduction to the theory of aeroelasticity*. Courier Dover Publications, 2008.

[123] Bernard Jaffe, William R Cook, and Hans Jaffe. “Piezoelectric ceramics”. In: (1971).

[124] Thomas R Shrout and Shujun J Zhang. “Lead-free piezoelectric ceramics: Alternatives for PZT?” In: *Journal of Electroceramics* 19.1 (2007), pp. 113–126.

[125] Daniel J Inman. “Engineering vibration”. In: (1996).

[126] David J Ewins. *Modal testing: theory and practice*. Vol. 15. Research studies press Letchworth, 1984.

[127] Ray W Clough. “Analysis of structural vibrations and dynamic response”. In: *Recent advances in matrix methods of structural analysis and design* (1971), pp. 441–486.

[128] M Provansal, C Mathis, and L Boyer. “Bénard-von Kármán instability: transient and forced regimes”. In: *Journal of Fluid Mechanics* 182 (1987), pp. 1–22.

[129] Ioan Ursu et al. “Mathematical modeling of a V-stack piezoelectric aileron actuation”. In: *INCAS Bulletin* 8.4 (2016), p. 141.

[130] Marius Stoia. “Surface Pressure Sensitivities for the Measurement of the Mach Number and Angle of Attack of unsteady Flows”. In: *Proceedings of the 2016 Congress Mathematical Problem In Engineering, Aerospace And Science* (2016).

[131] Marius Stoia. “Aeroelastic investigations of disc wing UAV”. In: *Proceedings of the 2016 Congress Mathematical Problem In Engineering, Aerospace And Science* (2016).

[132] Florin Mingireanu and Marius Stoia-Djeska. “A local sensitivity analysis of some performances of reactive projectiles, rockets and missiles”. In: *Proceedings of the International Conference of Aerospace Sciences “Aerospatial 2016"* (2016).

[133] Daniela Enciu et al. “Piezo active sensors and piezo actuators for space and aerospace applications”. In: *Proceedings of the 41st Congress of the Roman-American Academy of Art and Science* (2017).

[134] Dragos D Guta et al. “A V-stack piezoelectric actuator for active mitigation of flutter – design and laboratory tests”. In: *Proceedings of the 5th International Workshop on Numerical Modelling in Aerospace Sciences* (2017).

[135] Oana Dumitrescu, Bogdan Gherman, and Valeriu Dragan. “Study of the Instability due the Different Position of an Aileron”. In: *Proceedings of the 13th International Conference on System Science and Simulation in Engineering* (2017).

[136] Ioan Ursu et al. “Aeroelastic investigations of disc wing UAV”. In: *Proceedings of the 6th CEAS Air & Space Conference* (2017).